



**Department of Materials Science and Engineering
University of Sheffield**

The Influence of Steel Composition on the Strain Ageing Response of High Strength Pearlitic Wire

Benjamin Jones

**This thesis is submitted as a requirement for the degree of
*Doctor of Engineering***

Submitted December 2020

Abstract

The aim of the EngD was to identify if cost effective compositional adjustments can be made to a commercial high carbon steel to retard or even eliminate the strain ageing reaction observed in cold drawn high strength wire. This was tested via the production of a set of experimental steels, with systematically varied compositions, identified after a literature review, discussions with British Steel on previous work/experience and thermodynamic modelling of the cementite stability. The experimental steels were produced in a vacuum induction melt furnace to ensure precise control over composition, forged and hot rolled to rod. The rod samples were then heat treated to the appropriate starting microstructure (fully pearlitic) and drawn to wire. The set of experimental steels were artificially aged and tested alongside a commercially produced steel wire for comparison. A selection of available global and localised experimental techniques was used to characterise the strain ageing response: DSC, Torsion and Tensile Testing, Magnetic Sensors, (S)TEM and APT.

Generally, high variation was observed during testing. The heterogeneous pearlitic microstructure following severe plastic deformation and the subsequent strain ageing response leads to localised regions of enhanced cementite dissolution, which leads to variation of mechanical properties during testing. Differential scanning calorimetry measurements suggested a nickel addition may partially delay the initial stage of strain ageing. Magnetic sensor measurements showed clear differences between steel compositions, although the differences cannot be exclusively attributed to the strain ageing response, as the redistribution of alloying elements or carbide precipitation is likely contributing.

Chemical analysis of carbon resulted a great deal of measurement error, which made accurate determination of carbon concentration challenging. Measured differences between steel compositions in the carbon concentration of cementite were attributed to error and experimental variation. Significantly more chemical analysis data is required to ascertain if alloying elements can improve cementite stability with strain ageing. However, energy dispersive x-ray spectroscopy suggested carbon may be segregating to dislocations, which has also been reported in the literature. Thus, suggesting a dislocation based mechanism of cementite dissolution may be active.

The effects of silicon, nickel, cobalt and vanadium on the strain ageing kinetics require further characterisation over a wider range of drawing and ageing conditions to determine their suitability for commercial use. However, when considering the improved ductility of a nickel containing steel shown in section 3.1 - British Steel R&D Study - Influence of Nickel on Pearlite Stability and the potentially delayed initial stage of strain ageing, as observed by DSC observations (Figure 6:1), a nickel addition may in fact have a minor beneficial effect on torsional ductility with strain ageing. Reducing manganese content as much as reasonably achievable is also recommended. Therefore, alternative alloying additions may be required to meet tensile strength specifications. Silicon may be a suitable alternative. Vanadium is also effective at increasing tensile strength and may be suitable. Vanadium carbides or nitrides may provide alternative strengthening following the dissolution of cementite, or where amorphous cementite is present following severe wire drawing.

Correspondence

Ben Jones
+447790182490
Jones25677@gmail.com

Acknowledgements

I would like to thank my supervisors Prof. Mark Rainforth and Shaun Hobson for your continued patience, understanding and guidance. I am grateful to Dr Martin Strangwood and Dr Sally Parker for their valuable help with thermodynamic modelling; Dr Mohsen Aghadavoudi-Jolfaei for your continued enthusiasm in the development of magnetic sensors; Dr Peng Gong and Dr John Nutter for their frequent guidance and assistance with equipment.

I am also thoroughly grateful to all staff at British Steel, Bekaert and the University of Sheffield who have been extremely accommodating throughout my EngD.

Contents

Abstract.....	2
Correspondence.....	4
Acknowledgements.....	4
List of Figures	11
List of Tables	23
List of Equations.....	29
1 Introduction	30
1.1 Aims & Objectives	32
2 Literature Review.....	33
2.1 Steel Wire Production	33
2.2 Drawn Pearlitic Steel Wire	34
2.3 The Strain Ageing Response	43
2.4 Methods to Observe Strain Ageing.....	47
2.4.1 Global Experimental Techniques	47
2.4.2 Localised experimental techniques	54
2.5 Cementite Dissolution.....	62
2.6 Steel Composition	72
2.7 Summary	83

3	Experimental Steel Development	87
3.1	British Steel R&D Study - Influence of Nickel on Pearlite Stability	88
3.1.1	Atom Probe Tomography.....	90
3.2	Thermodynamic Modelling	92
3.2.1	Methodology.....	92
3.2.2	Cementite Thermal Stability	96
3.2.3	Alloying Element Distribution	113
3.2.4	Multi Element Simulations.....	123
3.3	Experimental Steel Composition Selection	126
3.3.1	Manganese.....	127
3.3.2	Nickel.....	128
3.3.3	Silicon	129
3.3.4	Cobalt	130
3.3.5	Vanadium	131
3.3.6	Alloy Cost	132
3.3.7	Chromium and Molybdenum.....	132
3.4	Chapter summary.....	134
4	Materials and Methods.....	135
4.1	Experimental Steel Production	135
4.1.1	Rod Heat Treatment Trials.....	137

4.2	Wire Drawing Methodology.....	145
4.2.1	Single Pass Lab Drawing Bench.....	147
4.2.2	Wire Drawing Summary.....	154
4.3	Artificial Ageing.....	155
4.4	Tensile Testing.....	156
4.5	Torsion Testing.....	157
4.6	Magnetic Sensors.....	158
4.7	Differential Scanning Calorimetry.....	160
4.7.1	Data Analysis.....	162
4.8	Microscopy.....	164
4.9	Atom Probe Tomography.....	165
4.9.1	FIB - Lift out method.....	165
4.10	Chapter Summary.....	167
5	Results.....	168
5.1	Tensile Testing.....	168
5.1.1	UTS and 0.2% Proof Stress Summary.....	169
5.1.2	Tensile Elongation to Failure Summary.....	171
5.1.3	0.2% Proof Stress to UTS Ratio Summary.....	173
5.1.4	Tensile Testing Results Summary.....	175
5.2	Torsion Testing.....	178

5.2.1	Revolutions to Failure Summary.....	179
5.2.2	Torsion Testing Results Summary.....	181
5.3	Magnetic Sensors.....	185
5.4	Differential Scanning Calorimetry.....	187
5.4.1	Differential Scanning Calorimetry Results Summary.....	191
5.5	Micrographs.....	192
5.5.1	Commercial Steel.....	192
5.5.2	0.8Si + 0.5Ni + 0.1Co Steel BJ5.....	196
5.5.3	0.8Si + 0.5Ni + 0.1Co + 0.1V Steel BJ6.....	202
5.5.4	Cementite Lamellae Thickness Summary.....	206
5.6	Chemical Analysis.....	209
5.6.1	STEM Energy Dispersive X-ray Spectroscopy.....	209
5.6.2	Atom Probe Tomography.....	215
5.6.3	Chemical Analysis Summary.....	222
6	Discussion.....	225
6.1	Mechanical Testing.....	225
6.2	Magnetic Sensors.....	227
6.3	DSC.....	229
6.4	Transmission Electron Microscopy.....	233
6.5	Chemical Analysis.....	234

6.6	Commercial Steel	235
6.7	Steel BJ3	236
6.8	Steel BJ4	236
6.9	Steel BJ5	238
6.10	Steel BJ6.....	239
6.11	Cementite Dissolution	241
6.12	Discussions Summary	242
7	Conclusions	244
7.1	Recommendations and Future work.....	247
8	References	249
9	Appendix.....	260
9.1	Multi-Pass Wire Drawing Machine - Bekaert Technology Centre	260
9.1.1	Rod Preparation and Characterisation	260
9.1.2	Wire Drawing	263
9.1.3	Spark Analysis	268
9.1.4	Multi-pass Wire Drawing Machine Summary.....	273
9.2	Tensile Testing Data	274
9.2.1	Commercial Steel	274
9.2.2	0.8Si Steel (BJ3).....	282
9.2.3	0.8Si + 0.5Ni Steel (BJ4).....	290

9.2.4	0.8Si + 0.5Ni + 0.1Co Steel (BJ5)	298
9.2.5	0.8Si + 0.5Ni + 0.1Co + 0.1V Steel BJ6.....	306
9.3	Torsion Testing Data.....	314
9.3.1	Commercial Steel	314
9.3.2	0.8Si Steel (BJ3).....	322
9.3.3	0.8Si + 0.5 Ni Steel (BJ4).....	330
9.3.4	0.8Si + 0.5Ni + 0.1Co Steel (BJ5)	338
9.3.5	0.8Si + 0.5Ni + 0.1Co + 0.1V Steel (BJ6)	345
9.4	Differential Scanning Calorimetry Data	353
9.4.1	Commercial Steel	353
9.4.2	0.8 Si Steel (BJ3)	354
9.4.3	0.8 Si + 0.5 Ni Steel (BJ4).....	355
9.4.4	0.8 Si + 0.5 Ni + 0.1 Co Steel (BJ5).....	356
9.4.5	0.8 Si + 0.5 Ni + 0.1 Co + 0.1 V Steel (BJ6).....	357

List of Figures

Figure 2:1 - Rod microstructure prior to wire drawing.	35
Figure 2:2 - Texture development during wire drawing, micrographs taken during preliminary EngD study.	35
Figure 2:3 - Variation in pearlite realignment based on initial orientation to drawing direction [4].	36
Figure 2:4 - HRTEM image of ferrite cementite interface [7].	37
Figure 2:5 - a. Undeformed cementite, b. low-strain deformed cementite and c. heavily deformed cementite [7].	37
Figure 2:6 - Transverse cross section of a drawn wire undergoing curling of pearlite grains due to wire drawing [8].	38
Figure 2:7 - Curling resulting in apparent lamellae spacing variation [9].	39
Figure 2:8 – Brightfield STEM micrograph of drawn pearlite ($\epsilon=2.03$).	40
Figure 2:9 - 180° Clockwise rotation of atom probe tomography approximation of cementite lamellae morphology (7 at. %C iso-surface). Image corresponds to atom probe data set shown in Figure 5:36.	41
Figure 2:10 - Illustration of the change in mechanical properties with strain ageing.	44
Figure 2:11 - Carbon-dislocation interaction illustration [23].	46
Figure 2:12 - a. Ductile type A torsion fracture of an as drawn wire b. Brittle Type C torsion fracture of an aged wire.	47
Figure 2:13 - DSC Analysis change due to differing heat treatments [14].	49
Figure 2:14 - a. DSC Scan of a cold drawn pearlitic wire $\epsilon = 5$. b. Electrical resistivity of cold drawn pearlitic wire $\epsilon = 5$ [1].	51

Figure 2:15 - TEP and Internal Friction background evolution of as drawn wires [29].	52
Figure 2:16 - Change in rate of cementite dissolution with drawing strain [9].	53
Figure 2:17 - STEM Image with EELS C concentration plot [37].	55
Figure 2:18 - iso-strain and iso-stress conditions.	56
Figure 2:19 - APT reconstruction of carbon atoms. Parallel to drawing direction [44].	58
Figure 2:20 - APT reconstruction perpendicular to drawing direction [44].	59
Figure 2:21 - 3D atom maps of C and Fe in wires with a drawing strain of 2 and 5. 2% of Fe atoms and 20% of C atoms are displayed [45].	60
Figure 2:22 - TEM Measurements of the change in ILS and cementite lamellae thickness with drawing strain [47].	63
Figure 2:23 - Simplified illustration of dislocation drag mechanism [52].	68
Figure 2:24 - Change in UTS with drawing strain [9].	69
Figure 2:25 - Change in yield strength with drawing strain [29].	69
Figure 2:26 - Change in UTS and Yield strength with drawing strain [8].	69
Figure 2:27 - Variation of net charge/bond energy with solute atom in cementite [55].	72
Figure 2:28 - Atom probe reconstruction of pearlite, vanadium and carbon distribution [63].	76
Figure 3:1 - 80x80x210nm Atom probe tomography reconstruction of a drawn pearlitic wire[68].	90
Figure 3:2 - Carbon concentration across line scan [68].	90
Figure 3:3 - Element concentration across line scan [68].	91
Figure 3:4 - Example cooling simulation. A circle highlights where the cementite transformation temperature was measured.	94

Figure 3:5 - Silicon distribution during austenite to pearlite transformation.	95
Figure 3:6 - Influence of cobalt on cementite transformation behaviour.....	97
Figure 3:7 - Influence of cobalt content on cementite start and finish transformation temperature.....	97
Figure 3:8 - Influence of chromium on cementite transformation behaviour.....	99
Figure 3:9 - Influence of chromium content on cementite start and finish transformation temperature.....	99
Figure 3:10 - Influence of copper on cementite transformation behaviour.	101
Figure 3:11 - Influence of copper content on cementite start and finish transformation temperature.....	101
Figure 3:12 - Influence of manganese on cementite transformation behaviour.....	103
Figure 3:13 - Influence of manganese content on cementite start and finish transformation temperature.....	103
Figure 3:14 - Influence of molybdenum on cementite transformation behaviour.	105
Figure 3:15 - Influence of molybdenum content on cementite start and finish transformation temperature.....	105
Figure 3:16 - Influence of nickel on cementite transformation behaviour.	107
Figure 3:17 - Influence of nickel content on cementite start and finish transformation temperature.....	107
Figure 3:18 - Influence of silicon on cementite transformation behaviour.	109
Figure 3:19 - Influence of silicon content on cementite start and finish transformation temperature.....	109
Figure 3:20 - Influence of vanadium on cementite transformation behaviour.....	111

Figure 3:21 - Influence of vanadium content on cementite start and finish transformation temperature.....	111
Figure 3:22 - Effect on cementite transformation temperature of each simulated alloying element.....	112
Figure 3:23 - Simulated cobalt distribution during equilibrium cooling.....	114
Figure 3:24 - Simulated chromium distribution during equilibrium cooling.	115
Figure 3:25 - Simulated copper distribution during equilibrium cooling.	116
Figure 3:26 - Simulated manganese distribution during equilibrium cooling.	117
Figure 3:27 - Simulated molybdenum distribution during equilibrium cooling.	118
Figure 3:28 - Simulated nickel distribution during equilibrium cooling.	119
Figure 3:29 - Simulated silicon distribution under equilibrium cooling.	120
Figure 3:30 - Simulated vanadium distribution under equilibrium cooling.	121
Figure 3:31 - Multi element thermodynamic simulation calculated cementite transformation temperatures.	124
Figure 3:32 - Empirical relationship derived by Y. Kanetsuki et al. [58].....	130
Figure 4:1 - 0.8Si steel volume fraction point count results.....	139
Figure 4:2 - 0.8 Si + 0.5Ni Steel plotted volume fraction point count results.	141
Figure 4:3 - 0.8 Si + 0.5 Ni + 0.1 Co Steel plotted volume fraction point count results.	142
Figure 4:4 - 0.8 Si + 0.5 Ni + 0.1 Co + 0.1 V Steel plotted volume fraction point count results.	143
Figure 4:5 - Rod Feedstock Micrographs.	150
Figure 4:6 - Average measured pearlite lath spacing plotted with 95% confidence limits...	151
Figure 4:7 - Single pass lab drawing bench.....	153

Figure 4:8 - 0.2% Proof Stress Calculation.....	156
Figure 4:9 - Wire Torsion Test Fracture Classification [71].....	157
Figure 4:10 - Magnetic measurements of a 60mm length of wire ($\epsilon = 1.52$) [72].....	159
Figure 4:11 - Magnetic measurements of a 60mm length of wire ($\epsilon = 1.88$) [72].	159
Figure 4:12 - Machine baseline data.....	161
Figure 4:13 - Anchor points for calculate fitted line.	162
Figure 4:14 - Fitted line (Red) Plotted over sample data with machine baseline subtracted (Black).....	163
Figure 4:15 - Sample data - calculated deviation from fitted line.	163
Figure 4:16 - Curve integration to obtain enthalpy of change.	164
Figure 4:17 - FIB Lift out preparation technique [76].....	166
Figure 5:1 - UTS and 0.2 % proof stress mean with 95% confidence limits: a. Commercial Steel, b. Steel BJ3, c. Steel BJ4, d. Steel BJ5 and e. Steel BJ6.	169
Figure 5:2 - UTS and 0.2 % proof stress test data summary: a. Commercial Steel, b. Steel BJ3, c. Steel BJ4, d. Steel BJ5 and e. Steel BJ6.....	170
Figure 5:3 - Tensile elongation to failure mean with 95% confidence limits: a. Commercial Steel, b. Steel BJ3, c. Steel BJ4, d. Steel BJ5 and e. Steel BJ6.	171
Figure 5:4 - Tensile elongation to failure data summary: a. Commercial Steel, b. Steel BJ3, c. Steel BJ4, d. Steel BJ5 and e. Steel BJ6.	172
Figure 5:5 - 0.2% Proof Stress to UTS ratio mean with 95% confidence limits: a. Commercial Steel, b. Steel BJ3, c. Steel BJ4, d. Steel BJ5 and e. Steel BJ6.	173
Figure 5:6 - 0.2% Proof Stress to UTS ratio data summary: a. Commercial Steel, b. Steel BJ3, c. Steel BJ4, d. Steel BJ5 and e. Steel BJ6.	174

Figure 5:7 - Revolutions to failure mean with 95% confidence limits: a. Commercial Steel, b. Steel BJ3, c. Steel BJ4, d. Steel BJ5 and e. Steel BJ6.	179
Figure 5:8 - Revolutions to failure data summary: a. Commercial Steel, b. Steel BJ3, c. Steel BJ4, d. Steel BJ5 and e. Steel BJ6.	180
Figure 5:9 - Typical wire breakage caused by a non-metallic inclusion [68].	183
Figure 5:10 - Real inductance measured at a frequency of 100Hz [73].	185
Figure 5:11 - DSC mean peak temperatures with 95% confidence limits: a. Peak 1, b. Peak 2, c. Peak 3 and d. Peak 4.....	188
Figure 5:12 - DSC mean peak enthalpy of change with 95% confidence limits: a. Peak 1, b. Peak 2, c. Peak 3 and d. Peak 4.....	189
Figure 5:13 - Brightfield TEM: Commercial steel, 4 month artificial ageing condition 30k, 50k and 120k magnification.	192
Figure 5:14 - Commercial Steel, 4 month artificial ageing condition at 100k magnification: STEM Bright field, STEM HAADF and STEM Dark field. Scale bar = 0.5 μ m.....	193
Figure 5:15 - Commercial Steel, 4 month artificial ageing condition at 200k magnification: STEM Bright field, STEM HAADF and STEM Dark field. Scale bar = 0.2 μ m.....	194
Figure 5:16 - Apparent cementite lamellae thickness measurements.....	195
Figure 5:17 - Brightfield TEM: Steel BJ5, 4 month artificial ageing condition 30k, 50k and 120k magnification.	196
Figure 5:18 - Steel BJ5 4 month artificial ageing condition at 100k magnification: STEM Bright field, STEM HAADF and STEM Dark field. Scale Bar 0.5 μ m.	197
Figure 5:19 - Steel BJ5 4 month artificial ageing condition at 200k magnification: STEM Bright field, STEM HAADF and STEM Dark field. Scale bar 0.2 μ m	198

Figure 5:20 - Apparent cementite lamellae thickness measurements.....	199
Figure 5:21 - Steel BJ5 4 month artificial ageing condition at 500k magnification: STEM Bright field, STEM HAADF and STEM Dark field.	200
Figure 5:22 - Steel BJ5 4 month artificial ageing condition at 800k magnification: STEM Bright field, STEM HAADF and STEM Dark field.	201
Figure 5:23 – Bright field TEM: Steel BJ5, 4 month artificial ageing condition 30k, 50k, 120k and 1.2M magnification.....	202
Figure 5:24 - Steel BJ6 4 month artificial ageing condition at 100k magnification: STEM Bright field, STEM HAADF and STEM Dark field. Scale bar is 0.5 μ m.	203
Figure 5:25 - Steel BJ6 4 month artificial ageing condition at 200k magnification: STEM Bright field, STEM HAADF and STEM Dark field.	204
Figure 5:26 Apparent cementite lamellae thickness measurements.....	205
Figure 5:27 - Steel BJ5 4 month artificial ageing condition at 500k magnification: STEM Bright field, STEM HAADF and STEM Dark field	206
Figure 5:28 - Mean apparent cementite lamellae thickness with 95% confidence limits. ...	208
Figure 5:29 - Commercial Steel 4 month artificial ageing condition STEM HAADF - EDS Line Scan.....	209
Figure 5:30 - Steel BJ5 4 month artificial ageing condition STEM HAADF EDS line scan.....	211
Figure 5:31 - BJ6 4 month artificial ageing condition STEM HAADF - EDS Line Scan.	213
Figure 5:32 - 2 month artificial ageing condition: Commercial steel sample 1, atom probe reconstruction.....	215
Figure 5:33 - Commercial Steel Sample 1: 7 at.% C Iso concentration surface Proxigram: a. carbon concentration, b. manganese and silicon concentration.	216

Figure 5:34 - 2 month artificial ageing condition: Commercial steel sample 2, atom probe reconstruction.....	217
Figure 5:35 - Commercial Steel Sample 2: 7 at.% carbon Iso-surface Proxigram: a. carbon concentration, b. manganese and silicon concentration.	218
Figure 5:36 - Steel BJ5 4 month artificial ageing condition, atom probe reconstruction.	220
Figure 5:37 - 7 at.% carbon iso-surface average concentration: a. carbon and silicon concentration, b. manganese, nickel and cobalt concentrations.....	221
Figure 6:1 - DSC Scans of the commercial steel and steel BJ4. Observed delay in first stage of ageing with nickel and silicon addition.	231
Figure 9:1 - 5.5mm to 2.5mm wire drawing parameters.	263
Figure 9:2 - 2.5mm - 1.65mm Wire Drawing Parameters.	266
Figure 9:3 - Spark Analysis Report - 17BQ3F10 2.5mm Wire.	269
Figure 9:4 - Spark Analysis Report- 17BQ4 2.5mm wire.....	270
Figure 9:5 - Spark Analysis Report - 17BQ5F5 2.5mm wire.	271
Figure 9:6 - Spark Analysis Report - 17BQ6F7 2.5mm wire.	272
Figure 9:7 - Tensile testing data of the commercial steel in the as-drawn condition.	274
Figure 9:8 - Commercial steel as drawn tensile fractures.	275
Figure 9:9 - Tensile testing data of the commercial steel in the 1 month artificial ageing condition.	276
Figure 9:10 - Commercial Steel 1 month artificial ageing condition tensile fractures.....	277
Figure 9:11 - Tensile testing data of the commercial steel in the 2 month artificial ageing condition.	278
Figure 9:12 - Commercial Steel 2 month artificial ageing condition tensile fractures.....	279

Figure 9:13 - Tensile testing data of the commercial steel in the 2 month artificial ageing condition.	280
Figure 9:14 - Commercial Steel 4 month artificial ageing condition tensile fractures.	281
Figure 9:15 - Tensile testing data of steel BJ3 in the as-drawn condition.	282
Figure 9:16 - Steel BJ3 as drawn tensile fractures.	283
Figure 9:17 - Tensile testing data of steel BJ3 in the 1 month artificial ageing condition. ...	284
Figure 9:18 - Steel BJ3 1 month artificial ageing condition tensile fractures.	285
Figure 9:19 - Tensile testing data of steel BJ3 in the 2 month artificial ageing condition. ...	286
Figure 9:20 - Steel BJ3 1 month artificial ageing condition tensile fractures.	287
Figure 9:21 - Tensile testing data of steel BJ3 in the 4 month artificial ageing condition. ...	288
Figure 9:22 - Steel BJ3 1 month artificial ageing condition tensile fractures.	289
Figure 9:23 - Tensile testing data of steel BJ4 in the as-drawn condition.	290
Figure 9:24 - Steel BJ4 1 as-drawn tensile fractures.	291
Figure 9:25 - Tensile testing data of steel BJ4 in the 1 month artificial ageing condition. ...	292
Figure 9:26 - Steel BJ4 1 month artificial ageing condition tensile fractures.	293
Figure 9:27 - Tensile testing data of steel BJ4 in the 2 month artificial ageing condition. ...	294
Figure 9:28 - Steel BJ4 2 month artificial ageing condition tensile fractures.	295
Figure 9:29 - Tensile testing data of steel BJ4 in the 4 month artificial ageing condition. ...	296
Figure 9:30 - Steel BJ4 4 month artificial ageing condition tensile fractures.	297
Figure 9:31 - Tensile testing data of steel BJ5 in the as-drawn condition.	298
Figure 9:32 - Steel BJ5 as-drawn condition tensile fractures.	299
Figure 9:33 - Tensile testing data of steel BJ5 in the 1 month artificial ageing condition. ...	300
Figure 9:34 - Steel BJ5 1 month artificial ageing condition tensile fractures.	301

Figure 9:35 - Tensile testing data of steel BJ5 in the 2 month artificial ageing condition....	302
Figure 9:36 - Steel BJ5 2 month artificial ageing condition tensile fractures.	303
Figure 9:37 - Tensile testing data of steel BJ5 in the 4 month artificial ageing condition. ...	304
Figure 9:38 - Steel BJ5 4 month artificial ageing condition tensile fractures.	305
Figure 9:39 - Tensile testing data of steel BJ6 in the as-drawn condition.....	306
Figure 9:40 - Steel BJ6 as-drawn tensile fractures.....	307
Figure 9:41 - Tensile testing data of steel BJ6 in the 1 month artificial ageing condition. ...	308
Figure 9:42 - Steel BJ6 1 month artificial ageing condition tensile fractures.	309
Figure 9:43 - Tensile testing data of steel BJ6 in the 2 month artificial ageing condition. ...	310
Figure 9:44 - Steel BJ6 2 month artificial ageing condition tensile fractures.	311
Figure 9:45 - Tensile testing data of steel BJ6 in the 4 month artificial ageing condition. ...	312
Figure 9:46 - Steel BJ6 4 month artificial ageing condition tensile fractures.	313
Figure 9:47 - Torsion testing plot of the commercial steel in the as-drawn condition.	314
Figure 9:48 - Commercial steel as-drawn, type A fractures.	315
Figure 9:49 - Torsion testing plot of the commercial steel in the 1 month artificial ageing condition.	316
Figure 9:50 - Commercial steel 1 month artificial ageing condition, type A fracture.	317
Figure 9:51 - Torsion testing plot of the commercial steel in the 2 month artificial ageing condition.	318
Figure 9:52 - Commercial steel 2 month artificial ageing condition, 3 type C and 1 type A fracture.	319
Figure 9:53 - Torsion testing plot of the commercial steel in the 4 month artificial ageing condition.	320

Figure 9:54 - Commercial steel 4 month artificial ageing condition, type A fracture.	321
Figure 9:55 - Torsion testing plot of steel BJ3 in the as-drawn condition.....	322
Figure 9:56 - Steel BJ3 Torsion test fractures.	323
Figure 9:57 - Torsion testing plot of steel BJ3 in the 1 month artificial ageing condition. ...	324
Figure 9:58 - Steel BJ3 1 month artificial ageing torsion test fractures.	325
Figure 9:59 - Torsion testing plot of steel BJ3 in the 2 month artificial ageing condition. ...	326
Figure 9:60 - Steel BJ3 2 month artificial ageing condition, type A fractures.	327
Figure 9:61 - Torsion testing plot of steel BJ3 in the 4 month artificial ageing condition. ...	328
Figure 9:62 - Steel BJ3 4 month artificial ageing condition, type A fracture.	329
Figure 9:63 - Torsion testing plot of steel BJ4 in the as-drawn condition.....	330
Figure 9:64 - Steel BJ4 as-drawn, type A fracture.....	331
Figure 9:65 - Torsion testing plot of steel BJ4 in the 1 month artificial ageing condition. ...	332
Figure 9:66 - Steel BJ4 1 month artificial ageing condition, type A fracture.	333
Figure 9:67 - Torsion testing plot of steel BJ4 in the 2 month artificial ageing condition. ...	334
Figure 9:68 - Steel BJ4 2 month artificial ageing condition, type A fracture.	335
Figure 9:69 - Torsion testing plot of steel BJ4 in the 4 month artificial ageing condition. ...	336
Figure 9:70 - Steel BJ4 4 month artificial ageing condition, type A fracture.	337
Figure 9:71 - Torsion testing plot of steel BJ5 in the as-drawn condition.....	338
Figure 9:72 Steel BJ5 as-drawn, type A fractures.	339
Figure 9:73 - Torsion testing plot of steel BJ5 in the 1 month artificial ageing condition. ...	340
Figure 9:74 - Steel BJ5 1 month artificial ageing condition, type A fractures.	340
Figure 9:75 - Torsion testing plot of steel BJ5 in the 2 month artificial ageing condition. ...	341
Figure 9:76 Steel BJ5 2 month artificial ageing condition, type A fractures.	342

Figure 9:77 - Torsion testing plot of steel BJ5 in the 4 month artificial ageing condition. ...	343
Figure 9:78 - Steel BJ5 4 month artificial ageing condition, type A fractures.	344
Figure 9:79 - Torsion testing plot of steel BJ6 in the as-drawn condition.	345
Figure 9:80 Steel BJ6 as-drawn, type A fractures.	346
Figure 9:81 - Torsion testing plot of steel BJ6 in the 1 month artificial ageing condition. ...	347
Figure 9:82 Steel BJ6 1 month artificial ageing condition, type A fractures.	348
Figure 9:83 - Torsion testing plot of steel BJ6 in the 2 month artificial ageing condition. ...	349
Figure 9:84 - Steel BJ6 3 month artificial ageing condition, type A fractures.	350
Figure 9:85 - Torsion testing plot of steel BJ6 in the 4 month artificial ageing condition. ...	351
Figure 9:86 - Steel BJ6 4 month artificial ageing condition, type A fractures.	352
Figure 9:87 - Commercial Steel DSC heat flow plots.	353
Figure 9:88 - Steel BJ3 DSC heat flow plots.	354
Figure 9:89 - Steel BJ4 DSC heat flow plots.	355
Figure 9:90 - Steel BJ5 DSC heat flow plots.	356
Figure 9:91 - BJ6 DSC heat flow plots.	357

List of Tables

Table 2:1 - Dislocations observed in cementite by Inoue and Masumoto [56].	73
Table 2:2 - Gavriljuk cementite dissolution Mossbauer spectroscopy measurements [35].	79
Table 2:3 - Reported Carbon-Dislocation binding enthalpy [35].	79
Table 2:4 - Summary of the effects of Alloying Additions.	85
Table 3:1 - Plain carbon and nickel steel compositions (wt.%).	88
Table 3:2 - Torsion testing results from British Steel R&D study [68].	89
Table 3:3 - Commercial grade TC84B chemical composition (measured) and simulated composition.	93
Table 3:4 - Influence of cobalt content on cementite transformation temperature.	96
Table 3:5 - Influence of chromium content on cementite start and finish transformation temperature.	98
Table 3:6 - Influence of copper content on cementite start and finish transformation temperature.	100
Table 3:7 - Influence of manganese content on cementite start and finish transformation temperature.	102
Table 3:8 - Influence of molybdenum content on cementite start and finish transformation temperature.	104
Table 3:9 - Influence of nickel content on cementite start and finish transformation temperature.	106
Table 3:10 - Influence of silicon content on cementite start and finish transformation temperature.	108

Table 3:11 - Influence of vanadium content on cementite start and finish transformation temperature.....	110
Table 3:12 - Summary of cementite transformation temperatures with a 0.5wt.% alloying addition.....	113
Table 3:13 - Cobalt distribution simulation composition.....	113
Table 3:14 - Chromium distribution simulation composition.....	115
Table 3:15 - Copper distribution simulation composition.....	116
Table 3:16 - Manganese distribution simulation composition.....	117
Table 3:17 - Molybdenum distribution simulation composition.....	118
Table 3:18 - Nickel distribution simulation composition.....	119
Table 3:19 - Silicon distribution simulation composition.....	120
Table 3:20 - Vanadium distribution simulation composition.....	121
Table 3:21 - Summary of calculated element distribution	122
Table 3:22 - Multi element thermodynamic simulation calculated cementite transformation temperatures.....	124
Table 3:23 - Final Experimental Steel Compositions.....	126
Table 3:24 - Alloy cost estimates.....	132
Table 4:1 – Experimental Steel Compositions (wt.).....	136
Table 4:2 - Carrier Coil Composition (wt.).....	138
Table 4:3 - Volume Fraction Point Count - Commercial Coil.....	138
Table 4:4 - 0.8Si steel volume point count.....	140
Table 4:5 - 0.8 Si + 0.5Ni Steel volume point count.....	141
Table 4:6 - 0.8 Si + 0.5 Ni + 0.1 Co Steel volume point count.....	142

Table 4:7 - 0.8 Si + 0.5 Ni + 0.1 Co + 0.1 V Steel volume point count.....	143
Table 4:8 - Cooling Rate Requirements to achieve 12% resolvable pearlite.....	144
Table 4:9 - Grade X85LM Cast Analysis (wt.%).	147
Table 4:10 - Single pass lab drawing bench rod cooling rates.....	147
Table 4:11 - 0.8 Si Steel measured rod cooling rates.	148
Table 4:12 - 0.8 Si + 0.5Ni Steel measured rod cooling rates.	148
Table 4:13 - 0.8 Si + 0.5 Ni + 0.1 Co Steel measured rod cooling rates.	148
Table 4:14 - 0.8 Si + 0.5 Ni + 0.1 Co 0.1 V Steel measured rod cooling rates.....	148
Table 4:15 - Commercial Steel Rod Heat Treatments	149
Table 4:16 - Rod Tensile Test Results.....	149
Table 4:17 - Average Measured Rod Pearlite Spacing.....	151
Table 4:18 - Single Pass lab drawing bench Wire drawing schedule.....	152
Table 4:19 - Temperatures used to calculate artificial ageing heat treatments.	155
Table 4:20 - Artificial ageing heat treatments.	155
Table 4:21 - Measured calibration samples.....	160
Table 5:1 - British Steel, Steel grade designations and Compositions (wt.%).	168
Table 5:2 - Tensile results for Commercial Steel.	175
Table 5:3 - Tensile results for 0.8 Si Steel.	175
Table 5:4 - Tensile results for 0.8Si + 0.5Ni Steel.....	175
Table 5:5 - Tensile results for 0.8Si + 0.5Ni + 0.1Co Steel.....	175
Table 5:6 - Tensile results for 0.8Si + 0.5Ni + 0.1Co + 0.1V Steel.	175
Table 5:7 – Torsion results for commercial steel.....	181
Table 5:8 - Torsion results for 0.8Si steel.....	181

Table 5:9 - Torsion results for 0.8Si + 0.5Ni steel.	181
Table 5:10 - Torsion results for 0.8Si + 0.5Ni + 0.1Co steel.	181
Table 5:11 - Torsion results for 0.8Si + 0.5Ni + 0.1Co + 0.1V.....	181
Table 5:12 - DSC Peak 1-4 data summary.	190
Table 5:13 - Apparent cementite lamellae thickness values.	195
Table 5:14 - Apparent cementite lamellae thickness values.	199
Table 5:15 - Apparent cementite lamellae thickness measurement values.	205
Table 5:16 - Commercial Steel Sample 1: 7 at% C iso-concentration average composition of cementite and ferrite matrix.	216
Table 5:17 - Commercial Steel Sample 2: 7 at% C iso-concentration average composition of cementite and ferrite matrix.	219
Table 5:18 - Steel BJ5: 7 at% C iso-concentration average composition of cementite and ferrite matrix.	222
Table 6:1 - Commercial and Experimental Steel Compositions (wt.%).	225
Table 6:2 - Mean coefficient of variance of 3 measured cementite lamellae.....	233
Table 6:3 - Chemical Analysis Summary.	234
Table 6:4 - Alloying element location summary.	243
Table 9:1 - 17BQ3 F1 - F10 Rod Characterisation.	260
Table 9:2 - 17BQ4 F1 - F10 Rod Characterisation.	261
Table 9:3 - 17BQ5 F1 - F10 Rod Characterisation.	261
Table 9:4 - 17BQ6 F1 - F10 Rod Characterisation.	262
Table 9:5 - BTC Drawing Schedule 5.5mm rod to 2.5mm diameter wire.....	264
Table 9:6 - 0.8 Si Steel 2.5mm Drawing Summary.....	264

Table 9:7 - 0.8 Si + 0.5 Ni Steel 2.5mm Drawing Summary.	264
Table 9:8 - 0.8 Si + 0.5 Ni + 0.1 Co Steel 2.5mm Drawing Summary.	265
Table 9:9 - 0.8 Si + 0.5 Ni + 0.1 Co + 0.1 V Steel 2.5mm Drawing Summary.	265
Table 9:10 - BTC Schedule 2.5mm to 1.65mm.....	267
Table 9:11 - 0.8 Si 1.65mm Drawing Summary.....	267
Table 9:12 - 0.8 Si + 0.5 Ni 1.65mm Drawing Summary.	267
Table 9:13 - 0.8 Si + 0.5 Ni + 0.1 Co 1.65mm Drawing Summary.	267
Table 9:14 - 0.8 Si + 0.5 Ni + 0.1 Co + 0.1 V 1.65mm Drawing Summary.	267
Table 9:15 - Tensile testing results of the commercial steel in the as-drawn condition.....	274
Table 9:16 - Tensile testing results of the commercial steel in the 1 month artificial ageing condition.	276
Table 9:17 - Tensile testing results of the commercial steel in the 2 month artificial ageing condition.	278
Table 9:18 - Tensile testing results of the commercial steel in the 2 month artificial ageing condition.	280
Table 9:19 - Tensile testing results of steel BJ3 in the as-drawn condition.	282
Table 9:20 - Tensile testing results of steel BJ3 in the 1 month artificial ageing condition. .	284
Table 9:21 - Tensile testing results of steel BJ3 in the 2 month artificial ageing condition. .	286
Table 9:22 - Tensile testing results of steel BJ3 in the 4 month artificial ageing condition. .	288
Table 9:23 - Tensile testing results of steel BJ4 in the as drawn condition.....	290
Table 9:24 - Tensile testing results of steel BJ4 in the 1 month artificial ageing condition. .	292
Table 9:25 - Tensile testing results of steel BJ4 in the 2 month artificial ageing condition. .	294
Table 9:26 - Tensile testing results of steel BJ4 in the 4 month artificial ageing condition. .	296

Table 9:27 - Tensile testing results of steel BJ5 in the as-drawn condition.	298
Table 9:28 - Tensile testing results of steel BJ5 in the 1 month artificial ageing condition. .	300
Table 9:29 - Tensile testing results of steel BJ5 in the 2 month artificial ageing condition. .	302
Table 9:30 - Tensile testing results of steel BJ5 in the 4 month artificial ageing condition. .	304
Table 9:31 - Tensile testing results of steel BJ6 in the as-drawn condition.	306
Table 9:32 - Tensile testing results of steel BJ6 in the 1 month artificial ageing condition. .	308
Table 9:33 - Tensile testing results of steel BJ6 in the 2 month artificial ageing condition. .	310
Table 9:34 - Tensile testing results of steel BJ6 in the 4 month artificial ageing condition. .	312
Table 9:35 - Torsion testing results of the commercial steel in the as-drawn condition.	314
Table 9:36 - Torsion testing results of the commercial steel in the 1 month artificial ageing condition.	316
Table 9:37 - Torsion testing results of the commercial steel in the 2 month artificial ageing condition.	318
Table 9:38 - Torsion testing results of the commercial steel in the 4 month artificial ageing condition.	320
Table 9:39 - Torsion testing results of steel BJ3 in the as-drawn condition.	322
Table 9:40 - Torsion testing results of BJ3 in the 1 month artificial ageing condition.	324
Table 9:41 - Torsion testing results of BJ3 in the 2 month artificial ageing condition.	326
Table 9:42 - Torsion testing results of BJ3 in the 4 month artificial ageing condition.	328
Table 9:43 - Torsion testing results of steel BJ4 in the as-drawn condition.	330
Table 9:44 - Torsion testing results of BJ4 in the 1 month artificial ageing condition.	332
Table 9:45 - Torsion testing results of BJ4 in the 2 month artificial ageing condition.	334
Table 9:46 - Torsion testing results of BJ4 in the 4 month artificial ageing condition.	336

Table 9:47 - Torsion testing results of steel BJ5 in the as-drawn condition.....	338
Table 9:48 - Torsion testing results of BJ5 in the 1 month artificial ageing condition.	340
Table 9:49 - Torsion testing results of BJ5 in the 2 month artificial ageing condition.	341
Table 9:50 - Torsion testing results of BJ5 in the 4 month artificial ageing condition.	343
Table 9:51 - Torsion testing results of BJ6 in the as-drawn condition.	345
Table 9:52 - Torsion testing results of BJ6 in the 1 month artificial ageing condition.	347
Table 9:53 - Torsion testing results of BJ6 in the 2 month artificial ageing condition.	349
Table 9:54 - Torsion testing results of BJ6 in the 4 month artificial ageing condition.	351
Table 9:55 - Commercial Steel DSC data points.....	353
Table 9:56 - Steel BJ3 DSC data points.....	354
Table 9:57 - Steel BJ4 DSC data points.....	355
Table 9:58 - Steel BJ5 DSC data points.....	356
Table 9:59 - Steel BJ6 DSC data points.....	357

List of Equations

Equation 4:1 - Hundy Equation for calculating artificial ageing time [70].....	155
--	-----

1 Introduction

The exceptional mechanical properties of nanostructured drawn pearlitic steel wires have been extensively documented and reviewed [1]. As such, steel wire products are often used for safety critical applications such as bridge wires, mooring cables, lifting ropes, tyre reinforcement and automotive springs. However, pearlitic wires are susceptible to a detrimental change in mechanical properties over time in service. This is known as strain ageing. The initial stages of strain ageing increase the strength and crucially, reduce the ductility of the drawn wire, which can lead to premature failure in service.

Strain ageing is an issue for manufacturers and end users of wire products. Processing parameters such as drawing speed, temperature and reduction schedule all influence the severity of the strain ageing response. Therefore, strain ageing forces manufacturers to operate at reduced production efficiency, increasing manufacturing cost. For end users, the possibility of a premature failure in service requires monitoring and for certain applications, periodic replacement of wire products.

The underpinning mechanisms of strain ageing remain unclear. The heterogeneous dissolution of pearlitic cementite lamellae has been extensively reported, during and after wire drawing. The redistribution of carbon atoms which occur due to cementite dissolution is believed to drive the change in mechanical properties. Cementite dissolution has been confirmed with a number of experimental techniques. What is driving the cementite

dissolution, however, remains an open question. Several mechanisms have been proposed, but none are universally accepted.

An increased understanding of strain ageing would be advantageous for manufacturers and end users. The changes in microstructure which occur due to strain ageing also impact work hardening rates, limiting the development of wires with increased strength. There is a strong drive in markets such as automotive tyre cord reinforcement to increase strength. Increased strength would provide a weight saving, improving fuel efficiency. Wires with more stable properties could increase the service life of wire products, which is especially important for certain applications, such as lifting ropes. Whilst the cost of replacing a rope is not always significant, machine or platform downtime can result in severe costs to end users.

The variety of experimental approaches, rod production methods, wire drawing parameters and heat treatments make combining published results on strain ageing a challenge. The heterogenous nature of strain ageing inherently produces large variation, especially in high resolution or atomic scale techniques. A number of variables have been shown to influence the rate of cementite dissolution. Initial pearlitic microstructure, for example, has been shown to influence the amount of cementite dissolution. Increased wire drawing speed and temperatures have also been shown to increase cementite dissolution. Studies on composition are often limited to one or two variations in alloying elements and are targeted for specific applications. A comprehensive review of the influence of composition is yet to be completed. Hence, this EngD will attempt to isolate composition as a variable and study its effect on the strain ageing response of a wire.

1.1 Aims & Objectives

The aim of the EngD research was to identify if compositional adjustments can be made to a commercial high carbon steel to ascertain if steel composition can influence or retard the strain ageing response of a wire microstructure. The influence of composition was assessed via the production of several experimental steel compositions. The experimental steels were characterised alongside a commercially produced steel composition for comparison.

The composition has been selected as the focus of this research due to the following:

- Investigating the influence of composition may lead to a better understanding of strain ageing and initiate the development of alloys more resistant to strain ageing.
- A study of composition may reveal which mechanisms of strain ageing are dominant.

2 Literature Review

This literature review has 3 main objectives. To review the current understanding of strain ageing, to identify effective experimental techniques used to characterise strain ageing and to identify alloying elements which may influence the strain ageing response. As several features of the microstructure and the production of steel wires has been correlated with strain ageing, wire production and drawn pearlite must be discussed before delving into strain ageing.

2.1 Steel Wire Production

To produce steel wire, a cast bloom or ingot must first be hot rolled to rod via reaustenitising and hot rolling to the required diameter followed by controlled cooling through the austenite to pearlite transformation to produce a randomly orientated pearlitic microstructure. Both the austenite grain size and cooling rate influence the transformation kinetics and hence microstructure of the finished rod. The majority of rod feedstock is utilised for wire production, whereby the rod feedstock is drawn through multiple dies of reducing diameter to produce the desired diameter of cold drawn wire.

Prior to wire drawing, rod must be descaled, cleaned and coated. Rod is either mechanically worked (rollers and brushing) or acid cleaned (pickled) to remove scale. A phosphate coating is then added for temporary corrosion protection and a carrier to promote adhesion of drawing lubrication prior to die entry. If corrosion protection is required, a further cleaning and coating process is required after wire drawing. Wires can be coated in polymers or metals

to provide corrosion protection. Hot dip galvanising is commonly used to coat wires. This procedure dips wire into a bath of molten zinc, up to 450°C, for short periods of time.

For high strength applications relevant to this research, steel compositions are generally near eutectoid composition or hyper eutectoid. A commercial steel grade for wire drawing usually contains a manganese addition between 0.5-0.8 wt.%, to reduce the adverse effects of sulphur, but also to improve hardenability. Improved hardenability can influence transformation kinetics to produce finer pearlitic microstructure, which increases tensile strength. Silicon and chromium are also common alloying additions, used to improve the tensile strength of as drawn wire. Commercial steel grades for wire drawing generally contain low levels of alloying additions. Richer compositions can affect drawability and the work hardening rate of the material during wire drawing. Poor steel cleanliness can result in inclusions, which lead to wire breakages during wire drawing.

2.2 Drawn Pearlitic Steel Wire

Pearlite is essentially a composite material, made from alternating lamellae of ferrite and cementite. Ferrite is the relatively ductile body centre cubic (BCC) phase of steel. Cementite is much harder, due to its composition and atomic bonding and has an orthorhombic crystal structure [2]. The stoichiometric composition of cementite is 3:1 Fe:C (Fe_3C). The mechanical properties of each phase contribute to the overall exceptional properties of near eutectoid drawn pearlite.

Cold drawn pearlitic steel wires can achieve exceptional strengths of up to 5GPa whilst maintaining reasonable levels of ductility. Wire drawing is a cold deformation process and so work hardens the material, refines grains and produces a strongly textured microstructure.

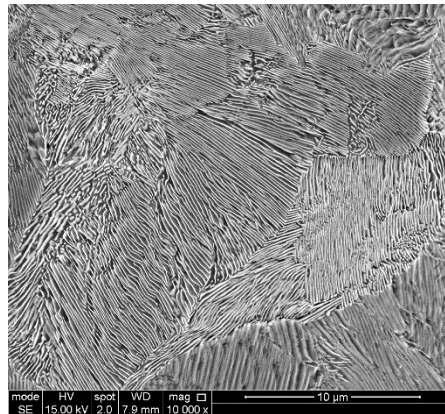


Figure 2:1 - Rod microstructure prior to wire drawing.

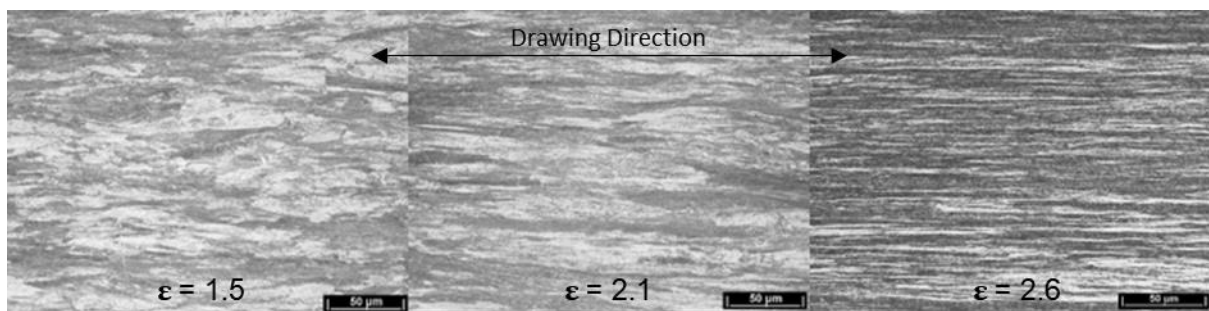


Figure 2:2 - Texture development during wire drawing, micrographs taken during preliminary EngD study.

Pearlitic lamellae realignment towards the drawing direction also changes lamella morphology. Pearlite grains which are orientated within $30\text{-}60^\circ$ of the drawing direction generally realign with minor bending of lamellae and subsequently undergo thinning [3]. Pearlite grains which lay between 60 and 90° to the drawing direction undergo the greatest degree of realignment, often resulting in buckling or fragmentation of cementite lamellae [4].

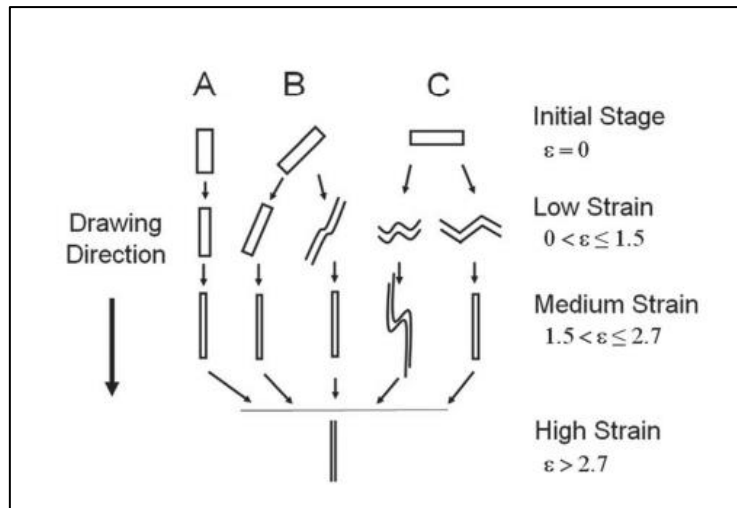


Figure 2:3 - Variation in pearlite realignment based on initial orientation to drawing direction [4].

Whilst Fang et al. demonstrated with XRD the development of the (110) texture in ferrite is not fully completed until a drawing strain of 2.0 [3], 97% of lamellae are realigned to within 30° of the drawing direction at a drawing strain of 1.5 [4]. Therefore, the microstructure is considered predominantly realigned towards the drawing direction at a drawing strain of 1.5. Above a strain of 3.7, Zhang et al. reports a limit of lamella refinement as cementite lamella thickness approaches the critical edge length of a cementite unit cell, 0.6nm. A significant change in lamellae morphology is also noted at such high drawing strains, the lamellae become predominantly platelets which are distributed along the interphase interfaces [4]. This change in microstructure is brought about via the dissolution of cementite lamellae during and after wire drawing. The driving forces behind cementite dissolution are unclear, although cementite dissolution has been correlated with the change in mechanical properties which have been observed with strain ageing. Cementite dissolution will be discussed in section: 2.5 Cementite Dissolution.

The bulk properties of cementite are known to be brittle with a limited capacity for slip or plasticity. However, the ability of cementite to plastically deform within a steel microstructure has been reported since the 1960s [5][6]. More recently, Fang et al. completed comprehensive HRTEM analysis of cementite deformation in pearlitic drawn wire. Fang et al. summarised the findings in the following way: for low strains, deformation is controlled by dislocation motion from adjacent ferrite layers through a coherent interface, creating many sub grains within cementite at the interface. Higher drawing strains reduced the coherency of the ferrite cementite interface, increasing accumulation of dislocations at the interface. To further accommodate deformation, the newly formed cementite sub grains at the interface slip and rotate providing a much greater ductility that bulk pearlite has the capacity for [7]. This mechanism of cementite deformation is summarised in Figure 2:4 and Figure 2:5.

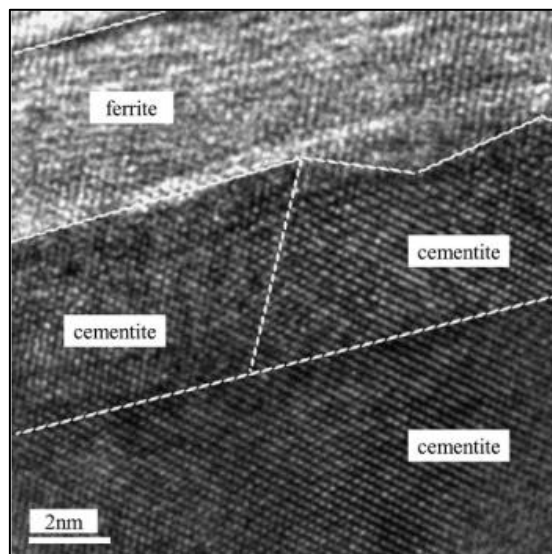


Figure 2:4 - HRTEM image of ferrite cementite interface [7].

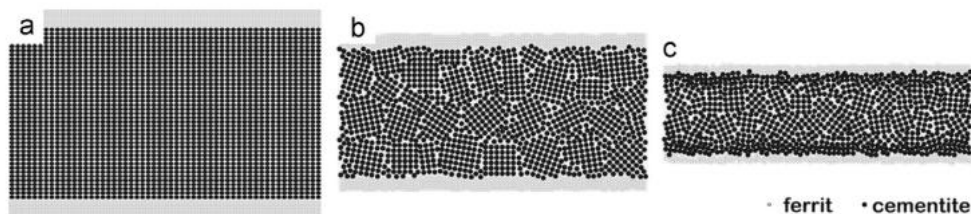


Figure 2:5 - a. Undeformed cementite, b. low-strain deformed cementite and c. heavily deformed cementite [7].

Whilst the sub grains present at the interface can be clearly seen in Figure 2:4, the mechanism responsible for the rotation of cementite can be much more simply explained. Borchers and Kirchheim suggested dislocation motion across the interface alters the orientation slightly [1]. The inherently different slip systems in ferrite and cementite mean dislocations must change slip systems whilst moving across the interface, resulting in individual changes to the orientation of each phase. With increased drawing strain the accumulation of slight changes in orientation, manifests as changes in overall orientation relationships between ferrite and lamella cementite.

During wire drawing, a wire microstructure also undergoes changes in the transverse cross section of a wire, as shown in Figure 2:6. Pearlite grains begin to curl under bending and stretching [8]. Curling can appear as inconsistent lamellae spacing as show by Guelton et al. in Figure 2:7 [9]. This effect can also be seen in Figure 2:8.



Figure 2:6 - Transverse cross section of a drawn wire undergoing curling of pearlite grains due to wire drawing [8].

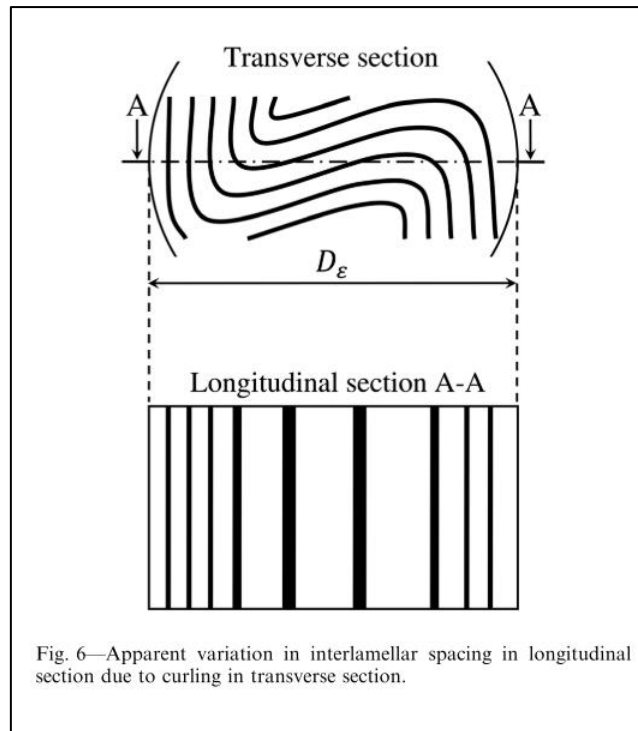


Figure 2:7 - Curling resulting in apparent lamellae spacing variation [9].

Lamellae thickness is drastically reduced during wire drawing. Even a relatively mild drawing schedule ($\epsilon = 2$) can result in an interlamellar spacing as fine as 50 nanometres.

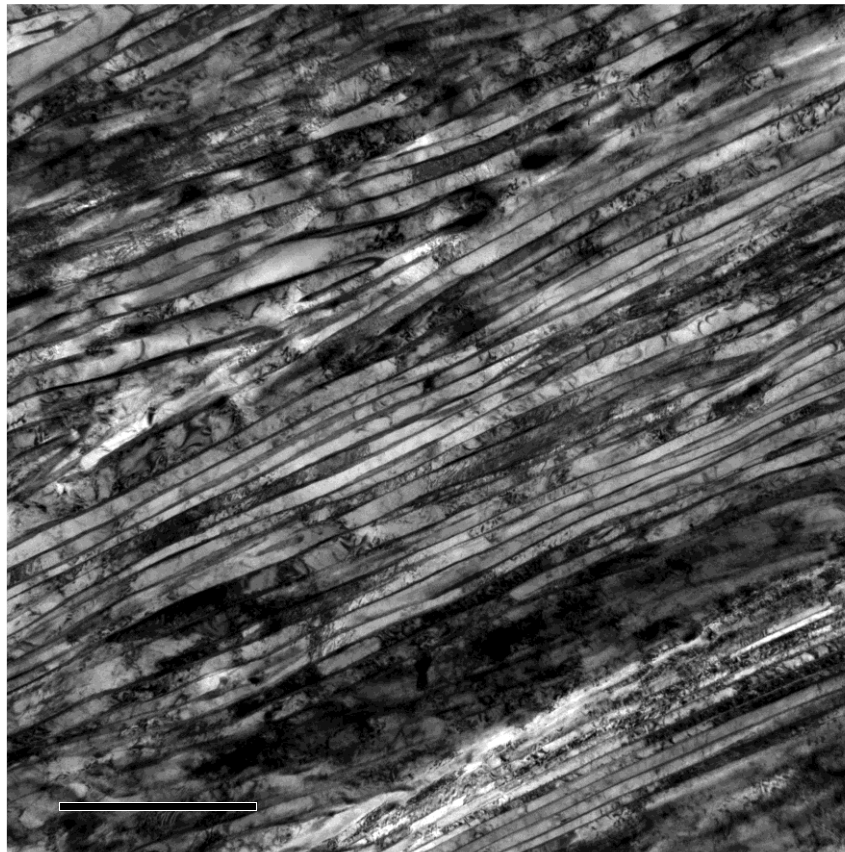


Figure 2:8 – Brightfield STEM micrograph of drawn pearlite ($\epsilon=2.03$).

The thinning of lamellae during drawing increases the interfacial free energy per unit area of cementite lamellae. The differing mechanical properties and slip systems between ferrite and cementite results in complex interface interaction and results in areas of increased localised plasticity throughout the microstructure. Plastic deformation, therefore, increases both the surface area and produces a great deal of variation in lamella morphology, as shown in Figure 2:9.

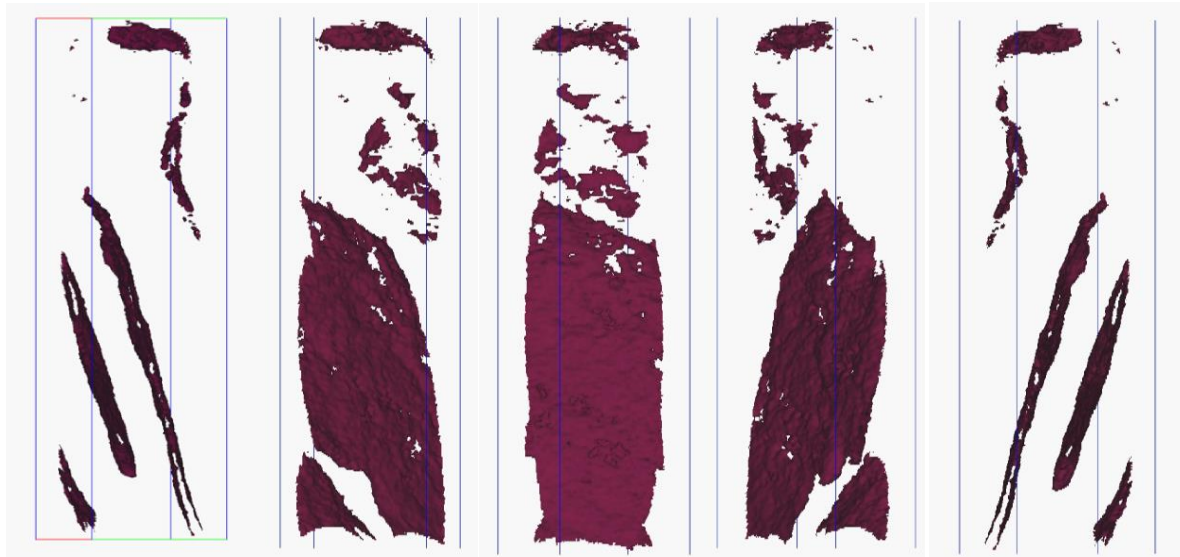


Figure 2:9 - 180° Clockwise rotation of atom probe tomography approximation of cementite lamellae morphology (7 at. %C iso-surface). Image corresponds to atom probe data set shown in Figure 5:36.

Heterogeneous plastic deformation results in differing orientation relationships (OR) between ferrite and cementite. The three most commonly observed are:

The Isaichev OR [10]:

$$(103)_\theta \parallel (110)_\alpha \quad [010]_\theta \parallel [111]_\alpha \quad [311]_\theta 0.91^\circ \text{ from } [111]_\alpha$$

The Bagaryatskii OR [10]:

$$(001)_\theta \parallel (112)_\alpha \quad [100]_\theta \parallel [011]_\alpha \quad [010]_\theta \parallel [111]_\alpha$$

The Pitsch-Petch OR [10]:

$$(001)_\theta \parallel (521)_\alpha \quad [100]_\theta 2.61^\circ \text{ from } [131]_\alpha \quad [010]_\theta 2.6^\circ \text{ from } [113]_\alpha$$

However, Zhang et al. report these orientation relationships have been determined by selected area electron diffraction, where experimental error can be as large as $\pm 3 - 5^\circ$. Zhang et al. suggest that in fact, these are inaccurate. Zhang et al. used convergent beam kikuchi line diffraction patterns to confirm the Isaichev orientation relationship, whilst identifying several new orientation relationships, concluding the two most commonly observed, the Pitsch-Petch and Bagaryatskii orientation relationships, probably do not exist [10]. Kim et al. also confirmed the Isaichev OR, a near Bagaryatskii OR and near Pitsch-Petch OR. The interfacial energy associated with each OR differed. The possible orientation relationships further contributing to variation in lamella and interface morphology, as orientation relationships effect the Burgers vectors and spacing of dislocations at the interface [11].

Another key feature of wire drawing is the generation of a high dislocation density in the microstructure. Differing slip systems in ferrite and cementite results in dislocations accumulating at the ferrite/cementite interface. Dislocation motion between ferrite and cementite is influenced by the orientation relationship between ferrite and cementite lamellae. This barrier to dislocation motion is partially responsible for the excellent strength of drawn pearlite. Severe plastic deformation results in a great deal of energy being stored in the microstructure, estimated to be in the order of GPa [12]. As wire drawing strain increases, ultimate tensile strength and yield strength also increase, but so does the severity of the strain ageing response.

2.3 The Strain Ageing Response

Strain ageing is defined by Watté et al. as: “The change in mechanical and physical properties of a deformed solid as a function of time and temperature.” [13]. Note, strain ageing is referred to as unintentional ageing in some studies. Time and temperature both contribute to the change in mechanical properties. Strain ageing occurs at room temperature and even when wire is kept in a freezer. Freezing wire samples can slow the strain ageing response but does not stop it entirely. Elevated temperatures accelerate the strain ageing response. Strain ageing which occurs during the wire drawing process is referred to as dynamic strain ageing. Strain ageing which occurs after production, i.e. when the product is in storage or service, is known as static strain ageing.

Strain ageing causes the mechanical properties of a wire product to change in service. As a wire strain ages, a substantial increase in yield strength and a loss of ductility occurs, a slight increase in UTS has also been reported [14]. When a rope is under tension in service, individual strands become more brittle and become more susceptible to fracturing due to the shearing forces generated from the interactions at wire cross-over points within the cross section of the rope. Therefore, a reduced ductility during ageing can make individual strands and even the full rope susceptible to premature failure. After the initial increase in strength, the microstructure softens leading to the recovery of mechanical properties, eventually producing an over-ageing effect, whereby the strength is lower and ductility higher than the original as-drawn properties immediately after wire manufacture. As the strain ageing response is also dependent on temperature, the coating of wires for corrosion resistance, such as galvanising, can involve short periods of exposure of the steel wire to elevated

temperature up to 450°C, further enhancing the strain ageing response of a wire. Post drawing heat treatments differ between studies and affect the evolution of the wire microstructure significantly [15][16][17].

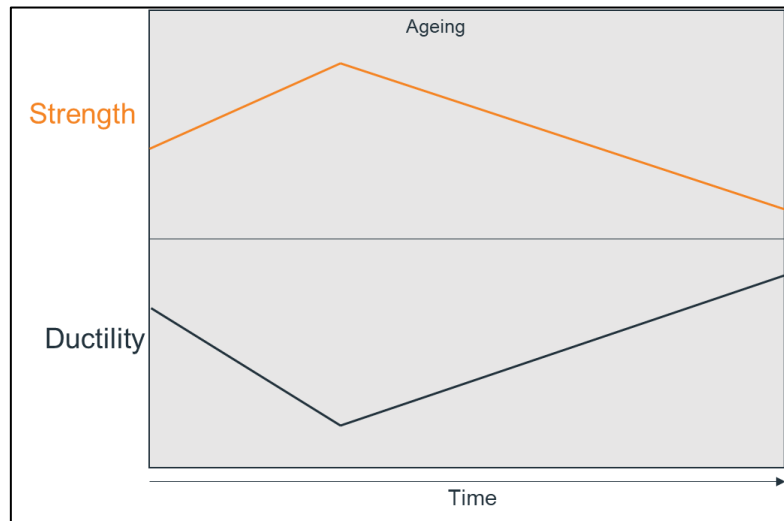


Figure 2:10 - Illustration of the change in mechanical properties with strain ageing.

During production, manufacturers have found that the wire drawing parameters could influence the severity of the strain ageing response. More severe drawing speeds, temperatures, drawing schedules, die designs, lubrication (or lack of) and alignment all contributed to the as-drawn properties and ageing sensitivity [14][18]–[20]. Hono et al. reported at a drawing strain of 5.1, cementite decomposition is complete [21]. Thus, a balance must be achieved between the need to slow production to reduce ageing sensitivity and maintain high production efficiency, to reduce manufacturing cost. As such, wire drawing parameters remain closely guarded secrets of manufacturers.

Initially there were significant improvements to be obtained from wire drawing technology. Crucially, cooling during wire drawing reduced ageing sensitivity and improved the as-drawn properties of wires. Direct cooling during wire drawing was initially difficult and costly to

implement, with trials utilising water and air directed onto the wire but modern wire drawing machines now utilise water cooled capstans and water cooled drawing dies, so that the cooling water does not come into direct contact with the wires. This avoids the difficulties of direct cooling on the drawing lubricant and the disposal of contaminated water [19]. This has proved a very effective method and is universally adopted for modern wire drawing machines.

The redistribution of carbon atoms has been correlated to the change in mechanical properties [22]. Carbon-dislocation interaction and the dissolution of cementite lamellae play a key role in the redistribution of carbon atoms [1]. The pinning of dislocations by interstitial atoms in the ferrite in the pearlite (both C and N) are thought to be responsible for the initial increase in strength. Carbon atoms are the most numerous and are therefore predominantly responsible. The dissolution of cementite lamellae during strain ageing significantly increases the number of carbon atoms available to pin dislocations. Initially, minor cementite dissolution occurs combined with the interstitial carbon solid solution in the ferrite which diffuses to and pins dislocations. This has been referred to as the first stage of ageing [13][14]. Further cementite dissolution, which begins immediately upon drawing, depletes the pearlitic cementite lamellae of carbon atoms, feeding carbon into the ferrite, producing a supersaturated state. This process has been referred to as the second stage of ageing [13][14][22]. As pinned carbon atoms begin to cluster and form carbides, dislocations are freed and the microstructure softens, which eventually leads to an over ageing effect. This has been referred to as the third stage of ageing by some authors [14]. Carbide formation eventually leads to an over ageing effect.

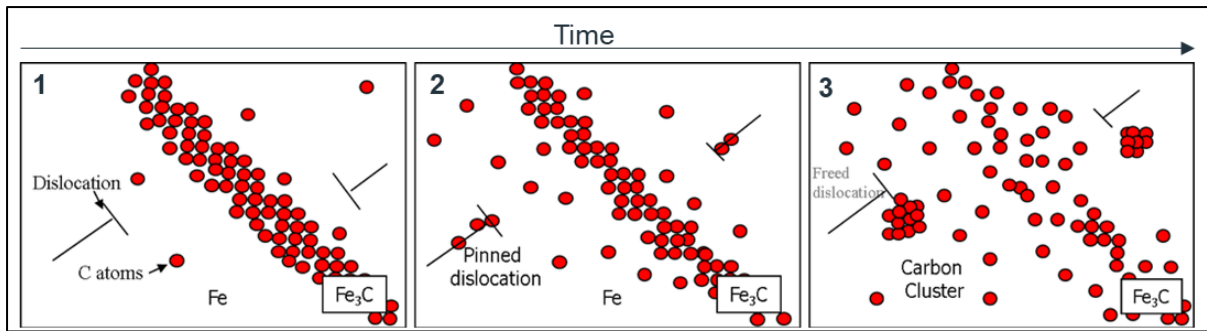


Figure 2:11 - Carbon-dislocation interaction illustration [23].

Steps 1 and 2, in Figure 2:11, show the increase in strength and partial dissolution of cementite. Step 3, in Figure 2:11, shows carbon clustering and the recovery process.

2.4 Methods to Observe Strain Ageing

A fine pearlitic wire microstructure and atomic scale cementite dissolution make direct observation of strain ageing a challenge. A diverse experimental approach has proven to be effective when studying strain ageing. Experimental techniques are generally divided into two categories: Global techniques, which are less sensitive to microstructural heterogeneities and site specific or localised experimental techniques.

2.4.1 Global Experimental Techniques

The most commonly used global experimental technique to observe strain ageing is mechanical testing. Strain ageing can be clearly identified by the change in mechanical properties of a wire over time. A variety of mechanical property tests are effective at detecting strain ageing. Tensile and torsion testing are commonly used in academia, whilst torsion, tensile, reverse bend testing and shear testing are commonly used by rod and wire manufacturers. Shear and torsion testing are particularly useful to manufacturers as they more closely resemble the forces of an individual wire within a strand of a rope in service. Mechanical testing is accessible, inexpensive and reliable, providing enough repeats are performed. An increase of up to 250MPa in UTS, an increase of up to 500 MPa in the yield stress and a loss of 1% in elongation to failure have been reported as a result of ageing [14]. The loss of torsional ductility during the initial stages of strain ageing can often be seen via a change in failure type of torsion tests, as shown in Figure 2:12.

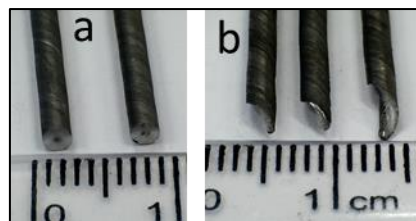


Figure 2:12 - a. Ductile type A torsion fracture of an as drawn wire b. Brittle Type C torsion fracture of an aged wire.

The temperature sensitivity of strain ageing makes it ideal for thermal analysis techniques. Watte et al. used differential scanning calorimetry (DSC) and thermo-electric power measurements to quantify several distinct stages of strain ageing [13]. The activation energy for this stage was calculated as 68 kJ/mol. Prior to this study, the initial stage had been attributed to the reserve of carbon atoms in ferrite lamellae diffusing to dislocations. Watte et al. concluded there were not enough carbon atoms present in the ferrite lamellae available to pin all the dislocations at this stage and carbon diffusion alone was unlikely to produce such high heat fluxes. Therefore, Watte et al. proposed that another mechanism must be active during this stage. Recent analysis has confirmed cementite dissolution occurs immediately upon drawing, proving Watte et al. to be correct [9]. Watte et al. calculated a higher activation energy (81 kJ/mol) for the second stage of strain ageing. Watte et al. concluded the change in activation energy and change in time exponents calculated from thermo-electric power results were in line with the dissolution of the cementite phase.

More recent DSC analysis has confirmed at least three stages of strain ageing are present [14]. Joung et al. performed DSC analysis of an as drawn wire with a drawing strain of 1.55 which reveals the initial stage of strain ageing occurs around 150 °C, the second stage occurs at around 300°C and the third around 450°C [23]. Not all studies consistently detect all three stages of ageing. Borchers reported two distinct peaks at 150°C (130 J/mol) and 300°C (250 J/mol) in wire with a drawing strain of 5 [1]. Hinchliffe and Smith reported 4 exothermic events at 160°C, 330°C, 450 °C and 530°C [24].

Lamontagne et al. performed DSC analysis on a cold drawn pearlitic steel with a strain of 3.42, the second and third stages were present but not the first [25]. Wires which have received heat treatments performed before DSC analysis tend not to exhibit the initial stage of strain ageing. Fang et al. simulated galvanising treatments and was only able to identify the third stage at 450°C with DSC analysis [26], highlighting the temperature dependence of strain ageing. Lamontagne et al. also confirmed this by completing two differing heat treatments on DSC samples prior to analysis to investigate the effects of heat treatments, as shown in Figure 2:13 [14].

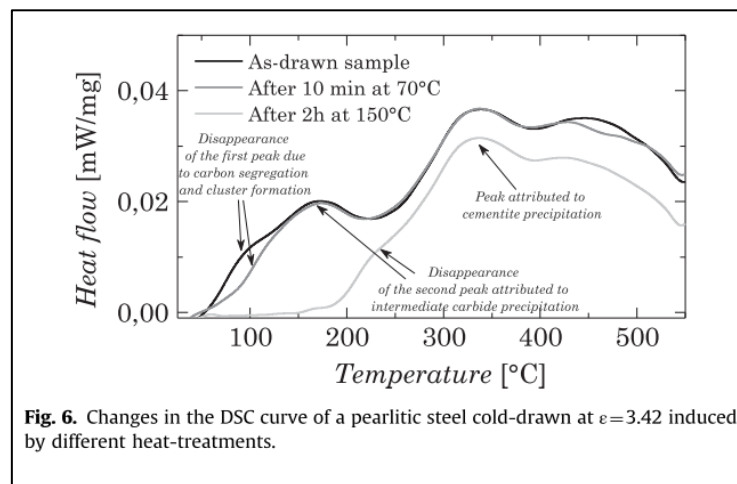


Figure 2:13 - DSC Analysis change due to differing heat treatments [14].

Fang et al., in a study on the effect of vanadium, did not identify the first stage of strain ageing even with a mild drawing strain of 1.83 and an average reduction per pass of 14 % [27]. The time between wire drawing and testing was not reported, the wire microstructure may have aged beyond the initial stage prior to testing. Fang et al. also reported a vanadium addition was capable of increasing the temperature at which the second stage of strain ageing occurs by 17°C but reduced the temperature at which the third stage occurs by 5°C [27]. It appears only a single sample is analysed per composition. Given the heterogeneous nature of strain

ageing and the small sample masses used in DSC, this difference may be attributed to experimental variation. Nevertheless, providing enough samples are scanned, the study demonstrates that DSC is ideally suited for studying the effects of steel composition on strain ageing.

Fang. et al. also used DSC to study the effects of a rod with an inherited texture. It appears an inherited texture increases the temperature at which the second stage of strain ageing was identified by 10°C and the third occurred 5°C higher [28].

The exothermic events identified by DSC as stages of strain ageing have also been confirmed with the application other global techniques such as internal friction, thermoelectric power and electrical resistivity measurements. Buono et al. combined tensile testing with internal friction and electrical resistivity measurements to establish low temperature (60°C -100°C) ageing produced a minor yield strength increase with a decrease in electrical resistivity and background damping, in line with the first stage of ageing. At higher ageing temperatures (120°C -200°C) Buono et al. found the change in yield strength increased more significantly, paired with an increased background damping, suggesting the locking of dislocations and a positive change in electrical resistivity, which Buono et al. attributes to cementite dissolution [22]. Borchers clearly demonstrates electrical resistivity peaks occurring in line with a DSC scan, shown in Figure 2:14 [1].

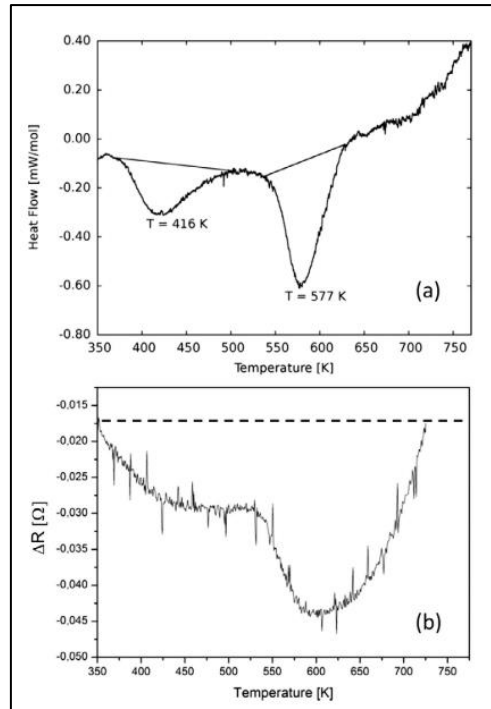


Figure 2:14 - a. DSC Scan of a cold drawn pearlitic wire $\varepsilon = 5$. b. Electrical resistivity of cold drawn pearlitic wire $\varepsilon = 5$ [1].

The change in electrical resistivity with drawing strain and subsequent annealing treatments has been reported in several studies [14], [22], [29]. Borchers and Kircheim have shown a correlation between electrical resistivity measurements and dislocation density over a series of heat treatments [1]. Electromagnetic sensors have been used effectively to characterise various physical properties of rods and steel products [30][31][32]. Ali et al. used magnetic measurements to investigate carbon-vacancy interaction in a high Cr (25wt.%) steel alloy after quenching and post quenching annealing treatments [33]. A recent collaboration between British Steel R&D and Warwick University led to the development of electromagnetic sensors capable of detecting the strain ageing response of a wire. This is detailed in section 4.6 - Magnetic Sensors.

Lamontagne et al. applied internal friction and thermoelectric power measurements to as drawn wire samples at room temperature with increasing drawing strain [29]. An inflection occurred at a drawing strain of 1.5, as shown in Figure 2:15.

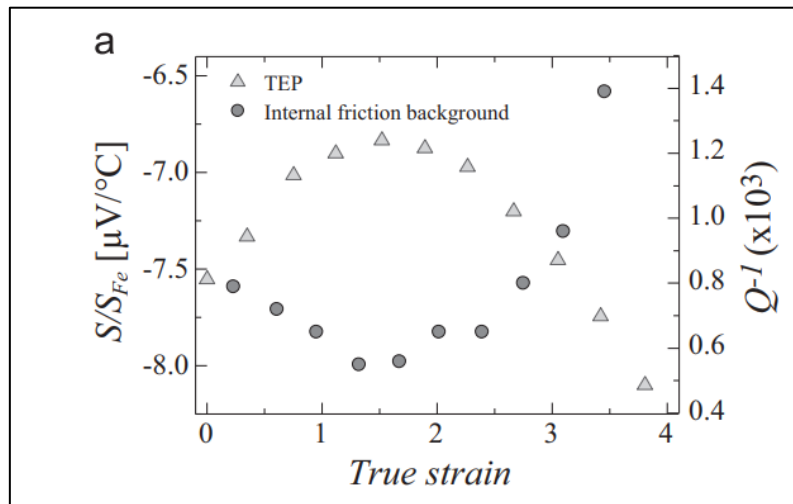


Figure 2:15 - TEP and Internal Friction background evolution of as drawn wires [29].

Lamontagne et al. reported thermoelectric power (TEP) measurements in pearlitic wires are predominantly influenced by interstitial carbon atoms [29]. The contribution of interstitial carbon atoms is negative and much higher in absolute value when compared to other elements in solution. Therefore, the TEP measurements increase as carbon atoms leave solution to precipitate or pin dislocations. The TEP measurements become negative above a drawing strain of 1.5 following the dissolution of cementite, significantly increasing the number interstitial carbon atoms in ferrite. Lamontagne et al. divides strain ageing into two stages, separate to those identified by DSC measurements. The initial stage, up to a drawing strain of 1.5, is attributed primarily to lamellae realignment, with a minor contribution from initial dislocation pinning. The second stage, above a drawing strain of 1.5, was attributed to cementite dissolution.

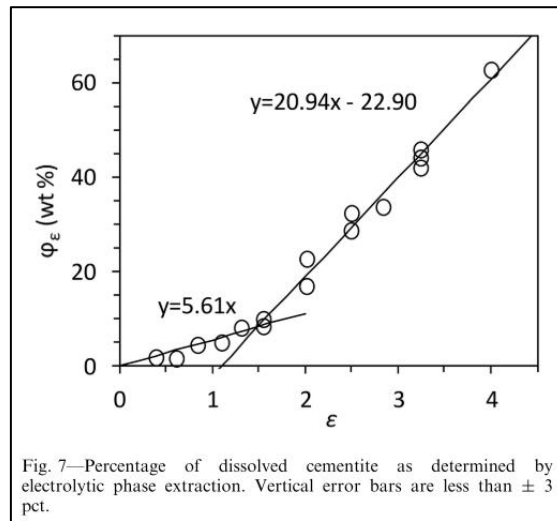


Figure 2:16 - Change in rate of cementite dissolution with drawing strain [9].

Gluelton et al. has used electrolytic phase extraction to quantify the amount of cementite dissolution which is occurring with increasing drawing strain. Electrolytic phase extraction is currently the only global experimental technique that is able to precisely measure cementite dissolution. As shown in Figure 2:16, cementite dissolution is occurring immediately upon drawing and a significant increase in the rate of cementite dissolution occurs above a drawing strain of 1.5. Confirmation of cementite dissolution below a strain of 1.5 clarifies the additional mechanism which occurs during the first stage of strain ageing, which was proposed by Watte et al. [13]. Figure 2:16 shows there are two linear rates of cementite dissolution which occur with increasing drawing strain. The initial regime, up to a true strain of 1.5, has a gradient of 5.61. The second, which occurs above a drawing strain of 1.5 has a gradient of 20.94. This is a 3.7 times larger rate of dissolution above a drawing strain of 1.5. The application of this technique to cementite dissolution is without doubt a breakthrough, especially in quantifying the rate of cementite dissolution immediately upon wire drawing. Electrolytic phase extraction is reported as repeatable and consistent, with the worst

reported error bar of $\pm 3\%$. Measuring the amount of cementite dissolution prior to the application of electrolytic phase extraction by Guelton et al. was measured with localised experimental techniques.

2.4.2 Localised experimental techniques

Localised experimental techniques are capable of directly characterising site specific, microstructural features of the strain ageing response. This includes dislocation state, lamellae morphology and chemical composition on a near atomic or atomic column level of precision. Localised techniques have contributed significantly to the current understanding of strain ageing.

Mossbauer spectroscopy has been used to quantify cementite dissolution. Mossbauer spectroscopy is a technique based on the recoilless emission of gamma rays during electron energy level transitions. Thus, providing detailed information of an atom's local environment. Using Mossbauer spectroscopy, Nam et al. demonstrated a finer pearlitic microstructure results in an increased amount of cementite dissolution [34]. Gavriljuk used Mossbauer spectroscopy to estimate the amount cementite dissolution was around 50%, depending on the drawing strain and steel composition [35].

Using conventional TEM (CTEM), Danoix et al. imaged a wire with a drawing strain of 3.5 and noted a large contrast variation was present. This was attributed to interfacial stress fields [36]. Using Scanning Transmission Electron Microscopy (STEM), Languillaume et al. reported the dissolution of cementite lamellae when observing ferrite lamellae separated by grain boundaries and not cementite as expected [37]. Thus, demonstrating the capability of STEM

and electron energy loss spectroscopy (EELS) in precisely measuring carbon distribution within the microstructure, as shown in Figure 2:17.

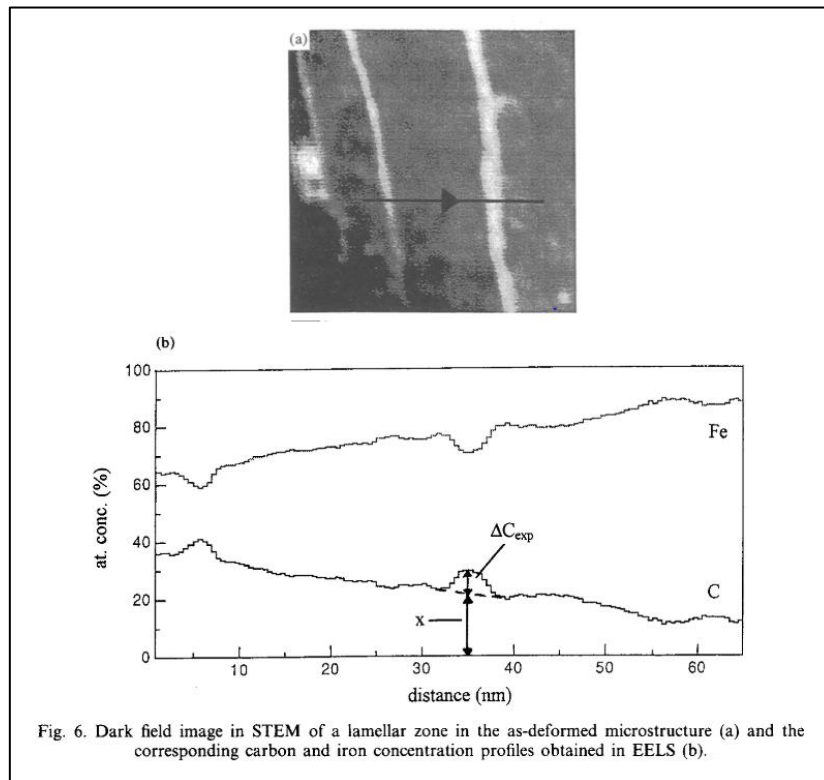


Figure 2:17 - STEM Image with EELS C concentration plot [37].

STEM differs from CTEM in that it collects a transmission image by scanning, much the same as an SEM [38]. TEM is capable of precisely mapping element distribution in several ways. As the diffraction of electrons through a thin foil produces X-rays, a TEM can perform quantitative X-ray analysis provided the correct detector is fitted to the instrument. Electron energy loss spectroscopy (EELS) is the analysis of the energy that electrons lose in going through a thin foil. An EELS detector can provide precise chemical and structural information from electron energy loss events [38]. High Resolution TEM has also been used effectively to characterise cementite morphology in localised regions of wire microstructure [39].

Atom Probe Tomography (APT) is another localised technique which has been effectively applied to strain ageing and cementite dissolution. APT has been widely used by researchers as it is precise enough to map element distribution on a near atomic scale [1] [26] [30] [65]. Using ATP, Min et al. reported the presence of a carbon rich region in a wire drawn to 2.89. The ferrite cementite interface had a depleted carbon concentration of 8-14 at.%, which was around half the carbon concentration of stoichiometric cementite (25 at.% C) [41]. The study also found a higher concentration of carbon in the ferrite (~1 at.%), than the expected thermodynamic equilibrium concentration.

Bang et al. also reported a large concentration of carbon atoms at the ferrite cementite interface, around 3 at.%. Bang et al. also reported the amount of cementite dissolution increased under iso stress conditions when compared to iso strain conditions using APT [42]. Iso-stress is perpendicular to lamellae and iso-strain is parallel with lamellae, shown in Figure 2:18.

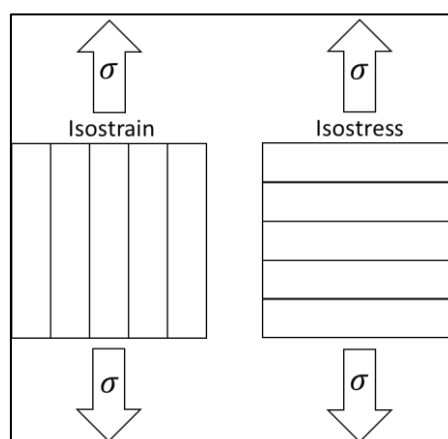


Figure 2:18 - iso-strain and iso-stress conditions.

Hono et al. effectively combined TEM and APT to demonstrate the fragmentation and reordering of cementite into nanoscale grains at drawing strain of 4.22, measuring carbon concentration in cementite to be 16 at.%. A heterogeneous carbon distribution in ferrite lamellae is also reported, between 0.2 – 3 at. %, with increased carbon concentration in ferrite where the interlamellar spacing is smaller. Silicon enrichment at the interface is also reported [43].

Takahashi et al. demonstrated the sample orientation and preparation can produce misleading results in atom probe tomography. The application of the FIB lift-out technique prepared samples perpendicular to the drawing direction, instead of parallel which had been the conventional approach prior to this study. Takahashi et al. reported a combination of damage from FIB preparation and analysis completed parallel to the drawing direction found almost homogeneously distributed carbon atoms, which resulted in an overestimation of cementite dissolution. This was demonstrated in the zone of the sample which contained more than 2 at.% gallium, the carbon appeared homogeneously distributed with a concentration between 3-4%, which would suggest complete cementite dissolution. This analysis is shown in Figure 2:19.

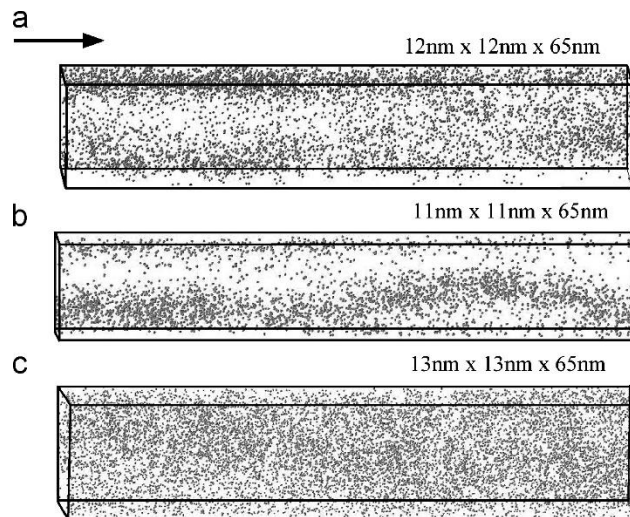


Figure 2:19 - APT reconstruction of carbon atoms. Parallel to drawing direction [44].

When a sample from the same material was analysed perpendicular to the drawing direction, the presence of lamellar cementite was clear. Some carbon rich regions contained up to 25 at. % carbon. However, there was a region in this sample with homogeneously distributed carbon of less than 5 at.%, Figure 2:20b. The analysis parallel to the drawing direction was likely a similar region and hence why it appeared significantly more cementite dissolution had occurred.

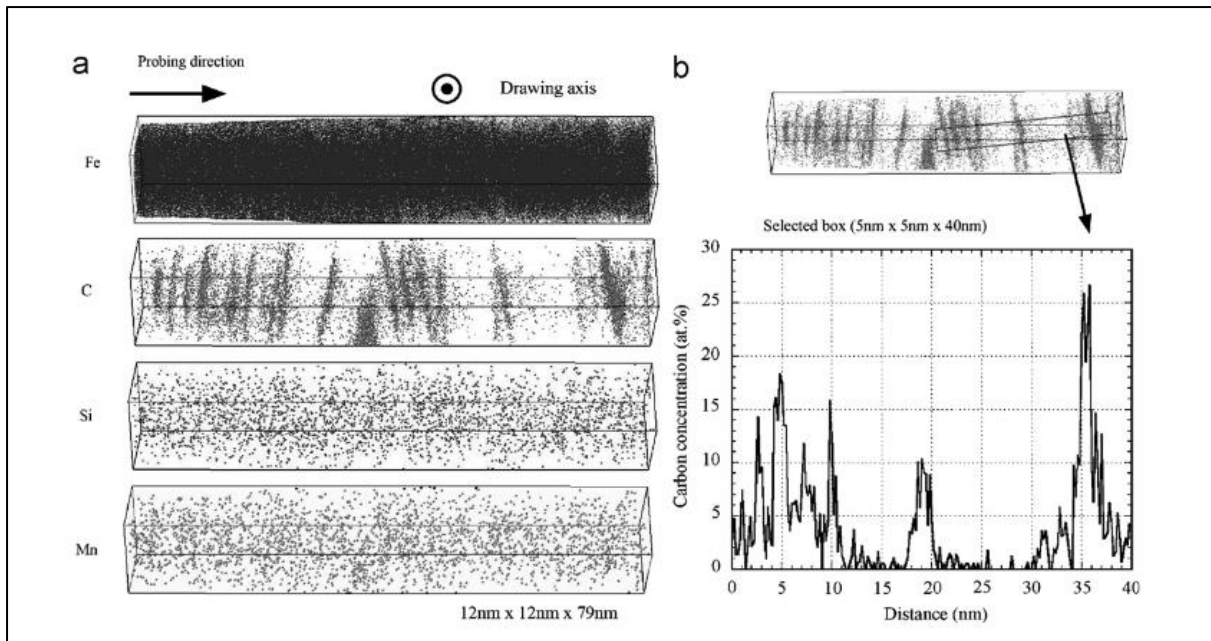


Figure 2:20 - APT reconstruction perpendicular to drawing direction [44].

Li et al. al reported the carbon concentration in a cementite lamella at a drawing strain of 2 was 20-25 at.% (5.1-6.7 wt.%) and the carbon concentration in a cementite lamella at a drawing strain of 5 was only 10-15 at.% (2.3-3.6 wt.%) [45]. The 3D atom map of this data is shown in Figure 2:21. Li et al. also reported carbon concentration as a function of cementite lamellae thickness. It was observed that at higher drawing strains which resulted in cementite lamellae thickness of less than 8nm, carbon concentration is significantly reduced below the stoichiometry and a gradual change to amorphous cementite occurs with increased drawing or strain ageing [45].

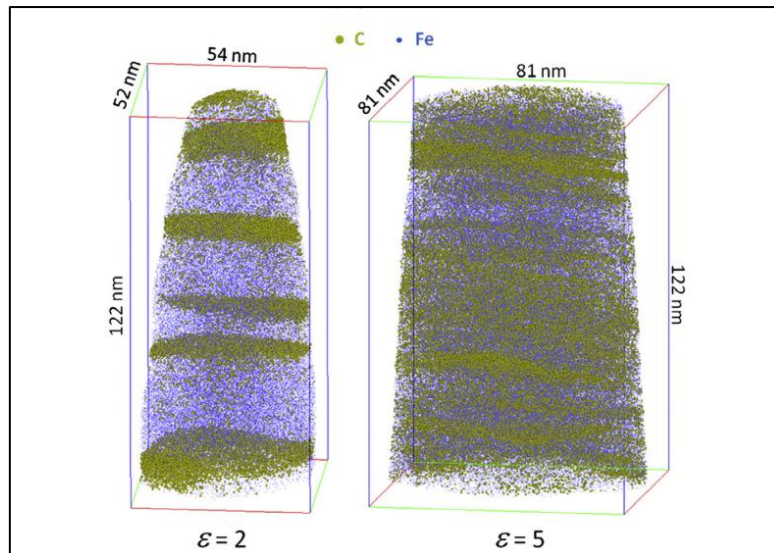


Figure 2:21 - 3D atom maps of C and Fe in wires with a drawing strain of 2 and 5. 2% of Fe atoms and 20% of C atoms are displayed [45].

The application of atom probe tomography has confirmed three features of cementite dissolution. The reduction of carbon concentration in cementite lamellae is more severe with increased drawing strain. A carbon rich region occurs at the interface between ferrite and cementite. Following cementite dissolution, carbon concentration in ferrite lamellae is often higher than the equilibrium thermodynamic capacity. Borchers and Kirchheim suggested the high levels of dislocations generated during wire drawing increase the carbon capacity of ferrite [1].

Both TEM and APT have produced substantial variation when attempting to measure carbon redistribution. Some variation can be attributed to the difference in experimental approach, material and processing conditions. A heterogeneous microstructure and cementite dissolution, shown in Figure 2:20b, means it is a challenge to obtain a result which is truly representative of the microstructure. An atom probe tomography tip can be less than 300x60x60nm and a thin foil TEM sample can be less than 150nm thick. The question of

whether such a small sample is representative of a microstructure is especially prudent when considering strain ageing.

Analysing the tens or hundreds of samples necessary to create a representative data set for a microstructure is not reasonably achievable in many cases. Site-specific FIB preparation and APT is prohibitively expensive. Nevertheless, localised techniques have proven to be effective in the study of strain ageing. Moreover, several studies have shown that a combination of global and localised experimental techniques is an effective way of quantifying the evolution of cementite morphology [13][5][6][8].

2.5 Cementite Dissolution

Cementite dissolution is thoroughly documented via global and localised experimental techniques. Some observations of cementite dissolution, which will be considered when discussing the potential mechanisms of cementite dissolution in this section, are presented below:

- Guelton et al. demonstrated that cementite dissolution occurs immediately upon drawing, with a 3.7 times higher linear rate above a drawing strain of 1.5, shown in Figure 2:16 [9].
- Pearlitic interlamellar spacing prior to wire drawing influences strain ageing kinetics [34] [45].
- Cementite dissolution effects the number of interstitial carbon atoms available to pin dislocations, leading to the change in mechanical properties [22].
- Li et al. reported an upper limit in the carbon saturation of ferrite at higher drawing strains ($\epsilon=3.5 - 4$) [45].

Whilst the dominant mechanism(s) of cementite dissolution remain unclear, several mechanisms have been proposed. The mechanism proposed by Grindev is based on carbon dislocation interaction. Grindev suggests the binding enthalpy between carbon atoms and

dislocations in the ferrite is energetically favourable over the cementite bond energy [46]. This creates a driving force for cementite dissolution, facilitated via diffusion and carbon-dislocation interaction. Of particular relevance to this project, a review by Gavriljuk suggested both carbon-dislocation binding enthalpy and cementite bond energy could be influenced by composition [35].

An alternative mechanism, proposed by Languillaume et al., attributes cementite dissolution to the substantial increase in interfacial free energy during wire drawing [37]. The substantial increase in interfacial free energy is attributed to lamella thinning and the creation of slip steps, leading to fragmentation in cementite during deformation. For cementite lamellae, this results in the surface area energy component becoming much more significant than the volume energy component, thus creating a driving force for cementite dissolution.

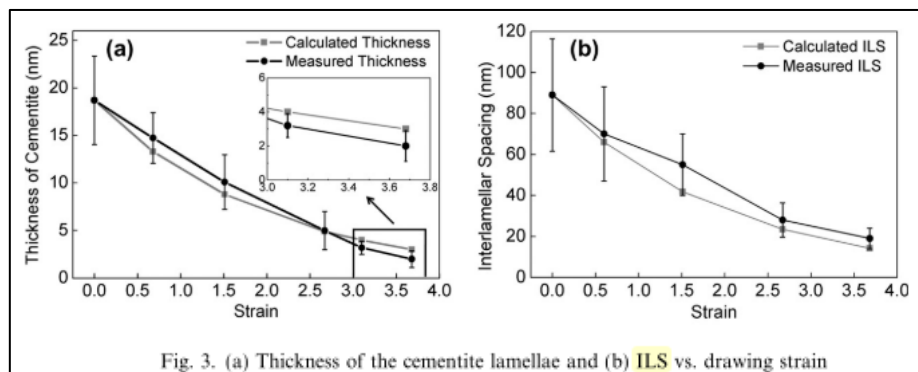


Figure 2:22 - TEM Measurements of the change in ILS and cementite lamellae thickness with drawing strain [47].

For simplicity, Gavriljuk's mechanism shall be referred to as the binding energy mechanism and Languillaume et al.'s mechanism, the interfacial free energy mechanism. An initial comparison of the two proposed mechanisms responsible for cementite dissolution in drawn wire is as follows. The first observation is that cementite dissolution occurs immediately upon wire drawing and the rate of cementite dissolution increases by 3.7 times above a drawing

strain of 1.5 [9]. Sevillanio et al. reported distinct slip band formation in cementite at a drawing strain of only 0.43 [48]. Observed slip band formation in such low drawing strains suggests interfacial energy may be contributing immediately upon drawing. Nam et al. demonstrated a clear difference in cementite dissolution between steels with different interlamellar spacing, concluding that a finer interlamellar spacing was responsible for the increased cementite dissolution [34]. However, the dissolution cannot be entirely attributed to lamellar thickness. It is possible to produce an as-transformed rod microstructure, which has a finer interlamellar spacing than an as drawn microstructure, highlighted by Guelton et al. [9]. Cementite dissolution does not occur in undeformed pearlite, whereas it would occur in the drawn wire with a larger interlamellar spacing. Therefore, the interlamellar spacing cannot be solely responsible.

Also, if cementite lamellae thickness or interlamellar spacing were predominantly responsible, one would expect a distinct inverse correlation between cementite lamellar thickness or interlamellar spacing and cementite dissolution. This does not appear to be the case, as shown previously in Figure 2:16. Figure 2:16 shows two distinct linear regimes of cementite dissolution. Moreover, Zhang et al. published TEM measurements of interlamellar spacing and cementite lamellae thickness in wires with drawing strains up to 3.7, shown in Figure 2:22 [47].

Whilst there is an inverse correlation, interlamellar spacing does decrease as cementite dissolution increases. There does not appear to be a distinct change in the rate of interlamellar spacing or cementite thickness at a strain of 1.5. Therefore, it is unlikely that the

reduction in interlamellar spacing is exclusively responsible for the increase in the rate of cementite dissolution. Assuming the interfacial free energy mechanism is correct, the fragmentation and creation of slip bands during deformation must be primarily responsible for the increase in the rate of cementite dissolution.

Once the reorientation of cementite lamellae is predominantly completed at a drawing strain of 1.5, it is plausible the activation of different deformation mechanisms may be responsible for the change in the rate of cementite dissolution. Sevillano et al. suggested thin cementite lamellae may be susceptible to failure by shear [48]. Shear or another deformation mechanism may require a critical cementite lamellar thickness to become the dominant mode of deformation. Therefore, interlamellar spacing may be indirectly responsible, hence the lack of a distinct correlation.

Li et al. suggests the influence of cementite lamellae thickness can be ascribed to dislocations [49]. Li et al. suggested that a thinner cementite lamellae thickness would increase the volume of phase boundaries present, increasing the number of dislocations present at the interface, facilitating increased cementite dissolution. Li et al. also suggested the dissolution of cementite in this way may lead to small particles being further cut by dislocations. Dislocation cutting of small cementite particles would increase the interfacial energy, leading to further dissolution via the Gibbs-Thompson effect. The dissolution of cementite further increases the phase boundary interface area and an increasing rate of dissolution. Li et al. attributes cementite dissolution to carbon dislocation interaction and states that interfacial free energy may contribute following initial dissolution via dislocation interaction [49].

The binding energy mechanism also accounts for cementite dissolution immediately on drawing. Wire drawing generates dislocations, which accumulate at the ferrite cementite interface. A higher binding enthalpy between dislocations and carbon atoms make it energetically favourable for carbon atoms to leave cementite to bind with a dislocation, thus creating the driving force for carbon diffusion and cementite dissolution. It is very challenging to precisely measure or calculate the binding enthalpy between carbon atoms and dislocations in a drawn wire microstructure. In the review of Borchers and Kirchheim, a variety of values were obtained from the literature, 0.4 - 0.7eV, depending on the experimental or modelling approach [1].

In line with the binding energy mechanism, Guelton and Francois proposed that a change in deformation mechanism is responsible for the change in cementite dissolution regime [9]. They propose the initial regime occurs as dislocation glide is confined to ferrite lamellae. The regime changes after ferrite is predominantly realigned to the drawing axis and dislocations begin to cut through cementite lamellae [9]. Atomistic simulations of the Bagaryatskii orientation relationship, completed by Guziewski et al., supports this mechanism [50]. Guziewski et al. found ferrite plastically deformed first in all simulations regardless of orientation and dislocation loops which nucleated at the interface readily propagated into ferrite matrix. Bhadeshia also reports that the Burgers vectors of dislocations in cementite are much higher than in ferrite, making the transfer of slip to cementite difficult during the initial stages of deformation [2].

Fang et al. demonstrated that creating a rod microstructure with a degree of inherited texture prior to wire drawing is an effective way of reducing the amount of bent or fragmented pearlitic lamellae [28]. This would require less drawing strain to realign the majority of the pearlite grains to the drawing direction and result in less fragmented cementite lamellae. An increase in torsional ductility and tensile strength were reported in the rod with an inherited texture. It is unfortunate this study did not extend to compare the amount of cementite dissolution between the microstructures. This would be an ideal way to test the mechanism proposed by Guelton and Francois [9].

Deformation and dislocation motion are essential to both of the aforementioned mechanisms. The binding energy mechanism relies on carbon-dislocation motion and interaction. The interfacial free energy mechanism is based on an increase of interfacial free energy through the deformation of cementite, through lamella thinning and slip band formation. In light of this, Li et al. proposed a dislocation-based mechanism for cementite dissolution [51]. Li et al. suggested dislocations which cut through cementite lamellae drag carbon atoms out of cementite. This will be referred to as the dislocation drag mechanism. Whilst this is compatible with both binding energy and interfacial free energy mechanism, it may also be operating independently.

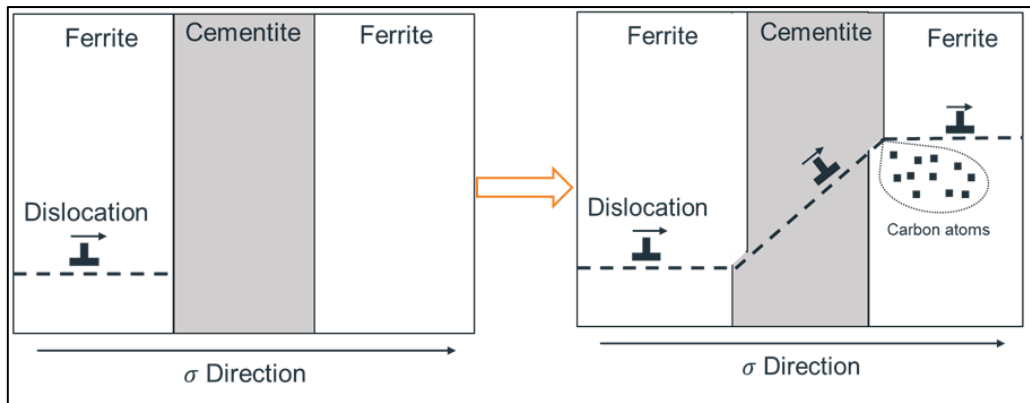


Figure 2:23 - Simplified illustration of dislocation drag mechanism [52].

Nematollahi et al. used a multiscale simulation approach to demonstrate screw dislocations in cementite are able to transport carbon atoms along their associated glide planes. Nematollahi et al. found binding energy between carbon and a dislocation was dominated by elastic interactions of the carbon atom with the strain field of the dislocation and calculated that under certain conditions carbon-dislocation interaction could indeed be energetically favourable [53].

A correlation between the rate of cementite dissolution and increase in both UTS and yield strength is widely reported. Guelton et al. reported the evolution of tensile strength in wires produced in the same manner as wires analysed by electrolytic phase extraction to reveal a change in concavity at a strain of 1.5, shown in Figure 2:24 [9].

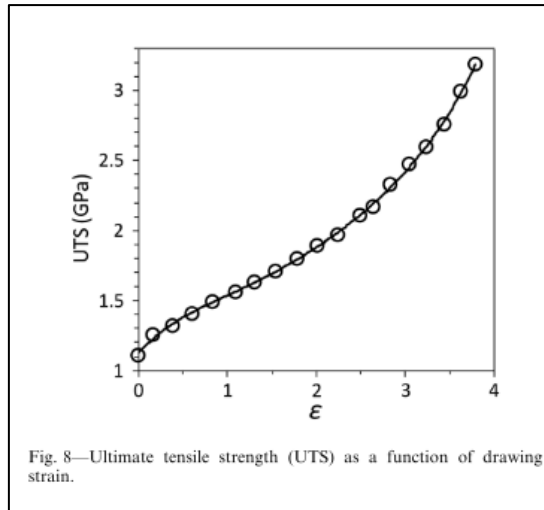


Figure 2:24 - Change in UTS with drawing strain [9].

Lamontagne plotted the evolution of yield stress in as-drawn wires against drawing strain, shown in Figure 2:25, which shows a change in linear relationship occurring at a drawing strain of 1.5. Zelin also reported the evolution of UTS and yield strength in as-drawn wires, Figure 2:26.

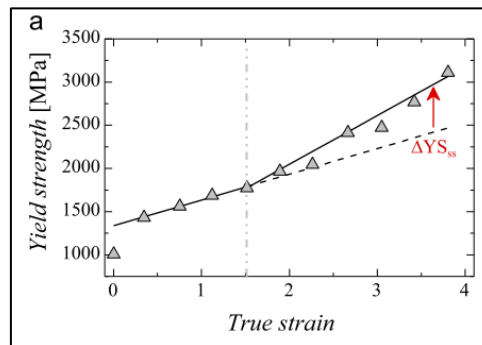


Figure 2:25 - Change in yield strength with drawing strain [29]

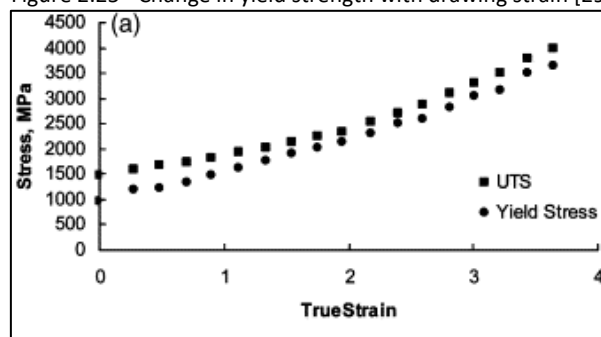


Figure 2:26 - Change in UTS and Yield strength with drawing strain [8]

The evolution of yield strength has a direct correlation with cementite dissolution, also consisting of an increased linear relationship above a drawing strain of 1.5. Larger drawing strains generate increased dislocation densities and further work hardening. In particular, yield strength is determined by dislocation motion and interaction. There is a distinct correlation between the evolution of yield strength and the rate of cementite dissolution, shown in Figure 2:25 and Figure 2:16 respectively.

Kresse et al. found with an increased wire drawing strain it is possible to increase the diffusion coefficient of nickel in ferrite by up to 6 orders of magnitude when compared to unstrained ferrite. Note, this result was measured in the ferrite only, avoiding interphase interfaces and grain boundaries. The result was attributed to carbon vacancy complexes, with additional carbon content and drawing strain, diffusion in ferrite significantly increases. This observation was attributed to an increased amount of vacancy carbon complexes [54], suggesting increased carbon content and drawing strain would further increase the diffusion of interstitial carbon atoms during strain ageing.

Bang et al. reported an increase cementite dissolution in cementite lamellae which had undergone increased bending during wire drawing [42]. Lamellae which had undergone significant bending and reorientation, i.e. increased deformation by dislocation motion, were measured to have a reduced carbon concentration compared to a lamella which underwent minor bending to realign. Although, this observation could equally be attributed to an increase in interfacial free energy due to slip band formation during deformation etc.

Li et al. presents further evidence attributing dislocations to cementite dissolution via the upper limit of carbon saturation in ferrite, which occurs at around a drawing strain of 4 [45]. Li et al. also reported X-ray dislocation density measurements of ferrite lamellae, finding that dislocation density did not significantly increase above drawing strains of 4 [45]. Li et al. also used APT to show the distribution of carbon atoms is closely related to the distribution of dislocations. Heterogeneous dislocation structures have been observed in ferrite during wire drawing, which accounts for the heterogeneous nature of cementite dissolution [45].

Cementite dissolution through dislocation interaction is in agreement with observations from the literature. Experimental evidence points to carbon-dislocation interaction being the dominant mechanism of cementite dissolution. The carbon dislocation drag mechanism may also be active in conjunction with the binding energy mechanism. This does not entirely discount the interfacial free energy mechanism. As highlighted by Li et al. [45], this mechanism may well be contributing after initial dislocation cutting has occurred.

An inconsistency exists with the binding energy mechanism, which relies on the ratio of carbon-dislocation binding enthalpy to cementite bond energy to determine the rate of cementite dissolution. Elements which increase the thermodynamic stability of cementite, i.e. increase cementite bond strength, have been found to increase the amount of cementite dissolution. This suggests that the determination of the carbon-dislocation binding energy is not entirely chemical. Thus, the study of steel composition may reveal which mechanism of cementite dissolution is dominant.

2.6 Steel Composition

Steel composition is capable of influencing both inter cementite metallic bond energy and carbon-dislocation binding enthalpy. Two interatomic bond types exist within cementite, metal to metal (metallic) and metal to carbon (covalent). Mizuno et al. used first principles molecular orbital calculations to show solute atoms in cementite have little effect on the metal to carbon bond energy but can influence metal to metal bond energy [55].

Mizuno et al. concluded from the observed slip planes (001), which are predominantly metallic planes, the metal to metal bond is likely to determine the critical stress for dislocation motion in cementite. Figure 2:27 shows titanium, vanadium, chromium and manganese increase cementite metallic bond energy, whereas cobalt and nickel reduce cementite metallic bond energy [55]. Further discussion of cementite bond energy will therefore be referring to the metallic bonds.

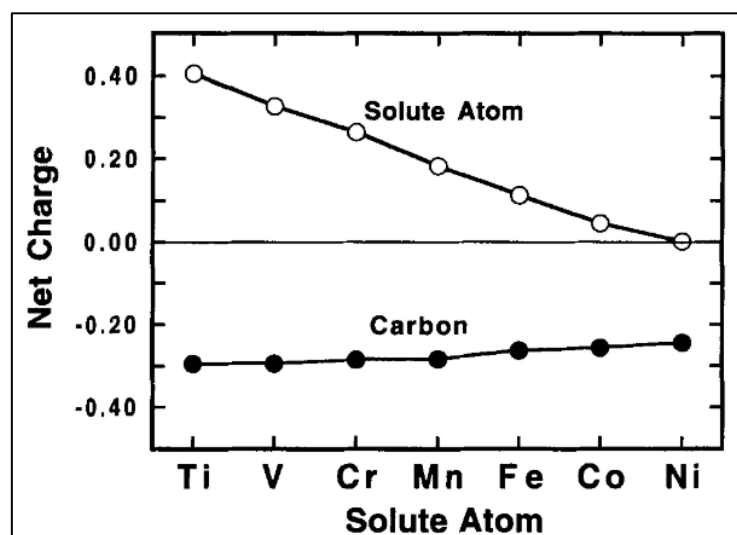


Figure 2:27 - Variation of net charge/bond energy with solute atom in cementite [55].

Inoue and Masumoto observed deformation of cementite containing manganese, chromium, nickel, and cobalt via TEM. Inoue and Masumoto observed the slip planes activated in cementite alloyed with chromium were (110) and (001), for plain carbon and manganese cementite observed slip planes were (100), (001) {110}, and for cementite containing nickel slip planes (110), (010), (001) and {110} were observed. The predominant slip planes of cementite containing cobalt were not confirmed.

Table 2:1 - Dislocations observed in cementite by Inoue and Masumoto [56].

Cementite	Cold Rolling at RT	Tensile deformation at 500°C
Fe_3C	S.D	S.D, E.D., Loop Cusp, Dipole Sub-Boundary
$(Fe, Cr)_3C$	Low Cr: S.D High Cr: N.D	S.D
$(Fe, Mn)_3C$	S.D Stacking Fault	S.D, E.D, P.D Loop Stacking Fault
$(Fe, Ni)_3C$	S.D, E.D	S.D, E.D Sub-boundary
N.D: No Dislocation, S.D: Screw Dislocation E.D: Edge Dislocation, P.D: Partial Dislocation		

Dislocation densities were found to decrease in the order of chromium, manganese and then nickel. Nickel contained the lowest dislocation density, cobalt and nickel additions increased the plasticity of cementite. It was also reported that manganese not only increased cementite hardness, but activated the same slip planes as pure cementite during deformation [56]. Given the increase in hardness, with the same active slip planes, it is likely that manganese increases the inter cementite bond energy. Also, Inoue and Masumoto reported the formation of stacking faults and the disassociation of dislocations becomes easier with increasing manganese addition. This confirms that cementite composition can influence dislocation motion and plasticity. Producing a deformed cementite microstructure with less

or altered dislocation densities and structures through cementite composition may influence the rate of cementite dissolution.

Wang and Yan studied the effect of nickel and cobalt on the structural stability of cementite with density functional theory [57]. It was found that cobalt and nickel in cementite increased the lattice parameter and volume. Nickel and cobalt also lead to a higher formation energy of Fe_3C , implying cobalt and nickel may destabilise cementite, leading to increased dissolution.

Kanetsuki et al. confirmed that a cobalt addition improved drawability and reduced grain boundary cementite precipitation in higher carbon steel wires [58]. This is in agreement with the reported increase in cementite plasticity due to reduced bond energy strength reported by Inoue and Masumoto [56] and Wang and Yan [57].

Coronado and Rodriguez reported chromium and vanadium were effective at increasing the strength of cementite, with chromium being more effective at strengthening, but a vanadium addition resulted in increased fracture toughness, even over unalloyed cementite [59]. Solano-Alvarez et al. reported rail steels containing vanadium had half the wear rate of non vanadium containing alloys and suggested that vanadium improves the stability and toughness of cementite. Solano-Alvarez showed via microscopical observations and thermodynamic simulations, vanadium partitions into cementite during the pearlite transformation [60]. Karabulut and Gunduz, in agreement with Coronado and Rodrigue, found a 0.14 wt. % vanadium addition improved tensile elongation to failure, although reported a drop in yield and UTS [61]. This was attributed to the reduction in interstitial

carbon and/or nitrogen present. Contrary to these findings, Fang et al. reported a steel micro alloyed with vanadium resulted in increased strength, but also increased fragmentation of cementite during deformation. Fang et al. presented atom probe reconstruction of a cementite lamella which suggested increased concentration of manganese, chromium and vanadium was present in a cementite lamella. However, the concentrations are not confirmed through graphical presentation of atomic concentrations [27]. De Moor et al. also demonstrated a steel containing vanadium and increased nitrogen levels resulted in increased strength of rod. The strength increase was attributed to vanadium nitride precipitates, although this was not confirmed with micrographs [62].

Maejima et al. suggested an alternative strengthening mechanism occurs with a vanadium addition. When isothermally held at 873K for 180 seconds Maejima observed no vanadium carbides during TEM or via 3D atom probe microscopy, shown in Figure 2:28a. Also, under these conditions a vanadium addition did not enhance work hardening behaviour as estimated by Ashby's work-hardening theory of dispersion hardened crystals. Yet a strength increase was measured without the presence of vanadium carbides. This was attributed to a lattice strain increment which was experimentally estimated with x-ray diffraction. A theoretical calculation completed during the study suggested a change in cementite lattice constant could result in an increased ferrite/cementite misfit, causing the lattice strain increment [63].

However, when held isothermally at 873K for 3600 seconds, fine vanadium carbides were observed in ferrite lamellae (Figure 2:28b). Therefore, Maejima concluded the vanadium

carbides were formed by ageing precipitation. This suggests that under certain conditions vanadium has the potential to relocate or diffuse during strain ageing. The effect of vanadium on the microstructure of drawn wire is therefore influenced by the combined vanadium, carbon and nitrogen content, and processing conditions such as temperatures and ageing treatments.

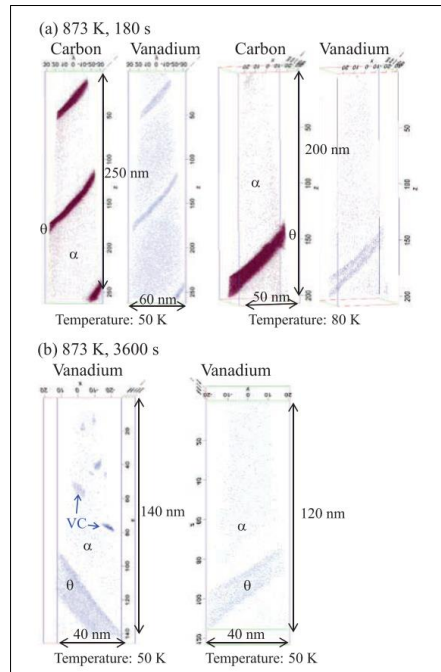


Figure 2:28 - Atom probe reconstruction of pearlite, vanadium and carbon distribution [63].

Hinchliffe and Smith presented 3D atom maps showing the distribution of silicon, vanadium, manganese and chromium. Silicon was located predominantly in ferrite, while vanadium and chromium were located almost exclusively in cementite. Manganese is present in ferrite and cementite, but in a significantly higher concentration in cementite [24].

In heavily drawn wires ($\epsilon = 6.02$), Li et al. reported the formation of coarse hexagonal sub grains after annealing at 673K for 30 minutes [17]. APT of the microstructure also showed

carbon and silicon segregated to the ferrite sub grain boundaries whilst manganese and chromium accumulated at the interphase interface.

Pereloma et al. studied the effect of chromium and molybdenum on strain ageing behaviour in lower carbon steels. Pereloma et al. reported chromium reduces the rate of strain ageing by 3 times compared to a non-alloyed low carbon steel. The beneficial effect of chromium was attributed to a reduction in the amount of carbon present to pin dislocations, due to chromium carbide formation. In contrast, molybdenum accelerated the strain ageing response by a factor of 0.7 [64].

Zhou et al. also reported a reduced torsional ductility and increased delamination in wires with an increasing chromium addition [65]. Although, for this study, this effect could not be entirely attributed to the influence of chromium on cementite stability. Many processing variables must be standardised before valid conclusions can be drawn regarding the influence of composition on cementite dissolution. In this study, steel with differing chromium contents were given identical heat treatments, resulting in differing interlamellar spacings. Alloying additions can act as significant grain refiners, or alter the transformation kinetics (hardenability), requiring differing cooling rates to achieve a consistent interlamellar spacing. This is paramount in isolating composition as a variable, given interlamellar spacing influences the amount of cementite dissolution which occurs [34].

In a technical review, Tarui et al. confirmed the benefits of chromium and silicon in delaying spheroidisation, which is equivalent to the third stage of strain ageing. Silicon has a very low

solubility in cementite and therefore segregates to the ferrite cementite interface. As the spheroidisation rate in a steel containing silicon is determined by the diffusion of silicon at the ferrite cementite interfaces, an increased amount of silicon results in slower diffusion and the rate of spheroidisation subsequently decreases. Conversely, chromium is a strong carbide former and enriches the cementite. The slow diffusion rate of chromium in cementite contributes to slowing the rate of spheroidisation by inhibiting the growth of carbides [20].

Pennington et al. also found a silicon addition reduced the effects of spheroidisation during ageing. A higher silicon addition enhanced the strength of as drawn and aged wires. This was attributed to increased resistance to dislocation motion, due to silicon being in solid solution in ferrite lamellae [66]. Raemdonck highlighted that a silicon addition is especially suited to galvanised applications, where silicon increases the strength of as drawn and aged wires. Increased rod strength requires a smaller drawing reduction to achieve tensile requirements, which slows the rate of cementite dissolution. A silicon addition also reduces the associated strength loss due to spheroidisation during galvanising treatment. Raemdonck reviewed the benefits of a chromium addition, whilst highlighting a manganese addition is detrimental to pearlite stability during strain ageing [19].

A review was completed by Gavriljuk on the effect of steel composition. With large alloying additions, Gavriljuk reported cementite dissolution could be mitigated entirely, shown in Table 2:2 [35]. Although little detail is given on materials and testing conditions during this study, samples appear to be cold rolled plate with a reduction of 91.5%, not drawn wire.

Table 2:2 - Gavriljuk cementite dissolution Mossbauer spectroscopy measurements [35].

Steel	Composition (at.%)	Cementite decomposition, $\pm 1\%$
80	3.94C	37.0
80Ni2	3.80C+2.12Ni	32.0
80Ni6	3.76C+6.05Ni	0
80Co2	3.80C+2.05Co	24.0
80Co6	3.70C+5.98Co	15.5
80V	3.89C+0.52V	3.5
80Mo	3.89C+0.51Mo	18.0
80Mn2	3.84C+2.02Mn	47.0
80Si2	3.89C+2.09is	36.0

Interestingly, nickel and cobalt reduced the amount of cementite dissolution the most significantly. This is contradictory to expectations, as results published by Wang and Yan showed nickel and cobalt reduced the thermodynamic stability of cementite [57]. Table 2:2 shows a vanadium and molybdenum addition were beneficial in reducing cementite dissolution, whilst manganese increases the amount of cementite dissolution. A silicon addition appears to have little effect on cementite dissolution. Gavriljuk also presents carbon-dislocation binding enthalpy estimates, measured by Beresnev et al. and Blanter et al. via internal friction, shown in Table 2:3.

Table 2:3 - Reported Carbon-Dislocation binding enthalpy [35].

Alloy composition (at.%)	$H_B \pm 0.02$ (eV)
α -Fe	0.78
Fe+5.0Co	0.39
Fe+5.0Ni	0.20
Fe+5.4Si	0.55
Fe+0.5V	0.60
Fe+3.9Mn	1.85
Fe+0.5Mo	1.86
Fe+1.0Cr	1.74

Manganese, which reduces the formation energy of cementite, making cementite more thermodynamically stable [2], increases cementite dissolution. Yet elements such as nickel and cobalt, which reduce cementite thermodynamic stability, reduce cementite dissolution. This is further evidence that the primary driving force of cementite dissolution is not thermodynamic.

Alloying elements which affect the chemical bonding in cementite appear to have the greatest effect on carbon-dislocation binding enthalpy measurements, shown in Table 2:3. Nickel and

cobalt reduce cementite bond energy and reduces cementite dissolution. Manganese increases cementite bond strength and promotes cementite dissolution. Chromium increases cementite bond energy, similarly to manganese. As shown in Table 2:3, chromium increases the carbon-dislocation binding enthalpy, although its effect on cementite dissolution is not reported in Table 2:2. However, Mizuno et al. calculated vanadium to have the highest cementite bond energy, yet it appears to reduce the amount of cementite dissolution [55]. These findings suggest it is not exclusively cementite bond energy which determines the rate of cementite dissolution.

Table 2:3 shows a silicon addition of 5.4 at.% (~2.7 wt.%), reduces carbon-dislocation binding enthalpy of 0.23 eV. Yet a silicon addition does not appear to reduce the amount of cementite dissolution that occurs. This suggests carbon-dislocation binding energy is also not the primary driving force for cementite dissolution. Silicon is rejected from cementite, as shown in various APT analysis [17] [24], yet silicon appears to reduce carbon-dislocation binding enthalpy, shown in Table 2:3. As silicon has negligible solubility in cementite, it is also unlikely to affect inter cementite bond energy significantly [67]. This implies silicon is influencing the carbon dislocation binding enthalpy by means other than cementite bond energy. Pennington et al. reported silicon increased the strength of ferrite lamellae through solid solution strengthening [66], which inhibits dislocation motion. Therefore, it may be possible to influence carbon dislocation binding enthalpy in several ways. These results suggest that on its own, silicon may not be effective in reducing the rate of cementite dissolution, but when combined with elements such as nickel it may enhance cementite stability. The reported accumulation of silicon at the ferrite cementite interface during spheroidisation may be

beneficial in reducing carbon dislocation interaction. Silicon enrichment at the interface is also reported [43], which may present a physical barrier to carbon diffusion, reducing carbon diffusion across the interface.

Alloying elements which have been shown to increase plasticity, slip on additional slip planes or promote ductility in cementite, appear to reduce the amount of cementite dissolution. This includes vanadium, nickel and cobalt. Inoue and Masumoto reported chromium makes slip more difficult in cementite and increases the strength of cementite [56]. Whilst chromium has shown to be effective in delaying spheroidisation and is effective in tying up interstitial carbon, its effect on the initial stages of strain ageing and cementite stability are unclear. Manganese promotes cementite dissolution yet increases the bond energy of cementite. Cementite containing manganese has increased strength, deforms on the same slip planes as Fe_3C and increases the dissociation of dislocations [56]. The influence of manganese on dislocation dissociation and interaction across the interface may promote cementite dissolution.

During production, a large manganese addition is often necessary to ensure wire products meet tensile and ductility specifications. Manganese improves hardenability and is beneficial in reducing hot shortness via the formation of manganese sulphides, which reduces the adverse effects of sulphur content on ductility. Therefore, cleaner steels are necessary to reduce manganese content and alternative means of strengthening should be investigated to reduce the necessary manganese addition.

In summary, nickel and cobalt appear to reduce the amount of cementite dissolution. Manganese appears to promote cementite dissolution. An effort should be made to reduce manganese levels through improved cleanliness of steels and alternative strengthening mechanisms. Silicon and chromium additions have proven effective in delaying spheroidisation, which is equivalent to the third stage of ageing. Although it is unclear of the effects of silicon in the earlier stages of ageing, the measured reduction in carbon-dislocation binding enthalpy suggests it should reduce cementite dissolution, yet it does not. The minor beneficial effects of silicon may be overwhelmed by the large drawing strains and temperatures generated during wire drawing. Chromium is reported as being effective in slowing spheroidisation, especially when combined with silicon. Chromium has also been reported as being effective at mopping up interstitial carbon atoms in low carbon steels [64]. Chromium drastically increased measured carbon-dislocation binding enthalpy, but its impact on cementite dissolution is unclear. Molybdenum is reported to both increase and decrease cementite dissolution, depending on the study [35] [64].

There are several ways in which steel composition may influence cementite dissolution. These include: alloying additions which can tie up and reduce the contribution of interstitial atoms (e.g. carbide and nitride formers V, Cr, Nb, B); elements which increase the strength of pearlitic rod to reduce the amount of carbon, manganese and drawing strain required. More directly, elements that have the potential to alter cementite bond energy and carbon-dislocation binding enthalpy may be beneficial. Elements can influence the deformation behaviour of both ferrite and cementite, which may influence how dislocations interact at the interface and between phases and so influence the extent of cementite dissolution.

The binding energy mechanism assumes the ratio of carbon-dislocation binding enthalpy to inter cementite bond energy is responsible in determining the rate of cementite dissolution. This does not appear to be the case. Conflicting reports for certain elements and the contribution of silicon and chromium to spheroidization, through diffusion, suggest cementite dissolution can be influenced by means other than the chemical stability of cementite. When considering the interfacial free energy mechanism, elements which affect cementite plasticity may affect lamella morphology during and after deformation, but the increased presence of dislocations in such regions points to other mechanisms. The dislocation drag mechanism is capable of accounting for inconsistencies in the cementite bond energy to carbon-dislocation binding enthalpy ratio. It can be inferred from the dislocation drag mechanism that cementite plasticity and dislocation motion contribute to determining the rate of cementite dissolution. This is in line with experimental observations that cementite with increased plasticity results in an altered dislocation structures and interactions, and reduced cementite dissolution. Composition is an ideal way to test how elements with increased cementite bond energy can influence the earlier stages of strain ageing, which may reveal which mechanisms are dominant.

2.7 Summary

The current understanding of the strain ageing mechanisms active in high carbon pearlitic steels both during and after wire drawing is briefly summarised in the following:

The initial stages of strain ageing in cold drawn high carbon wire are attributed to dislocation pinning and an initial breakdown of the pearlitic cementite lamellae. The second stage consists of cementite readily dissolving and the formation of some carbides. The final stage is linked to coarsening of the carbides, causing pinned dislocations to be freed, which eventually produces an over ageing effect. Strain ageing appears to be diffusion activated as the kinetics of the reaction are controlled by the extent of deformation (number of dislocations generated) and the temperature during and after cold deformation (controlling the diffusivity of the carbon and nitrogen in the ferrite). However, the contribution of each proposed mechanism of cementite dissolution remains unclear.

Consistent experimental evidence shows dislocation interaction is the most likely physical mechanism of cementite dissolution. However, given the difficulty in accurately determining the binding enthalpy between carbon atoms and dislocations within a drawn wire microstructure, the dislocation drag, or binding energy mechanism are yet to be conclusively proven. Conversely, the interfacial free energy mechanism is not completely disproven with observations linking cementite dissolution to dislocation interaction and deformation. Given interfacial energy is such a dominant driving force of many processes in material science, it is likely to be contributing. As none of the mechanisms have been categorically disproved, it is assumed each may be active and perhaps some additional mechanism(s) which are yet to be identified. As shown in Table 2:4, the effects of individual alloying elements have been reported in the literature, with occasionally conflicting claims.

Table 2:4 - Summary of the effects of Alloying Additions.

Element	Cementite Bond Energy/Thermodynamic stability	Strain ageing or Cementite Dissolution Effect	Carbon-Dislocation Binding Enthalpy	Element Location in Drawn Pearlite	Additional Information
Si	Appears to reduce cementite thermodynamic stability [2], However, this is likely a kinetic effect rather than thermodynamic [20].	Reduces rate of spheroidisation [66], negligible effect on cementite dissolution [35].	Reduces carbon-dislocation binding enthalpy [35].	Predominantly located in ferrite, slight accumulation at α/Fe_3C interface [24], Silicon is rejected from cementite [19]	-
V	Increases cementite Bond energy [55], increases cementite strength and fracture toughness [59], increase ductility but reduces strength [61], increased cementite fragmentation [27].	Beneficial in reducing cementite dissolution [35].	Reduces carbon-dislocation binding enthalpy [35].	Higher concentration within cementite [24] [27], also present in ferrite [19].	Strong Carbo-Nitride former.
Cr	Increases thermodynamic Stability [55], increases cementite strength significantly [59].	Reported reduction of Dynamic SA due to CrC and CrN precipitates [61], Reduction of strain ageing [64], effective at slowing spheroidisation [20].	Increases carbon-dislocation binding enthalpy [35].	Slight increased concentration within cementite [24] [27], also present in ferrite [19].	Carbide former, Cr containing platelets become cementite crystal particles during cold deformation [65].
Mn	Increases cementite bond energy and cementite hardness [55] [56].	Accelerates Cementite dissolution [19] [35].	Increases carbon-dislocation binding enthalpy [35].	Located in ferrite and cementite, higher concentration in cementite [19] [24] [27].	Similar slip planes to Fe_3C , increased disassociation of partial dislocations observed [56].
Co	Reduces thermodynamic stability [55] [57].	Significantly reduces cementite dissolution [35].	Reduces carbon-dislocation binding enthalpy [35].	-	Increased cementite plasticity with addition slip planes active [56], improved drawability and reduced GB cementite precipitation [58].
Ni	Reduces thermodynamic stability [55] [57].	6.05 at.% addition claimed stopped cementite dissolution entirely [35].	Reduces carbon-dislocation binding enthalpy [35].	Higher concentration present in cementite than ferrite (See section: 3.1 - British Steel R&D Study - Influence of Nickel on Pearlite Stability).	Increased cementite plasticity with additional slip planes active [56].
Mo	-	Accelerates strain ageing [64]. Also reported to reduce cementite dissolution [35].	Increases carbon-dislocation binding enthalpy [35].	-	-

It is worth noting elements such as manganese, chromium, vanadium and boron are potent at increasing a steels hardenability, which results in a pearlite refinement effect. This must be accounted for when heat treating rod to produce consistent interlamellar spacing, which has been shown to influence cementite dissolution [34].

Little has been reported on the effects of multiple alloying elements on the earlier stages of strain ageing. For example, the combined effects of chromium and silicon has been shown to be effective in slowing diffusion in cementite and ferrite, respectively. Therefore, a combination of alloying elements may provide an additional benefit over the benefit of individual alloying elements reported in the literature.

3 Experimental Steel Development

The most suitable way of investigating the influence of composition on strain ageing was via the development of experimental steels. This chapter details the experimental steel development procedure including a preliminary study completed by British Steel R&D, thermodynamic modelling, and the experimental alloy selection.

A set of steels with systematically varied compositions was the most cost effective way of investigating the effects of individual elements. Using industrially produced steel compositions was ruled out due to the potential for inconsistent chemical composition tolerances. Also, the presence of nitrogen and other interstitial alloying elements found in BOS production can influence strain ageing. Achieving a homogenous rod microstructure with varying composition was crucial to isolating the influence of composition. This level of precision and consistency could only be achieved using a lab scale VIM furnace to produce the ingots.

The project was limited to 4 experimental steels due to time, budget, and manufacturing constraints. Therefore, the first part of the procedure following the literature review was to refine the number of alloying elements to 4. The list was refined using thermodynamic modelling as a guide within the limitations of cost, processing parameters and practicality.

3.1 British Steel R&D Study - Influence of Nickel on Pearlite

Stability

British Steel R&D completed a study on the effect of nickel on pearlite stability in 2015. The results from this study have been included in this chapter as they were utilised throughout the development of experimental alloys for this project. The work was completed by S.Hobson at British Steel R&D.

The data included mechanical testing results and an atom probe tomography reconstruction of a drawn wire. The study concluded that a nickel addition of 0.26 wt.% promoted ductile fractures in torsion tests of artificially aged wires. Two steel compositions, one plain carbon and one with a 0.26 wt.% nickel addition were drawn to wire, artificially aged and tested. The steel compositions are shown in Table 3:1.

Table 3:1 - Plain carbon and nickel steel compositions (wt.%).

	C	Si	Mn	Ni
Plain C	0.81	0.23	0.7	-
Nickel Steel	0.81	0.23	0.7	0.26

Table 3:2 - Torsion testing results from British Steel R&D study [68].

Steel $\varepsilon = 3.0$	Wire Condition	Revolutions to Failure	Torsion Fracture Type
Plain C	As-Drawn	12	3A
	Aged 3 months	13	3C
	10s @ 450°C	3	3C
	60s @ 450°C	6	3C
C-Ni (0.26 Ni)	As-Drawn	16	3A
	Aged 3 months	14	3A
	10s @ 450°C	13	2A
	60s @ 450°C	10	1B

Table 3:2 summarises the torsion testing results. The final column shows wires with a nickel addition that maintained a ductile fracture (type A) in all except the most severe aging condition (type B). When compared with a plain carbon steel, aged samples failed in a brittle (type C) fracture. This suggests nickel has increased the torsional ductility of the wires after ageing.

3.1.1 Atom Probe Tomography

The study utilised atom probe tomography to map the element distribution of the C-Ni steel with 10 seconds of artificial ageing at 450°C, as shown in Table 3:2. Wire samples were prepared by the lift out method via SEM-FIB. Wire composition is shown in Table 3:1. 10 seconds artificial ageing at 450°C was completed to simulate a hot dip galvanising process.

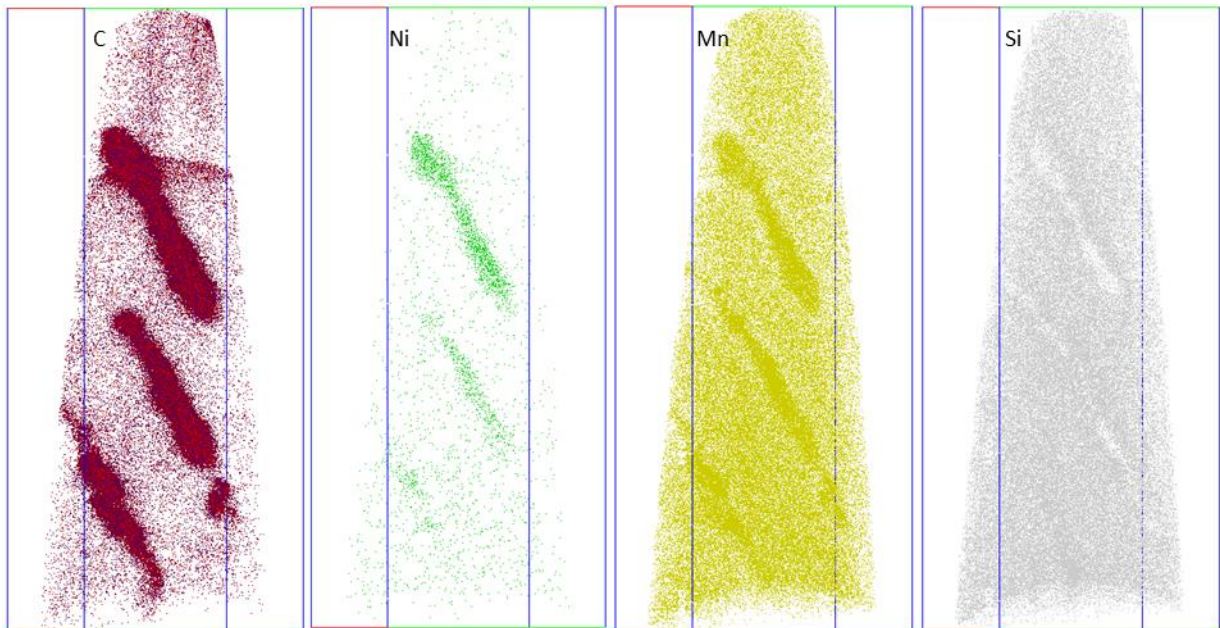


Figure 3:1 - 80x80x210nm Atom probe tomography reconstruction of a drawn pearlitic wire[68].

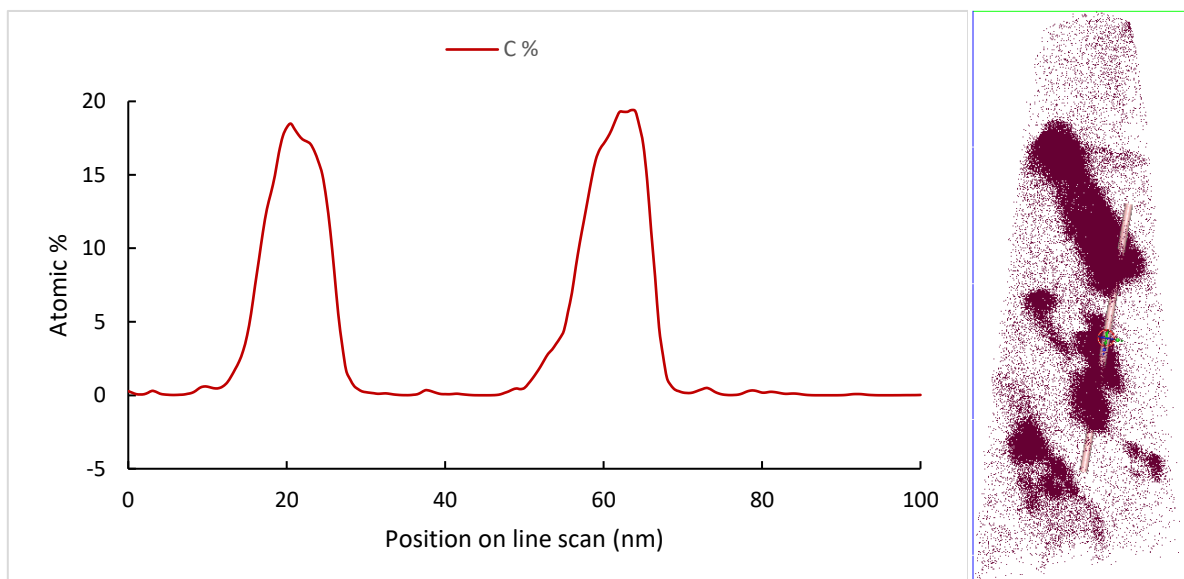


Figure 3:2 - Carbon concentration across line scan [68].

Figure 3:2 shows a line scan passing through two cementite laths at ~20nm and ~65nm.

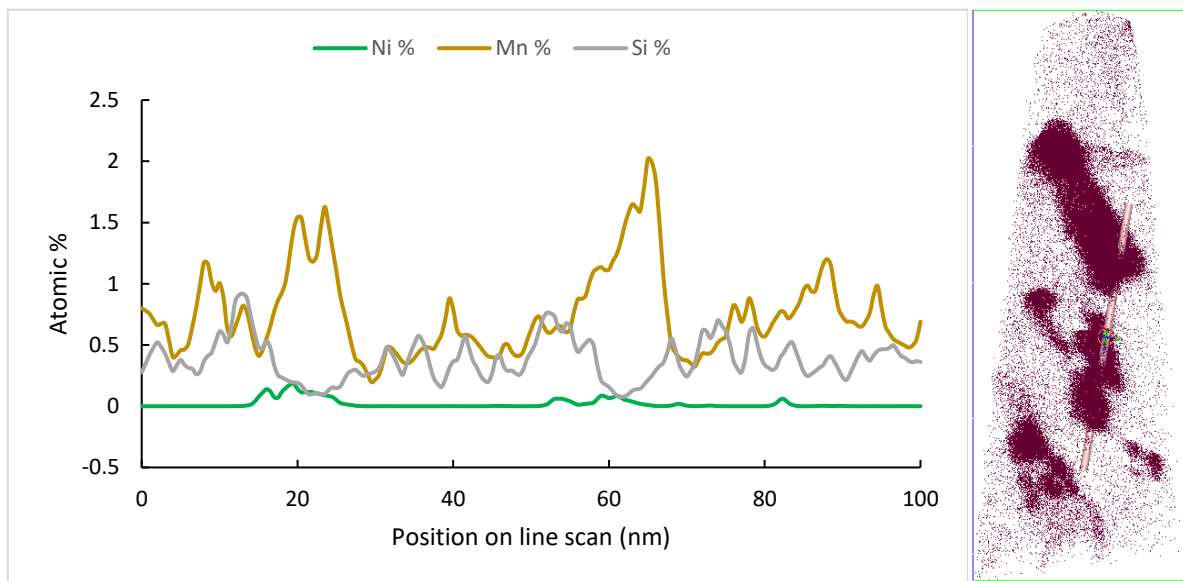


Figure 3:3 - Element concentration across line scan [68].

Figure 3:3 shows the element concentration across two cementite laths and the surrounding ferrite matrix. Two manganese peaks are present in line with the cementite laths at ~20nm and ~65nm containing approximately 1.5 at.% manganese. This suggests manganese is present throughout the ferrite matrix, although a higher concentration is located in the cementite.

The line scan also shows two distinct nickel peaks in line with the two cementite laths at ~20nm and ~65nm. Thus, suggesting nickel is predominantly located in the cementite. Silicon is present throughout ferrite matrix and has two troughs in line with the cementite laths at ~20nm and ~65nm. This suggests silicon is rejected from cementite.

3.2 Thermodynamic Modelling

Thermodynamic modelling was used to approximate alloying element distribution between phases and to predict the effect each alloying element would exhibit on cementite stability.

It was assumed alloying elements which affected physical or mechanical stability of cementite during strain ageing would also affect the thermal stability of cementite. Alloying additions which increased the cementite transformation temperature were assumed to also increase cementite stability and resistance to strain ageing. Thermodynamic modelling was used to approximate alloying element distribution and cementite transformation temperatures.

The model was simplified to only allow the formation of FCC_A1, cementite, and BCC_A2. It is therefore not possible from this data to predict the formation of any secondary phases, and their effect on cementite stability. Thermodynamic simulations are performed under equilibrium conditions representing bulk pearlite, not a drawn wire microstructure.

3.2.1 Methodology

Simulations were performed using Thermocalc 2016a with database: TCFE8.1. All simulations were performed at atmospheric pressure with a system mass of one kilogram. All simulations were performed between 1000 and 100 °C.

10 cooling simulations per alloying element were completed, the composition was altered incrementally by 0.1 wt.% between each simulation. Data points were extracted from Thermocalc and plotted in Origin. Each composition was plotted with a pure Fe-C system for comparison. Element distribution data was taken from the cooling simulation with 0.5 wt.%

of each alloying element. For each element, the initial cooling simulation was completed using a tertiary system with the following composition: 98.7Fe-0.82C-0.5X (wt.%), where X is an alloying element.

The cementite transformation temperature of a typical tyre cord composition was also calculated to obtain a base value for comparison. The point at which cementite is fully formed, T_f , was used as transformation temperature.

Table 3:3 - Commercial grade TC84B chemical composition (measured) and simulated composition.

Element (wt.%)	C	Mn	Si	P	S	N	B
Grade TC84B	0.82	0.5	0.2	0.01	0.007	0.004	0.0036
Simulated Composition	0.82	0.5	0.2	-	-	-	-

A common tyre cord composition was chosen as a base steel for comparison. This grade was selected as it contained boron and a coil was available for the project. Boron bonds with interstitial nitrogen atoms and reduces the contribution of nitrogen towards strain ageing.

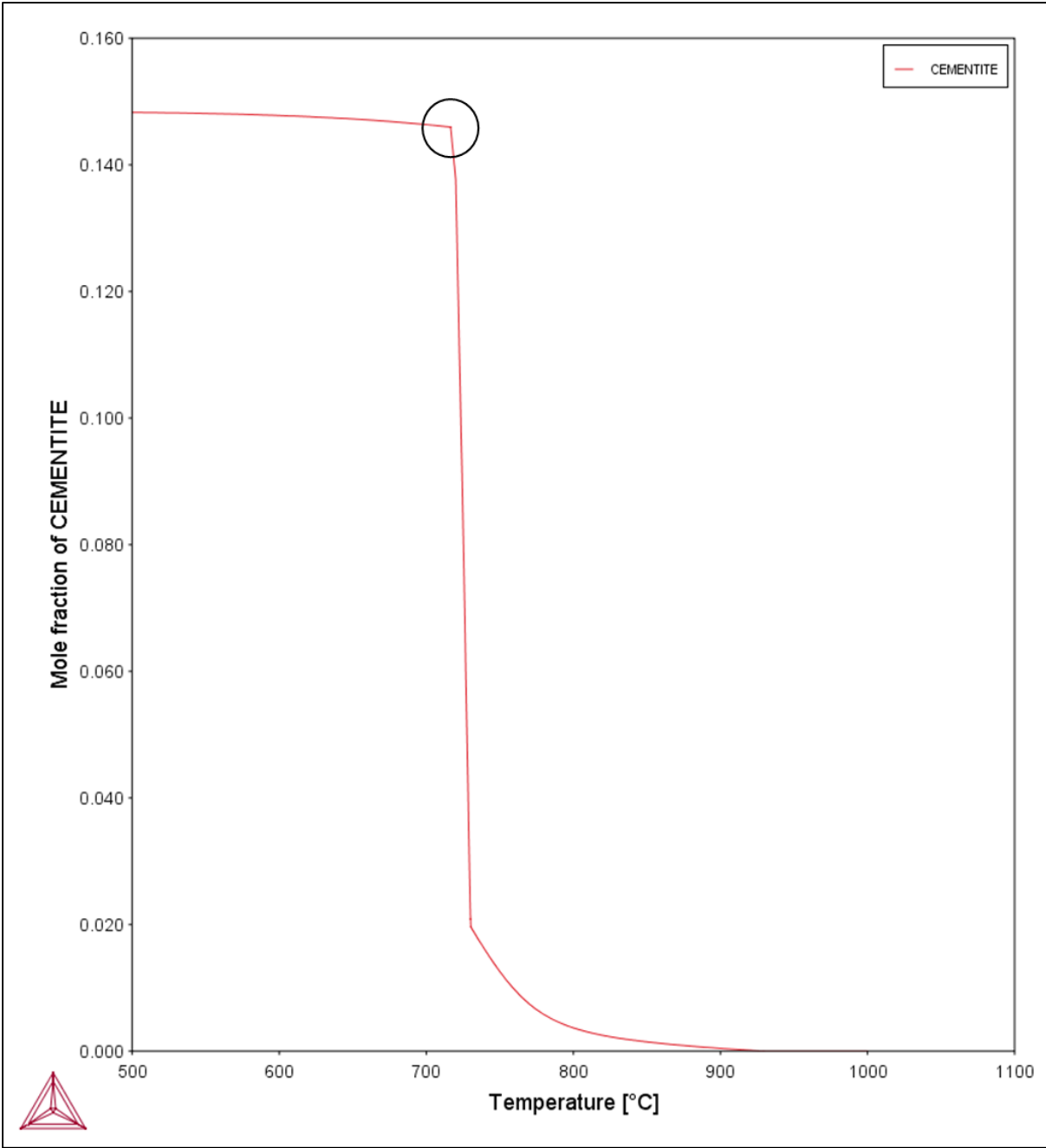


Figure 3:4 - Example cooling simulation. A circle highlights where the cementite transformation temperature was measured.

Figure 3:4 shows the formation of cementite during the transformation of austenite to pearlite. The measurement of cementite transformation temperature is highlighted within a circle in Figure 3:4.

Thermodynamic data from cementite transformation temperature calculations were also used to calculate the distribution of each alloying element. Elements that were rejected from both BCC_A2 and cementite phases were assumed to be present at the BCC_A2/cementite interface.

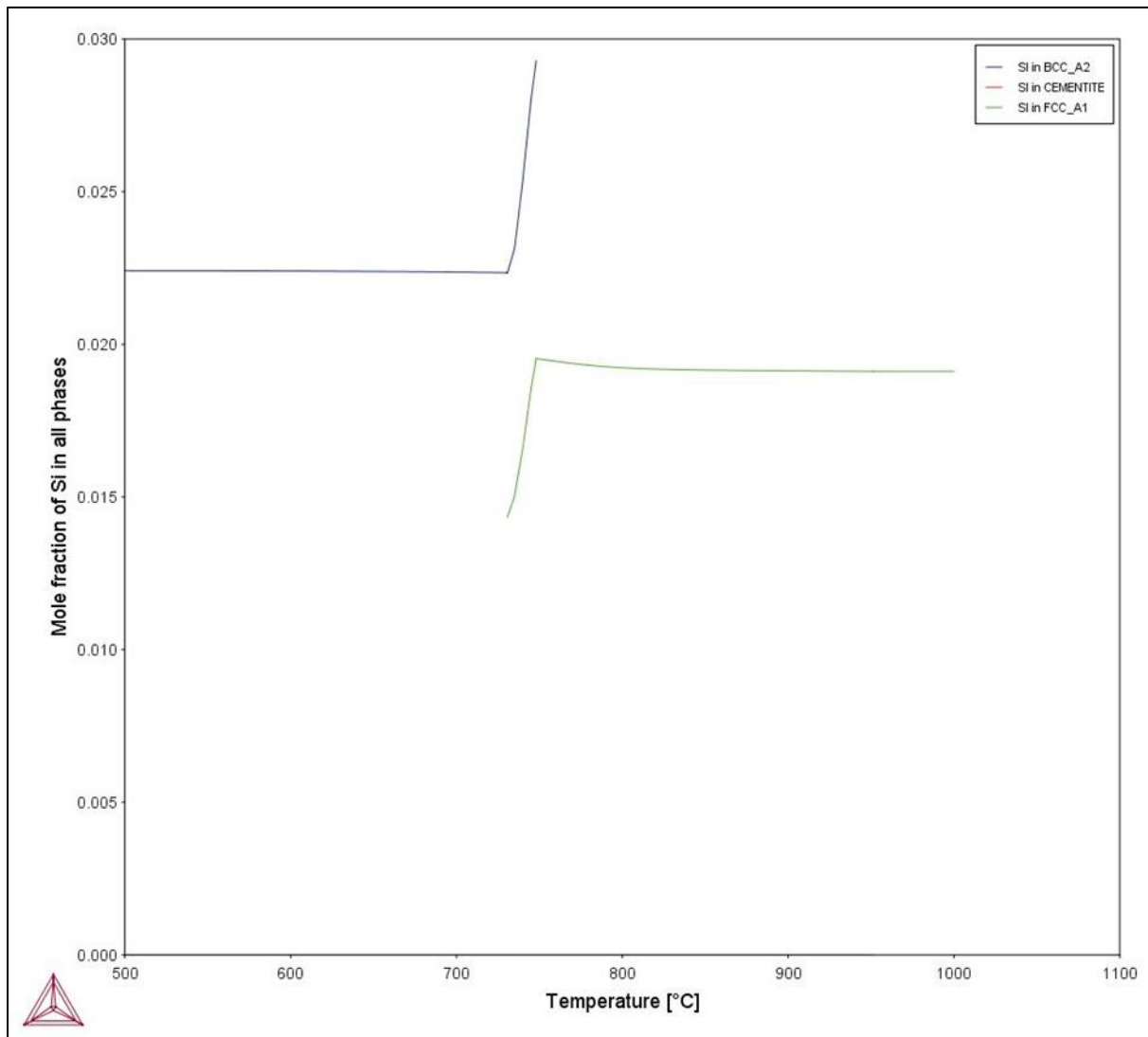


Figure 3:5 - Silicon distribution during austenite to pearlite transformation.

For example, Figure 3:5 shows how element distribution was obtained from the thermodynamic data. Figure 3:5 shows silicon located in the BCC_A2 and the FCC_A1, with no silicon located in the cementite.

3.2.2 Cementite Thermal Stability

Incremental additions of 0.1 wt.% of each alloying element were simulated and plotted with a pure Fe-0.82C system. Cementite start and finish transformation temperatures were also plotted.

3.2.2.1 Cobalt

Table 3:4, Figure 3:6 and Figure 3:7 show with increasing cobalt addition, an increase in cementite start and finish transformation temperature occurs. With a 1 wt.% cobalt addition, cementite start transformation temperature increases by 2°C and cementite finish transformation temperature by 5°C.

Table 3:4 - Influence of cobalt content on cementite transformation temperature.

Carbon (wt.%)	Cobalt (wt.%)	Cementite Start (°C)	Cementite Finish (°C)
0.82	0.0	750.3	726.6
0.82	0.1	750.6	727.2
0.82	0.2	749.7	727.8
0.82	0.3	750.9	728.3
0.82	0.4	750.9	728.9
0.82	0.5	750.9	729.5
0.82	0.6	750.9	730.0
0.82	0.7	751.7	730.6
0.82	0.8	752.1	731.2
0.82	0.9	752.3	731.7
0.82	1.0	752.1	732.3

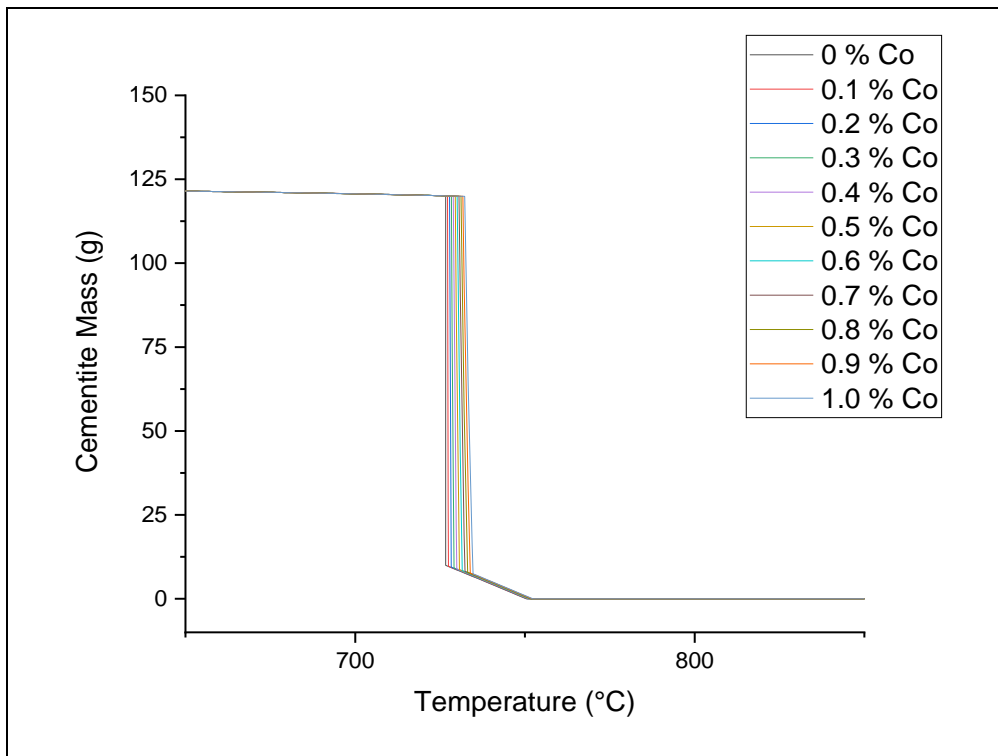


Figure 3:6 - Influence of cobalt on cementite transformation behaviour.

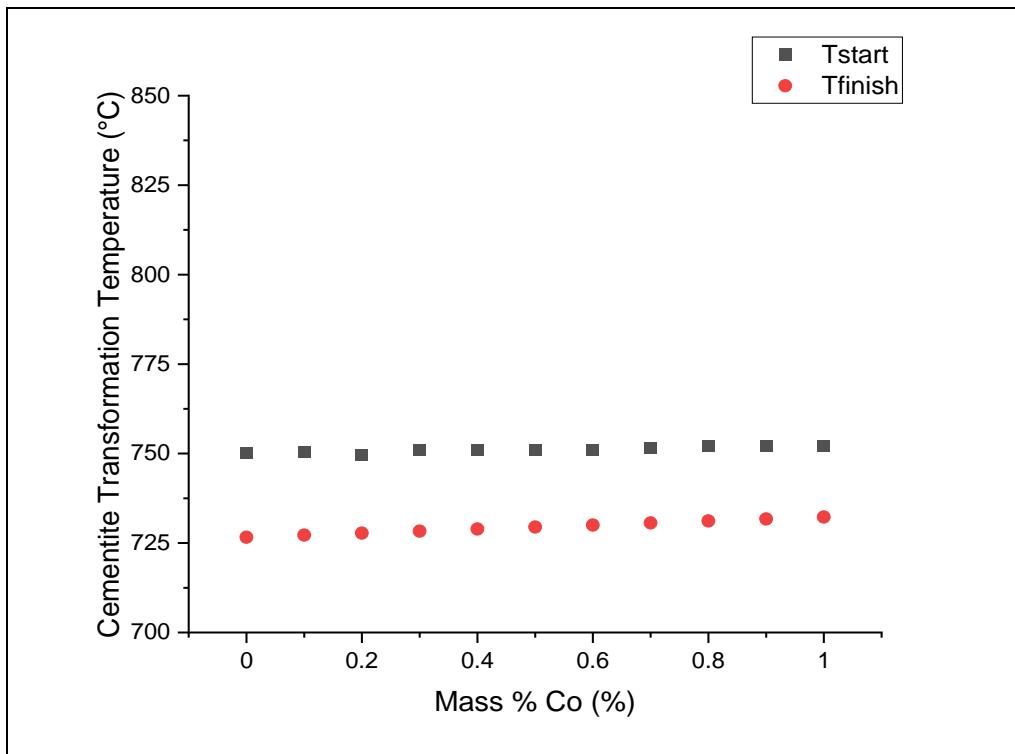


Figure 3:7 - Influence of cobalt content on cementite start and finish transformation temperature.

3.2.2.2 Chromium

Table 3:5, Figure 3:8 and Figure 3:9 show a 1 wt.% chromium addition increases the cementite start transformation temperature by 80 °C and increases the cementite finish transformation temperature by 11°C. This suggests chromium would improve cementite thermal stability.

Table 3:5 - Influence of chromium content on cementite start and finish transformation temperature.

Carbon (wt.%)	Chromium (wt.%)	Cementite Start (°C)	Cementite Finish (°C)
0.82	0.0	750.3	726.6
0.82	0.1	760.9	727.8
0.82	0.2	770.6	728.9
0.82	0.3	779.7	730.0
0.82	0.4	788.3	731.1
0.82	0.5	796.4	732.2
0.82	0.6	804.7	733.3
0.82	0.7	811.4	734.5
0.82	0.8	818.3	735.5
0.82	0.9	824.9	736.6
0.82	1.0	831.3	737.6

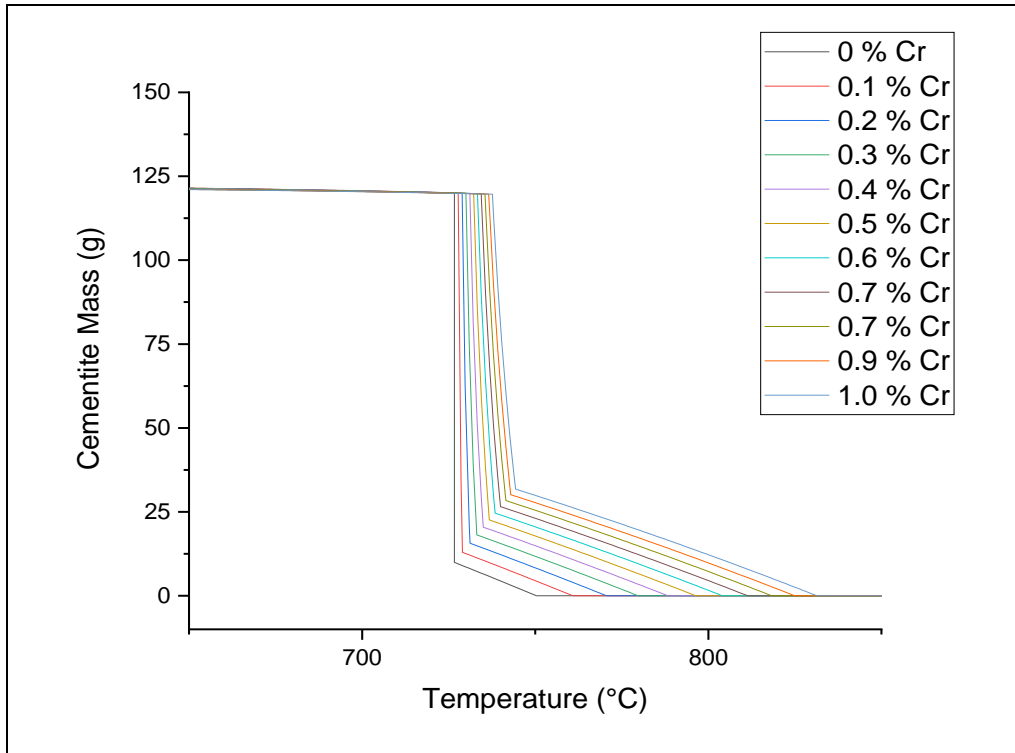


Figure 3:8 - Influence of chromium on cementite transformation behaviour.

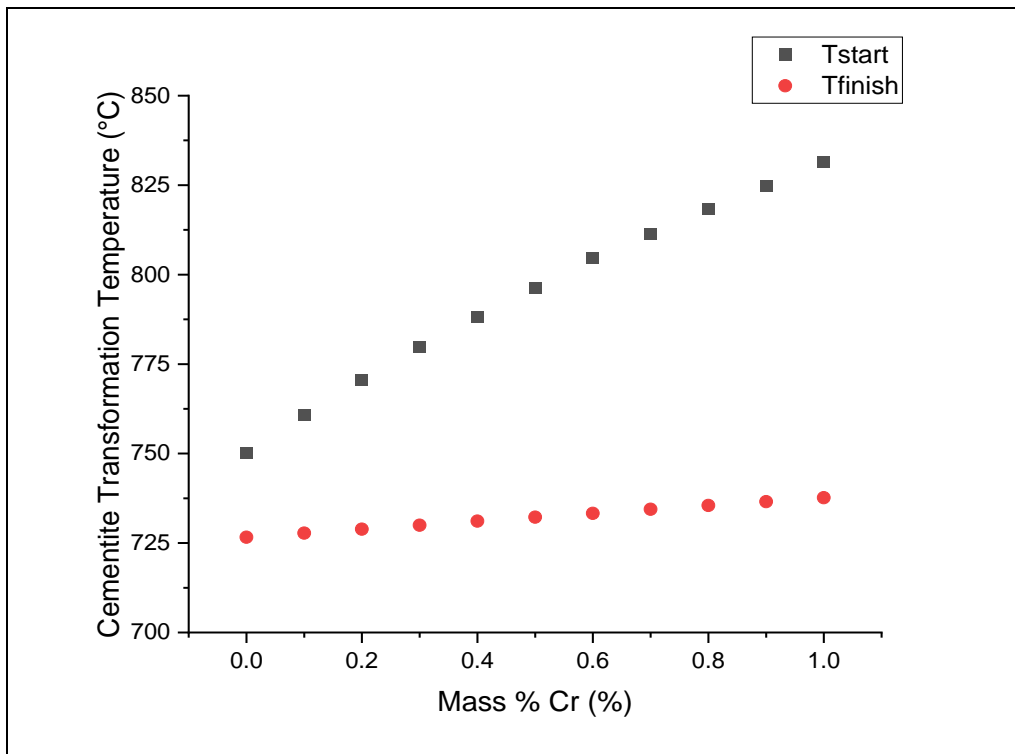


Figure 3:9 - Influence of chromium content on cementite start and finish transformation temperature.

3.2.2.3 Copper

Figure 3:10, Figure 3:11 and Table 3:6 suggested a 1 wt.% copper addition increases cementite start transformation temperature by 8°C and reduces cementite finish transformation by 9°C.

Table 3:6 - Influence of copper content on cementite start and finish transformation temperature.

Carbon (wt.%)	Copper (wt.%)	Cementite Start (°C)	Cementite Finish (°C)
0.82	0.0	750.3	726.6
0.82	0.1	751.1	725.1
0.82	0.2	751.9	723.7
0.82	0.3	752.6	722.2
0.82	0.4	753.4	720.7
0.82	0.5	755.0	719.2
0.82	0.6	754.4	717.8
0.82	0.7	755.8	717.5
0.82	0.8	756.6	717.5
0.82	0.9	757.4	717.5
0.82	1.0	758.2	717.5

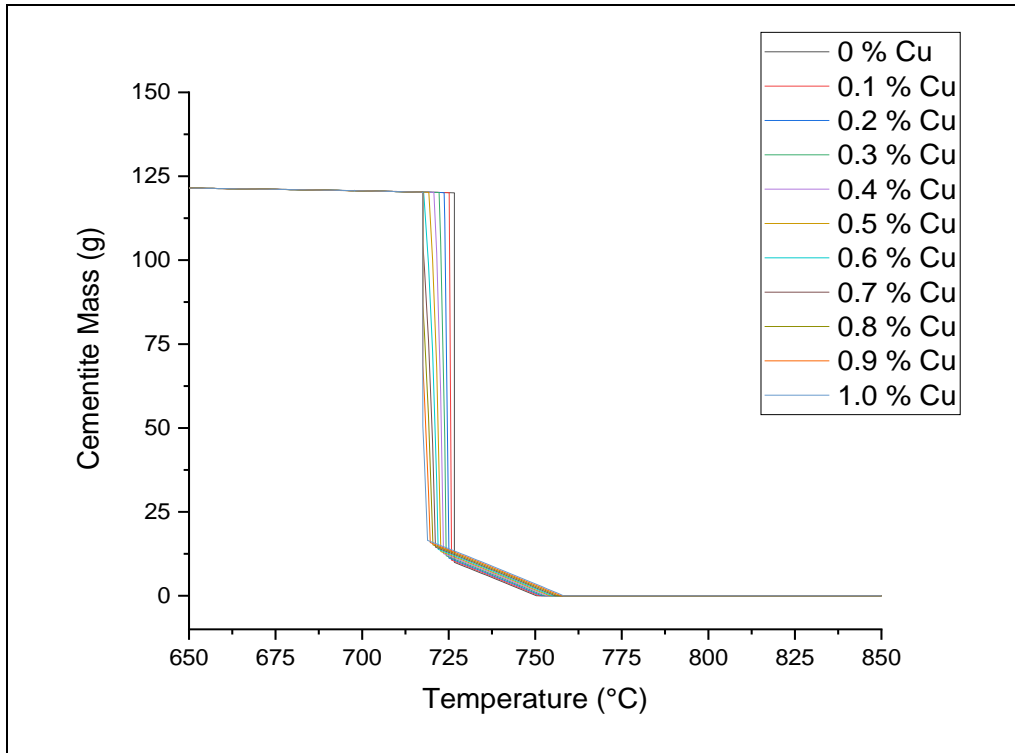


Figure 3:10 - Influence of copper on cementite transformation behaviour.

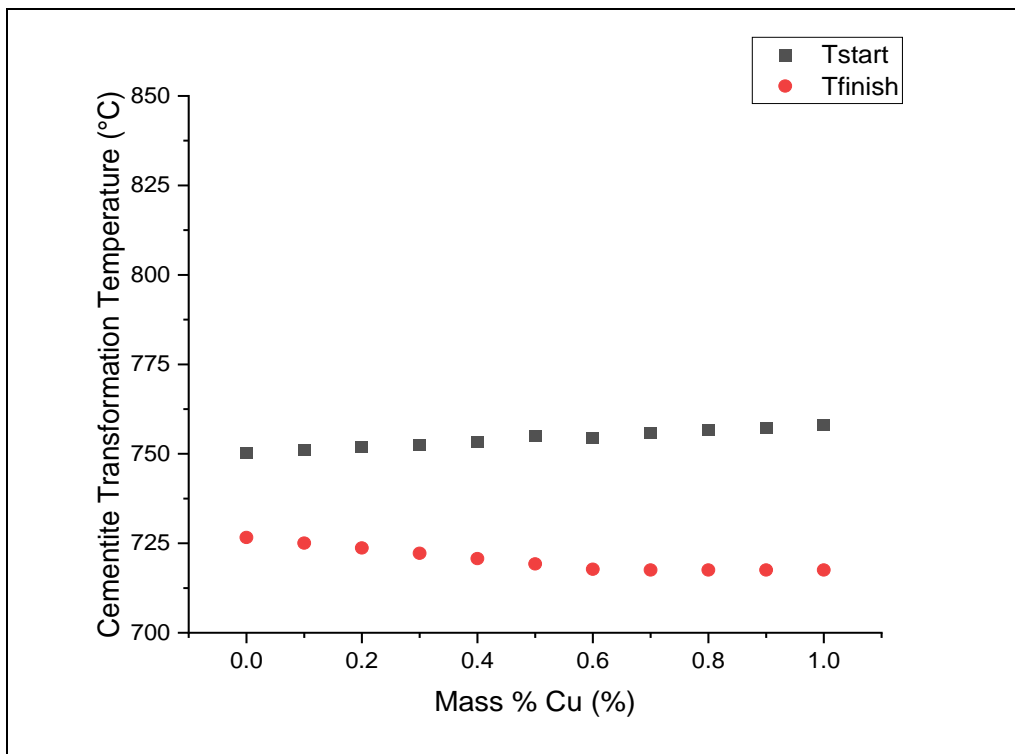


Figure 3:11 - Influence of copper content on cementite start and finish transformation temperature.

3.2.2.4 Manganese

As shown in Figure 3:12, Figure 3:13 and Table 3:7, a 1 wt. % manganese addition increases the cementite start temperature by 3°C and decreases the cementite finish temperature by 17°C.

Table 3:7 - Influence of manganese content on cementite start and finish transformation temperature.

Carbon (wt.%)	Manganese (wt.%)	Cementite Start (°C)	Cementite Finish (°C)
0.82	0.0	750.3	726.6
0.82	0.1	750.9	721.5
0.82	0.2	752.1	720.4
0.82	0.3	752.1	719.2
0.82	0.4	752.1	717.7
0.82	0.5	752.1	717.7
0.82	0.6	753.3	715.7
0.82	0.7	753.3	714.5
0.82	0.8	753.3	712.1
0.82	0.9	753.3	711.0
0.82	1.0	753.5	709.8

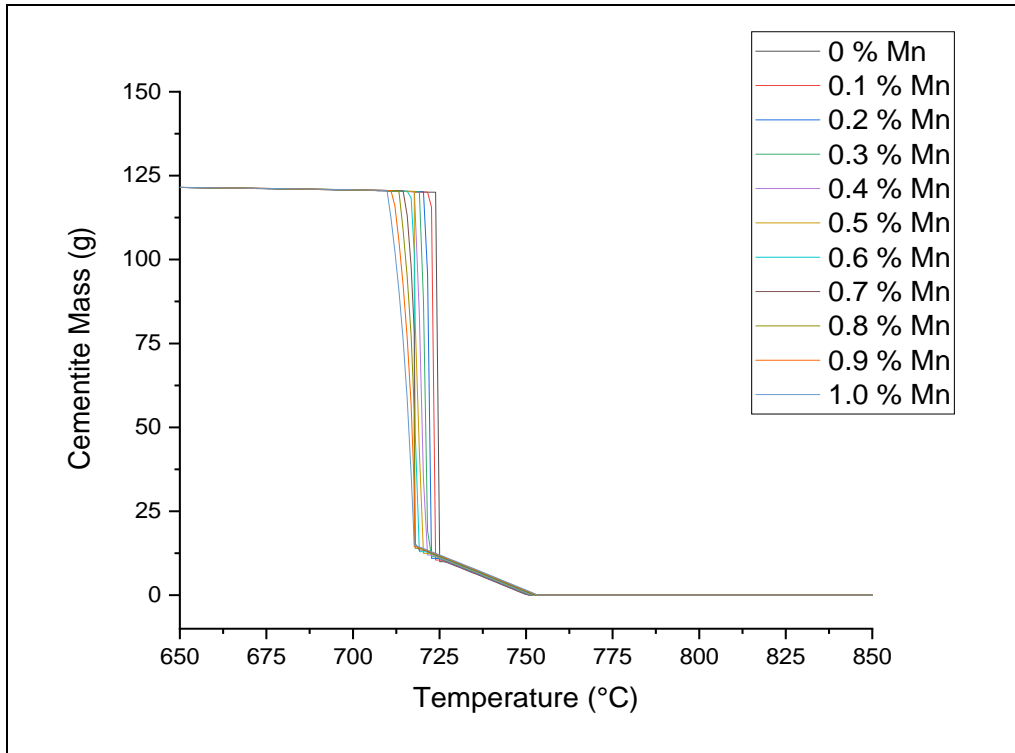


Figure 3:12 - Influence of manganese on cementite transformation behaviour.

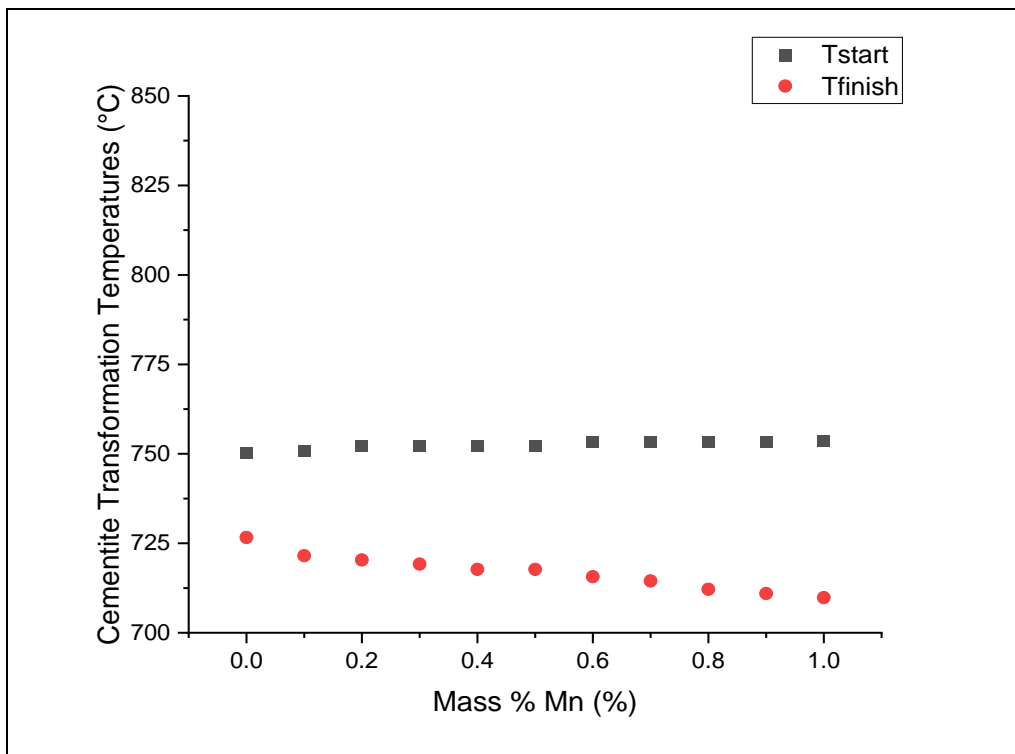


Figure 3:13 - Influence of manganese content on cementite start and finish transformation temperature.

3.2.2.5 Molybdenum

Table 3:8, Figure 3:14 and Figure 3:15 suggested a 1 wt.% molybdenum addition increased the cementite start transformation temperature by 10°C and increased the cementite finish transformation temperature by 5°C.

Table 3:8 - Influence of molybdenum content on cementite start and finish transformation temperature.

Carbon (wt.%)	Molybdenum (wt.%)	Cementite Start (°C)	Cementite Finish (°C)
0.82	0.0	750.3	726.6
0.82	0.1	752.1	732.1
0.82	0.2	753.3	733.3
0.82	0.3	754.4	733.3
0.82	0.4	755.6	733.3
0.82	0.5	755.6	733.6
0.82	0.6	756.8	733.6
0.82	0.7	758.0	733.6
0.82	0.8	759.1	733.6
0.82	0.9	760.3	733.6
0.82	1.0	760.4	731.1

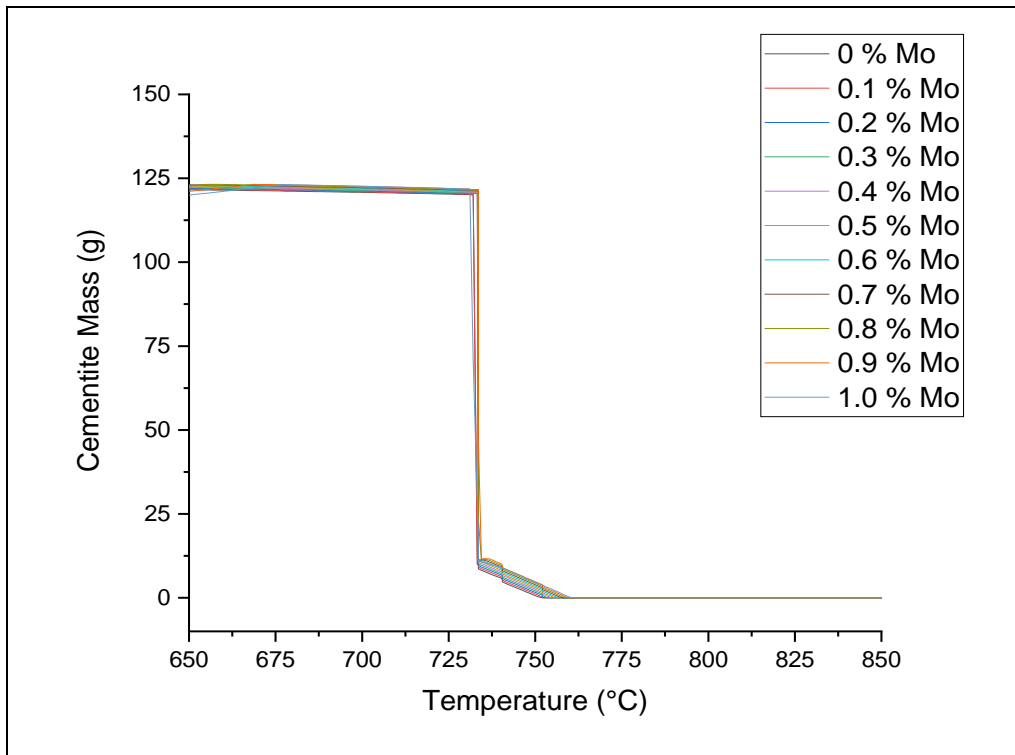


Figure 3:14 - Influence of molybdenum on cementite transformation behaviour.

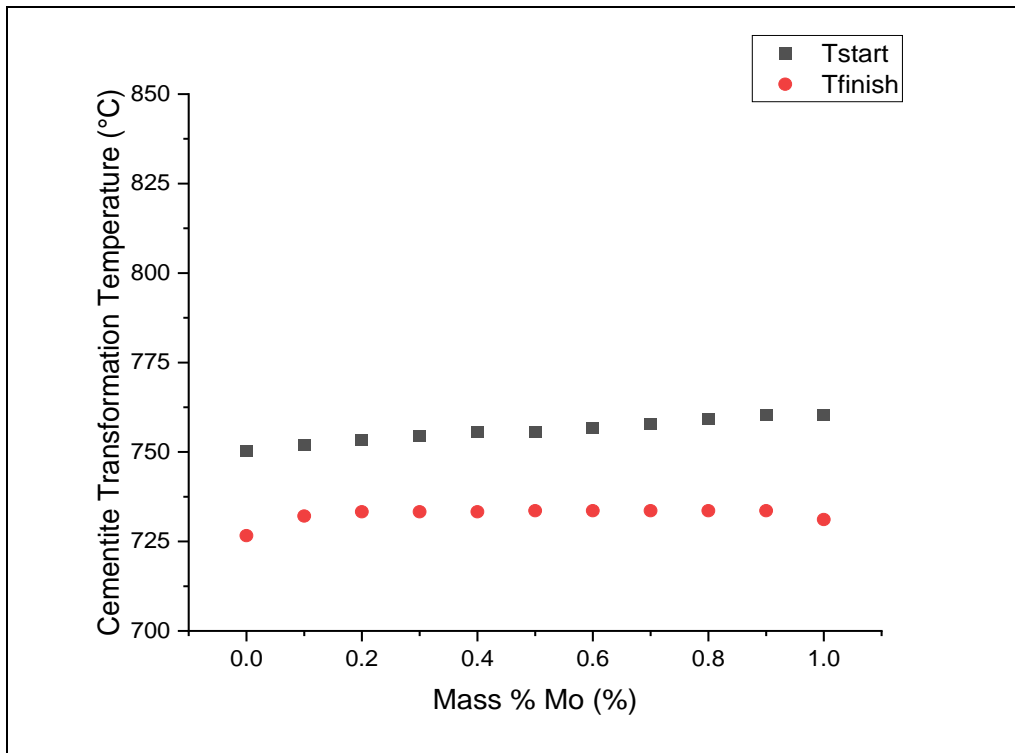


Figure 3:15 - Influence of molybdenum content on cementite start and finish transformation temperature.

3.2.2.6 Nickel

Table 3:9,

Figure 3:16 and Figure 3:17 show a 1 wt.% nickel addition increases cementite start transformation temperature by 3 °C and reduces cementite finish transformation temperature by 25°C.

Table 3:9 - Influence of nickel content on cementite start and finish transformation temperature.

Carbon (wt.%)	Nickel (wt.%)	Cementite Start (°C)	Cementite Finish (°C)
0.82	0.0	750.3	726.6
0.82	0.1	749.7	724.3
0.82	0.2	750.9	721.9
0.82	0.3	750.9	719.4
0.82	0.4	750.9	716.9
0.82	0.5	752.1	714.4
0.82	0.6	752.1	711.8
0.82	0.7	752.1	709.2
0.82	0.8	753.3	706.5
0.82	0.9	753.3	703.8
0.82	1.0	753.3	701.1

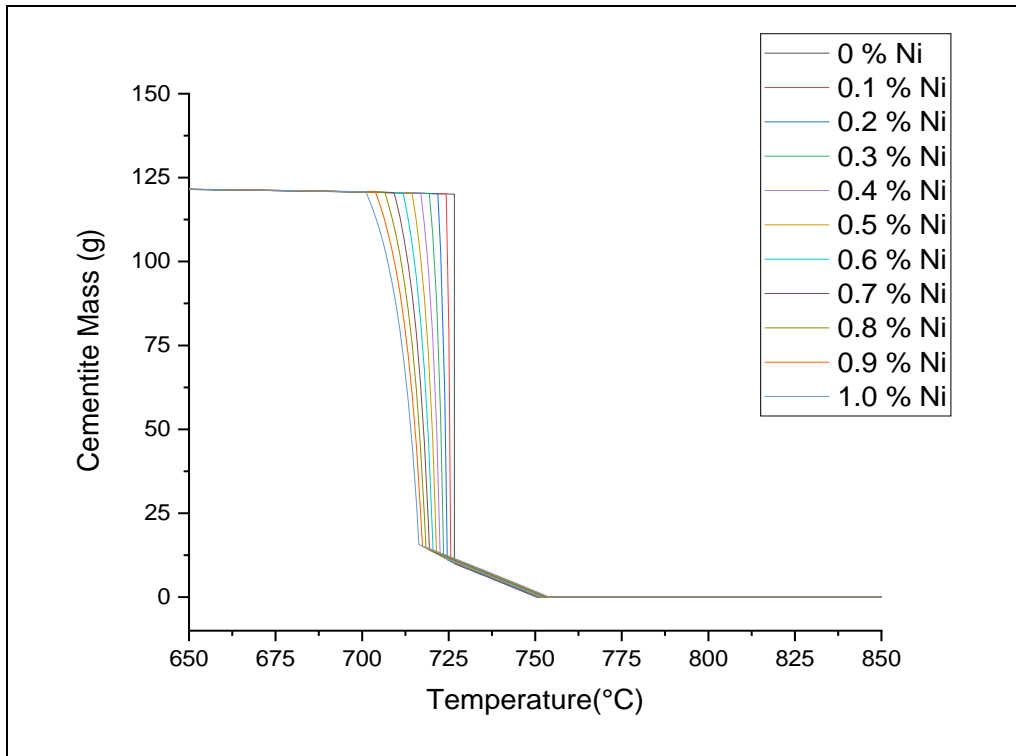


Figure 3:16 - Influence of nickel on cementite transformation behaviour.

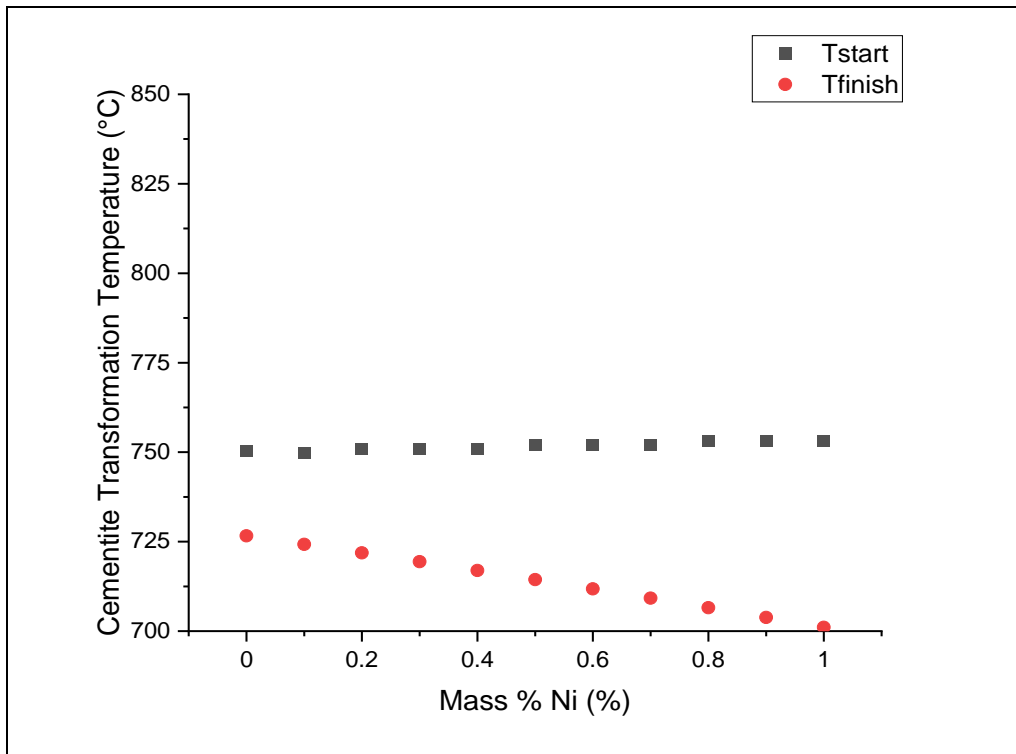


Figure 3:17 - Influence of nickel content on cementite start and finish transformation temperature.

3.2.2.7 Silicon

Table 3:10, Figure 3:18 and Figure 3:19 show that a 1 wt.% silicon addition increased the cementite start transformation temperature by 26°C and increased the cementite finish transformation temperature 13 °C.

Table 3:10 - Influence of silicon content on cementite start and finish transformation temperature.

Carbon (wt.%)	Silicon (wt.%)	Cementite Start (°C)	Cementite Finish (°C)
0.82	0.0	750.3	726.6
0.82	0.1	750.9	726.6
0.82	0.2	754.4	727.4
0.82	0.3	756.8	728.6
0.82	0.4	760.3	729.8
0.82	0.5	762.7	732.1
0.82	0.6	766.2	733.3
0.82	0.7	768.5	735.6
0.82	0.8	770.9	736.8
0.82	0.9	774.4	739.2
0.82	1.0	776.8	740.3

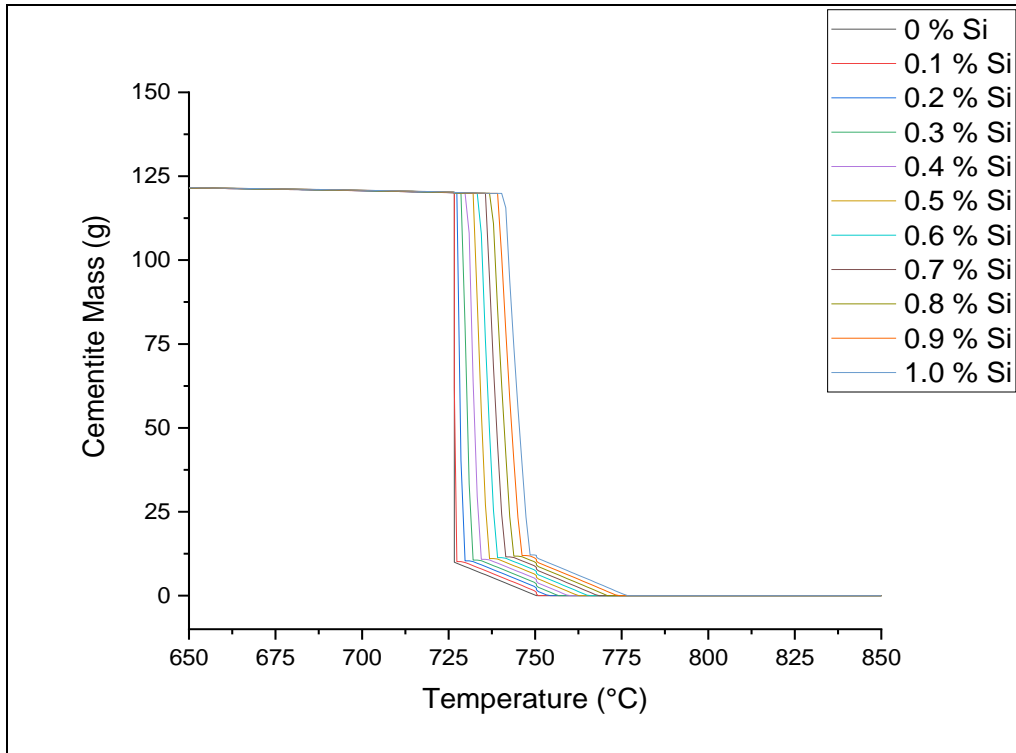


Figure 3:18 - Influence of silicon on cementite transformation behaviour.

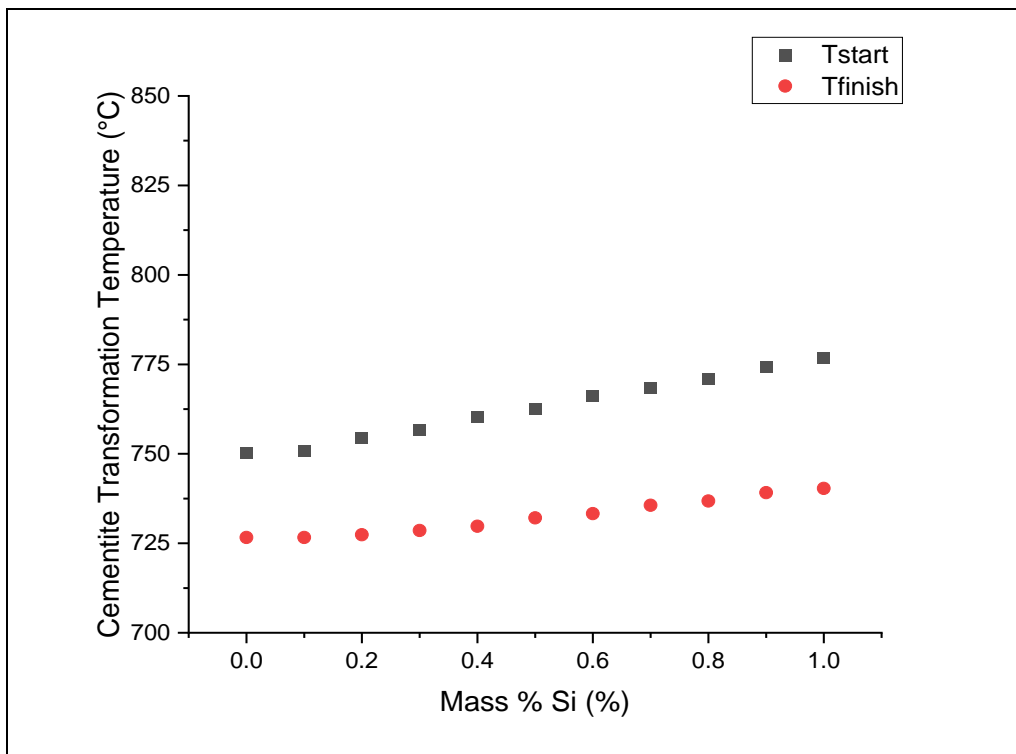


Figure 3:19 - Influence of silicon content on cementite start and finish transformation temperature.

3.2.2.8 Vanadium

Table 3:11, Figure 3:20 and Figure 3:21 show that a 1 wt.% vanadium addition reduced the cementite start transformation temperature by 23°C. It is worth noting this reduction occurred at 0.3 wt.% and remained constant for the subsequent simulations. Cementite start transformation temperature increased by 1°C and remained constant for all compositions with a vanadium addition. Figure 3:20 shows increasing vanadium content significantly reduces the total mass of cementite which forms.

Table 3:11 - Influence of vanadium content on cementite start and finish transformation temperature.

Carbon (wt.%)	Vanadium (wt.%)	Cementite Start (°C)	Cementite Finish (°C)
0.82	0.0	750.3	726.6
0.82	0.1	745.0	727.8
0.82	0.2	734.5	727.8
0.82	0.3	727.8	727.8
0.82	0.4	727.8	727.8
0.82	0.5	727.8	727.8
0.82	0.6	727.8	727.8
0.82	0.7	727.8	727.8
0.82	0.8	727.8	727.8
0.82	0.9	727.8	727.8
0.82	1.0	727.8	727.8

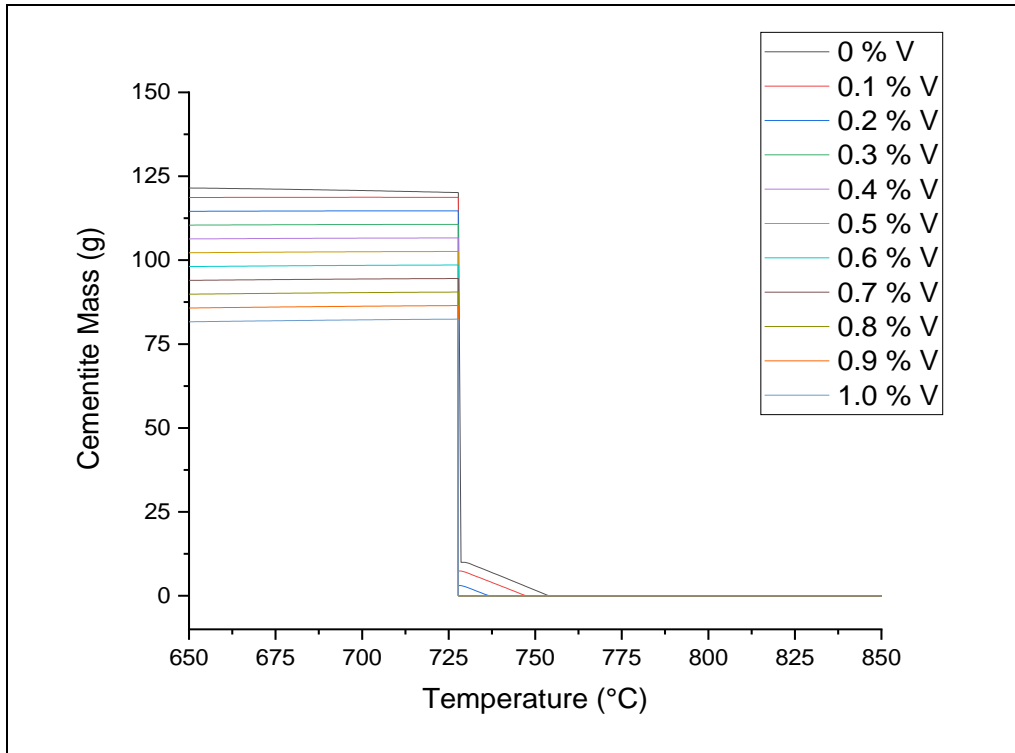


Figure 3:20 - Influence of vanadium on cementite transformation behaviour.

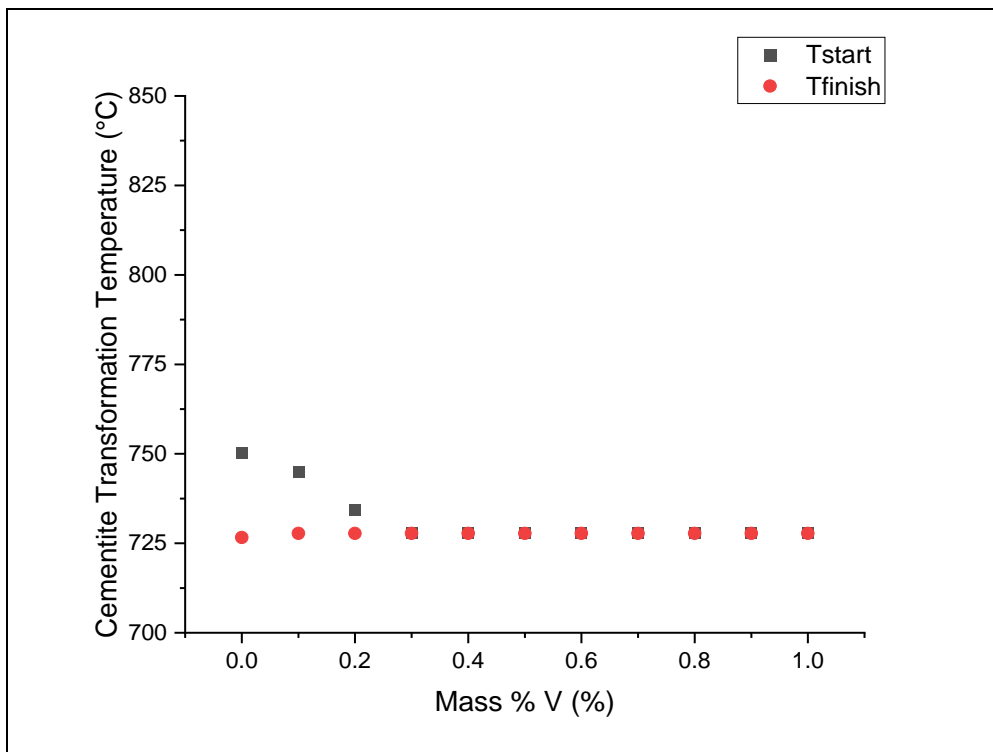


Figure 3:21 - Influence of vanadium content on cementite start and finish transformation temperature.

3.2.2.9 Summary of Cementite Transformation Temperatures

A summary of cementite thermal stability across all compositions simulated is shown in Figure 3:22. If cementite transformation temperature was higher than a pure Fe-C system, 726°C, the alloying addition was taken as an increase in cementite thermal stability. A dashed line is plotted at 726°C in Figure 3:22, to identify elements which either increase or decrease the thermal stability of cementite.

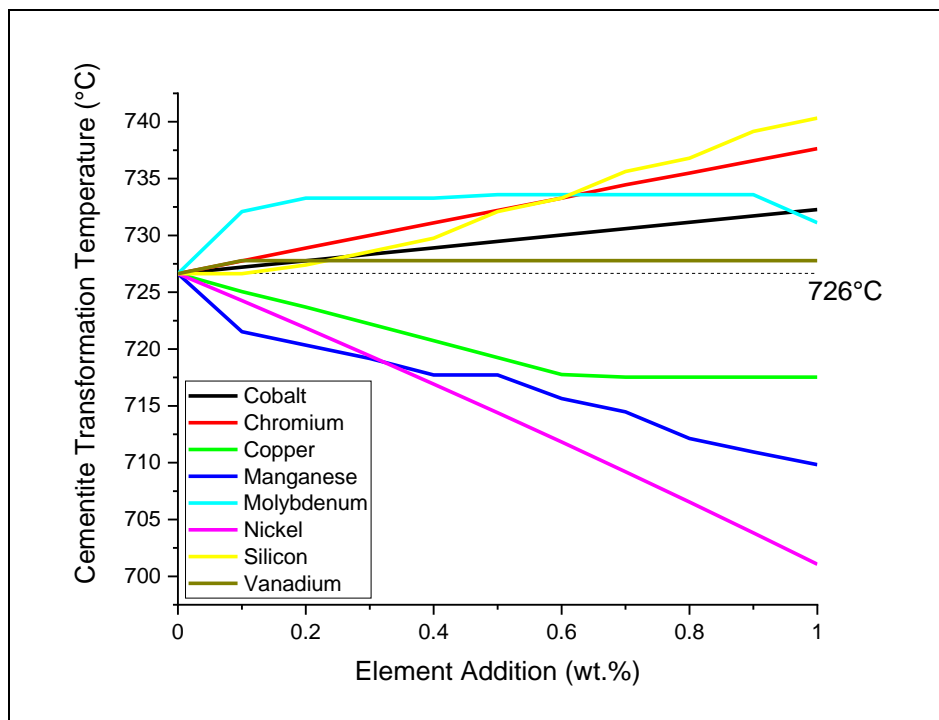


Figure 3:22 - Effect on cementite transformation temperature of each simulated alloying element.

In summary: nickel, copper and manganese appear to be detrimental to cementite thermal stability. Whilst silicon, chromium, molybdenum, cobalt, and vanadium appear to increase cementite thermal stability.

Table 3:12 - Summary of cementite transformation temperatures with a 0.5wt.% alloying addition.

Elements which increase Cementite T_f (°C)	Elements which decrease Cementite T_f (°C)
Cobalt, 729.5	Manganese, 717.7
Chromium, 732.2	Nickel, 714.4
Silicon, 732.1	Copper, 719.2
Vanadium, 727.8	-
Molybdenum, 733.6	-

3.2.3 Alloying Element Distribution

Thermodynamic data from the cementite thermal stability simulations in the previous section were also used to predict the distribution of each alloying element in the microstructure. The thermodynamic data from each 0.5 wt.% simulation was plotted to show the mass of an alloying element present in each phase.

3.2.3.1 Cobalt

Figure 3:23 shows cobalt located predominantly in the BCC_A2 phase. 0.1g of cobalt is present in cementite following the transformation to pearlite. However, the cobalt located in the cementite relocates to the BCC_A2 during cooling.

Table 3:13 - Cobalt distribution simulation composition.

Carbon (wt.%)	Cobalt (wt.%)
0.82	0.5

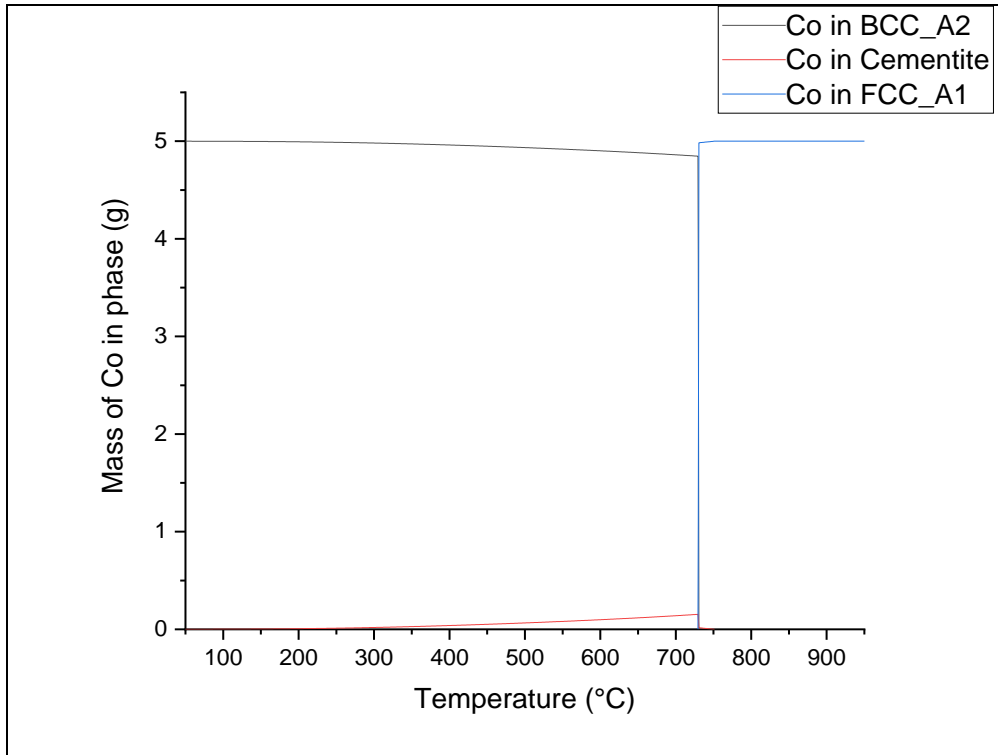


Figure 3:23 - Simulated cobalt distribution during equilibrium cooling.

3.2.3.2 Chromium

Figure 3:24 shows immediately after the pearlite transformation, chromium is predominantly located in cementite with 0.8g located in ferrite. With further cooling, chromium vacates the BCC_A2 almost entirely. At 350 °C chromium appears to relocate to an FCC_A1 phase. By the end of the simulation, at 50°C, chromium is almost entirely located in the FCC_A1 phase. This is erroneous, perhaps due to a miscibility gap which occurs under equilibrium conditions or due to the limitations placed on the simulation.

Table 3:14 - Chromium distribution simulation composition.

Carbon (wt.%)	Chromium (wt.%)
0.82	0.5

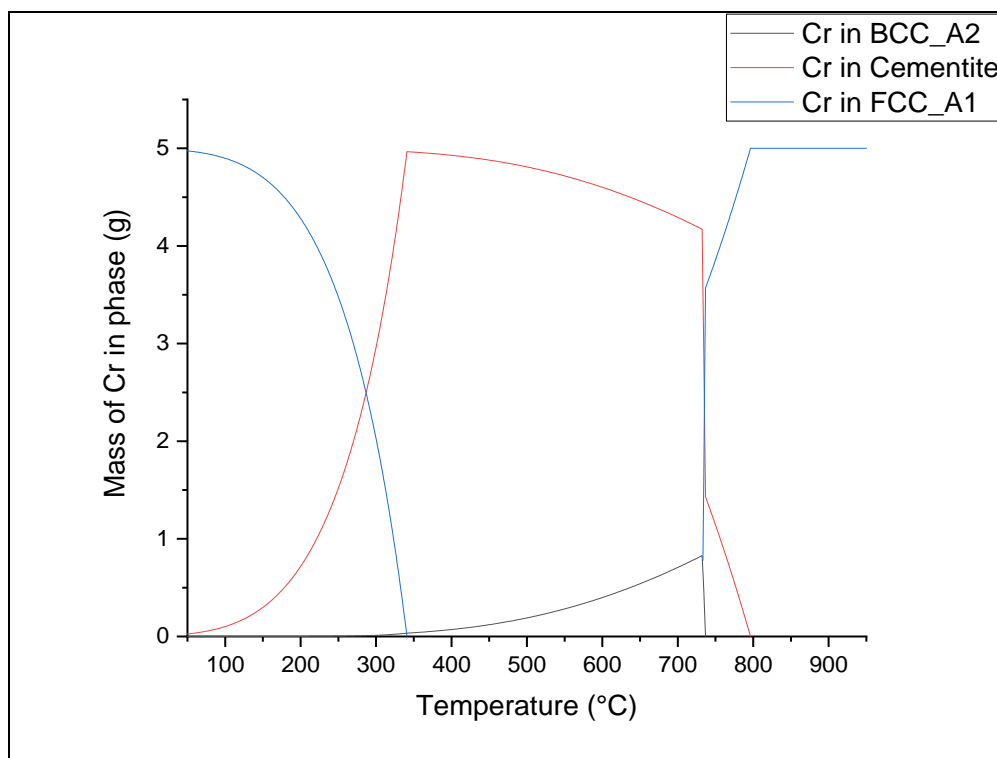


Figure 3:24 - Simulated chromium distribution during equilibrium cooling.

3.2.3.3 Copper

Figure 3:25 shows copper located entirely in an FCC_A1 phase by the end of the simulation at 50°C. The presence of an FCC_A1 phase is likely erroneous, perhaps due to a miscibility gap which occurs under equilibrium conditions or due to the limitations placed on the simulation.

Table 3:15 - Copper distribution simulation composition.

Carbon (wt.%)	Copper (wt.%)
0.82	0.5

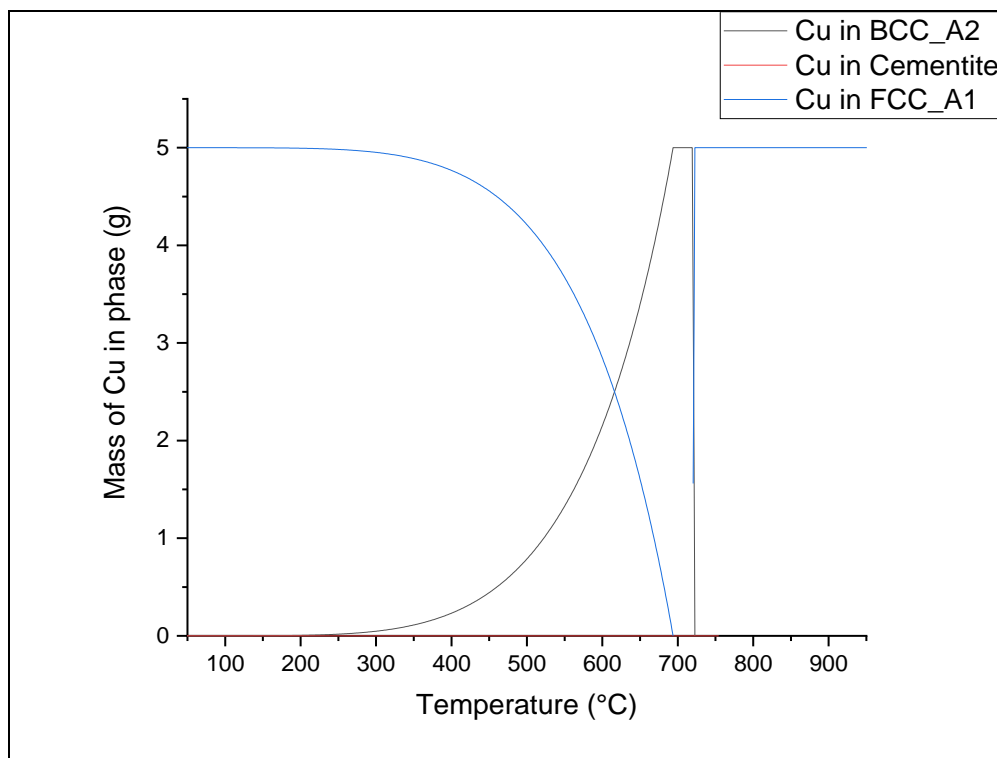


Figure 3:25 - Simulated copper distribution during equilibrium cooling.

3.2.3.4 Manganese

Figure 3:26 shows manganese located in cementite and ferrite after the pearlite transformation. Manganese relocated entirely at about 175°C to the BCC_A2 phase. Atom probe tomography (Figure 3:1), has shown manganese does not leave the cementite upon cooling and remains in a higher concentration in cementite than in the ferrite lamella.

Table 3:16 - Manganese distribution simulation composition.

Carbon (wt.%)	Manganese (wt.%)
0.82	0.5

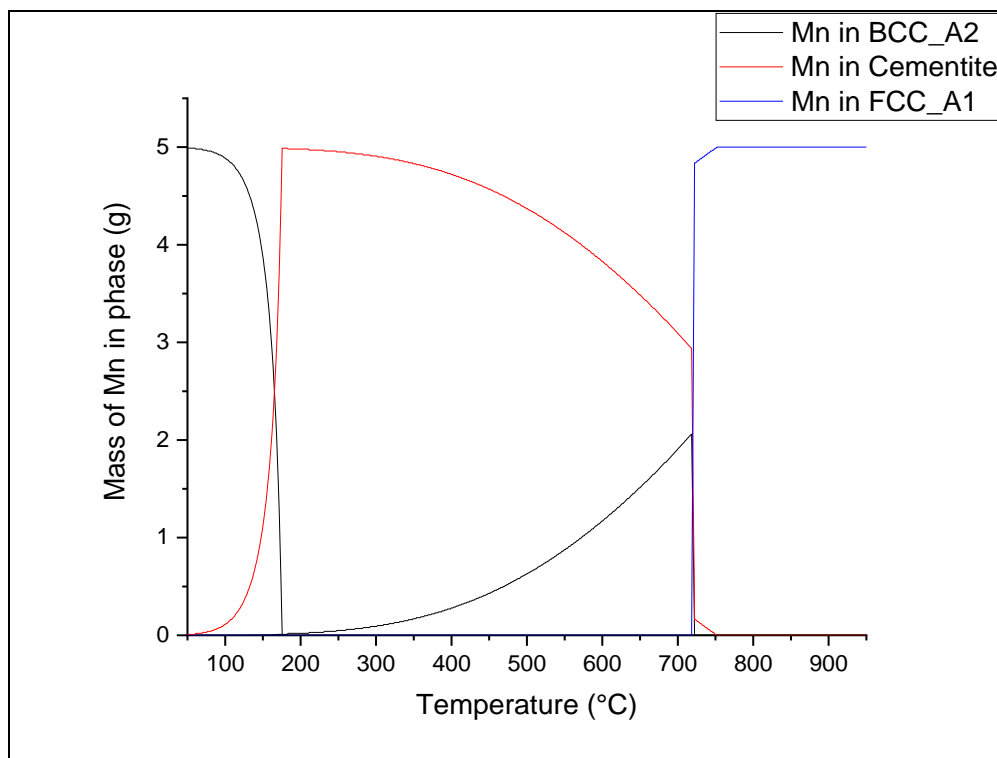


Figure 3:26 - Simulated manganese distribution during equilibrium cooling.

3.2.3.5 Molybdenum

Figure 3:27 shows immediately after the pearlite transformation, molybdenum is distributed amongst cementite and ferrite, with a slightly higher concentration present in the cementite. Upon further cooling, molybdenum is predominantly located in the FCC_A1 phase until 200°C, where an abrupt relocation to BCC occurs. This is erroneous, diffusion does not occur so readily at such low temperatures. A miscibility gap may be occurring under equilibrium conditions or due to the limitations placed on the simulation.

Table 3:17 - Molybdenum distribution simulation composition.

Carbon (wt.%)	Molybdenum (wt.%)
0.82	0.5

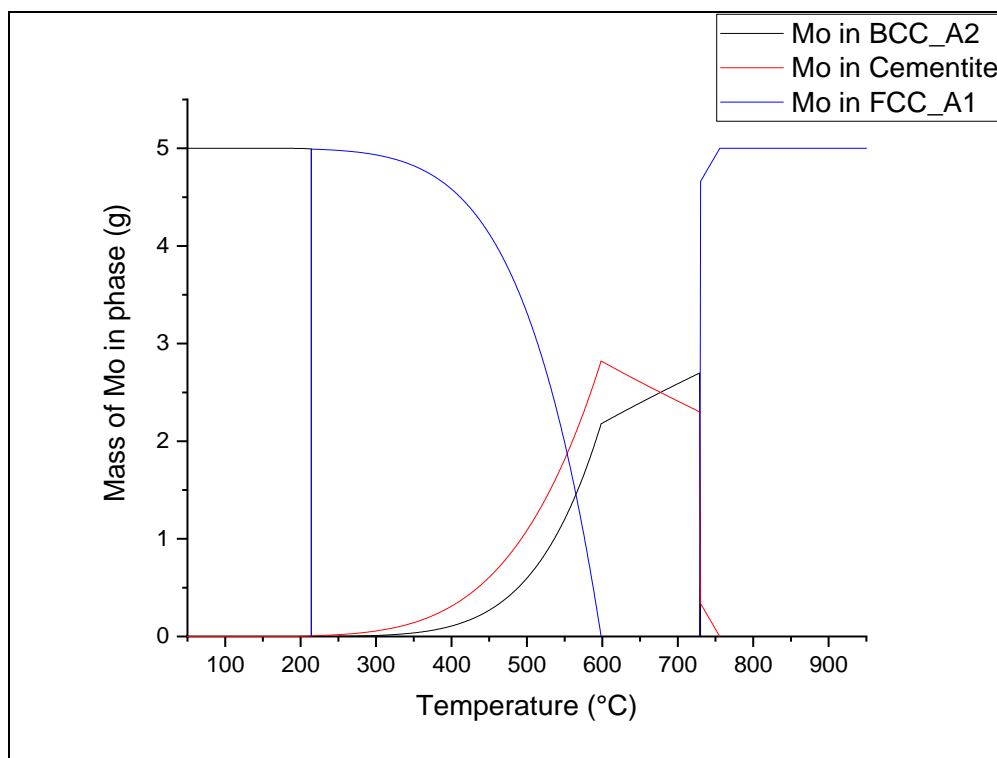


Figure 3:27 - Simulated molybdenum distribution during equilibrium cooling.

3.2.3.6 Nickel

Figure 3:28 shows nickel predominantly located in the BCC_A2 phase during cooling, with a small presence in cementite until 150°C. At around 130°C nickel appears to relocate from cementite and BCC_A2 to the FCC_A1 phase. This is erroneous, diffusion does not occur so readily at such low temperatures. Atom probe reconstruction, shown in Figure 3:1, shows nickel located in a higher concentration in cementite lamellae.

Table 3:18 - Nickel distribution simulation composition.	
Carbon (wt.%)	Nickel (wt.%)
0.82	0.5

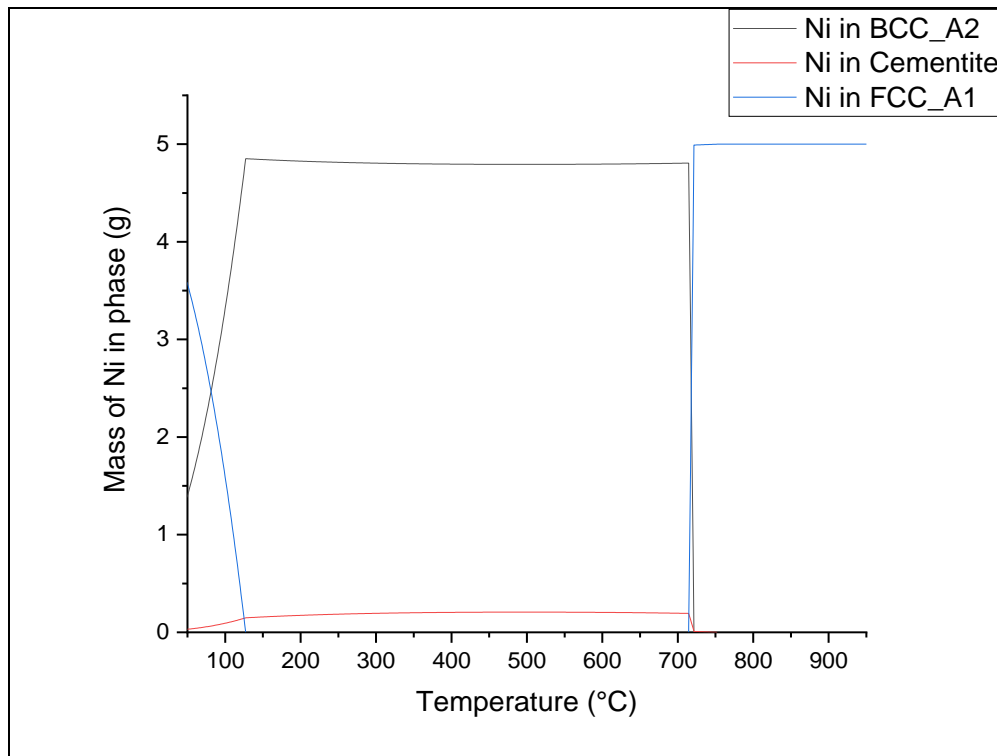


Figure 3:28 - Simulated nickel distribution during equilibrium cooling.

3.2.3.7 Silicon

Figure 3:29, in agreement with and atom probe reconstruction (Figure 3:1), shows silicon is rejected from cementite and is located predominantly within BCC_A2, ferrite.

Table 3:19 - Silicon distribution simulation composition.

Carbon (wt.%)	Silicon (wt.%)
0.82	0.5

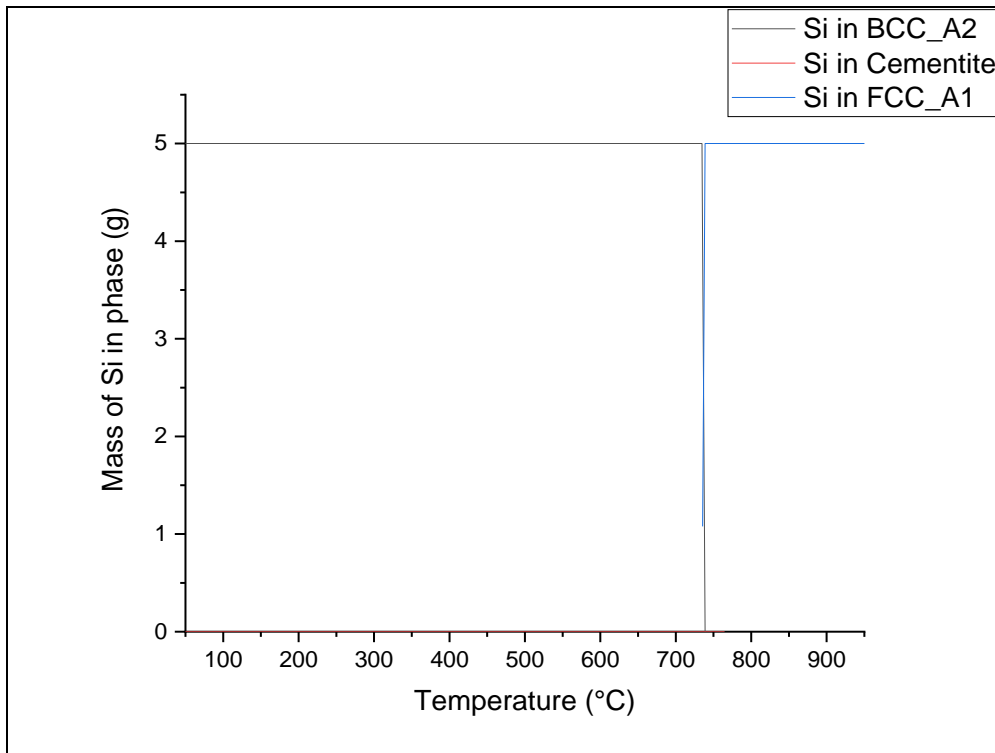


Figure 3:29 - Simulated silicon distribution under equilibrium cooling.

3.2.3.8 Vanadium

Figure 3:30 shows vanadium is not present in BCC_A2 or cementite below 400°C. Above 726°C, Vanadium is located in the FCC_A1 phase. Upon the formation of pearlite, vanadium partitions to the cementite, which is in agreement with a similar simulation completed by Solano-Alvarez et al. [60]. With cooling, vanadium relocates out of the cementite. It is unclear from this simulation, where vanadium may relocate to the ferrite/cementite interface or perhaps within the ferrite, to form a vanadium carbide. This is a surprising result as vanadium would be expected to enter and remain within cementite as a strong carbide former. The result may be due to a lack of experimental data in the thermocalc database or the constraints placed upon the simulation.

Table 3:20 - Vanadium distribution simulation composition.

Carbon (wt.%)	Vanadium (wt.%)
0.82	0.5

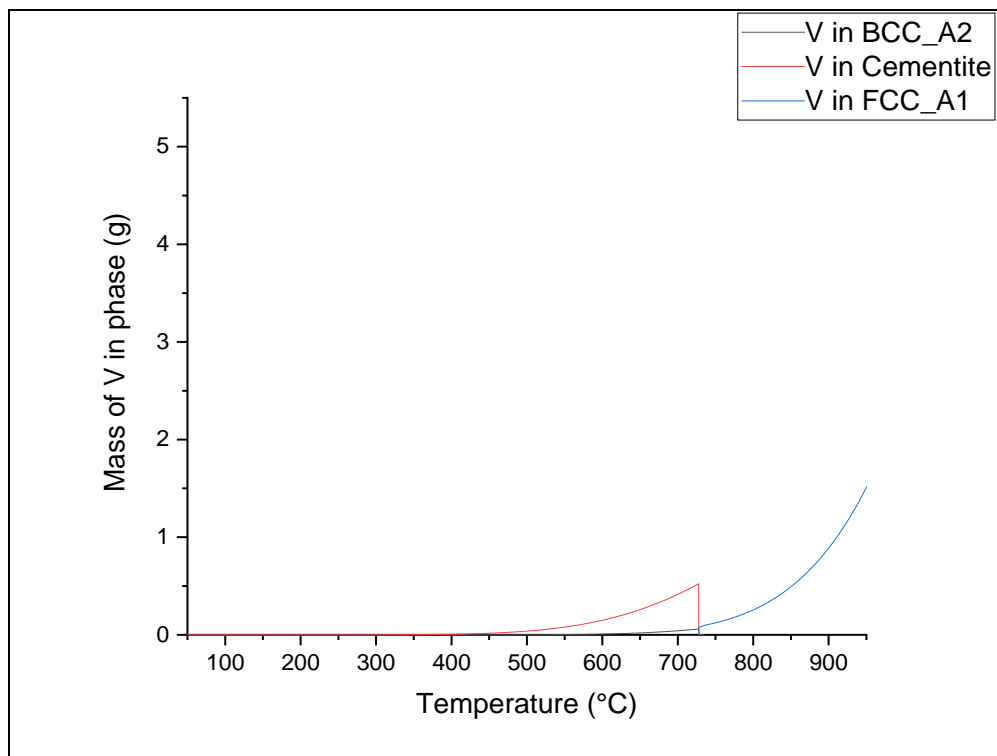


Figure 3:30 - Simulated vanadium distribution under equilibrium cooling.

3.2.3.9 Summary of Element Distribution

Table 3:21 summarises the calculated element distributions of all elements simulated. It is worth noting that for several elements such as chromium and copper, the thermodynamics predicted a second FCC_A1 that was stable and present at low temperatures. This is impossible with such a small alloying addition; it may be due to a miscibility gap which occurs under equilibrium conditions. The presence of the FCC_A1 phase could be due to the constraints imposed on the simulation that led to an incorrect result.

Table 3:21 - Summary of calculated element distribution

Element (0.5wt.%)	Mass of element in Cementite at 200°C (g)	Mass of element in FCC_A1 at 200°C (g)	Mass of element in BCC_A2 at 200°C (g)	Mass of Cementite Formed at 200°C (g)
Pure Fe-C	-	-	-	122.6
Cobalt	0.01	-	5.0	122.6
Chromium	0.71	4.3	0.0	107.3
Copper	0.00	5.0	0.0	122.6
Manganese	4.98	-	0.02	122.5
Molybdenum	0.00	-	5.0	79.2
Nickel	0.18	-	4.8	122.6
Silicon	0.00	-	5.0	122.6
Vanadium	0.00	-	0.0	98.2

Table 3:21 shows alloying additions which dissolve in metal carbides, but do not form carbides (Mn), and non-carbide forming elements (Cu,Si,Ni) that result in no change in the amount of cementite which forms. This is unexpected as elements such as silicon and manganese are often added to steel to suppress or increase cementite formation, respectively. These findings suggest the effects of silicon and manganese on cementite formation may be kinetic, rather than thermodynamic. Conversely, Table 3:21 shows carbide forming elements such as chromium, vanadium and molybdenum significantly reduce the mass of cementite that forms. This may be due to the formation of vanadium, chromium and molybdenum carbides

preferentially over cementite. The presence of an additional FCC phase identified during the thermodynamic modelling may be these carbides.

3.2.4 Multi Element Simulations

The requirements for an alloying element to be selected for the experimental steels were: Consistent and reliable reports from literature or previous studies; the location/distribution of the element in the wire microstructure; thermodynamic modelling data; cost, upscaling, and production considerations. This section presents multi-element thermodynamic simulations that were completed once certain elements had been selected. A brief explanation is presented below, however the selection process is detailed under section: 3.3.

Due to upscaling, production, and tensile requirements, a 0.3 wt.% manganese addition was necessary. Nickel was also selected as an element of interest due to the study reported in section: 3.1 of this chapter. The most likely nickel addition was 0.5 wt.% to attempt to improve on the results of the previous study which included a steel which contained 0.26 wt.% nickel. However, thermodynamic modelling identified nickel and manganese as elements that reduced the cementite thermal stability. Multi element simulations were performed to quantify the combined effects of nickel and manganese. Silicon was chosen as it has been reported to delay the effects of strain ageing in hot dip galvanised wires [66]. Silicon also shows the largest increase in cementite transformation temperature from the individually simulated alloying elements. A 1 wt.% silicon addition increased the cementite transformation temperature to 740°C. Therefore, thermodynamic modelling was used to predict how much silicon would be necessary to mitigate the adverse effects of manganese and nickel.

Table 3:22 - Multi element thermodynamic simulation calculated cementite transformation temperatures.

Simulated Composition (wt.%)	Silicon Content (wt.%)	Cementite Transformation Temperature (°C)
Pure Fe-C	-	726.7
Commercial Steel 0.82C-0.2Si-0.5Mn	0.2	721.2
0.82C-0.5Ni-0.3Mn	-	711.3
0.82C-0.3Si-0.5Ni-0.3Mn	0.3	717.0
0.82C-0.5Si-0.5Ni-0.3Mn	0.5	722.3
0.82C-0.8Si-0.5Ni-0.3Mn	0.8	726.0
0.82C-1.0Si-0.5Ni-0.3Mn	1.0	726.0

The final column in Table 3:22 shows an addition of 0.5wt.% nickel and 0.3wt.% manganese reduces the cementite transformation temperature to 711.3°C. The final column in Table 3:22 also shows the cementite transformation temperatures with increasing silicon content up to 1.0wt%. A silicon addition of 0.8 wt.% was enough to return the cementite transformation temperature to the pure Fe-C system. The further addition of 1.0wt.% appears to provide no additional benefit therefore 0.8 wt.% silicon was selected.

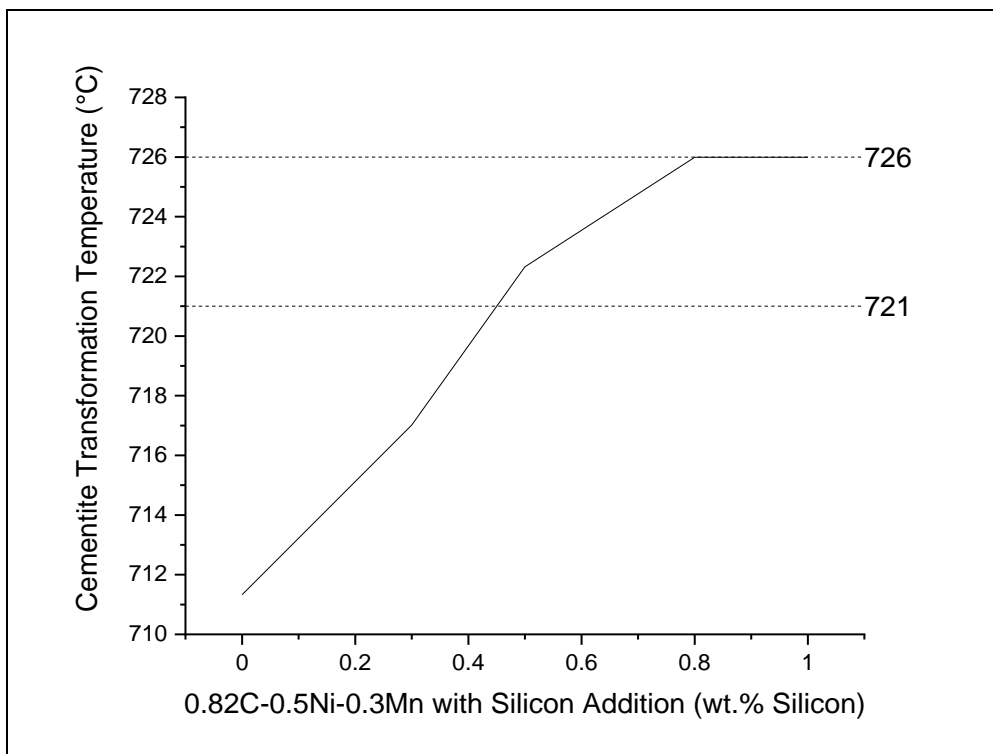


Figure 3:31 - Multi element thermodynamic simulation calculated cementite transformation temperatures.

Figure 3:31 is a graphical representation of Table 3:22. The commercial steel and pure Fe-C cementite transformation temperatures, 721.2°C and 726.7°C are plotted as horizontal lines for comparison.

3.3 Experimental Steel Composition Selection

The selection criteria for alloying elements were as follows:

- Consistent, reliable reports from either literature or previous studies.
- Location and distribution of an element in the wire microstructure.
- Thermodynamic modelling.
- Cost, upscaling, and production considerations.

Element distribution was of particular relevance to this study as targeting specific regions or phases of the microstructure is the most probable way of influencing strain ageing response. For example, elements that are able to bind within cementite and alter its chemical composition may increase (or decrease) the binding energy between atoms or mechanical properties, and therefore change the kinetics of cementite dissolution. As diffusion and dislocation mobility is crucial to designing against strain ageing, elements which reduce diffusion and dislocation motion in ferrite would be favoured. Elements which are located at the ferrite-cementite interface may also be able to influence strain ageing due to the large interfacial energies present in a drawn pearlitic microstructure. The final steel compositions are shown in Table 3:23.

Table 3:23 - Final Experimental Steel Compositions.

Steel Code	C	Mn	Si	Ni	Co	V
17BQ3	0.82	0.3	0.8	-	-	-
17BQ4	0.82	0.3	0.8	0.5	-	-
17BQ5	0.82	0.3	0.8	0.5	0.1	-
17BQ6	0.82	0.3	0.8	0.5	0.1	0.1

The split cast method of production results in the final alloy containing all 4 alloying elements. Therefore, it was necessary to reduce alloying additions as much as possible to prevent hardenability issues during production.

3.3.1 Manganese

The experimental alloys were designed with upscaling and commercial production in mind.

As such, a manganese addition was necessary. Manganese increases tensile strength of as-rolled pearlitic rod, allowing wire products to meet tensile strength requirements. Manganese also forms manganese sulphide inclusions reducing the adverse effects of sulphur on ductility and hot shortness during production. Gavriljuk reported that a manganese addition of 2 wt.% increases cementite decomposition by 47% [35]. Thermodynamic modelling also suggested manganese reduced cementite thermal stability which may promote cementite dissolution, shown in Table 3:7.

Thermodynamic modelling, shown in Figure 3:26, suggested manganese was predominantly located in cementite after the pearlite transformation, but relocated to BCC_A2 at low temperatures. Atom probe reconstruction of a drawn wire, shown in Figure 3:3, revealed manganese was present in ferrite and cementite, with a higher concentration in cementite.

Manganese also contributes to an increase in hardenability, resulting in martensite formation even at slow cooling rates where the manganese content is high enough. Martensite formation would result in difficulty unwinding the coil of rod and subsequent processing. Whilst higher strength commercial wire-rod grades usually feature manganese levels of 0.5 wt.% or higher, as discussed, it was necessary to add a little manganese as possible. An addition of 0.3 wt.% manganese would be sufficient to achieve the requirements. Multi element simulation, shown in section:3.2.4, suggested this adverse effect could be overcome with a silicon addition.

3.3.2 Nickel

Gavriljuk reported nickel reduced the effects of strain aging almost entirely with alloying additions of 6.05 wt.% [35]. An addition of 6 at.% nickel would increase cost beyond the cost saving of a more strain ageing resistant wire product. Such a large addition could also create processing problems or breakages during drawing. As shown in Table 3:2 , a study completed by British Steel R&D showed an addition of 0.26 wt.% nickel promoted ductile fractures in torsion tests of artificially aged wires. An increased addition of nickel of 0.5 wt.% could further increase ductility whilst still being cost effective.

Thermodynamic modelling suggested nickel reduced cementite transformation temperature. Thermodynamic data, shown in Figure 3:28, suggested a higher concentration of nickel was located in BCC_A2 after the pearlite transformation (the thermodynamic model prediction of Ni moving to an FCC phase at lower temperature was clearly physically wrong). Atom probe tomography (Figure 3:1) showed nickel predominantly located in cementite lamellae. The increased concentration of an alloying element in cementite may contribute to altering cementite binding energies associated with cementite dissolution. Furthermore, the results of the multi element simulations presented in Table 3:22 suggested the adverse effects of 0.5 wt.% nickel on cementite transformation temperature could be mitigated with a silicon addition of 0.8 wt.% silicon.

3.3.3 Silicon

Silicon has been effective in reducing the tensile strength loss due to the onset of spheroidisation, that typically occurs in wires after hot dip galvanising [20]. Pennington et al. observed a silicon addition retard spheroidization during ageing [66]. Pennington et al. also attributed an increase in strength to silicon, reporting that it inhibits dislocation motion in ferrite. A resistance to dislocation motion in ferrite and spheroidisation, which is equivalent to the third stage of ageing, may be beneficial in resisting the earlier stages of ageing.

Thermodynamic modelling, Figure 3:29, suggested that silicon was rejected from the cementite. This was confirmed by atom probe data, shown in Figure 3:1, which also revealed an elevated concentration of silicon at the ferrite cementite interface. An elevated silicon concentration at the ferrite cementite interface may act as a physical barrier to dislocation motion or diffusion, impeding the redistribution of carbon atoms.

Thermodynamic transformation temperature simulations, presented in Table 3:10, suggested silicon significantly increased the thermal stability of cementite. The split cast method of production results in the first experimental alloy having a single alloying element. Silicon was selected to be the first element to evaluate if an increase in cementite transformation temperature is affected in mitigating strain aging. Thus, allowing validation of the modelling approach.

A 0.8 wt.% silicon addition was finalised using multi-element thermodynamic simulations, shown in Figure 3:31. When simulated with a 0.5 wt.% nickel and 0.3 wt.% manganese

addition, a plateau in cementite transformation temperature at 0.8 wt.% silicon occurred. This therefore suggests any further increase in silicon content would not significantly affect cementite thermal stability.

3.3.4 Cobalt

Kanetsuki et al. have demonstrated cobalt can suppress grain boundary cementite precipitation in hypereutectoid steels containing less than 1.3 wt.% carbon, a cobalt addition improved both drawability and tensile strength when compared to a eutectoid steel [58]. Inhibiting the formation of grain boundary cementite could accommodate a larger carbon addition whilst maintaining a fully pearlitic microstructure. The study also suggested cobalt has the potential to improve ductility, this would be a beneficial combination with silicon and nickel, which are known to impact drawability.

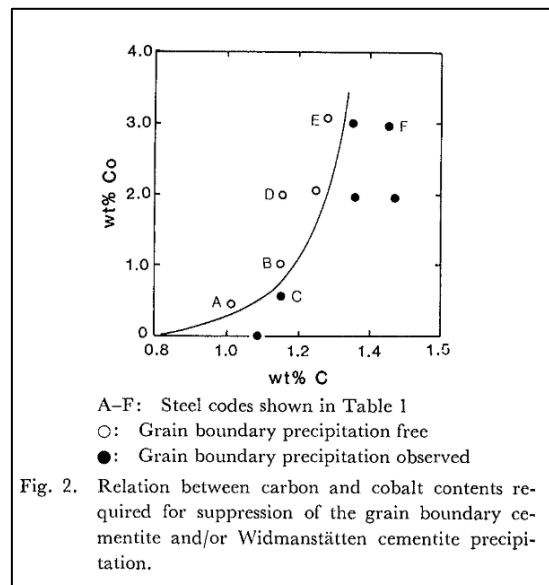


Figure 3:32 - Empirical relationship derived by Y. Kanetsuki et al. [58].

Figure 3:32 suggests a small cobalt addition can reduce pro eutectoid cementite precipitation in a steel with 0.82 wt.% carbon. Thermodynamic simulations also suggested cobalt increased

cementite thermal stability, shown in Table 3:4. Therefore, it was decided that 0.1 wt.% cobalt may be enough to have an impact on the ageing reaction.

3.3.5 Vanadium

Gavriljuk also reported an addition of 0.52 vanadium significantly reduced cementite dissolution associated with strain ageing [35]. Fang et al. presented atom probe tomography data which revealed micro-alloyed vanadium (0.06 wt.%) located predominantly in cementite lamellae [27]. Solano-Alvarez et al. reported an increase in wear resistance in rail steels containing vanadium, it was concluded this was due to increased stability and toughness of vanadium containing cementite [69].

Solano-Alvarez et al. also presented thermodynamic cooling simulations to reveal vanadium distribution, which is in agreement with Figure 3:30 [69]. Thermodynamic simulations of cementite transformation temperatures presented in Table 3:11 suggested a vanadium addition increased cementite transformation temperature. The absence of vanadium in the BCC_A2 phase and the cementite, shown in Figure 3:30, suggests vanadium could be partially located at the ferrite cementite interface.

As well as the potential for changing the mechanical properties, vanadium is also a strong nitride and carbide former. Thus, vanadium may tie up and reduce interstitial nitrogen contribution to strain ageing. When selecting the level of vanadium addition, two main factors contributed to the selection: the high cost of a vanadium addition and the rod hardenability. The hardenability was especially important as vanadium would feature in final of the four

experimental steels, so the richest composition of alloying elements. Therefore, 0.1 wt.% was decided upon.

3.3.6 Alloy Cost

Alloy cost estimates were calculated to predict whether the proposed alloying additions would be commercially viable. Larger cobalt additions were initially proposed, between 0.25 and 0.7wt.%, however this would have increased the cost of a TC84 cast by £60000-129000. The estimated costs of the alloys selected (in addition to the production of a TC84 grade) are as follows (all wt.%): a 0.8Si would cost an additional £3012, a 0.5Ni addition would cost an additional £18040, a 0.1Co addition would cost an additional £15574 and a 0.1V addition would cost an additional £4407. Alloying costs were estimated in 2017. The total cost estimates are shown below in Table 3:24.

Table 3:24 - Alloy cost estimates.

Steel Code	Si	Ni	Co	V	Total Cost
17BQ3 (BJ3)	0.8	-	-	-	TC84 + £3012
17BQ4 (BJ4)	0.8	0.5	-	-	TC84 + £25500
17BQ5 (BJ5)	0.8	0.5	0.1	-	TC84 + £33000
17BQ6 (BJ6)	0.8	0.5	0.1	0.1	TC84 + £37400

3.3.7 Chromium and Molybdenum

Chromium and molybdenum were not selected for the experimental steels during this study, partly due to limitations in budget and time, which restricted alloying additions to 4 Steel compositions/elements. Chromium and molybdenum are potent at enhancing rod hardenability. They were not selected primarily for this reason, as increasing hardenability makes rod manufacturing difficult. High hardenability results in a narrowing of the critical cooling rate window necessary for optimising the rod microstructure, i.e. avoiding

bainite/martensite. The effects of chromium and molybdenum on strain ageing are also unclear.

Chromium is a potent carbide former which has been reported to reduce the amount of interstitial carbon and nitrogen available to pin dislocations. Chromium has also been reported to significantly increase the hardness of cementite [59]. Chromium containing platelets become cementite crystal particles during cold deformation [65]. Thus suggesting a chromium addition may result in hard cementite which fragments, which may be detrimental to ageing. Given elements such as cobalt and nickel which improve the plasticity of cementite appear to reduce cementite dissolution, vanadium was selected instead of chromium. Vanadium is also a potent carbide and nitride former, yet vanadium appears to improve cementite toughness [59][61]. Although it is worth noting, vanadium has also been reported to result in fragmented cementite [27].

The effects of molybdenum on strain ageing are also unclear, two conflicting reports in the literature exist: Pereloma reported a molybdenum addition accelerates strain ageing [64], whereas Gavriljuk reported a molybdenum addition reduces cementite dissolution [35]. Neither studies are completed on high carbon wire, so the effects of molybdenum on strain ageing remain unclear.

3.4 Chapter summary

In conclusion, this chapter has outlined the finalising of experimental alloy compositions. It has presented all information that was available from literature, previous studies, thermodynamic modelling results.

However, in regard to element distribution, discrepancy between atom probe reconstruction and thermodynamic modelling highlighted the need for thermodynamic modelling to be used as a part of a diverse approach to reproducing a microstructure. It is likely due to the constraints placed upon the model and the difference between a drawn wire microstructure and equilibrium cooled bulk pearlite. Atom probe reconstruction has proved useful for comparison with thermodynamic modelling. As discussed in sections 3.2.2.9 and 3.2.3.9, It remains unclear why a second BCC_A2 and FCC_A1 phase occurs at lower temperatures for certain elements.

4 Materials and Methods

This chapter follows the production and processing of the four experimental steel compositions, from ingots to drawn wire. This includes rod heat treatment trials required for producing consistent rod microstructures, the heat treatments of two sets of rods and the two wire drawing methods utilised. This section also details the experimental methodology used to artificially age and characterise the strain ageing response of the experimental steel compositions and the commercial grade used for comparison.

4.1 Experimental Steel Production

The experimental steels were produced via a vacuum induction melt furnace at Swinden Technology Centre, TATA Steel. Two 60kg casts were split to produce 4 x 30kg ingots with systematically varied compositions. Ingots were ground in preparation for forging by Rotherham Stainless Steels and Nickel Alloys. The ingots were forged into 50mm^2 billets with chamfered edges by KT Forging. Billets were rolled ProRoll. The billets were hot rolled with an initial rolling temperature of 1150°C to a hot roll plug size of 6.8mm diameter. The end of rolling temperature was measured with a handheld pyrometer as 920°C . After rolling, the billets were furnace cooled down to 250°C , then air cooled to ambient. ProRoll then centreless ground the rods to 6mm, to remove decarburisation and surface imperfections prior to drawing. Rods were also cleaned and given a phosphate coating prior to drawing.

Table 4:1 – Experimental Steel Compositions (wt.%).

Steel Grade	C	Mn	Si	Ni	Co	V	P	S
BQ3/BJ3	0.82	0.3	0.8	-	-	-	0.01	0.007
BQ4/BJ4	0.82	0.3	0.8	0.5	-	-	0.01	0.007
BQ5/BJ5	0.82	0.3	0.8	0.5	0.1	-	0.01	0.007
BQ6/BJ6	0.82	0.3	0.8	0.5	0.1	0.1	0.01	0.007

4.1.1 Rod Heat Treatment Trials

As finer initial rod pearlite spacing has been correlated with increased cementite dissolution, a consistent pearlite spacing throughout all steel compositions prior to drawing was required.

This was achieved by varying the transformation cooling rate to account for the differing hardenability effects from the alloy additions. A series of heat treatments (detailed later) were completed on the experimental steel compositions to obtain the cooling rates necessary to match the initial pearlite spacing similar to a commercially produced steel.

Three 50mm samples from each experimental steel were austenitised at 950°C and 890°C, and cooled at 15 °C s^{-1} , 20°C s^{-1} and 25°C s^{-1} (cooling rates were measured at 700°C). A 1.3mm hole was drilled in the end of each sample, to accommodate a thermocouple and datalogger which recorded transformation data. The rods were mounted and polished in order for the resultant microstructures to be assessed by a volume fraction point count.

4.1.1.1 Commercial Steel

Grade TC84B was selected as it had relatively low alloying additions and material was readily available from Scunthorpe Rod Mill. The composition of the carrier coil is shown in Table 4:2.

Rod diameter was 5.5mm.

Table 4:2 - Carrier Coil Composition (wt.%).

Steel Grade	C	Mn	Si	Ni	Co	V	P	S	B	N
TC84B	0.82	0.5	0.19	0.017	0.006	0.002	0.012	0.01	0.0011	0.0052

The furnace drop out temperature of the carrier coil was 1180°C and the end of rolling lay temperature was 910°C. Free boron (that hasn't oxidised) will readily combine with N and form boronitride, reducing interstitial levels of nitrogen, which may be beneficial in reducing the ageing response of the microstructure. Therefore, a commercial grade containing boron may be beneficial. Grade TC84B contains a deliberate boron addition. The boron addition is added to tie up nitrogen to improve ductility, however this may also be beneficial in reducing the contribution of interstitial nitrogen to strain ageing. British Steel R&D has also found boron treated tyre cord has fewer larger oxides [68].

A resolvable pearlite count was performed on the front and back end of the coil. Measurements of interlamellar spacing were required in order to match the experimental steel rod microstructures to the carrier coil.

Table 4:3 - Volume Fraction Point Count - Commercial Coil.

	Unresolvable Pearlite (%)	Resolvable Pearlite (%)	Ferrite (%)	Bainite (%)	Martensite (%)
Front End	81.1	15.9	3.0	-	-
Back End	86.4	12.3	1.3	-	-

12% resolvable pearlite count was chosen as it more likely resembled the microstructure of the coil. The higher resolvable pearlite count in the front end was likely caused by a pile up of material on the cooling conveyor, reducing the effective cooling rate.

4.1.1.2 0.8 Si Steel (BQ3/BJ3)

Figure 4:1 summarises the results of the heat treatment trials shown in Table 4:4. For this composition, a cooling rate of 20°C per second with an austenitising temperature of 890°C was interpolated to produce 12% resolvable pearlite.

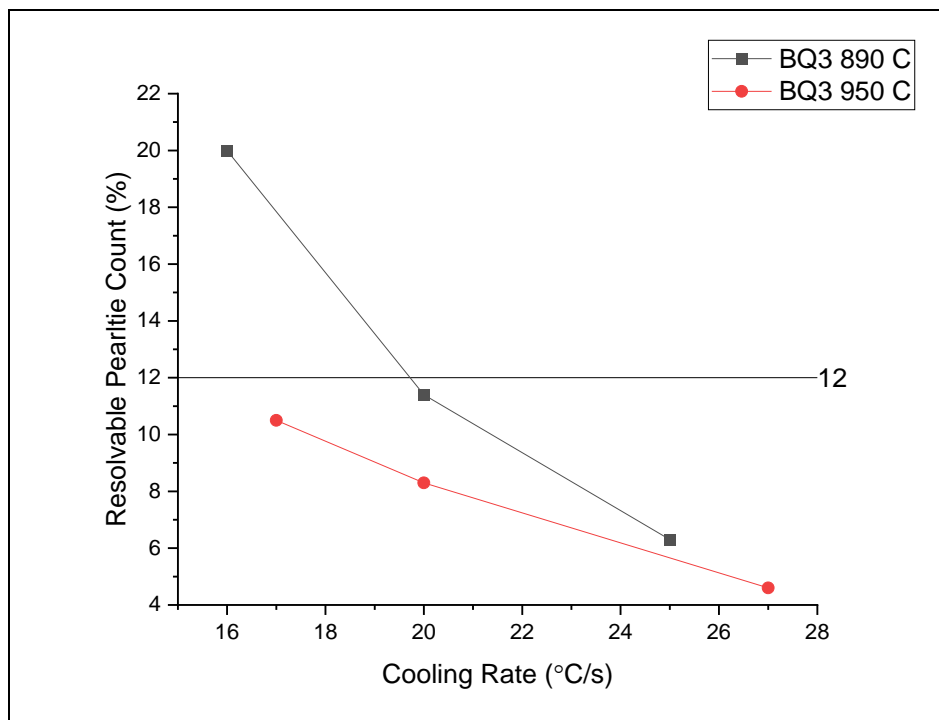


Figure 4:1 - 0.8Si steel volume fraction point count results.

Table 4:4 - 0.8Si steel volume point count.

Reaustenitising Temperature (°C)	Cooling rate ($\frac{^{\circ}\text{C}}{\text{s}}$)	Unresolvable pearlite (%)	Resolvable pearlite (%)	Ferrite (%)	Bainite (%)	Martensite (%)
950	17	89	10.5	0.5	-	-
950	20	90.7	8.3	1.0	-	-
950	27	94.6	4.6	0.8	-	-
890	16	78.7	20	1.3	-	-
890	20	87.4	11.4	1.2	-	-
890	25	92.4	6.3	1.3	-	-

4.1.1.3 0.8 Si + 0.5 Ni Steel (BQ4/BJ4)

Figure 4:2 summarises the results of the heat treatment trials shown in Table 4:5. For this composition, a cooling rate of 17°C per second with an austenitising temperature of 890°C was interpolated to produce 12% resolvable pearlite. Although the sample reaustenitised at 890°C with a cooling rate of 18 degrees per second is lower than expected and is likely erroneous.

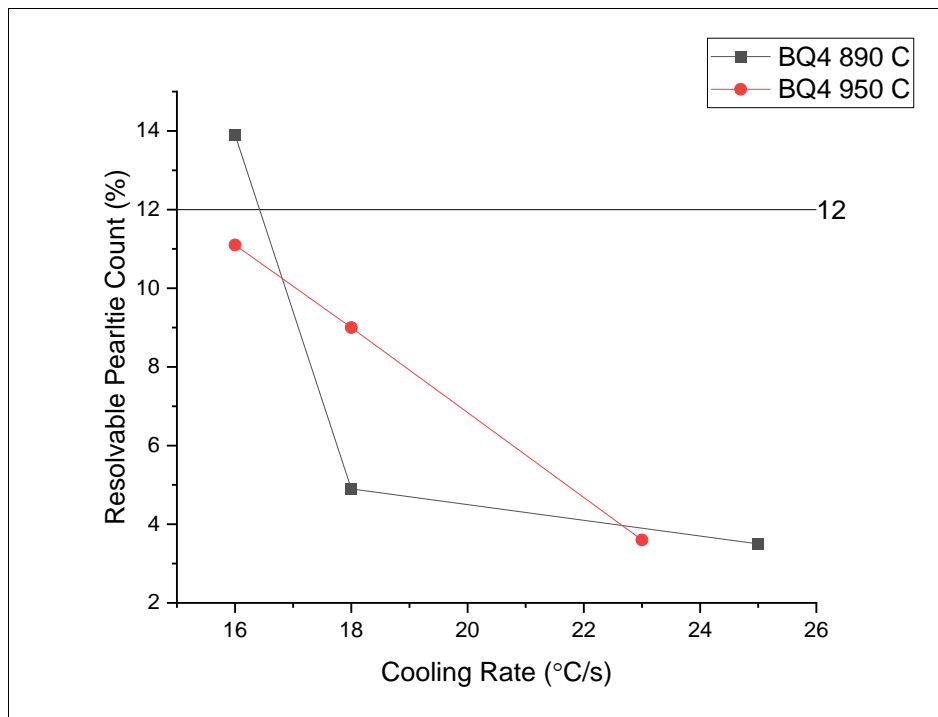


Figure 4:2 - 0.8 Si + 0.5Ni Steel plotted volume fraction point count results.

Table 4:5 - 0.8 Si + 0.5Ni Steel volume point count.

Reaustenitising Temperature (°C)	Cooling rate ($\frac{^{\circ}\text{C}}{\text{s}}$)	Unresolvable pearlite (%)	Resolvable pearlite (%)	Ferrite (%)	Bainite (%)	Martensite (%)
950	16	87.2	11.1	1.7	-	-
950	18	89.3	9	1.7	-	-
950	23	94.7	3.6	1.7	-	-
890	16	83.1	13.9	3	-	-
890	18	93.3	4.9	1.8	-	-
890	25	94	3.5	2.5	-	-

4.1.1.4 0.8 Si + 0.5 Ni + 0.1 Co Steel (BQ5/BJ5)

Figure 4:3 summarises the results of the heat treatment trials shown in Table 4:6. For this composition, a cooling rate of 18°C per second with an austenitising temperature of 890°C was chosen to produce 12% resolvable pearlite. Note, re-austenitising at 950°C produced bainite and martensite.

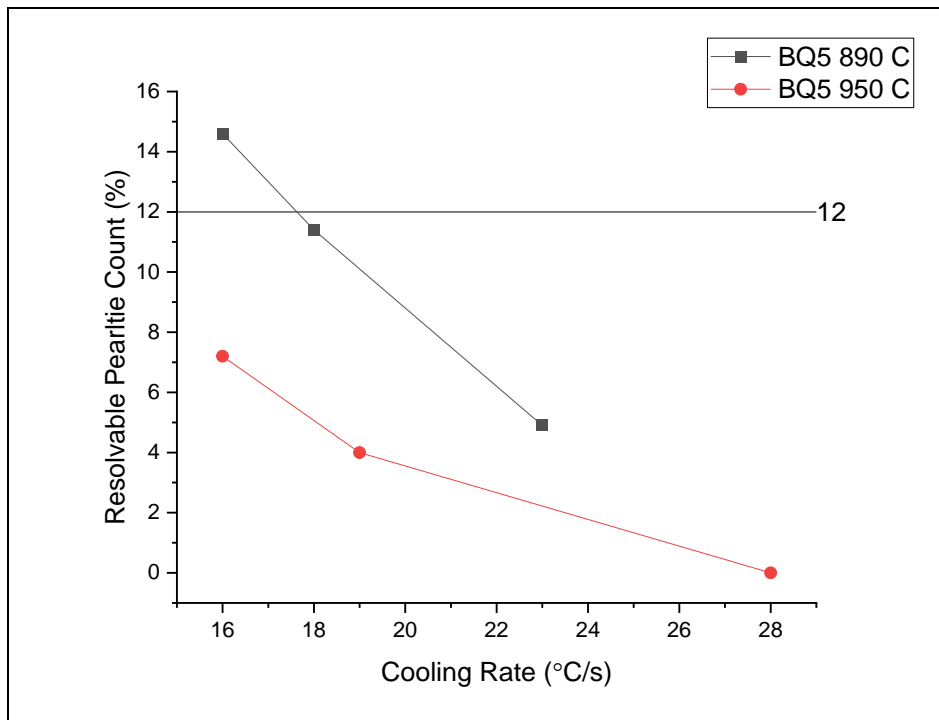


Figure 4:3 - 0.8 Si + 0.5 Ni + 0.1 Co Steel plotted volume fraction point count results.

Table 4:6 - 0.8 Si + 0.5 Ni + 0.1 Co Steel volume point count.

Reaustenitising Temperature (°C)	Cooling rate ($\frac{^{\circ}\text{C}}{\text{s}}$)	Unresolvable pearlite (%)	Resolvable pearlite (%)	Ferrite (%)	Bainite (%)	Martensite (%)
950	16	91	7.2	1.8	-	-
950	19	94.1	4	1.4	-	-
950	28	18.7	-	-	3.2	78.1
890	16	82.1	14.6	3.3	-	-
890	18	86.7	11.4	1.9	-	-
890	23	92.7	4.9	2.4	-	-

4.1.1.5 0.8 Si + 0.5 Ni + 0.1 Co + 0.1 V Steel (BQ6/BJ6)

Figure 4:4 summarises the results of the heat treatment trials shown in Table 4:7. For this composition, a cooling rate of 15°C per second with an austenitising temperature of 890°C was interpolated to produce 12% resolvable pearlite. Note, re-austenitising at 950°C produced bainite and martensite.

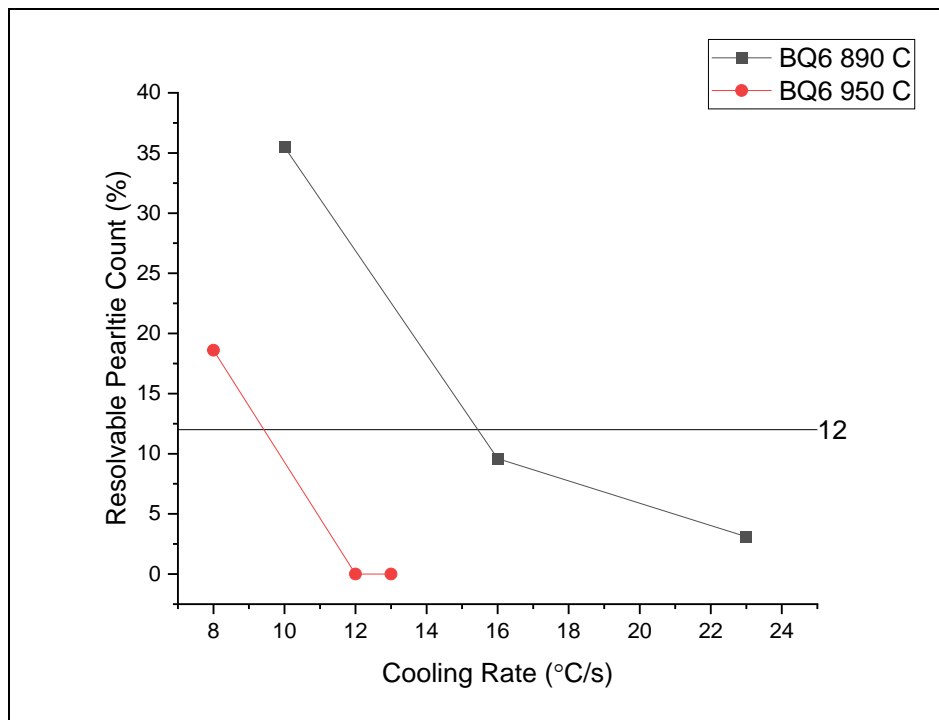


Figure 4:4 - 0.8 Si + 0.5 Ni + 0.1 Co + 0.1 V Steel plotted volume fraction point count results.

Table 4:7 - 0.8 Si + 0.5 Ni + 0.1 Co + 0.1 V Steel volume point count.

Reaustenitising Temperature (°C)	Cooling rate (°C/s)	Unresolvable pearlite (%)	Resolvable pearlite (%)	Ferrite (%)	Bainite (%)	Martensite (%)
950	8	80.2	18.6	1.2	-	-
950	12	83	-	-	15.4	1.6
950	13	54.4	-	-	-	45.6
890	10	63.2	35.5	1.3	-	-
890	16	88.5	9.6	1.9	-	-
890	23	94.1	3.1	2.8	-	-

4.1.1.6 Rod Heat Treatment Summary

890°C was selected as the re-austenitising temperature as 950°C produced bainite and martensite for the richer compositions, due to the larger prior austenite grain size (PAG)/increased hardenability. The cooling rates for each steel composition is shown in Table 4:8.

Table 4:8 - Cooling Rate Requirements to achieve 12% resolvable pearlite.

Steel Grade	Cooling Rate ($\frac{^{\circ}\text{C}}{\text{s}}$)
08 Si Steel	20
08 Si + 0.5 Ni Steel	17
08 Si + 0.5 Ni + 0.1 Co Steel	18
08 Si + 0.5 Ni + 0.1 Co + 0.1 V Steel	15

Rods were re-austenitised at 890°C in a tube furnace and cooled on a forced air-cooling rig to produce the cooling rates shown in Table 4:8. The maximum length of rod the tube furnace could accommodate was 300mm. Turbulent airflow and inconsistencies of the forced air-cooling rig resulted in a variation of $\pm 3^{\circ}\text{C}$ for rod cooling rates.

4.2 Wire Drawing Methodology

Two wire drawing methods were planned to assess the influence of composition across a variety of drawing strains and processing conditions. A multi pass pilot scale drawing machine was used to produce two different drawing strains: $\varepsilon = 1.6$ & 2.4 . A set of rods were also drawn to $\varepsilon = 2$ on a single pass lab drawing bench. The lab drawing bench drawing speed was around 1.5 m/min with temperatures less than 50°C. Significantly faster drawing speeds and temperatures, up to 100 m/min and 150°C, can occur whilst drawing on a multi pass drawing machine. Such high temperatures may overwhelm any compositional effects of the strain ageing response; thus, the single pass draw bench was also deemed necessary.

The multi pass wire drawing was completed on a pilot scale 9 pass multi-hole dry drawing machine at Bekaert Technology Centre (BTC). The maximum length of rod which could be heat treated in the available tube furnace was 300mm, prior to drawing. A pilot scale drawing machine typically requires several meters length of rod to begin drawing. Therefore, the experimental rods needed to be welded into a commercially produced carrier coil in order to be drawn. Despite being coated and painted, following the experimental steel rods through the 9-pass drawing machine proved difficult. Subsequent chemical analysis showed approximately 2 meters of wire per steel composition was correctly identified. 2 meters was an insufficient length of wire to comprehensively characterise the strain ageing response. The experimental methodology and future recommendations are detailed in the appendix: 9.1 Multi-Pass Wire Drawing Machine - Bekaert Technology Centre.

A single pass lab drawing bench is ideally suited to drawing 300mm lengths of rod. Therefore, subsequent testing and characterisation of the strain ageing response was completed on material drawn on the single pass lab drawing bench at Swinden Technology Centre (STC) unless otherwise stated. The experimental methodology is detailed in section: 4.2.1 Single Pass Lab Drawing Bench.

4.2.1 Single Pass Lab Drawing Bench

A single pass lab drawing bench was ideally suited to drawing 300mm lengths of rod. The risk of sample misidentification is almost eliminated. A different commercial grade, X85LM, was used due to lack of availability of the previously used TC84B. It was also necessary to ensure identical processing parameters and ageing conditions. The composition of grade X85LM is shown in Table 4:9.

Table 4:9 - Grade X85LM Cast Analysis (wt.%).

C	Si	Mn	S	P	N	Mo	Ni	Al	Cr	V
0.84	0.23	0.52	0.016	0.013	0.003	0.001	0.02	0.002	0.019	0.001

A single pass lab drawing bench allowed more control over processing parameters, compared to the multi pass machine. Speed and temperature were much higher on the multi-pass machine. Temperatures were estimated to reach over 100°C and drawing speeds of 100 meters per minutes were achieved in the final dies.

4.2.1.1 Rod Preparation and Characterisation

5 rods per experimental steel and 6 rods from the commercial steel were reaustenitised using the same forced air-cooling rig. However, rod microstructural measurements shown in Table 9:1, Table 9:2, Table 9:3 and Table 9:4 led to changes in the cooling rates, shown in Table 4:10.

Table 4:10 - Single pass lab drawing bench rod cooling rates.

Steel Grade	Cooling Rate $\pm 3 \left(\frac{^{\circ}\text{C}}{\text{s}} \right)$
Commercial Steel	20
08 Si Steel	20
08 Si + 0.5 Ni Steel	16
08 Si + 0.5 Ni + 0.1 Co Steel	18
08 Si + 0.5 Ni + 0.1 Co + 0.1 V Steel	15

Table 4:11 - 0.8 Si Steel measured rod cooling rates.

Steel Rod ID	Measured Cooling Rate ($\frac{^{\circ}\text{C}}{\text{s}}$)
18BJ31	22
18BJ32	22
18BJ33	18
18BJ34	18
18BJ35	18

Table 4:12 - 0.8 Si + 0.5Ni Steel measured rod cooling rates.

Steel Rod ID	Measured Cooling Rate ($\frac{^{\circ}\text{C}}{\text{s}}$)
18BJ41	16
18BJ42	16
18BJ43	16
18BJ44	15
18BJ45	16

Table 4:13 - 0.8 Si + 0.5 Ni + 0.1 Co Steel measured rod cooling rates.

Steel Rod ID	Measured Cooling Rate ($\frac{^{\circ}\text{C}}{\text{s}}$)
18BJ51	18
18BJ52	18
18BJ53	17
18BJ54	17
18BJ55	18

Table 4:14 - 0.8 Si + 0.5 Ni + 0.1 Co 0.1 V Steel measured rod cooling rates.

Steel Rod ID	Measured Cooling Rate ($\frac{^{\circ}\text{C}}{\text{s}}$)
18BJ61	13
18BJ62	15
18BJ63	14
18BJ64	15
18BJ65	15

6 rods were re-austenitised at 890°C with a cooling rate of 20°C/s⁻¹ to produce a microstructure consistent with the experimental steel rods.

Table 4:15 - Commercial Steel Rod Heat Treatments

Steel Rod ID	Measured Cooling Rate ($\frac{^{\circ}\text{C}}{\text{s}}$)
18BJ71	20
18BJ72	18
18BJ73	18
18BJ74	18
18BJ75	18
18BJ76	22

Two samples from each steel composition were tensile tested at Central Laboratories at Scunthorpe steel works.

Table 4:16 - Rod Tensile Test Results.

Sample	UTS (MPa)	Yield (MPa)	ROA (%)	EI (%)
Commercial Coil (front)*	1126	780	33	11
Commercial Coil (back)*	1134	777	35	13
18BJ5A4	1180	734	44	21
18BJ5A5	1195	744	45	21
18BJ3A2	1173	738	44	20
18BJ3A1	1171	737	43	17
18BJ6A3	1196	749	46	21
18BJ6A1	1187	740	44	17
18BJ4A4	1145	723	43	17
18BJ4A1	1142	718	44	17
*Commercial steel tested as rolled, not after forced air cooling treatment				

Note, as described in Table 4:16, the lower elongation to failure values of the commercial steel are probably due to differences in processing, as it was tested in the as-rolled condition, and so the pearlite grain size will have been different. The commercial steel rods were not tensile tested after re-austenitising as not enough material was available. To ensure the heat treatments had produced a consistent rod microstructure, 1cm was removed from each rod to measure the interlamellar spacing of the pearlite in an SEM. 3 measurements were taken per grain. 3 grains were measured per rod. A grain from the centre, mid-radial, and 200 μm subsurface was selected at random.

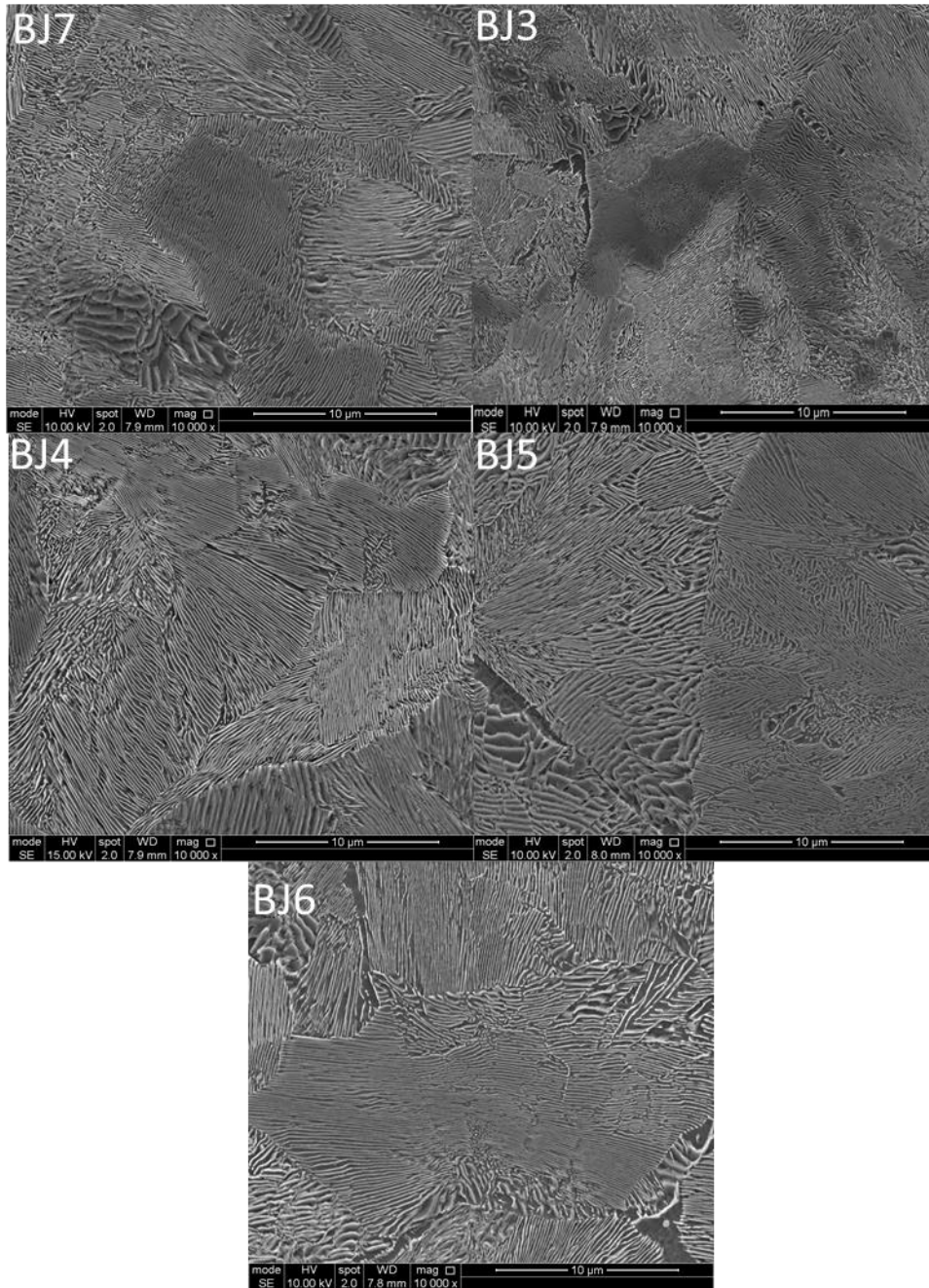


Figure 4:5 - Rod Feedstock Micrographs.

Average pearlite spacing measurements are shown in Table 4:17 and Figure 4:6. Variation in the air flow of the forced air-cooling rig and time constraints made absolute consistency between compositions difficult to achieve.

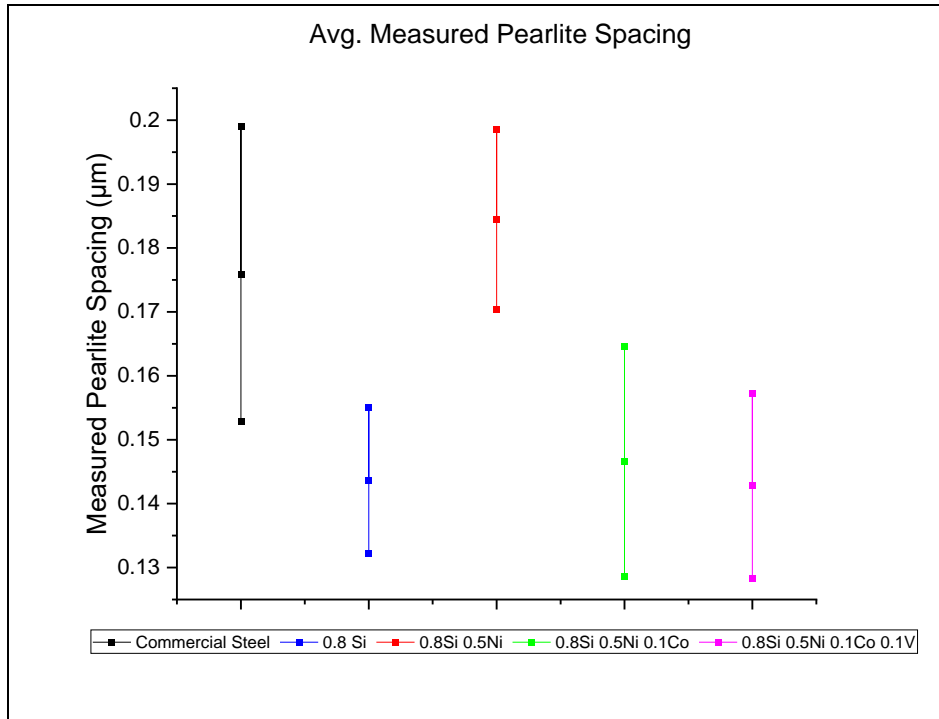


Figure 4:6 - Average measured pearlite lath spacing plotted with 95% confidence limits.

Table 4:17 - Average Measured Rod Pearlite Spacing.

Steel ID	Average Measured Pearlite Spacing (μm)	±95%CL (μm)
Commercial Steel (BJ7)	0.175	±0.023
0.8 Si Steel (BJ3)	0.143	±0.011
0.8 Si + 0.5 Ni Steel (BJ4)	0.184	±0.014
0.8 Si + 0.5 Ni + 0.1 Co Steel (BJ5)	0.146	±0.018
0.8 Si + 0.5 Ni + 0.1 Co + 0.1 V Steel (BJ6)	0.142	±0.014

As interlamellar spacing of the rod has been correlated to increased strain ageing kinetics and cementite dissolution, the difference in rod microstructure must be taken into consideration during analysis of testing [34]. Steel containing 0.8 Si + 0.5 Ni (BJ4) has an increase in pearlite spacing compared to all other experimental steel compositions. As the 95% confidence limits of the two values are do not overlap, this difference is likely real. As such, a minor reduction in cementite dissolution and ageing kinetics should be expected from this steel.

4.2.1.2 Wire Drawing

The single pass laboratory drawing bench, shown in Figure 4:7, draws at 1.5 m/min. No water cooling is possible, and so the slow drawing speed is essential to avoid excessive heat generation in the wire and the onset of dynamic strain ageing. Samples were clearly labelled to avoid any sample misidentification. The wire drawing schedule is shown in Table 4:18.

Table 4:18 - Single Pass lab drawing bench Wire drawing schedule.

Pass	Wire Diameter (mm)	True Strain	Reduction of Area (%)
-	6.00	-	-
1	5.40	0.21	19.00
2	4.68	0.50	24.89
3	4.09	0.77	23.62
4	3.65	0.99	20.36
5	3.28	1.21	19.25
6	2.97	1.41	18.01
7	2.70	1.60	17.36
8	2.46	1.78	16.99
9	2.26	1.95	15.60
10	2.17	2.03	7.81

As the wire drawing process took place over several days, the intermediate wires were stored in a freezer to reduce ageing. After drawing, wires were immediately returned to the freezer to minimise the strain ageing response.



Figure 4:7 - Single pass lab drawing bench.

No breakages were recorded during wire drawing, providing 7 meters of wire per steel composition.

4.2.2 Wire Drawing Summary

The single pass drawing bench produced sufficient material to proceed with an assessment of the strain ageing response. The single pass laboratory drawing bench is ideally suited to drawing shorter lengths of rod. However, the forced air-cooling rig was known to have an inconsistent air flow and so produced variations in the rod feedstock microstructures. An alternative method of cooling rods would be recommended in the future.

A pilot scale multi-pass machine requires an alternative approach. Welding of the experimental rods in a carrier coil resulted in frequent breakages and rod misidentification. In-line patenting of longer lengths of rod would be better suited, significantly reducing the number of welds required. An alternative method of production would be required to remove the need for welding entirely. Such as the casting of a small 2 tonne bloom which can be rolled in a rod mill, to produce a full coil. This method would incur significant costs, around £15000 for two blooms, which was significantly higher than the project budget would allow.

4.3 Artificial Ageing

A low temperature artificial ageing heat treatment was used to simulate room temperature ageing over an extended period of time, not to simulate an annealing or galvanising treatment. Artificial ageing heat treatments were completed in a water bath at 96°C. The Hundy equation [70] was used to calculate heat treatments to simulate 1, 2 and 4 months ageing in service.

$$\log_{10} \left(\frac{t_r}{t} \right) = H \left(\frac{1}{T_r} - \frac{1}{T} \right) - \log_{10} \left(\frac{T}{T_r} \right)$$

Equation 4:1 - Hundy Equation for calculating artificial ageing time [70].

Where t_r is time at room temperature, t is time at elevated temperature, T_r is room temperature and T is elevated temperature. H is a constant, which for carbon diffusion is 4400. It is worth noting, Nissanka commented that the equation was used on material that had been either temper rolled 4% or strained 5% in tension [70].

Table 4:19 - Temperatures used to calculate artificial ageing heat treatments.

	Temperature (°C)	Temperature (K)
Room Temperature	20.15	293.15
Elevated Temperature	96.15	369.15

365 days per year averaged over 12 months gives 30.41 days per month. 30.41 days in seconds is: 2.63E+6 seconds. Therefore, 2.63E+6 seconds was taken as the number of seconds in a month when calculating artificial ageing times at elevated temperature. Table 4:20 shows the calculated artificial ageing times.

Table 4:20 - Artificial ageing heat treatments.

Equivalent Ageing Condition	Artificial Ageing at 96°C
As drawn	-
1 Month	45 Minutes
2 Months	90 Minutes
4 Months	180 Minutes

4.4 Tensile Testing

Tensile testing of wire was completed on a Zwick Z100 with the following testing parameters: 100mm gauge length, 50N preload, 10mm/min preload speed and 30 mm/min test speed. 3 repeats were completed per ageing condition, per steel composition. UTS and elongation to failure values were measured. 0.2% proof stress and 0.2% proof to UTS ratio were calculated. Samples were kept at -18°C in a freezer for 4 weeks prior to testing.

0.2% proof stress was calculated using linear regression between a force of 2000 to 6000N. The linear regression data was offset by 0.2% strain and the intercept with the tensile data was taken as the 0.2% proof stress.

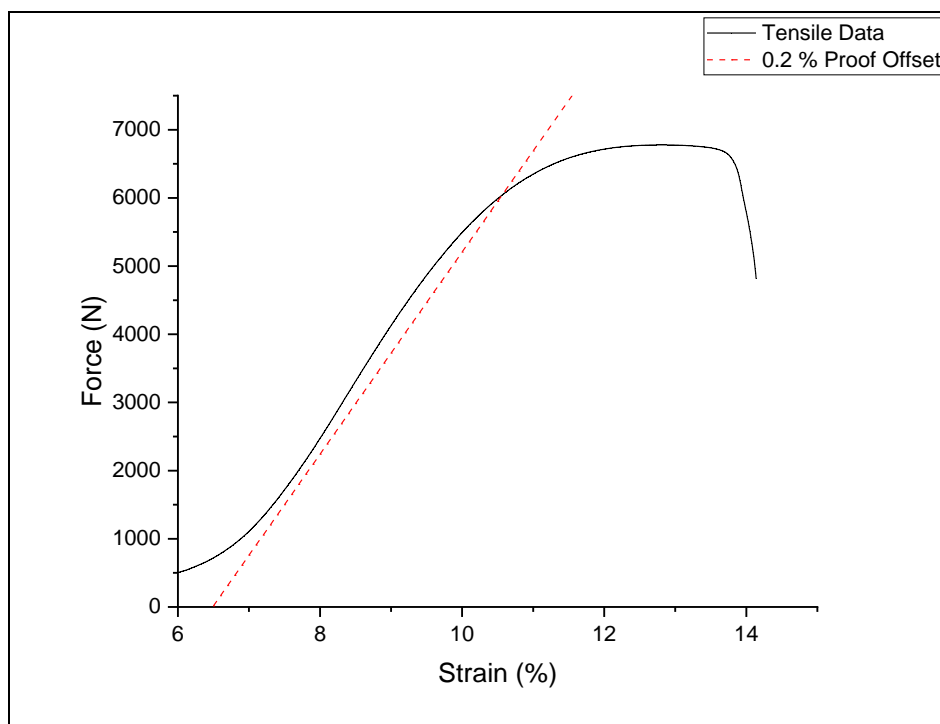


Figure 4:8 - 0.2% Proof Stress Calculation.

0.2% proof stress to UTS ratio was calculated to assess how much ductility remains in a wire microstructure.

4.5 Torsion Testing

Torsion testing was completed on an Instron MT2 at Swinden Technology Centre with the following parameters: 100mm gauge length, 30 revolutions per minute test speed with a 6kg load. Fracture types were classified according to BS ISO 7800 : 2012. Shown in Figure 4:9.




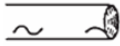

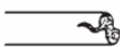
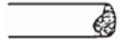



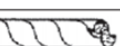
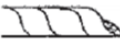

Type of fracture	Type no.	Aspect	Description and characteristics	Fracture plane
Normal torsion fracture	1a		Smooth: - fracture plane perpendicular to wire axis (or slightly oblique). - no cracks in fracture plane.	
	1b		Brittle: - fracture plane at an angle of 45° to wire axis. - no cracks in fracture plane.	
Fracture with local cracks or	2a		Smooth: - fracture plane perpendicular to wire axis and partially cracked.	
	2b		Stepped: - a part of the fracture plane is still smooth partially cracked.	
Irregular fracture (material defects)	2c		Irregular fracture plane: - no cracks in fracture plane.	
Fracture with spiral cracks over the whole length (or large part of it) Crack formation already occurs after a low number (3 to 5) of torsions and is best visible at that moment	3a		Smooth: - fracture plane perpendicular to wire axis and partially or entirely cracked.	
	3b		Stepped: - a part of the fracture plane is still smooth and partially or entirely cracked.	
	3c	 	Brittle: - fracture plane at an angle of 45° and partially or entirely cracked or Irregular fracture plane: - partially or entirely cracked	

Figure 4:9 - Wire Torsion Test Fracture Classification [71]

4.6 Magnetic Sensors

Researchers at Warwick University have developed magnetic sensors to improve process control on the rod mill. This collaboration has also led to the development of magnetic sensors capable of detecting the strain ageing response of drawn wire. Detection was by measuring the inductance of the sample as a function of frequency.

The initial magnetic measurements were completed on two sets of 4.68mm diameter wires. A larger diameter wire was chosen as the sensor had been originally developed for rod samples. 12 and 10mm diameter rods were drawn to 4.68mm creating different drawing strains at the same wire diameter. 10mm rod was drawn to 4.68mm with a drawing strain of 1.52 and the 12mm rod was drawn to 4.68mm with a drawing strain of 1.88. Two drawing strains and a variety of heat treatments were used to assess the sensitivity of the magnetic sensors in detecting the strain ageing response.

4 x 60mm lengths of wire were cut from each drawing strain. One sample was measured as drawn. One sample was spheroidised, and two were given artificial ageing heat treatments to simulate 1 and 2 months ageing at room temperature. Inductance was measured across a range of frequencies, shown in Figure 4:10 and Figure 4:11.

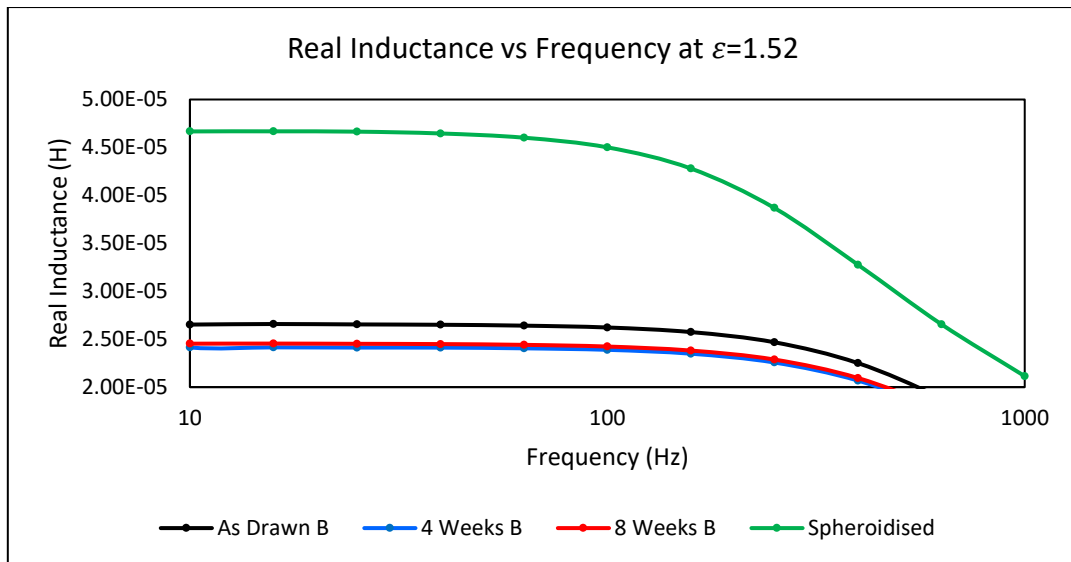


Figure 4:10 - Magnetic measurements of a 60mm length of wire ($\epsilon = 1.52$) [72]

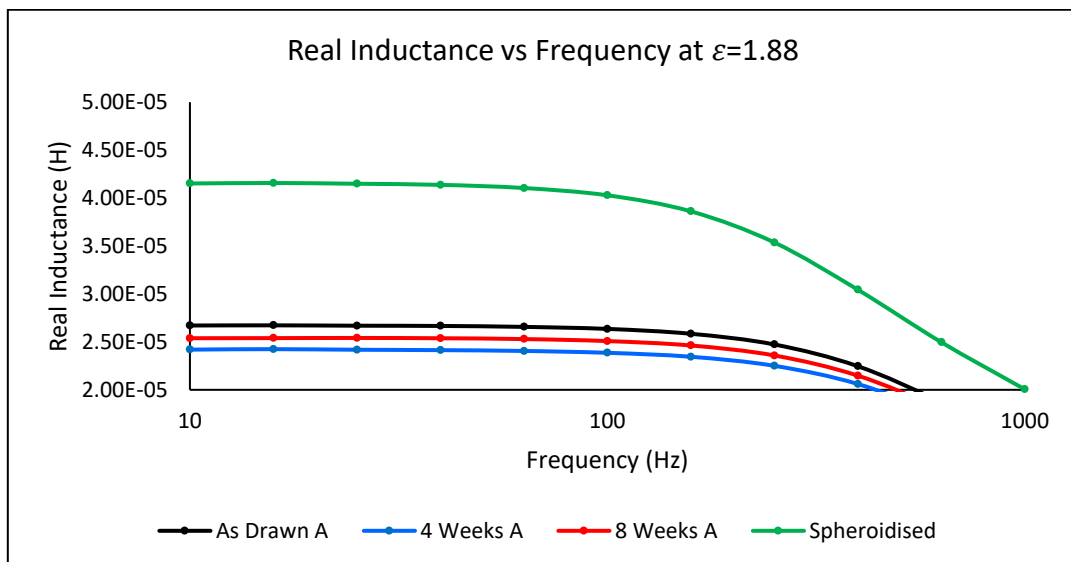


Figure 4:11 - Magnetic measurements of a 60mm length of wire ($\epsilon = 1.88$) [72].

Figure 4:10 and Figure 4:11 show the sensors were capable of detecting the strain ageing response, with the differences being more prevalent at the higher drawing strain. Following these results, magnetic sensors were developed specifically to measure smaller diameter wires to improve accuracy. The final iteration of the sensor consists of two aligned identical coils. One as an excitation coil and the other, a sensing coil. The sensor core was made from copper wire 3.2mm in diameter, the excitation coil was made from 0.24mm diameter copper

wire. Both coils had 30 turns. Coils were driven using an Impedance Analyser Solartron (SL 1260 A) with an AC voltage of 3V, at frequencies between 10-1000 Hz [73].

4.7 Differential Scanning Calorimetry

Differential Scanning Calorimetry (DSC) was completed on a PerkinElmer Diamond power compensation DSC. All heat flow results are plotted with endothermic peaks upwards. Wire samples for DSC analysis were taken from the centre of a coil. A 100mm length of wire was cut from a coil with wire cutters. 20mm was removed from each end using a water cooled secotom 50. The cutting parameters used were: 2000 RPM blade speed, 0.1 mm/s cutting speed with a Struers 10S20 blade. Wire was cut into thin discs of approximately 50mg. The wire was left to stand for 60 seconds between each cut, to reduce heating.

Samples were cleaned in an ultrasonic bath for 3 minutes prior to testing. PerkinElmer alumina pans, part number: N5190180 were used throughout testing. Calibration and baseline calculations were performed from 20°C to 600°C, at a heating rate of 20 °C per second, which was also the method used for the analysis. Furnace calibration was automated within the Pyris Software. All DSC scans were completed under argon gas with a flow rate of 20 mL/min.

Table 4:21 - Measured calibration samples.

	Indium Calibration Run	Zinc Calibration Run
Sample Mass (mg)	23.90	17.70
Transformation Temperature (°C)	157.78	425.18
Enthalpy of Change (J/g)	31.11	109.68

The machine baseline is shown in Figure 4:12. Baseline data was subtracted from each data set prior to analysis.

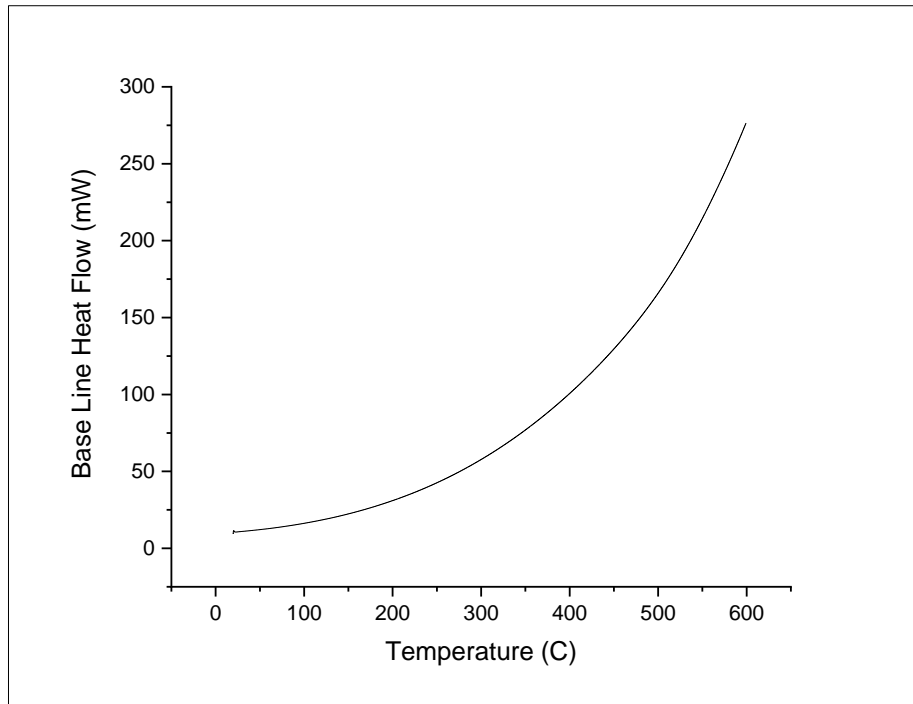


Figure 4:12 - Machine baseline data.

4.7.1 Data Analysis

Origin(Pro) software was used to determine a fitted baseline. Using the DSC data as anchor points, a fitted baseline was created with the Poly5 function. The Poly5 function produced the closest fit to the data and was used throughout. 1000 anchor points were consistently used throughout data analysis, as seen in Figure 4:13.

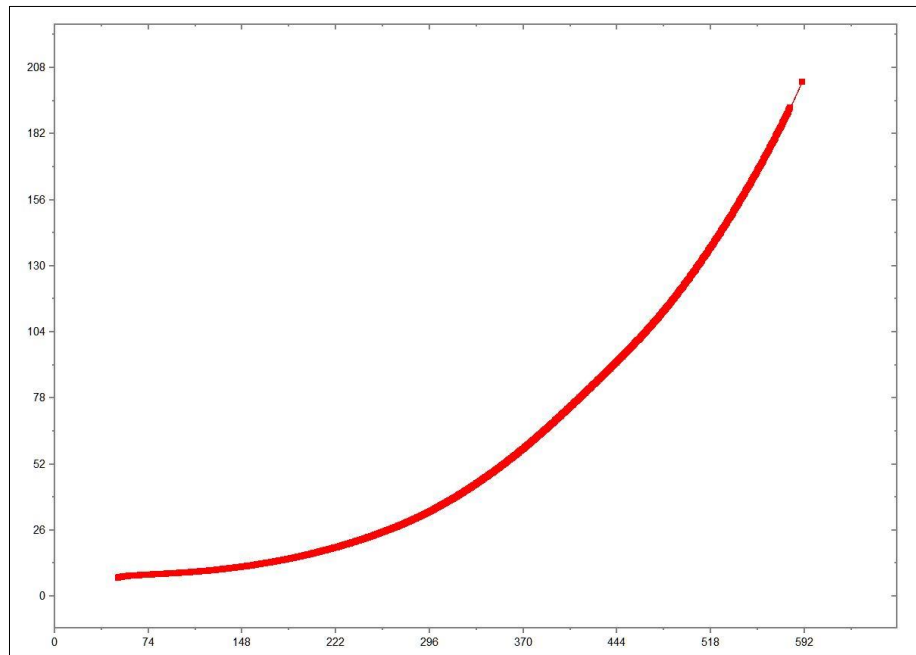


Figure 4:13 - Anchor points for calculate fitted line.

Once the fitted line had been produced, the deviation of the heat flow from the fitted baseline could be calculated. This procedure is shown in Figure 4:14 and Figure 4:15.

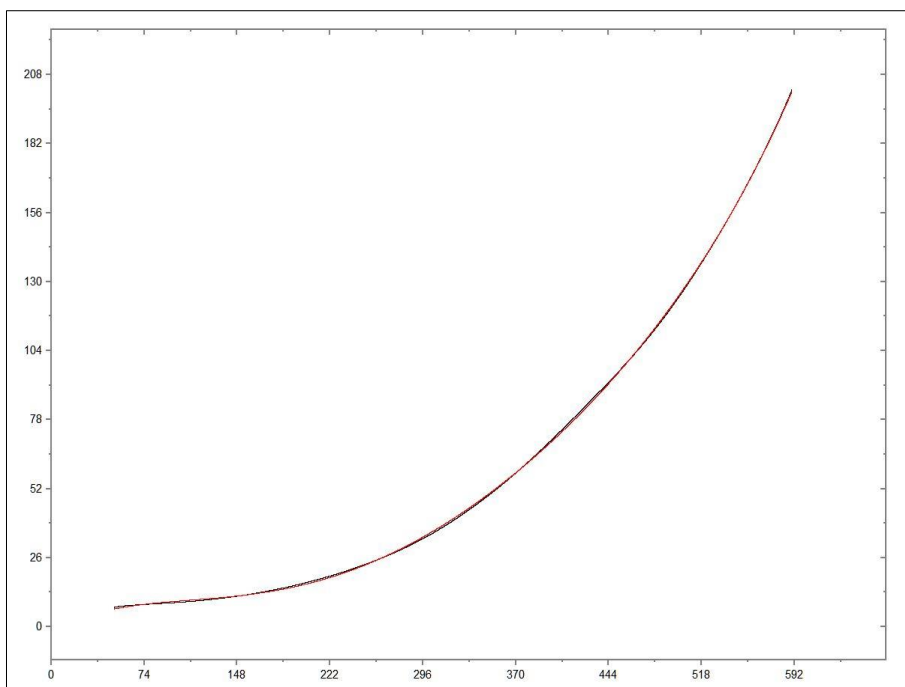


Figure 4:14 - Fitted line (Red) Plotted over sample data with machine baseline subtracted (Black).

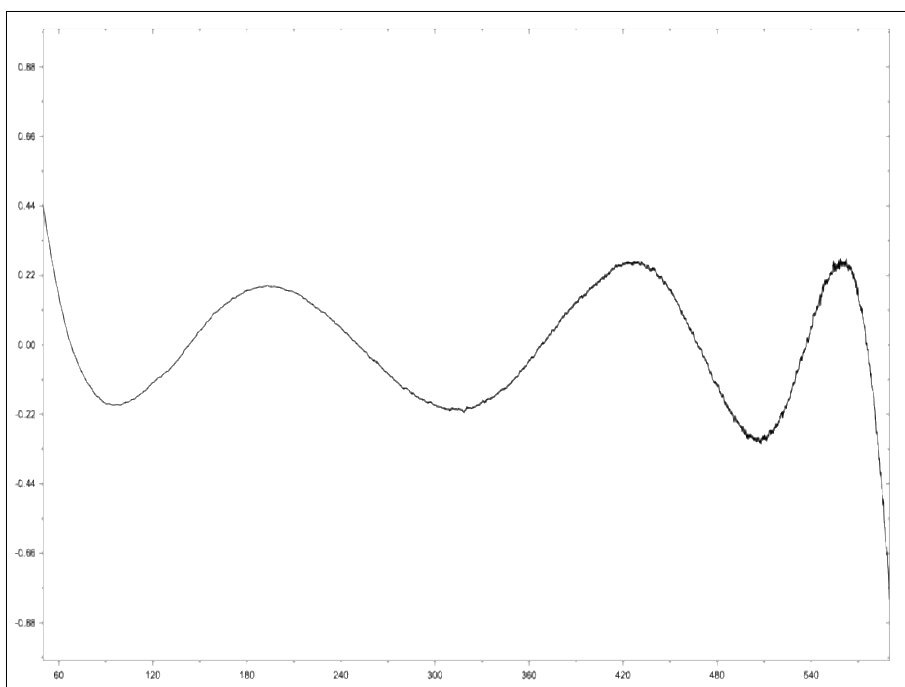


Figure 4:15 - Sample data - calculated deviation from fitted line.

Following data analysis, the temperature and exothermic enthalpy of change was calculated from each data set.

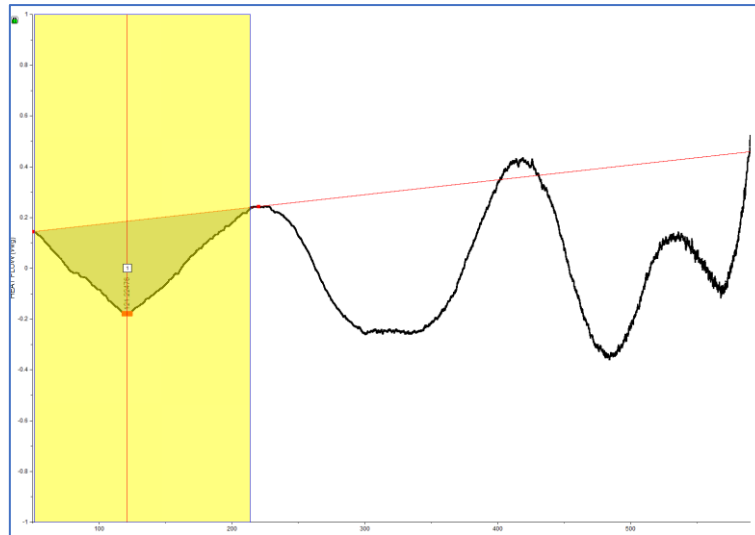


Figure 4:16 - Curve integration to obtain enthalpy of change.

Figure 4:16 shows the integration of the 1st exothermic event at 150°C to obtain enthalpy of change (ΔH) for each DSC scan. This was repeated for each exothermic event. Note, for some scans a 4th exothermic event could not be identified.

4.8 Microscopy

SEM was completed on an FEI Inspect F50. TEM and STEM imaging was completed on JEOL F200. Machine parameters and operators are noted in the results section. Cementite lamellae thickness was measured on an image with 200k brightfield magnification measurements were at intervals of 22.4nm. This results in 52 measurements per lath. Three laths from each image were chosen at random. The mean, 95% Confidence limits and coefficient of variance was calculated using Origin(Pro) software.

4.8.1.1 SEM & Optical Preparation

Samples were polished to 0.5 μ m diamond solution and etched with 2% nital.

4.8.1.2 TEM Sample Preparation

Samples were electropolished in a 3% perchloric acid, 37% 2-butoxyethanol and 60% methanol solution. Electropolishing was completed on a Struers Tenupol-5 at a voltage of 32 with a pump flow number 16.

4.8.1.3 Cementite Lamellae Thickness Measurements

Three cementite lamellae were chosen at random per micrograph, with a magnification of 200k. Cementite lamellae thickness was measured every 224nm along the length of the cementite lamellae, parallel with the drawing direction. The measurements were completed using Gatan DigitalMicrograph software. The coefficient of variance of each lamellar was calculated using origin(pro).

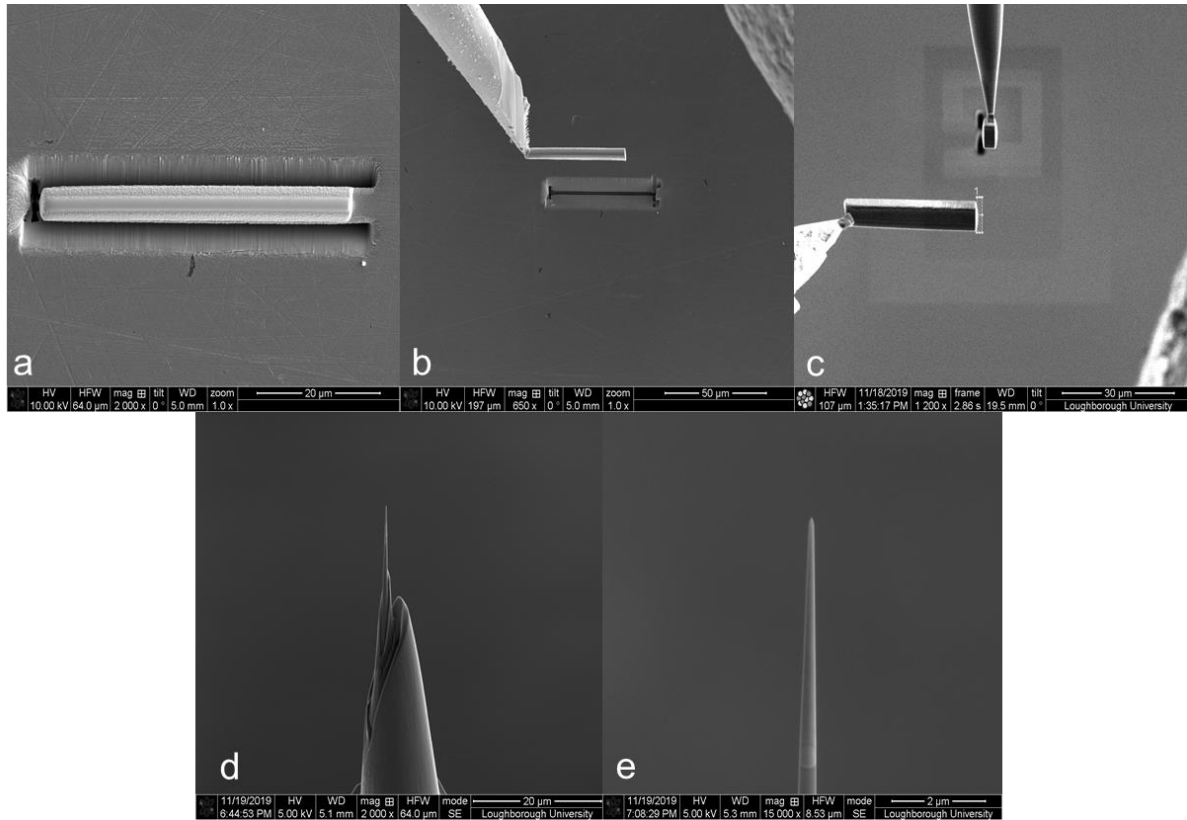
4.9 Atom Probe Tomography

Atom probe tomography was completed on a CAMECA LEAP 5000 at Oxford University, the operator was Dr Paul Baggot. Running conditions were: Laser mode at 50pJ, 50 kelvin and each sample was ran for 1 day. An iso concentration of 7 at.% carbon was selected as it was measured as the mid-point in carbon contents, 7 at.% was also used by Li et al. [45]. A proxigram was calculated as a function of of distance before/after the interface from all locations. A proxigram was chosen over a 1d line scan as this avoids any artefacts in field evaporation differences between phases [74].

4.9.1 FIB - Lift out method.

Atom probe tips were prepared using the standard lift out method detailed by Miller and Russell [75]. The focused ion beam milling was completed by Dr Scott Doak and Dr Stuart

Robinson at Loughborough University Materials Characterisation Centre. In preparation for the focused ion beam milling, samples were ground flat to the centre of the wire. The final polishing step was completed with 1-micron diamond solution.



The FIB lift out procedure is shown in Figure 4:17. The following is a description of each stage shown in Figure 4:17:

- a. A line of platinum is deposited on the surface of the sample. Three sides of a trench are milled to create a floating wedge in the surface of the material.
- b. A probe is inserted and welded to the floating wedge. Once the probe is attached, the final side of the wedge is milled away, allowing the probe to retract with the wedge attached.

- c. The wedge is then transferred to the APT coupon. The edge of the wedge is placed on top of a stand on the coupon, using deposition of platinum to hold it in place.
- d. The remaining wedge is then cut and moved away whilst the tip is shaped by further milling.
- e. Finished APT tip. The final milling current was 50 pA.

Samples were kept in a vacuum desiccator during transportation and prior to analysis.

4.10 Chapter Summary

This chapter has detailed the production and processing of the experimental steels and a commercial steel for comparison. Mechanical testing, DSC, Magnetic sensors, TEM and APT were selected to characterise the strain ageing response of the material. The experimental methodology of these techniques has also been reported.

5 Results

This chapter presents the results from the testing of the experimental steel and commercial steel wire. Note that all results presented are from the single pass lab drawing bench material unless otherwise stated. This is due to the limited amount of correctly identified material from the multi pass drawing bench wire drawing method. Therefore, the drawing strain is 2.03 and the wire diameter is 2.17mm unless otherwise stated. Experimental steels shall be referred to by their British Steel designation as shown in Table 5:1.

Table 5:1 - British Steel, Steel grade designations and Compositions (wt.%).

Steel Grade	C	Mn	Si	Ni	Co	V	P	S
Commercial Grade X85LM (BJ7)	0.84	0.52	0.23	0.02	-	0.001	0.013	0.016
BQ3/BJ3	0.82	0.3	0.8	-	-	-	0.01	0.007
BQ4/BJ4	0.82	0.3	0.8	0.5	-	-	0.01	0.007
BQ5/BJ5	0.82	0.3	0.8	0.5	0.1	-	0.01	0.007
BQ6/BJ6	0.82	0.3	0.8	0.5	0.1	0.1	0.01	0.007

5.1 Tensile Testing

Tabulated values of UTS, 0.2% Proof Stress, 0.2% Prof stress to UTS ratio and elongation to failure with tensile force-extension plots are presented in Appendix: 9.2 - Tensile Testing Data. The section presents a summary of the tensile testing data for comparison between compositions.

5.1.1 UTS and 0.2% Proof Stress Summary

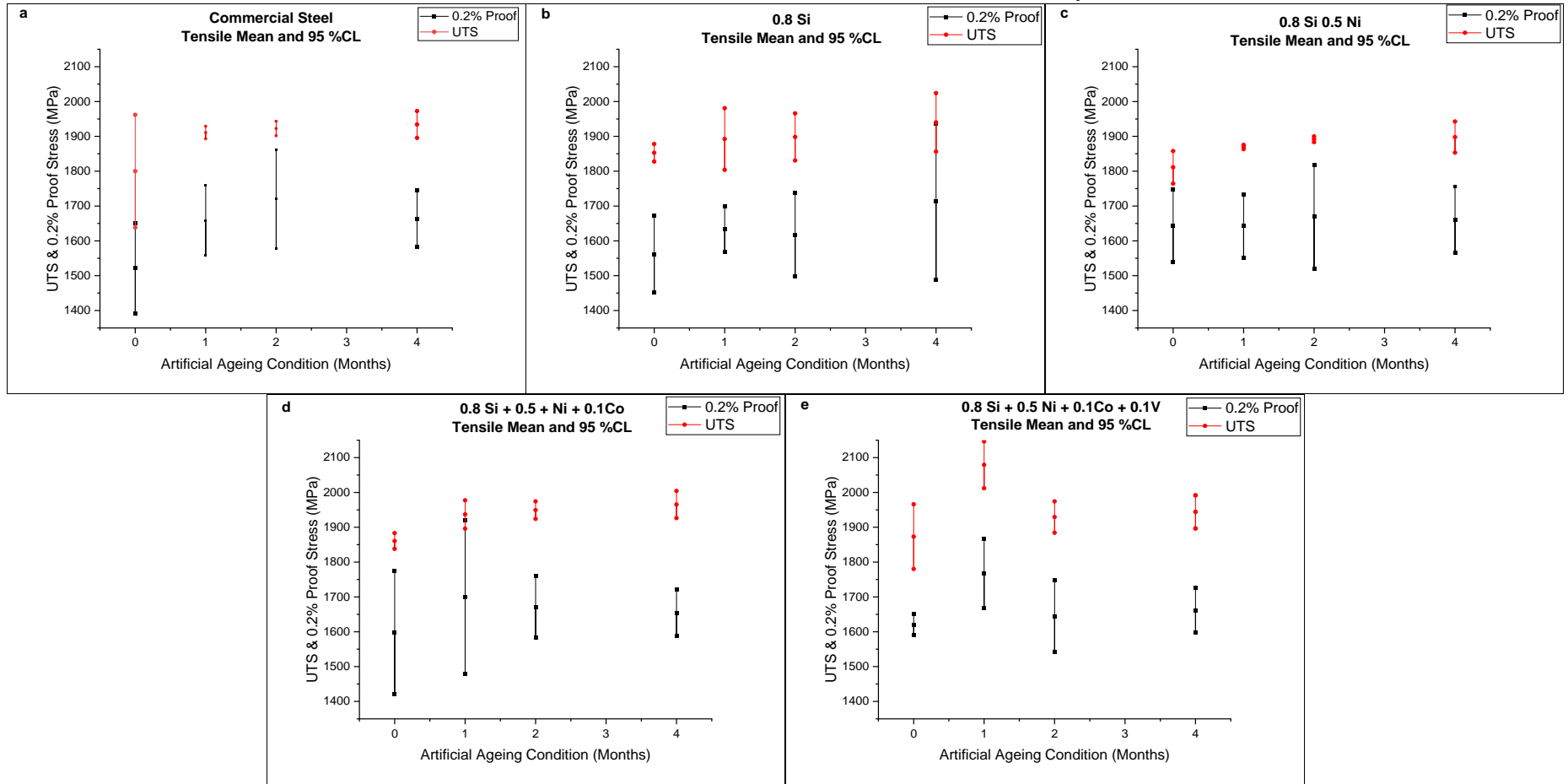


Figure 5:1 - UTS and 0.2 % proof stress mean with 95% confidence limits: a. Commercial Steel, b. Steel BJ3, c. Steel BJ4, d. Steel BJ5 and e. Steel BJ6.

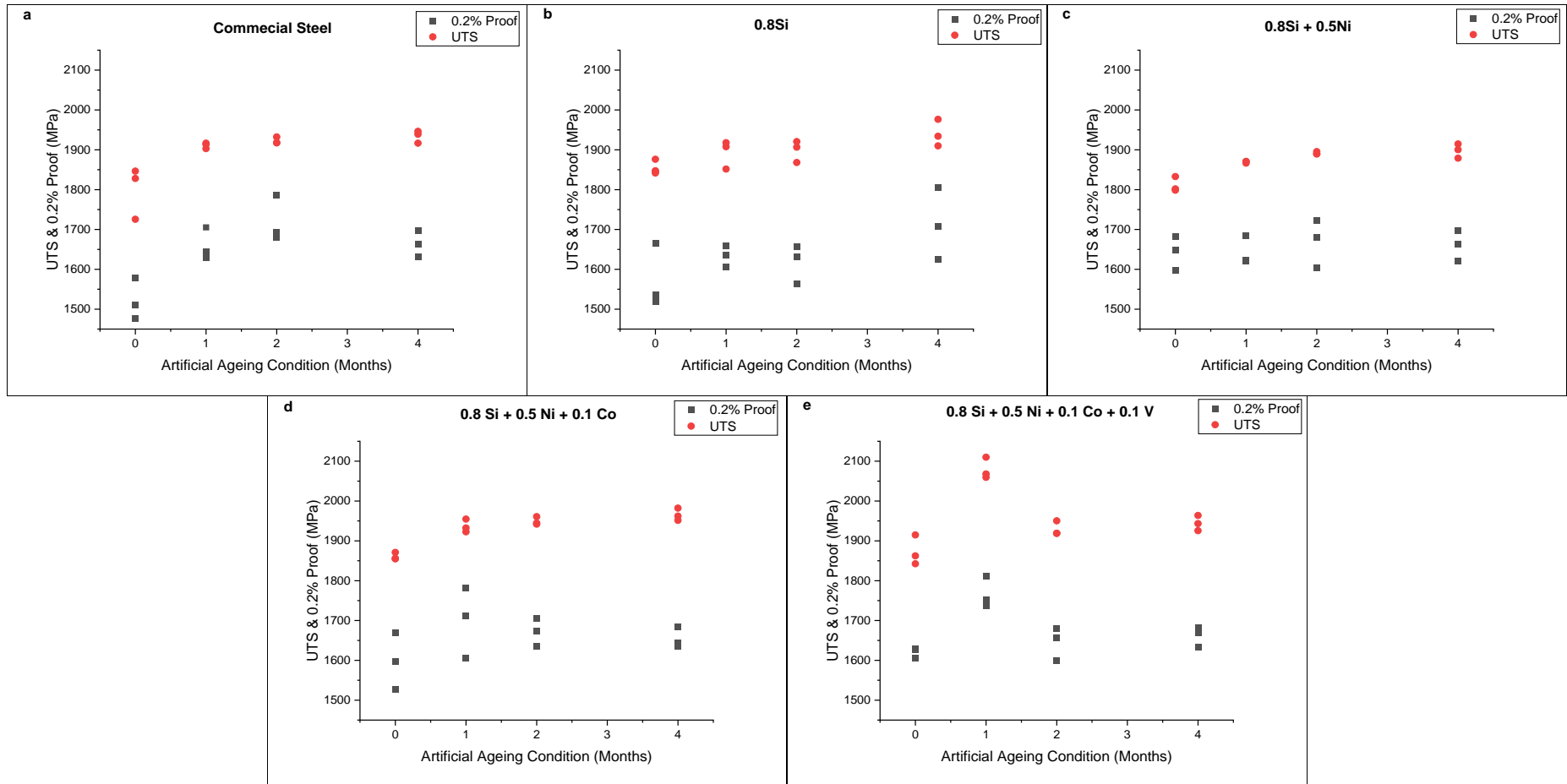


Figure 5:2 - UTS and 0.2 % proof stress test data summary: a. Commercial Steel, b. Steel BJ3, c. Steel BJ4, d. Steel BJ5 and e. Steel BJ6.

5.1.2 Tensile Elongation to Failure Summary

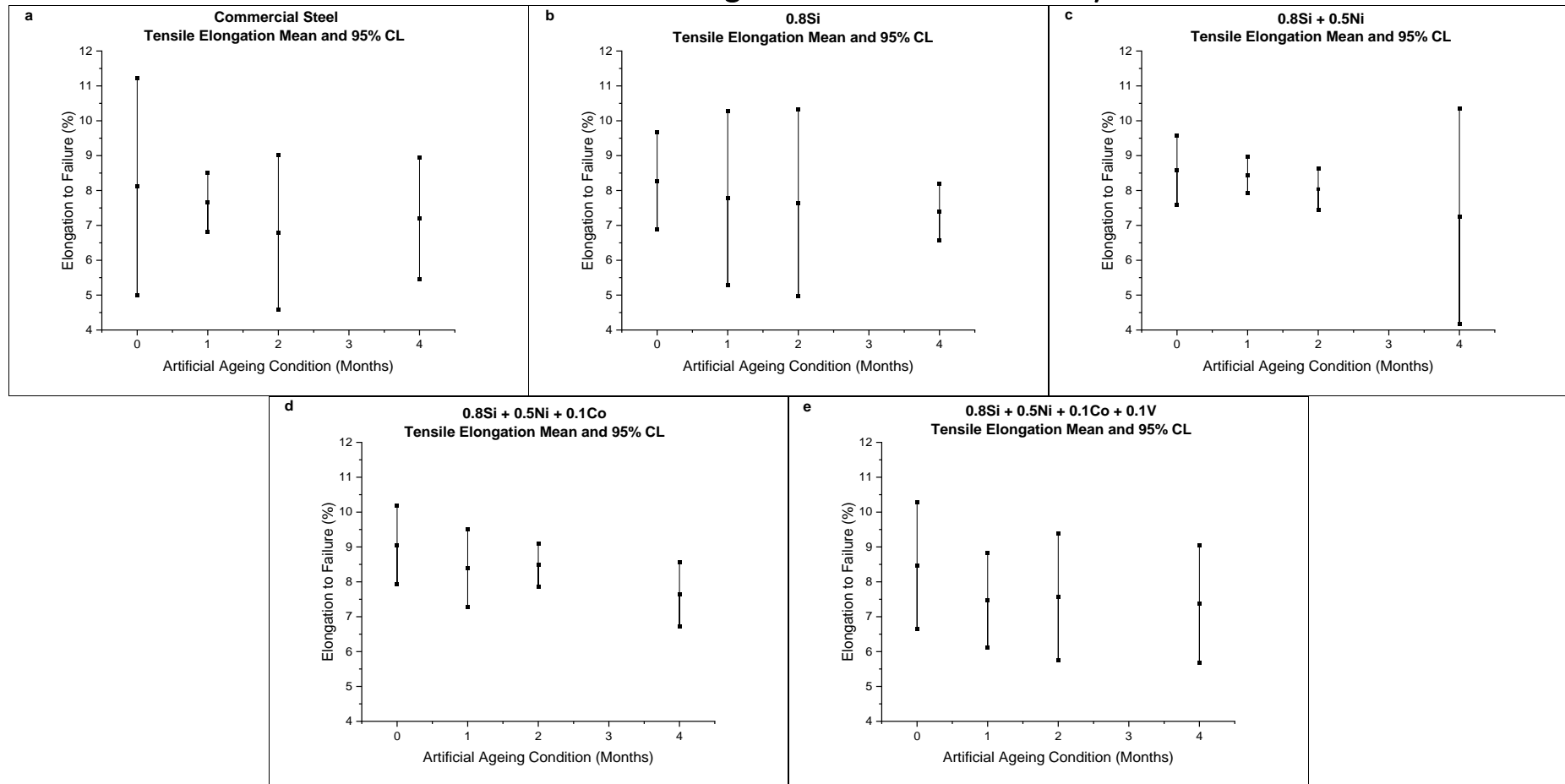


Figure 5:3 - Tensile elongation to failure mean with 95% confidence limits: a. Commercial Steel, b. Steel BJ3, c. Steel BJ4, d. Steel BJ5 and e. Steel BJ6.

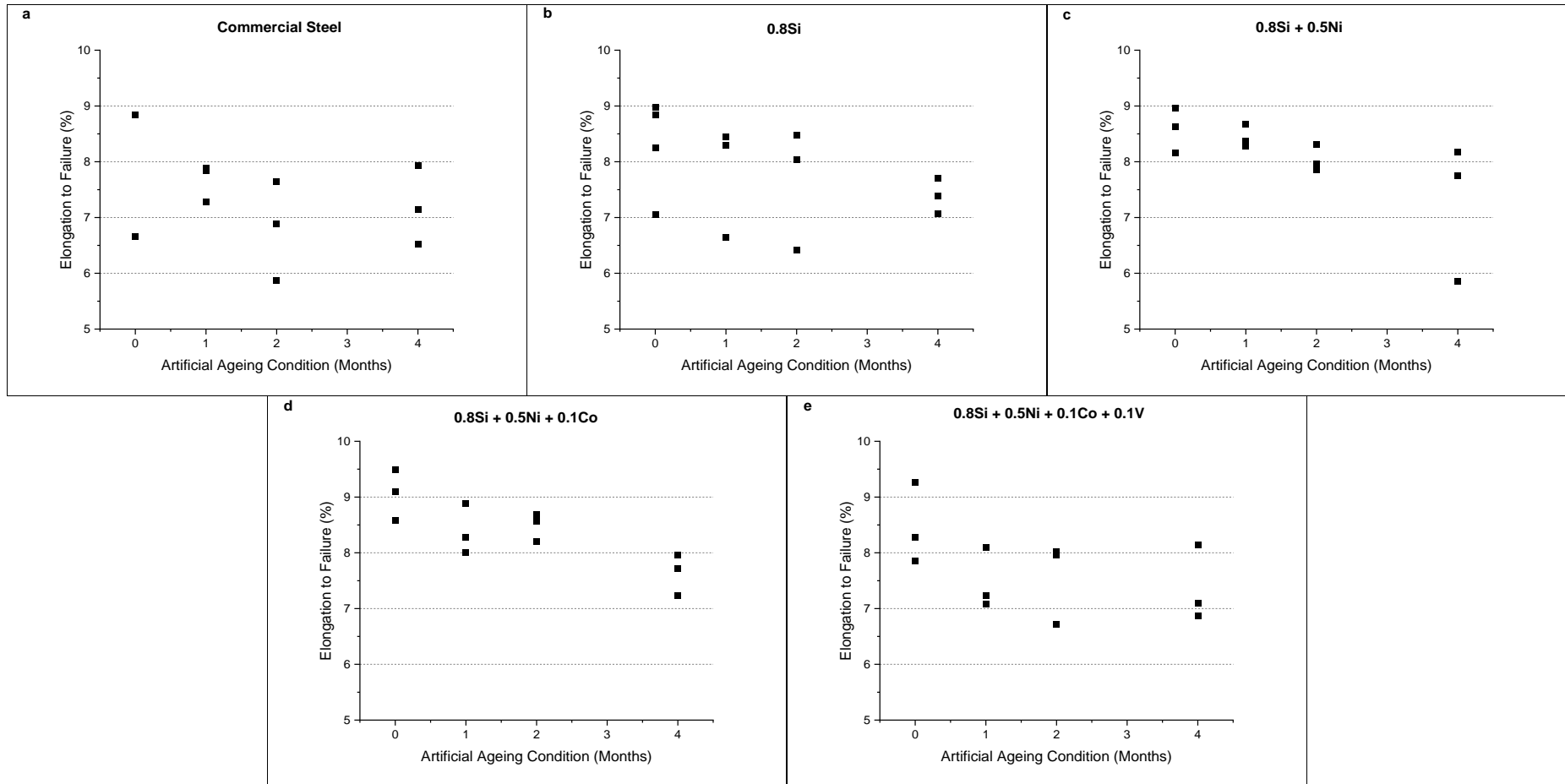


Figure 5:4 - Tensile elongation to failure data summary: a. Commercial Steel, b. Steel BJ3, c. Steel BJ4, d. Steel BJ5 and e. Steel BJ6.

5.1.3 0.2% Proof Stress to UTS Ratio Summary

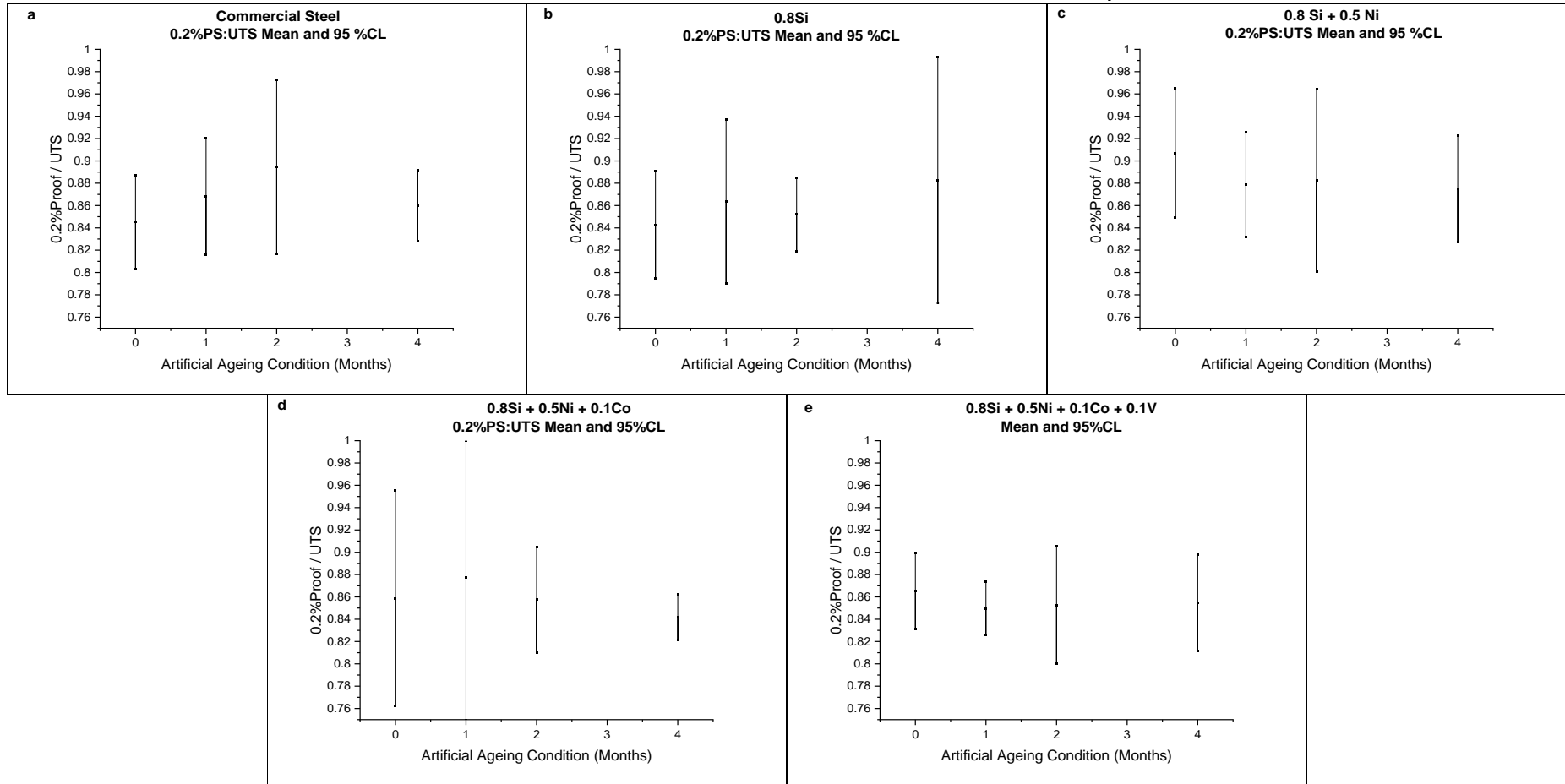


Figure 5:5 - 0.2% Proof Stress to UTS ratio mean with 95% confidence limits: a. Commercial Steel, b. Steel BJ3, c. Steel BJ4, d. Steel BJ5 and e. Steel BJ6.

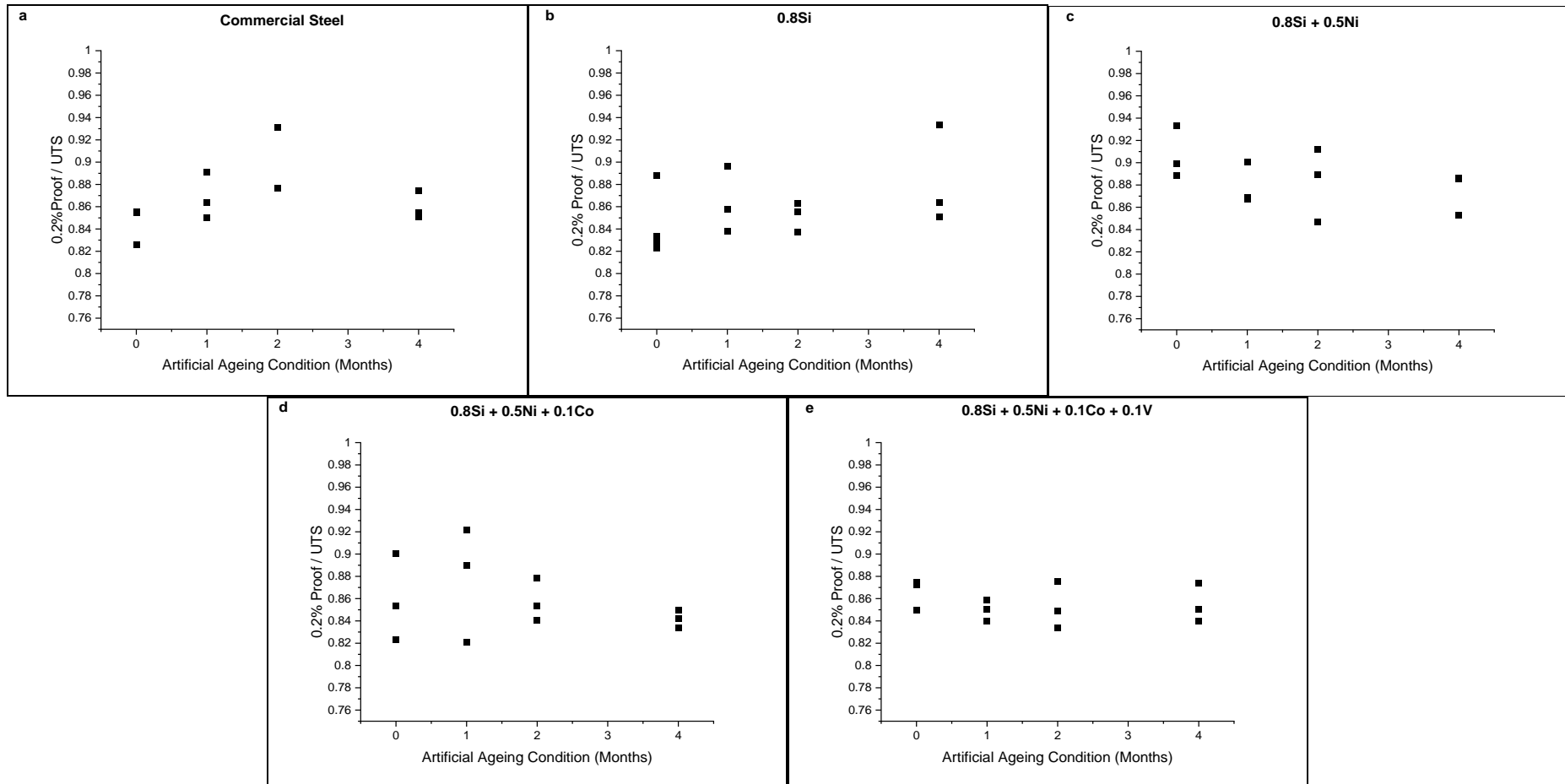


Figure 5:6 - 0.2% Proof Stress to UTS ratio data summary: a. Commercial Steel, b. Steel BJ3, c. Steel BJ4, d. Steel BJ5 and e. Steel BJ6.

5.1.4 Tensile Testing Results Summary

Table 5:2 - Tensile results for Commercial Steel.

Com. Steel	0.2% Proof Strength (Mpa)				UTS (Mpa)				0.2%Proof/UTS Ratio				Elongation to Failure (%)			
	AD	1M	2M	4M	AD	1M	2M	4M	AD	1M	2M	4M	AD	1M	2M	4M
Lower 95% CL	1392	1558	1578	1582	1638	1893	1902	1896	0.80	0.82	0.82	0.83	5.00	6.82	4.59	5.45
Mean	1522	1659	1720	1664	1800	1911	1922	1934	0.85	0.87	0.89	0.86	8.12	7.67	6.80	7.20
Upper 95% CL	1652	1760	1862	1745	1962	1929	1943	1973	0.89	0.92	0.97	0.89	11.23	8.51	9.01	8.95

Table 5:3 - Tensile results for 0.8 Si Steel.

BJ3	0.2% Proof Strength (Mpa)				UTS (Mpa)				0.2%Proof/UTS Ratio				Elongation to Failure (%)			
	AD	1M	2M	4M	AD	1M	2M	4M	AD	1M	2M	4M	AD	1M	2M	4M
Lower 95% CL	1451	1569	1498	1489	1828	1804	1831	1856	0.79	0.79	0.82	0.77	6.88	5.30	4.96	6.58
Mean	1562	1634	1618	1713	1853	1892	1898	1940	0.84	0.86	0.85	0.88	8.28	7.79	7.64	7.39
Upper 95% CL	1673	1699	1737	1936	1878	1981	1966	2024	0.89	0.94	0.88	0.99	9.67	10.29	10.33	8.19

Table 5:4 - Tensile results for 0.8Si + 0.5Ni Steel.

BJ4	0.2% Proof Strength (Mpa)				UTS (Mpa)				0.2%Proof/UTS Ratio				Elongation to Failure (%)			
	AD	1M	2M	4M	AD	1M	2M	4M	AD	1M	2M	4M	AD	1M	2M	4M
Lower 95% CL	1538	1552	1521	1661	1764	1863	1883	1853	0.85	0.83	0.80	0.83	7.59	7.92	7.45	4.18
Mean	1643	1643	1669	1565	1811	1869	1892	1898	0.91	0.88	0.88	0.87	8.59	8.44	8.04	7.26
Upper 95% CL	1747	1734	1817	1756	1858	1875	1900	1943	0.97	0.93	0.96	0.92	9.58	8.97	8.63	10.35

Table 5:5 - Tensile results for 0.8Si + 0.5Ni + 0.1Co Steel.

BJ5	0.2% Proof Strength (Mpa)				UTS (Mpa)				0.2%Proof/UTS Ratio				Elongation to Failure (%)			
	AD	1M	2M	4M	AD	1M	2M	4M	AD	1M	2M	4M	AD	1M	2M	4M
Lower 95% CL	1421	1479	1584	1588	1838	1896	1924	1926	0.76	0.75	0.81	0.82	7.94	7.27	7.87	6.72
Mean	1598	1699	1672	1654	1861	1937	1949	1965	0.86	0.88	0.86	0.84	9.06	8.39	8.48	7.64
Upper 95% CL	1775	1919	1759	1721	1883	1977	1974	2004	0.96	1.00	0.91	0.86	10.18	9.52	9.10	8.55

Table 5:6 - Tensile results for 0.8Si + 0.5Ni + 0.1Co + 0.1V Steel.

BJ6	0.2% Proof Strength (Mpa)				UTS (Mpa)				0.2%Proof/UTS Ratio				Elongation to Failure (%)			
	AD	1M	2M	4M	AD	1M	2M	4M	AD	1M	2M	4M	AD	1M	2M	4M
Lower 95% CL	1591	1668	1543	1597	1780	2012	1884	1897	0.83	0.83	0.80	0.81	6.66	6.12	5.75	5.69
Mean	1621	1767	1645	1662	1873	2079	1929	1944	0.87	0.85	0.85	0.85	8.47	7.47	7.57	7.37
Upper 95% CL	1651	1866	1748	1727	1966	2146	1974	1992	0.90	0.87	0.91	0.90	10.27	8.82	9.39	9.06

All tensile samples, of all compositions, failed in a ductile cup-cone type fracture, suggesting tensile ductility was not exhausted under these artificial ageing conditions. Images of tensile test fractures are shown in section 9.2 - Tensile Testing Data. Figure 5:1 summarises the change in tensile and 0.2% proof stress which has occurred with artificial ageing. Generally, high variation was observed, preventing definitive changes in the tensile properties being observed or quantified for some of the steel compositions assessed. Properties which measured the wires ability to deform, such as 0.2% proof stress and tensile elongation to failure, resulted in higher levels of variation. As the deformation behaviour of a wire is determined by dislocation motion and interaction, the heterogeneous microstructure and strain ageing response is expected to produce variation during deformation.

The high variation and relatively large increments of artificial ageing conditions may not be representative of the true strain ageing response curve of each composition. For example, if strain ageing resulted in the loss of ductility of one composition at 1.5 months, and the recovery does not occur at the same rate as the initial increase of strength, a slight peak at one or two months artificial ageing may lead to an incorrect conclusion whether the strength is still increasing or if recovery has begun. Thus, mean values of artificial ageing conditions have not been connected to prevent the identification of a potentially erroneous trend.

Figure 5:1 and Figure 5:2 show the 0.2% proof stress and UTS mean with 95% confidence limits and testing data points, respectively. No definitive differences were observed in proof stress, with the exception of an increase from the as-drawn condition to 1 month artificial

ageing condition in steel BJ6 (Figure 5:1e). Where 95% confidence limits do not overlap between ageing conditions, this is taken as a real difference has likely occurred. However, steel BJ4 shows two increases in UTS from as-drawn up to the one and then two month artificial ageing condition, suggesting strength is still increasing due to strain ageing and the softening of the microstructure has not yet begun with two months artificial ageing, shown in Figure 5:1c. Figure 5:1e shows the UTS undergoes an increase from the as-drawn condition to the one month artificial ageing condition, and then a decrease in the two month artificial ageing condition, which suggests that the softening of the microstructure has begun by the two month artificial ageing condition. Thus, this suggests that steel BJ6 has increased strain ageing kinetics compared to steel BJ4.

Figure 5:3 and Figure 5:4 show the mean tensile elongation with 95% confidence limits and test data points, respectively. As per 0.2% proof stress, the high variation in tensile elongation to failure results in no distinct differences being measured. No significant differences were observed in fracture types, with all samples tested failing in a ductile cup-cone type fracture. BJ5, shown in Figure 5:3d, exhibits the most consistent and smallest variation across the range of artificial ageing conditions. Figure 5:3c appears to have the least variation in the as drawn, one month and two month artificial ageing condition yet shows a great deal of variation in the 4 month artificial ageing condition.

Figure 5:5 and Figure 5:6 show the mean 0.2% Proof stress to UTS ratios and test data points, respectively. This ratio is indicative of the extent of dislocation pinning or free dislocations present in the bulk structure. A high variation is present throughout Figure 5:5 and Figure

5:6, with steel BJ6 showing the least variation (Figure 5:5e), although no distinct differences can be determined from this data. Data points from the testing of the commercial steel show a peak in the 2 month artificial ageing condition in Figure 5:6a, severely brittle torsion fractures (Figure 9:52) of the commercial steel in the 2 month artificial ageing condition suggest this is a valid observation. This implies that strain ageing is active in the commercial steel whereas there is no such direct evidence after ageing the experimental steel composition wires.

5.2 Torsion Testing

Revolutions to failure, peak torque, fractures and revolutions to failure - torque plots are presented in section: Appendix 9.3: Torsion Testing Data. This section presents a summary of the torsion testing data for comparison between compositions.

5.2.1 Revolutions to Failure Summary

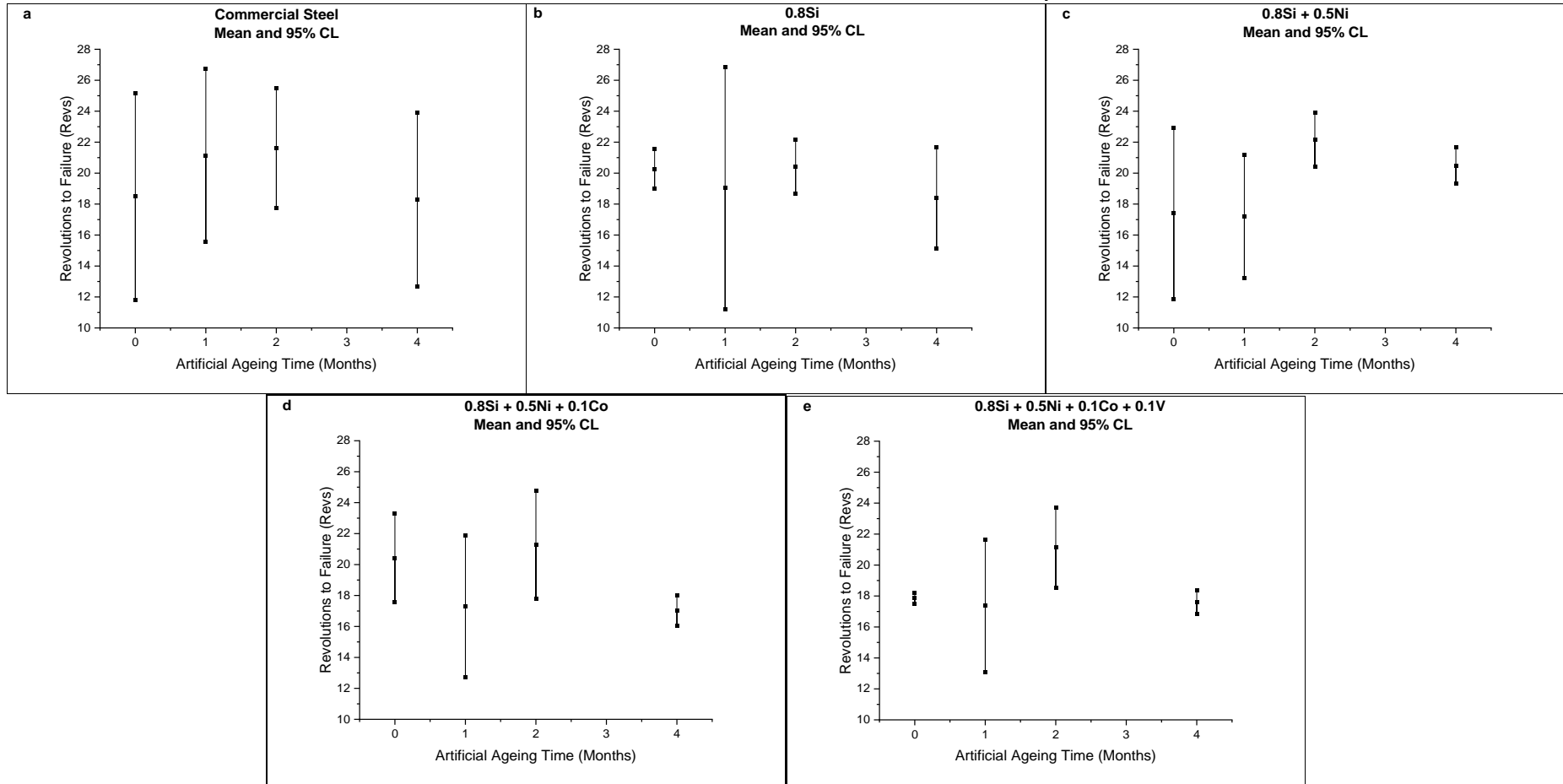


Figure 5:7 - Revolutions to failure mean with 95% confidence limits: a. Commercial Steel, b. Steel BJ3, c. Steel BJ4, d. Steel BJ5 and e. Steel BJ6.

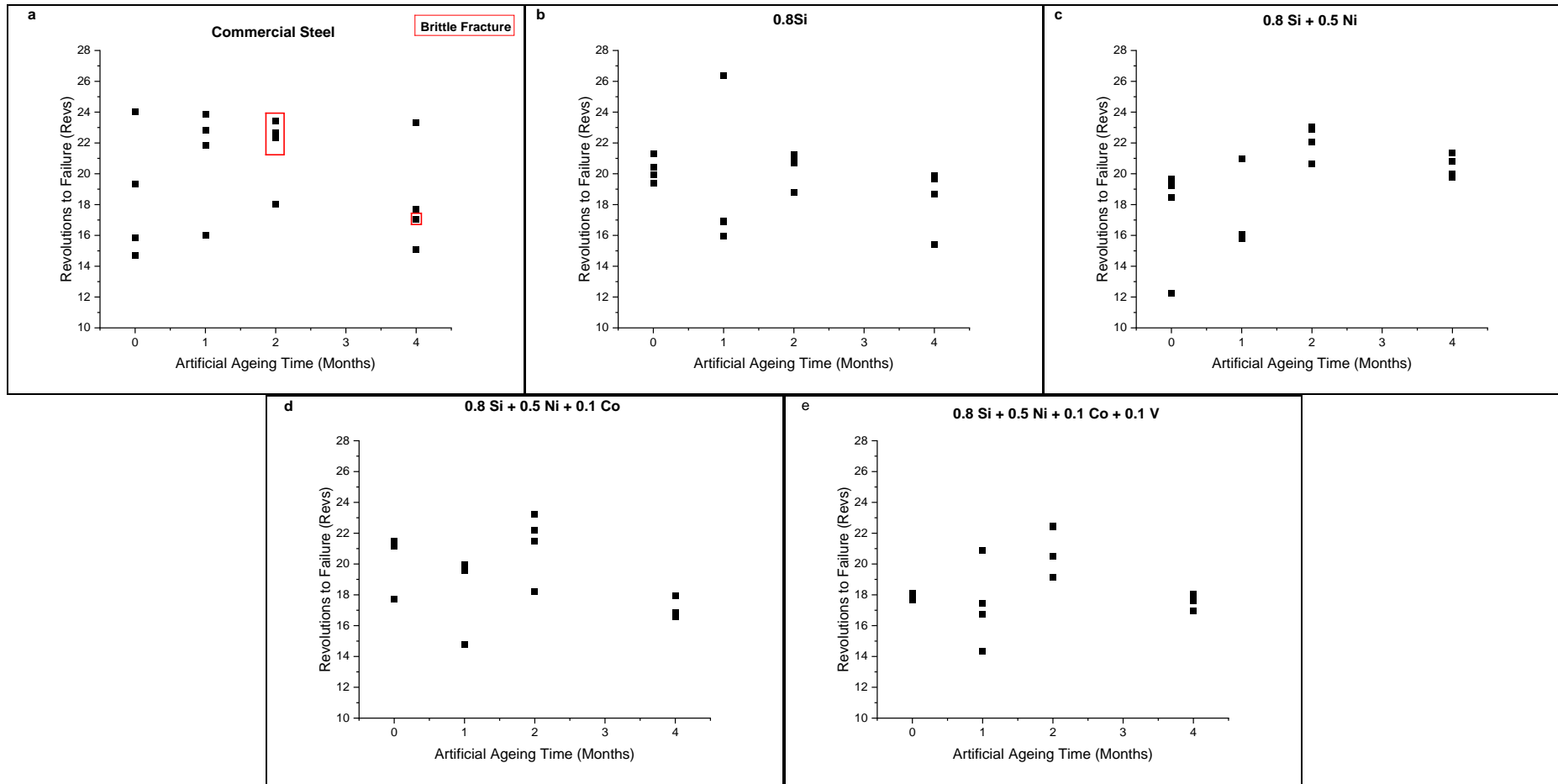


Figure 5:8 - Revolutions to failure data summary: a. Commercial Steel, b. Steel BJ3, c. Steel BJ4, d. Steel BJ5 and e. Steel BJ6.

5.2.2 Torsion Testing Results Summary

Table 5:7 – Torsion results for commercial steel.

Com. Steel	Revolutions to Failure (Revs)				Peak Torque (Nm)			
	AD	1M	2M	4M	AD	1M	2M	4M
Lower 95% CL	11.8	15.6	17.7	12.7	3.22	3.48	3.09	3.04
Mean	18.5	21.2	21.6	18.3	3.13	3.24	3.51	3.40
Upper 95% CL	25.2	26.8	25.5	23.9	3.31	3.72	3.93	3.76

Table 5:8 - Torsion results for 0.8Si steel.

BJ3	Revolutions to Failure (Revs)				Peak Torque (Nm)			
	AD	1M	2M	4M	AD	1M	2M	4M
Lower 95% CL	19.0	11.2	18.7	15.1	3.46	3.48	3.52	3.38
Mean	20.3	19.0	20.4	18.4	3.54	3.65	3.62	3.56
Upper 95% CL	21.5	26.9	22.2	21.7	3.61	3.81	3.73	3.73

Table 5:9 - Torsion results for 0.8Si + 0.5Ni steel.

BJ4	Revolutions to Failure (Revs)				Peak Torque (Nm)			
	AD	1M	2M	4M	AD	1M	2M	4M
Lower 95% CL	11.9	13.2	20.4	19.3	3.35	3.43	3.19	3.20
Mean	17.4	17.2	22.2	20.5	3.45	3.52	3.45	3.46
Upper 95% CL	22.9	21.2	23.9	21.7	3.56	3.61	3.70	3.71

Table 5:10 - Torsion results for 0.8Si + 0.5Ni + 0.1Co steel.

BJ5	Revolutions to Failure (Revs)				Peak Torque (Nm)			
	AD	1M	2M	4M	AD	1M	2M	4M
Lower 95% CL	17.6	12.7	17.8	16.1	3.16	3.57	3.18	3.43
Mean	20.4	17.3	21.3	17.0	3.37	3.72	3.43	3.55
Upper 95% CL	23.3	21.9	24.8	18.0	3.59	3.87	3.69	3.67

Table 5:11 - Torsion results for 0.8Si + 0.5Ni + 0.1Co + 0.1V

BJ6	Revolutions to Failure (Revs)				Peak Torque (Nm)			
	AD	1M	2M	4M	AD	1M	2M	4M
Lower 95% CL	17.5	13.1	18.6	16.9	3.28	3.27	3.41	3.24
Mean	17.9	17.4	21.1	17.6	3.46	3.48	3.59	3.44
Upper 95% CL	18.2	21.6	23.7	18.4	3.64	3.68	3.77	3.65

It is worth noting, the torque cell of the torsion machine was out of calibration, therefore the tabulated values in Table 5:7 to Table 5:11 are only suitable for comparison between results within this study. Figure 5:7 and Figure 5:8 shows the mean revolutions to failure with 95% confidence limits and test data, respectively. Generally, the variation is higher than observed in tensile results. This is expected as torsion testing is susceptible to surface defects of a wire, as the outermost regions of the wire will experience more deformation than the centre. To account for this, four torsion tests were completed per ageing condition. However, more repeats would be recommended for future studies. Figure 5:7 shows variation is predominantly too large to identify distinct trends with artificial ageing time. The exception in this case is in steel BJ6, Figure 5:7e, where there is no overlap of the 95% confidence limits, showing a decrease in revolutions to fracture between 2 and 4 month artificial ageing.

The most distinct differences observed during torsion testing was brittle fractures of the commercial steel in the 2 and 4 month artificial ageing condition, although it was not possible to ascertain if a corresponding reduction in the number of revolutions to fracture accompanied the brittle fractures, as would be anticipated. 75% of tests in the 2 month artificial ageing condition failed with type C brittle fractures (Figure 9:52). 25% of the tests in the 4 month artificial ageing condition failed with brittle type C fractures (Figure 9:54). The reduction in brittle fractures suggest the softening of the microstructure is underway. Torsion tests with brittle fractures are highlighted in Figure 5:8a.

Whilst there are several factors which can cause the premature failure of wires during wire drawing and testing, the embrittlement of the length of a torsion test sample is likely due to strain ageing. Carbon segregation, non-metallic inclusions and surface damage can all lead to wire breakages. Proeutectoid ferrite can act as reservoirs for free C/N which can cause a weak spot in a more ductile matrix. However, the aforementioned factors do not cause several brittle type C fractures across the length of a torsion sample as observed in Figure 9:52 and Figure 9:54. For example, a typical wire failure due to an inclusion is shown below in Figure 5:9. Inclusions act as crack initiation sites but are not likely to result in several brittle fractures across the length of a torsion test, as observed in the commercial steel, in the 2 month ageing condition.

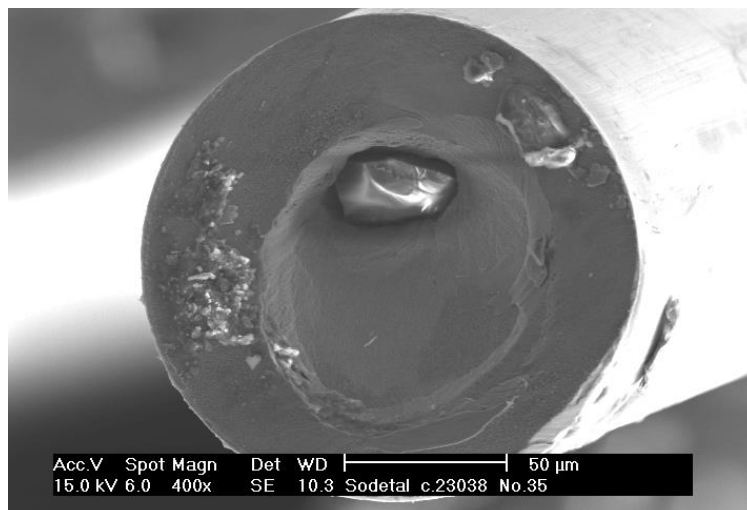


Figure 5:9 - Typical wire breakage caused by a non-metallic inclusion [68].

High sulphur content can lead to brittle type C fractures. However, for tyre cord grades as used in this study, customers impose very strict limits on sulphur levels. The sulphur levels are monitored, and the cast analysis showed sulphur levels were 0.0016.wt%. These sulphur levels are within spec (<0.02wt.%), and therefore high sulphur content is unlikely to be the cause of the brittle fractures. Carbon segregation would have to be severe to result in the

entire length of several torsion samples failing in a brittle type C fractures. Carbon segregation is tightly controlled and monitored during production, and is therefore unlikely to be responsible.

5.3 Magnetic Sensors

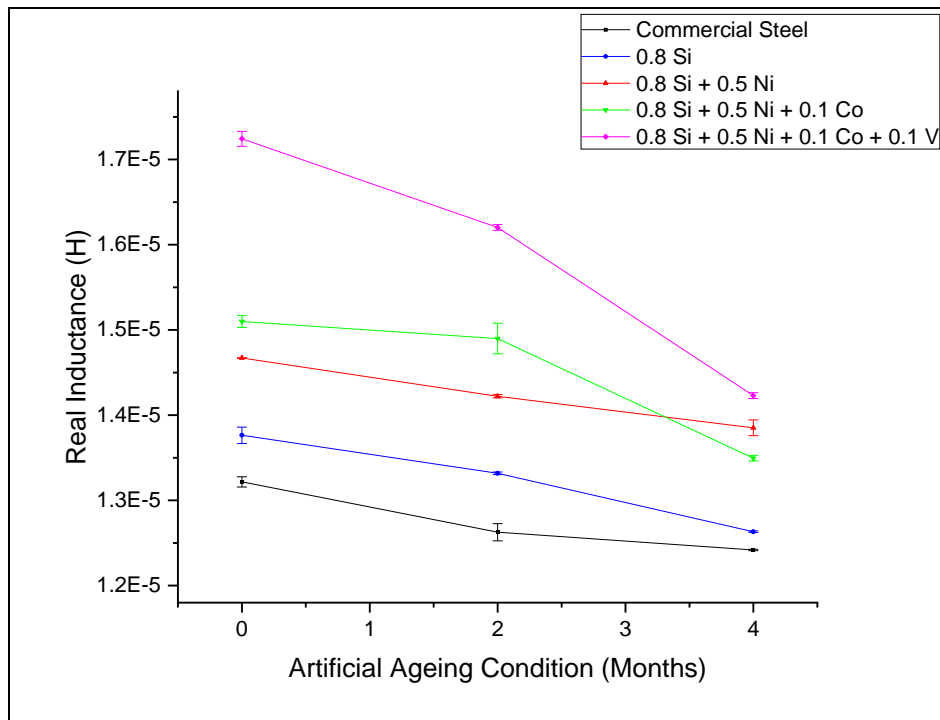


Figure 5:10 - Real inductance measured at a frequency of 100Hz [73].

Magnetic measurements were taken on 3 samples per ageing condition, per steel composition, and the variation is very low compared to the mechanical testing. The repeatability of this technique makes it an effective non-destructive global testing method.

The magnetic properties (real inductance) of the wires will be influenced by the ferrite phase within the pearlite and as such will be controlled by both the pearlitic interlamellar spacing and the alloy content. The onset of cementite dissolution during static strain ageing will feed carbon into the ferrite, thereby potentially altering its magnetic response by increasing the amount of carbon in solid solution within this phase and also by increasing the amount of ferrite, a consequence of the cementite dissolution process.

The measured real inductance variations can be interpreted as being due to the carbon depletion in cementite lamellar which results in the carbon super saturation of the ferrite phase, the subsequent pinning of dislocations by carbon atoms decreasing the mean free path for domain wall motion and pinning the domain walls. As well as the above-mentioned factors, precipitates can affect the real inductance (i.e. magnetic property) since precipitates can also act as pinning points, hence decreasing the real inductance.

Figure 5:10 shows the commercial steel and steel BJ4 exhibit a similar, slight increase in gradient in the two months artificial ageing condition. A clear difference is observed in the change of inductance in steels BJ3, BJ5 and BJ6, which show a reduction in gradient by the four month artificial ageing condition. Steel BJ6 appears to have the largest reduction in real inductance with artificial ageing time. Maejima concluded vanadium carbides can be formed by ageing precipitation during heat treatments [63]. As the wires samples were artificially aged, vanadium precipitates have likely been precipitated. Therefore, the significantly larger real inductance measured in steel BJ6 is likely due to vanadium precipitates, which can also pin magnetic domain walls, decreasing the real inductance.

Diffusion of alloy elements into the ferrite during the ageing process may also be a contributing factor, although further work would be required to demonstrate this. The inductance of the commercial steel, BJ3, BJ4 and BJ5 incrementally increased with alloying content, as expected. However, a significantly larger real inductance was measured in steel BJ6. This is potentially due to the presence of vanadium precipitates and/or relocation of vanadium.

5.4 Differential Scanning Calorimetry

DSC scan data is presented in Appendix - 9.4 Differential Scanning Calorimetry Data. This section presents a summary of DSC data for comparison between compositions.

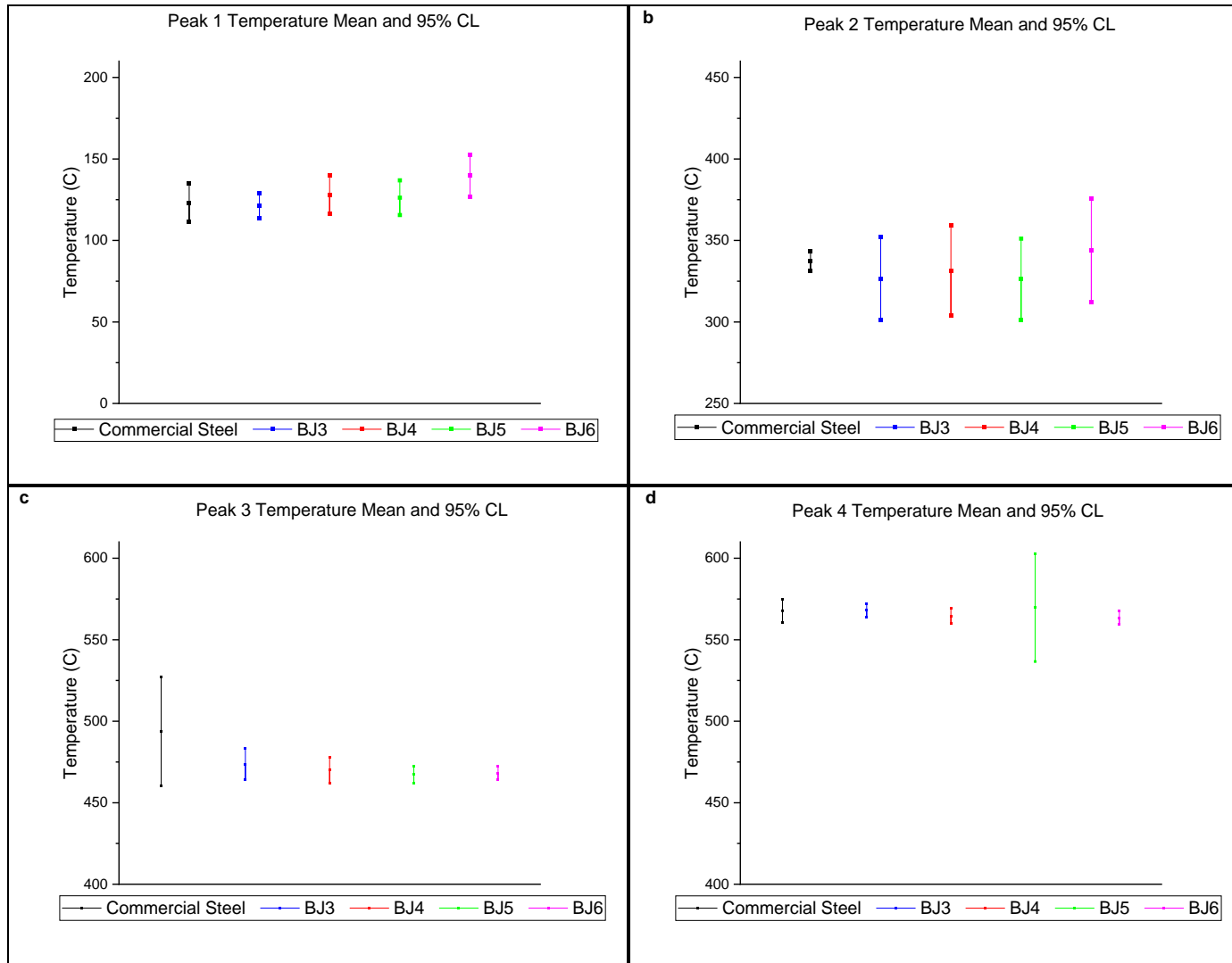


Figure 5:11 - DSC mean peak temperatures with 95% confidence limits: a. Peak 1, b. Peak 2, c. Peak 3 and d. Peak 4.

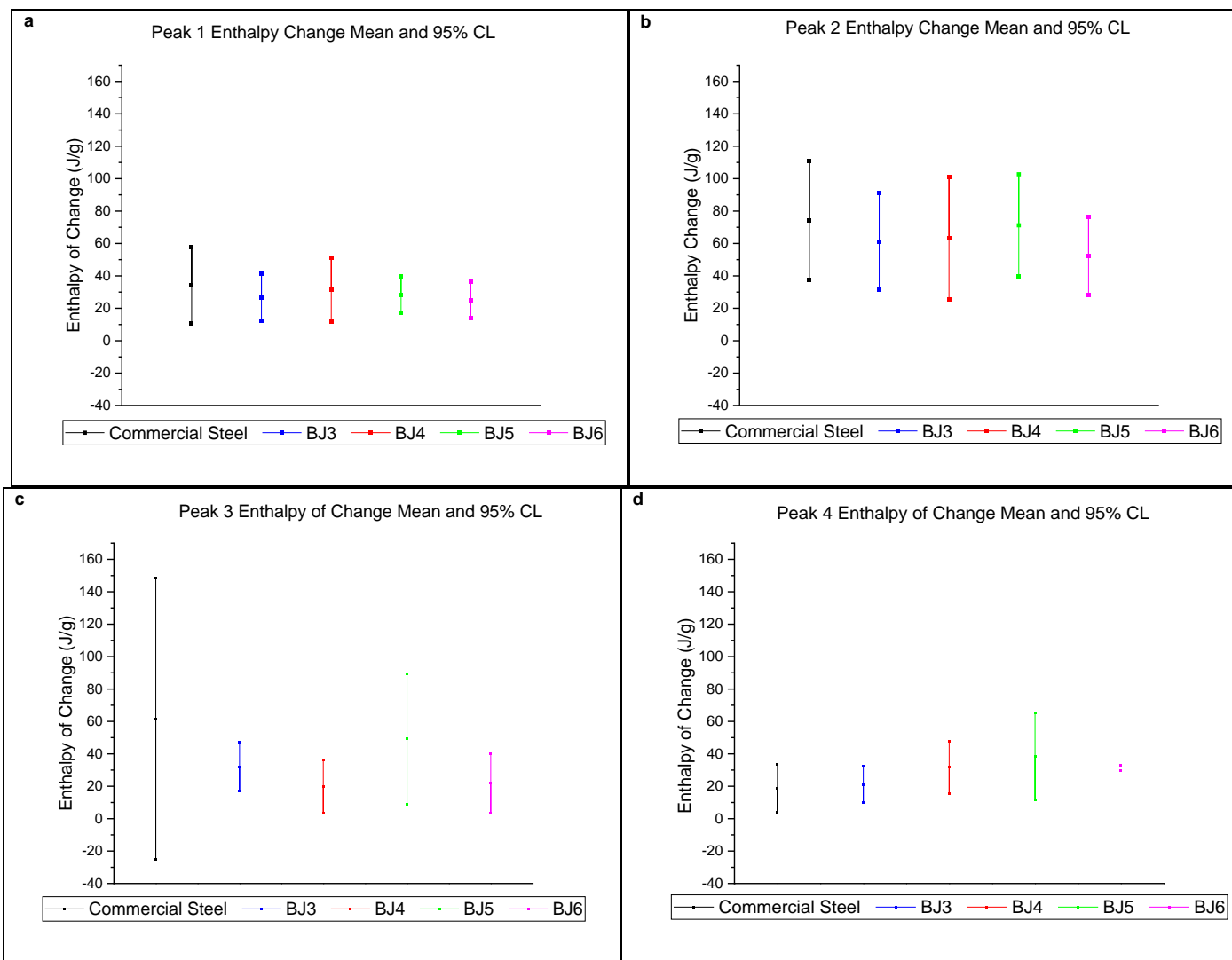


Figure 5:12 - DSC mean peak enthalpy of change with 95% confidence limits: a. Peak 1, b. Peak 2, c. Peak 3 and d. Peak 4.

Table 5:12 - DSC Peak 1-4 data summary.

Steel Composition (wt.%)	Mean Peak 1 Temperature (°C)	Mean Peak 1 ΔH (J/g) (exothermic Positive)	Mean Peak 2 Temperature (°C)	Mean Peak 2 ΔH (J/g) (exothermic)	Mean Peak 3 Temperature (°C)	Mean Peak 3 ΔH (J/g) (exothermic)	Mean Peak 4 Temperature (°C)	Mean Peak 4 ΔH (J/g) (exothermic)
Commercial Steel	123.1	34.0	337.4	74.1	493.8	61.7	567.8	19.0
0.8Si	121.5	26.6	326.7	61.3	473.6	32.0	568.2	21.1
0.8Si + 0.5 Ni	128.0	31.4	331.6	63.3	470.0	20.0	564.6	31.7
0.8Si + 0.5 Ni + 0.1Co	126.2	28.3	326.1	71.2	467.4	49.4	569.6	38.5
0.8Si + 0.5 Ni + 0.1Co + 0.1V	139.7	25.1	344.1	52.2	468.4	21.9	563.5	29.6

5.4.1 Differential Scanning Calorimetry Results Summary

The first three exothermic events, termed the stages of strain ageing within the literature, were consistently identified throughout analysis. A fourth exothermic event was identified in all samples from steels BJ3 and BJ4, yet not in the commercial steel and steels BJ5 and BJ6. Table 9:55, Table 9:58 and Table 9:59 show samples which did not contain a fourth peak. The first exothermic peak occurred around 130°C, the second around 330°C, the third around 470°C and the fourth at around 570°C. This is within 30 °C observed across the literature [1][23][24]. The variation of the measured temperatures within the literature is likely due to the variety of analysis techniques and steel compositions. It is worth noting that the first exothermic peak of steels BJ4, BJ5 and BJ6 appears to consist of two exothermic events which can be seen in Figure 9:89, Figure 9:90 and Figure 9:91 respectively. The initial peak occurs consistently throughout all compositions at 130 °C, is consistent with literature.

5.5 Micrographs

Samples of the commercial steel, steels BJ5 and BJ6 were imaged in the 4 months artificial ageing condition. BJ3 and BJ4 were not imaged due to time constrains. Each STEM micrograph is presented with its corresponding HAADF and dark field micrograph for comparison. Electropolishing was completed by Dr Peng Gong and STEM imaging was completed by Dr John Nutter. Samples were frozen for 18 months prior to testing.

5.5.1 Commercial Steel

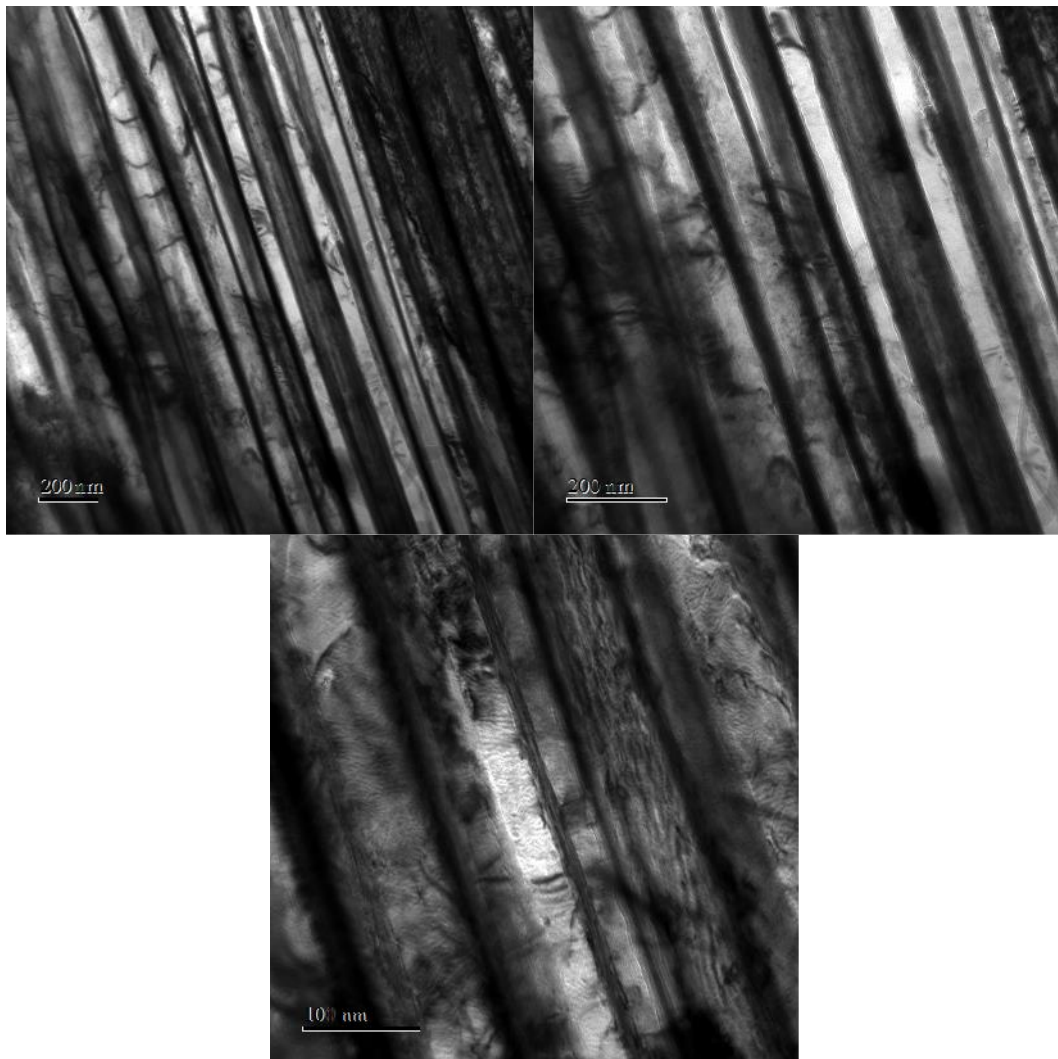


Figure 5:13 - Brightfield TEM: Commercial steel, 4 month artificial ageing condition 30k, 50k and 120k magnification.

Figure 5:13a shows the microstructure of the commercial steel in the 4 month artificial ageing condition. Lamellae morphology appears relatively homogenous. However, with increasing magnification, shown in Figure 5:13b and Figure 5:13c, cementite lamellae become less distinct.

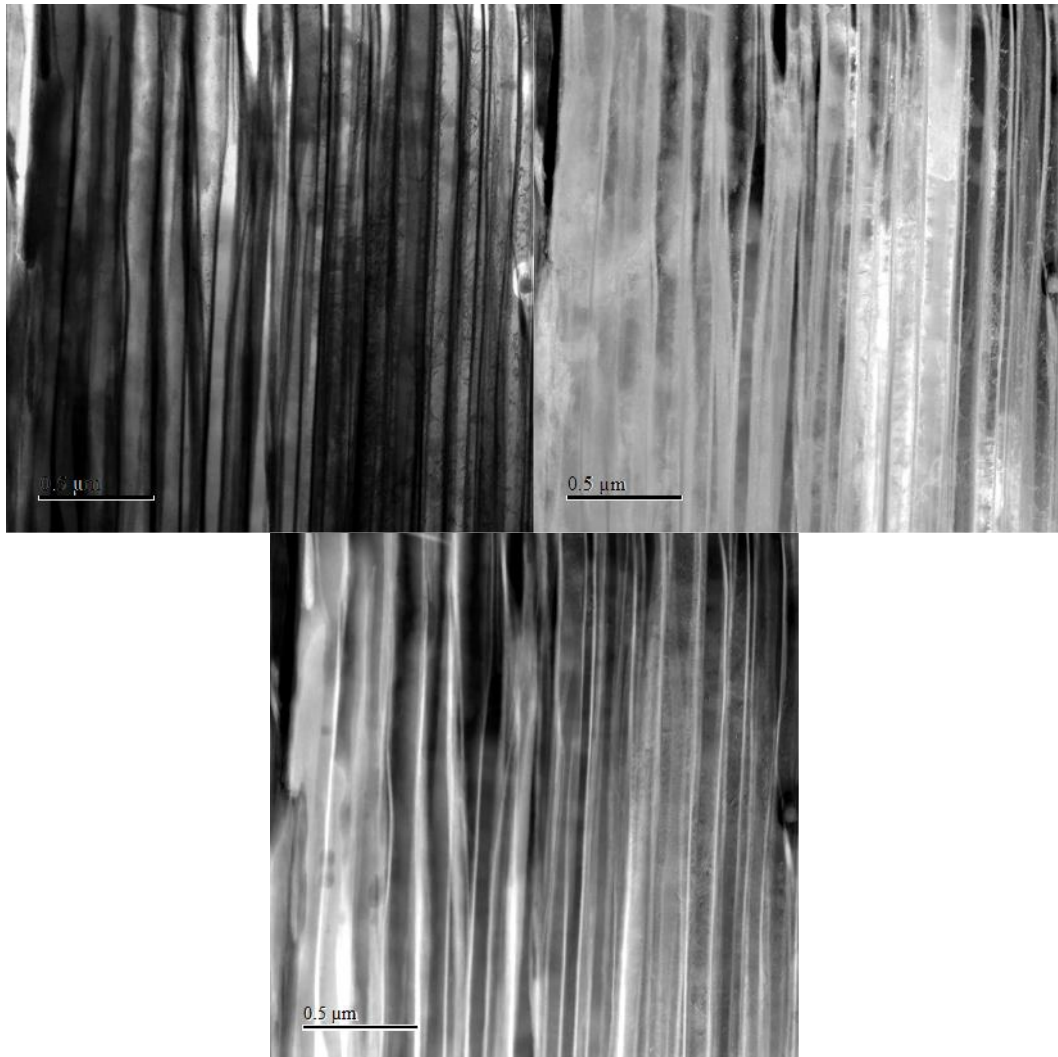


Figure 5:14 - Commercial Steel, 4 month artificial ageing condition at 100k magnification: STEM Bright field, STEM HAADF and STEM Dark field. Scale bar = $0.5\mu m$.

Figure 5:14a shows a higher density of dislocations on the right hand side of the image, with the left hand side appearing entirely free from dislocations. No distinct regions of cementite dissolution can be confirmed without an as draw sample for comparison. Lamellae appear relatively distinct and homogeneous.

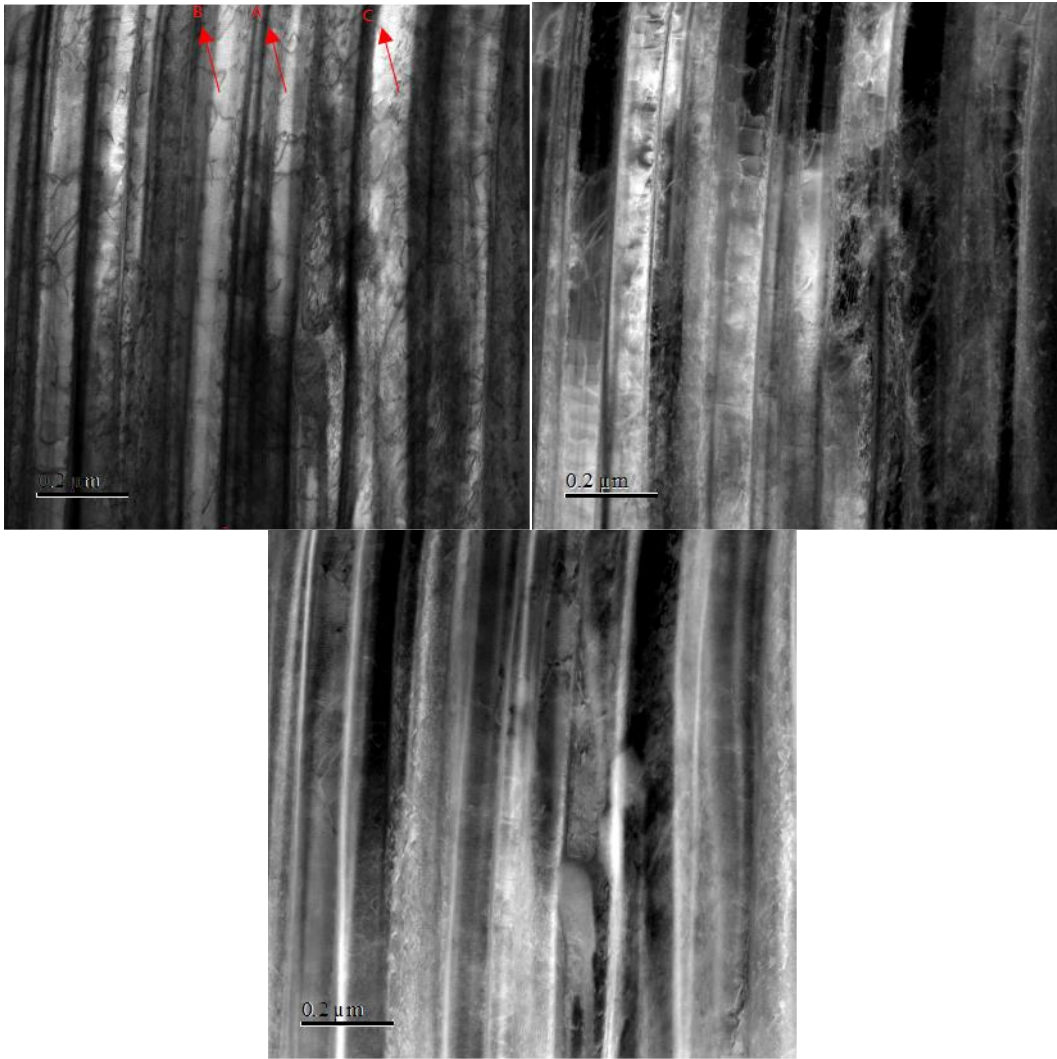


Figure 5:15 - Commercial Steel, 4 month artificial ageing condition at 200k magnification: STEM Bright field, STEM HAADF and STEM Dark field. Scale bar = $0.2\mu m$.

Figure 5:15 shows a higher magnification image of the dislocation structures identified in Figure 5:14. At higher magnifications, dislocation structures become apparent. In Figure 5:15.a, cementite lamellar immediately to the right of the scale bar are significantly less distinct, with high dislocation densities present in this region. Figure 5:16 and Table 5:13 show cementite lamellae thickness measurements of cementite lamellae A, B and C labelled in Figure 5:15.

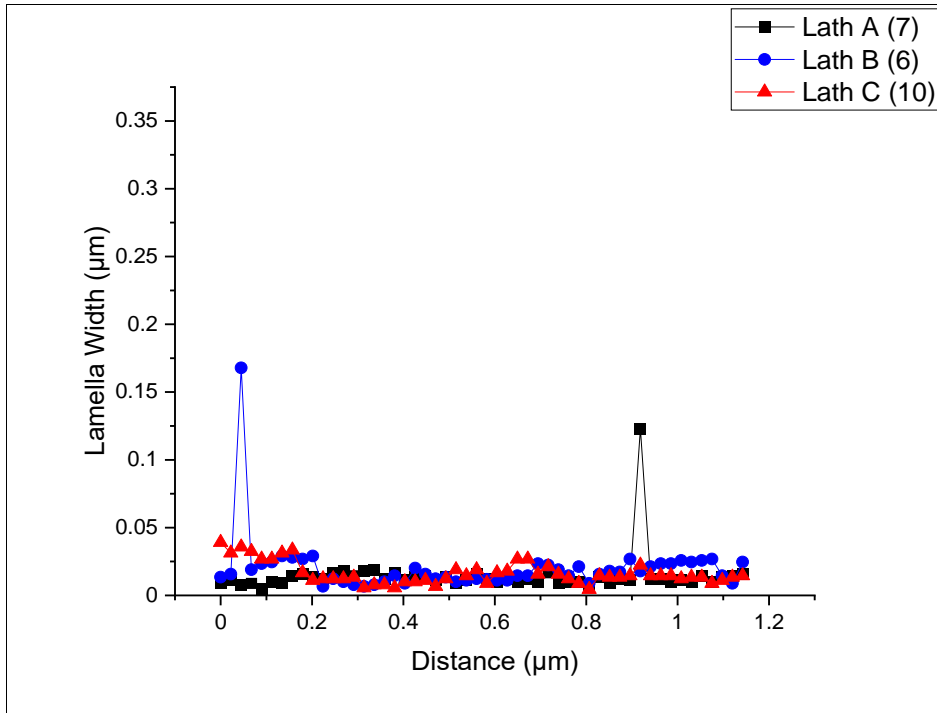


Figure 5:16 - Apparent cementite lamellae thickness measurements.

Table 5:13 - Apparent cementite lamellae thickness values.

	Mean Apparent Lamellar thickness (μm)	Standard Deviation (μm)	Lower 95% CL of Mean (μm)	Upper 95% CI of Mean (μm)	Coefficient of Variation
Lamellar A	0.014	0.016	0.010	0.019	1.094
Lamellar B	0.020	0.022	0.014	0.026	1.091
Lamellar C	0.016	0.008	0.014	0.019	0.509

5.5.2 0.8Si + 0.5Ni + 0.1Co Steel BJ5

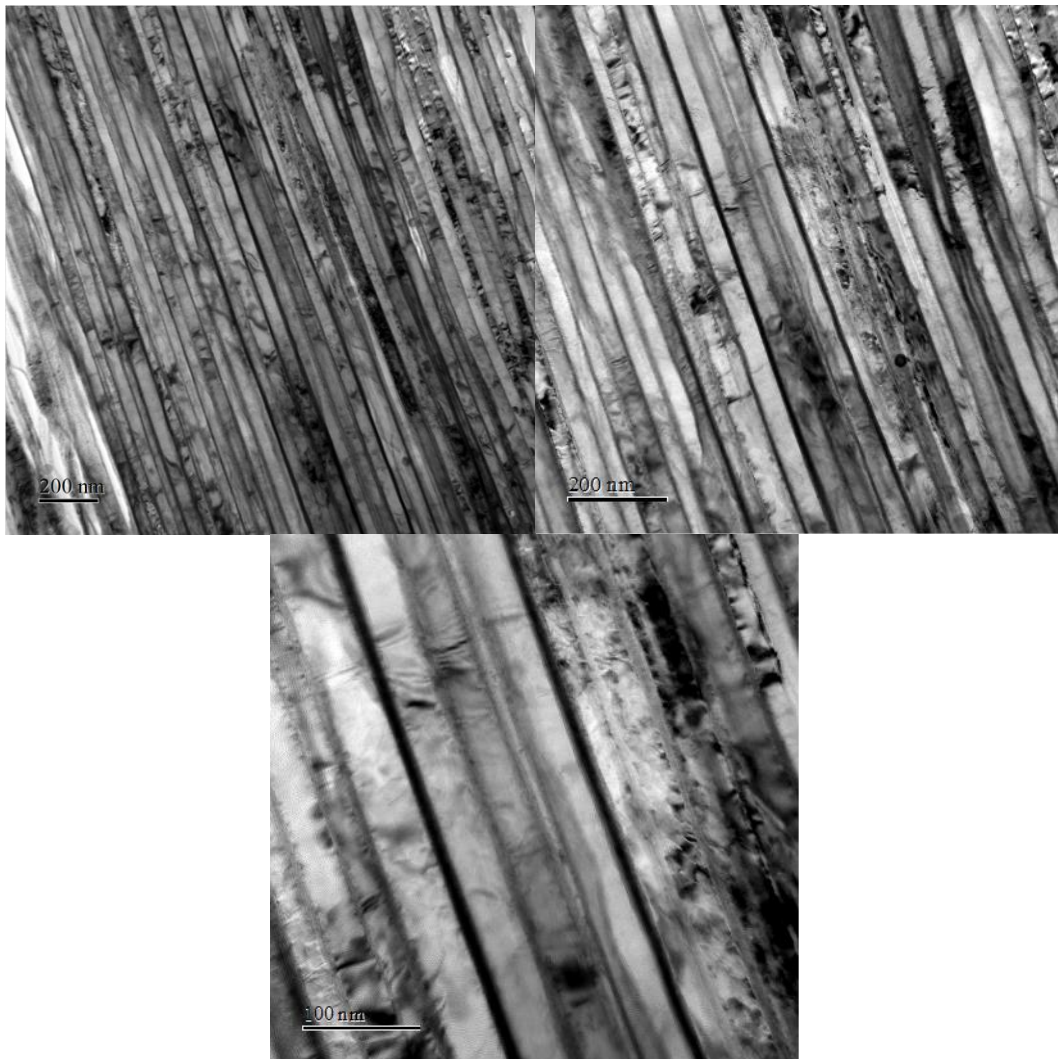


Figure 5:17 - Brightfield TEM: Steel BJ5, 4 month artificial ageing condition 30k, 50k and 120k magnification.

Figure 5:17a depicts relatively homogenous and distinct cementite lamellae. With increasing magnification, as shown in Figure 5:17b and Figure 5:17c, lath morphology becomes less distinct.

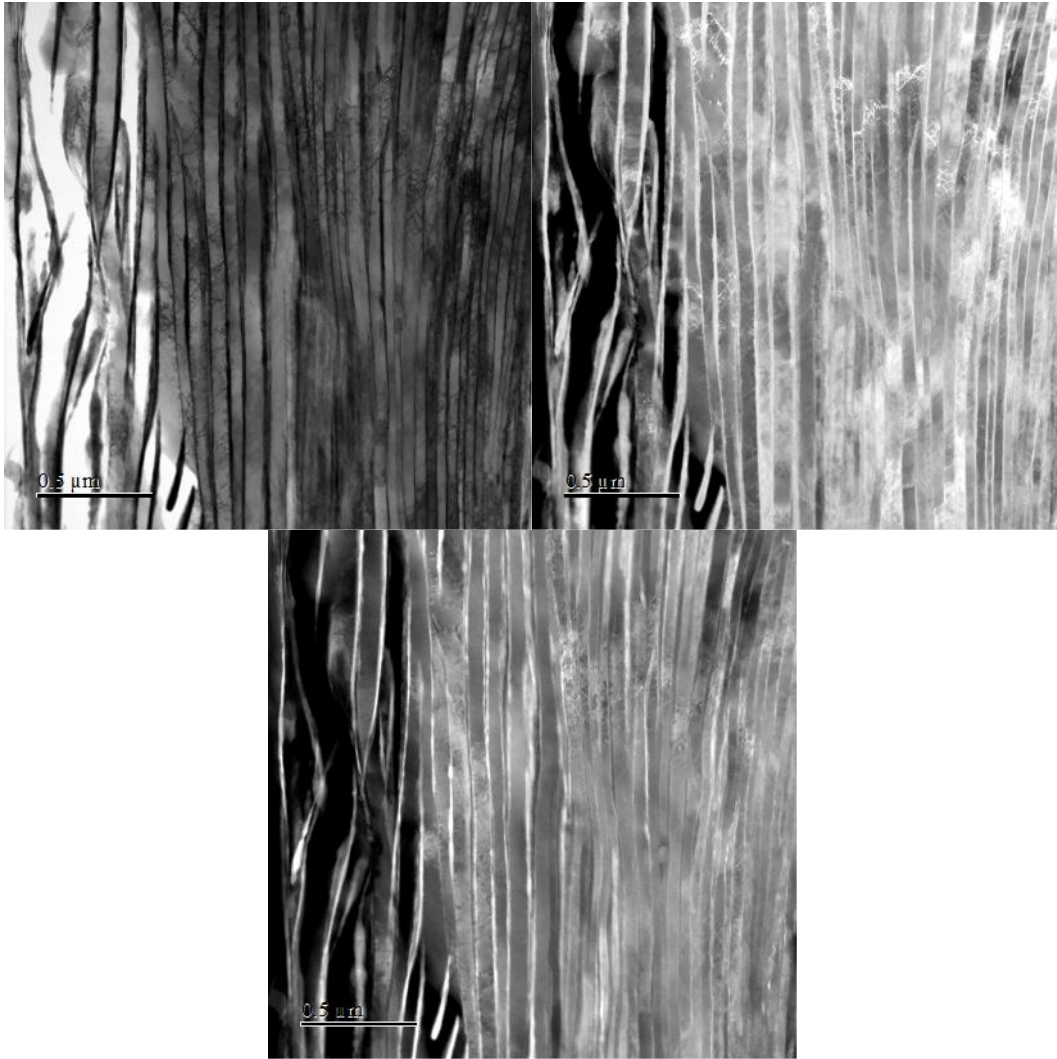


Figure 5:18 - Steel BJ5 4 month artificial ageing condition at 100k magnification: STEM Bright field, STEM HAADF and STEM Dark field. Scale Bar $0.5\mu\text{m}$.

Figure 5:18 also shows a relatively homogeneous microstructure with regions of higher dislocation density. The deformed lamellae on the left of the image is due to the region of the microstructure being adjacent to the hole generated during electropolishing, this region is susceptible to deformation during the transportation and storage of samples.

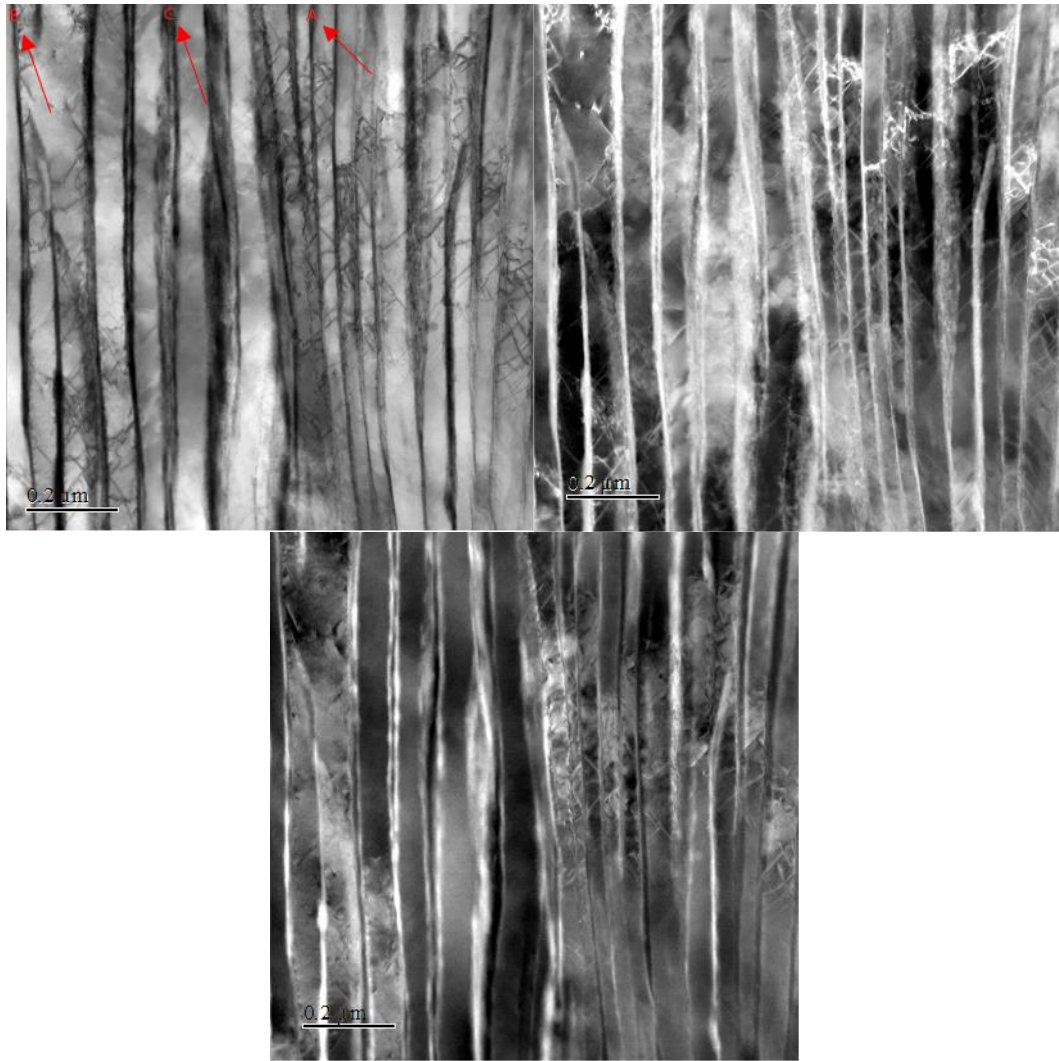


Figure 5:19 - Steel BJ5 4 month artificial ageing condition at 200k magnification: STEM Bright field, STEM HAADF and STEM Dark field. Scale bar $0.2\mu\text{m}$

Figure 5:19 shows higher magnification images of the region with increased dislocation density shown in Figure 5:18. At 200k magnification cementite lamellae vary in thickness across the length of the image, with some regions a clear lamellae structure is no longer present. Figure 5:20 and Table 5:14 show cementite lamellae thickness measurements of cementite lamellae A, B and C labelled in Figure 5:19.

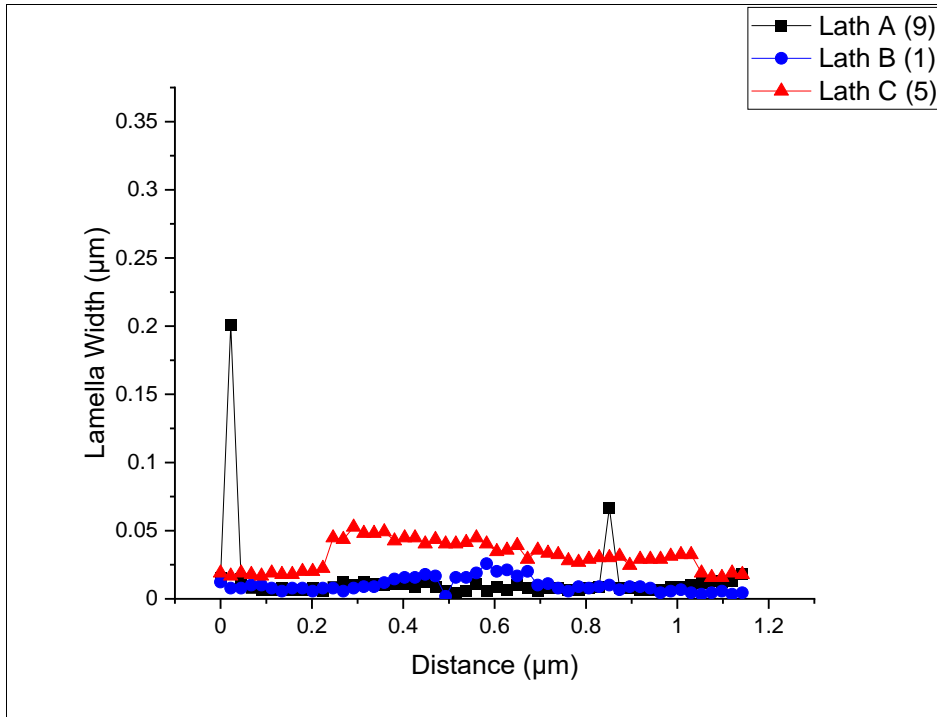


Figure 5:20 - Apparent cementite lamellae thickness measurements.

Table 5:14 - Apparent cementite lamellae thickness values.

	Mean Apparent Lamellar thickness (μm)	Standard Deviation (μm)	Lower 95% CL of Mean (μm)	Upper 95% CI of Mean (μm)	Coefficient of Variation
Lamellar A	0.014	0.028	0.006	0.022	2.004
Lamellar B	0.010	0.005	0.009	0.012	0.529
Lamellar C	0.031	0.011	0.028	0.034	0.342

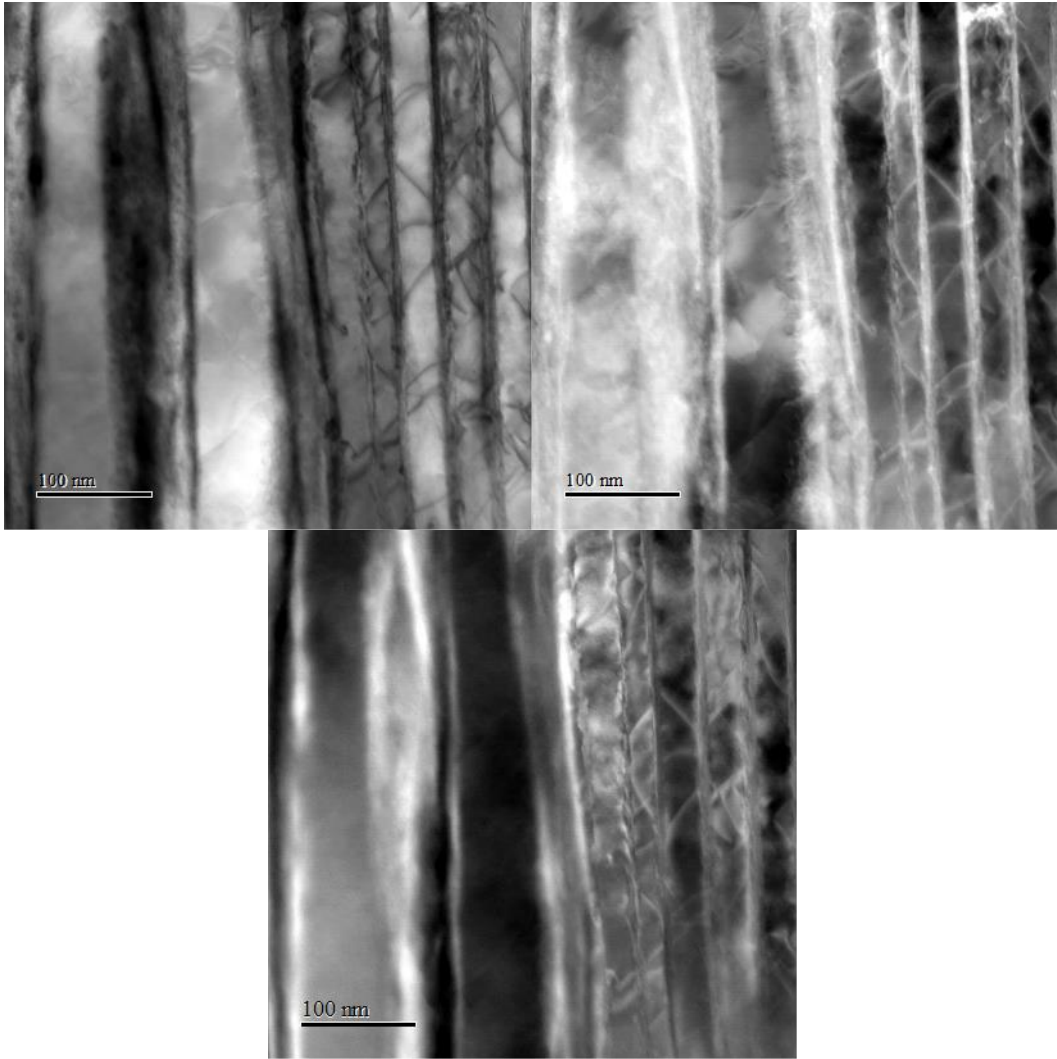


Figure 5:21 - Steel BJ5 4 month artificial ageing condition at 500k magnification: STEM Bright field, STEM HAADF and STEM Dark field.

Figure 5:21 shows the variation in lamellar thickness and morphology, suggesting cementite dissolution has occurred, however micrographs of the as drawn sample would be required to confirm this. The right half of Figure 5:21 shows a higher dislocation density is present where the lamellar appear the least distinct.

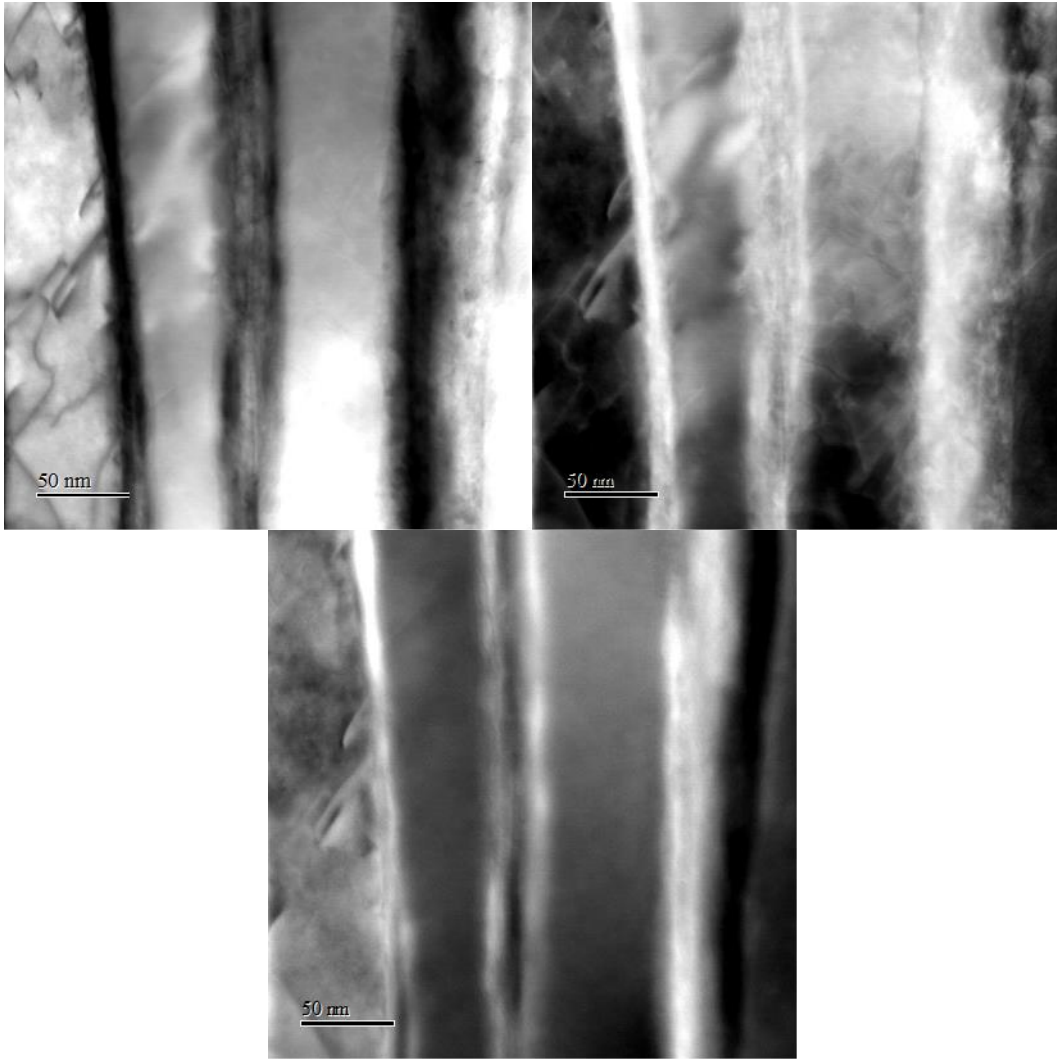


Figure 5:22 - Steel BJ5 4 month artificial ageing condition at 800k magnification: STEM Bright field, STEM HAADF and STEM Dark field.

Figure 5:22a shows three cementite lamellae, a dislocation structure is observed within the ferrite lamellar, parallel with the lamellar/drawing direction. The dislocations present in the adjacent ferrite lamellae can be observed more clearly in the HAADF image in Figure 5:22.

5.5.3 0.8Si + 0.5Ni + 0.1Co + 0.1V Steel BJ6

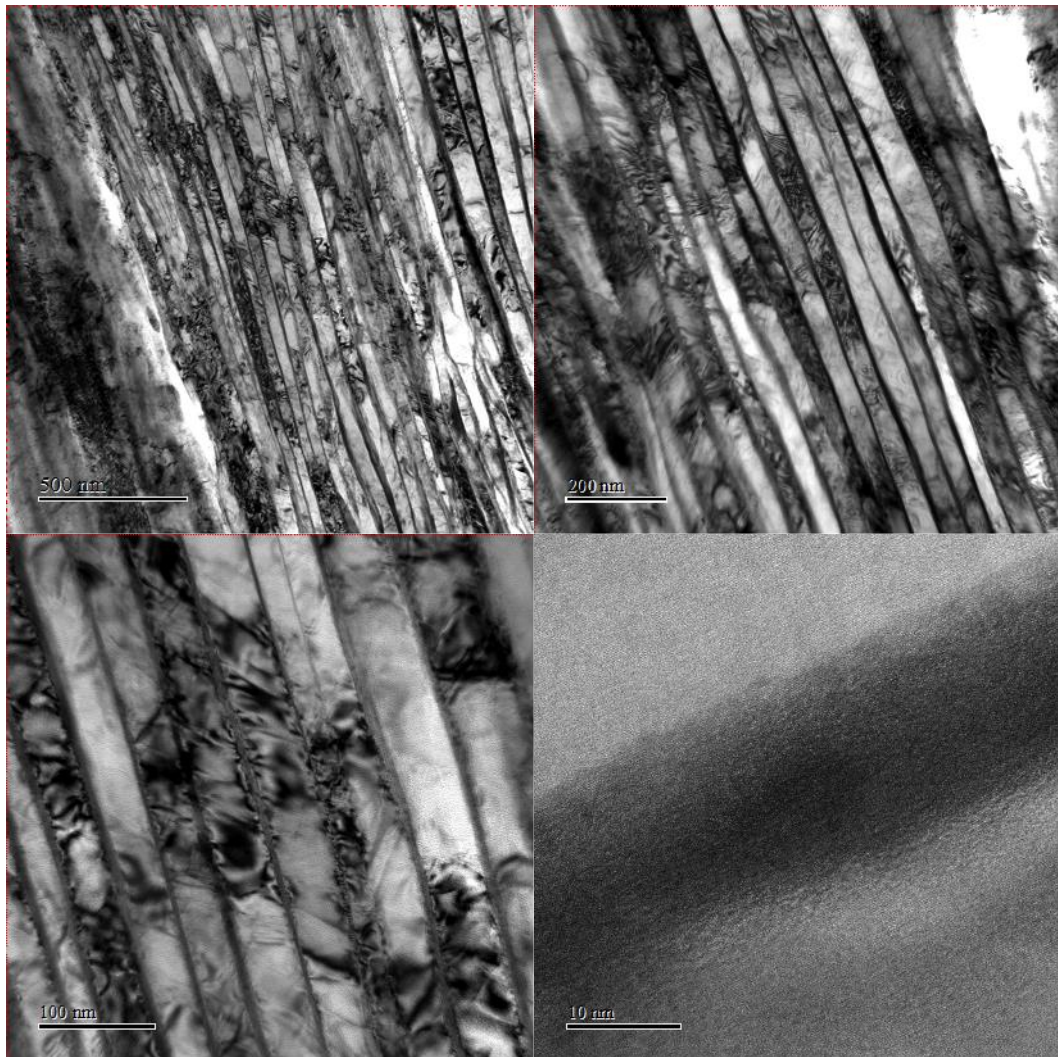


Figure 5:23 – Bright field TEM: Steel BJ5, 4 month artificial ageing condition 30k, 50k, 120k and 1.2M magnification.

Figure 5:23a shows the microstructure of steel BJ6 in the 4 month artificial ageing condition. Steel BJ6 appears notably less homogeneous than the commercial steel and steel BJ5. As with the commercial steel and steel BJ5, increased magnification shown in Figure 5:23b reveals regions of less distinct cementite lamellae.

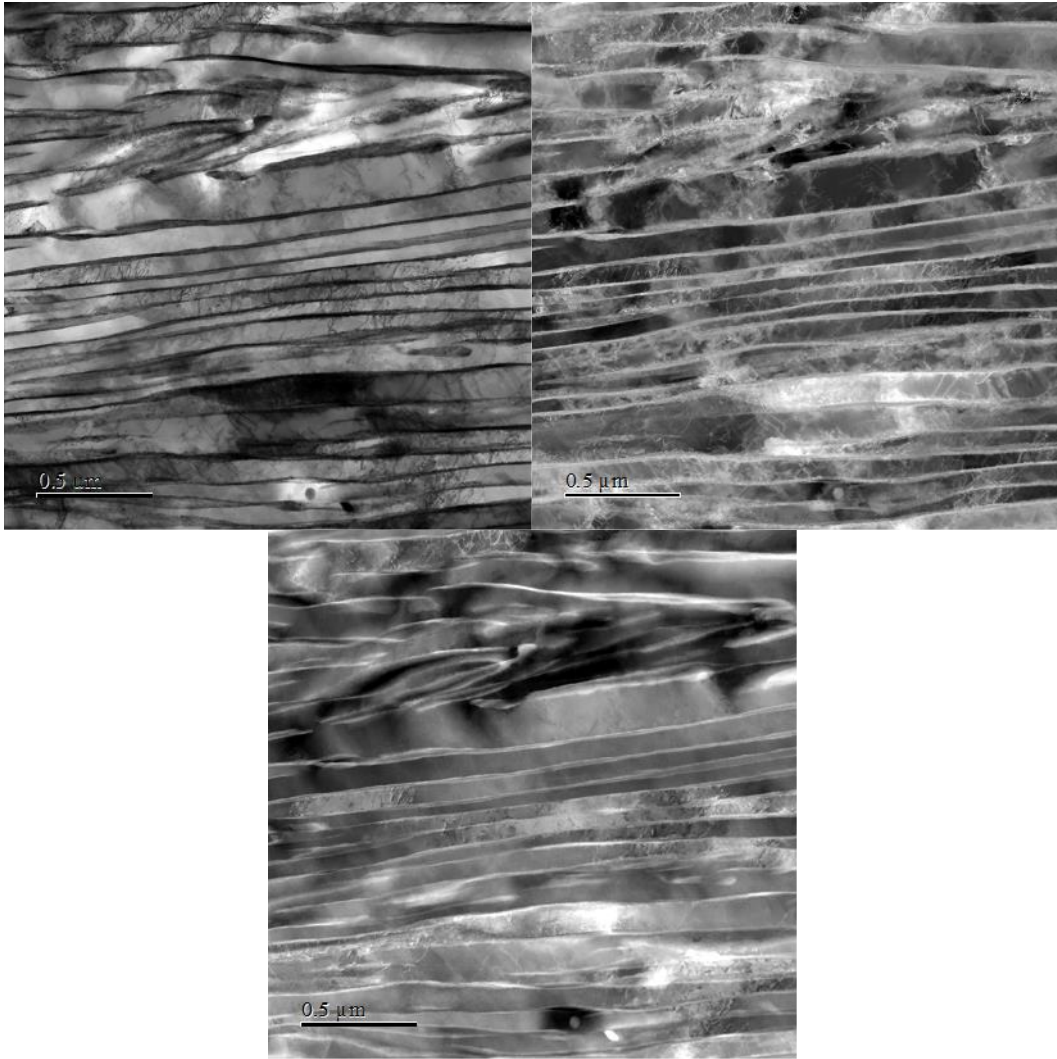


Figure 5:24 - Steel BJ6 4 month artificial ageing condition at 100k magnification: STEM Bright field, STEM HAADF and STEM Dark field. Scale bar is 0.5μm.

Bright field and HAADF STEM shown in Figure 5:24a and Figure 5:24b show regions of high dislocation density, with a less homogeneous lamellae structure in the upper region of the image.

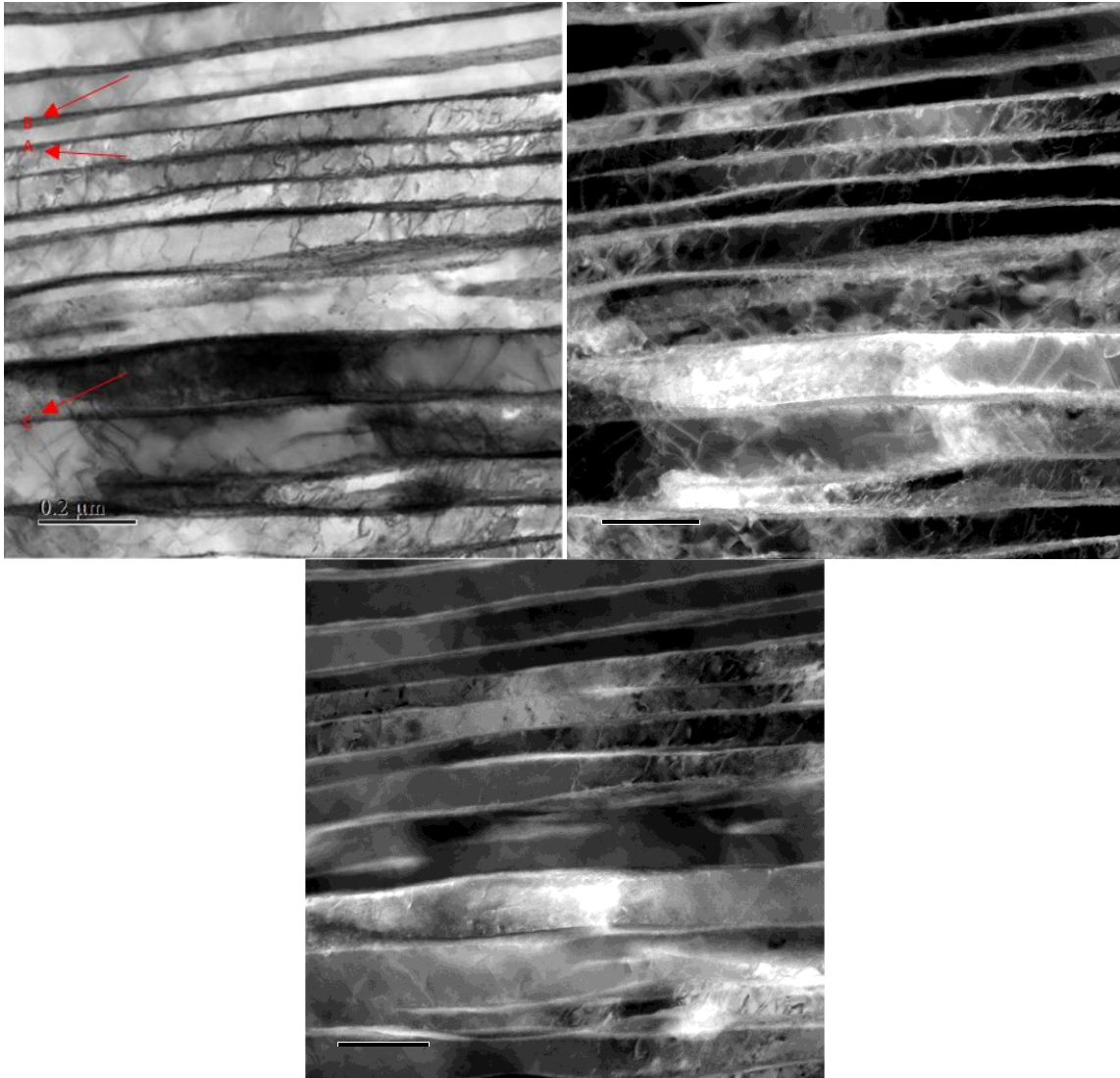


Figure 5:25 - Steel BJ6 4 month artificial ageing condition at 200k magnification: STEM Bright field, STEM HAADF and STEM Dark field.

Variation of cementite lamellae morphology shown in Figure 5:25 also suggests the presence of heterogeneous cementite dissolution, although micrographs of the as drawn microstructure would be necessary to confirm this. Lamellae in the upper region appear more distinct, with lamellae in the centre of the image showing the greatest variation in thickness. The HAADF image (Figure 5:25b) reveals dislocations throughout the microstructure. Figure 5:26 and Table 5:15 shows apparent cementite lamellae thickness measurements of cementite lamellae A, B and C labelled in Figure 5:25.

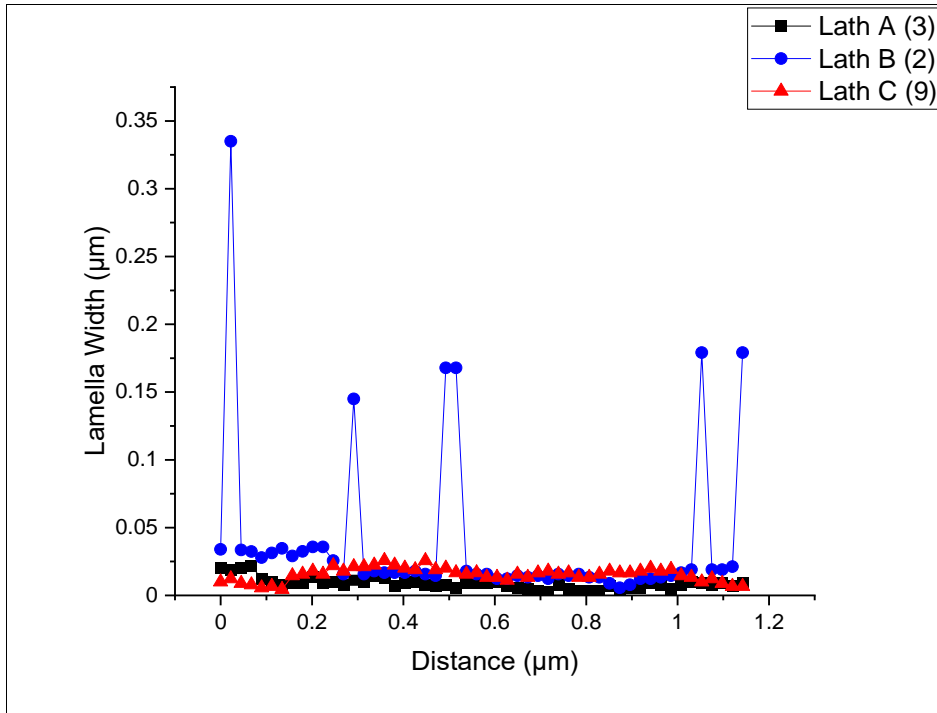


Figure 5:26 Apparent cementite lamellae thickness measurements.

Table 5:15 - Apparent cementite lamellae thickness measurement values.

	Mean Apparent Lamellar thickness (μm)	Standard Deviation (μm)	Lower 95% CL of Mean (μm)	Upper 95% CI of Mean (μm)	Coefficient of Variation
Lamellar A	0.009	0.004	0.008	0.010	0.489
Lamellar B	0.039	0.062	0.022	0.057	1.563
Lamellar C	0.015	0.005	0.014	0.017	0.326

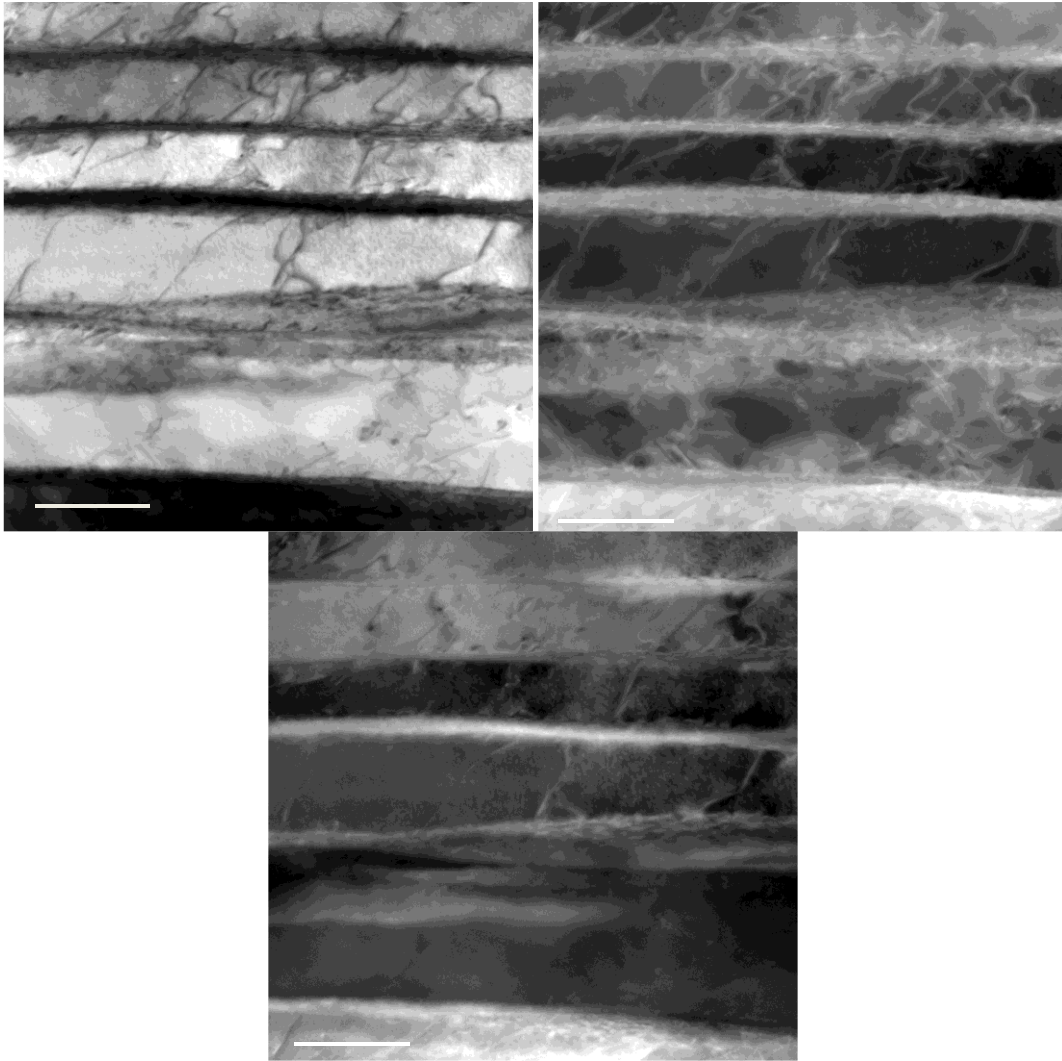


Figure 5:27 - Steel BJ5 4 month artificial ageing condition at 500k magnification: STEM Bright field, STEM HAADF and STEM Dark field

With an increased magnification of 500k, shown in Figure 5:27, dislocation structures can be seen within ferrite lamellae.

5.5.4 Cementite Lamellae Thickness Summary

Whilst the change in the coefficient of variance in cementite lamellae thickness is capable of assessing differences in apparent cementite lamellae morphology, this is not necessarily a measure of cementite dissolution. The data obtained in this study is limited, it was only

possible to measure three cementite lamellae per steel composition due to time constraints. Measurements were taken from samples in the 4 month artificial ageing condition. Significantly more measurements across several ageing conditions would be necessary to produce representative values. A summary of mean apparent cementite lamellae thickness is shown in Figure 5:28.

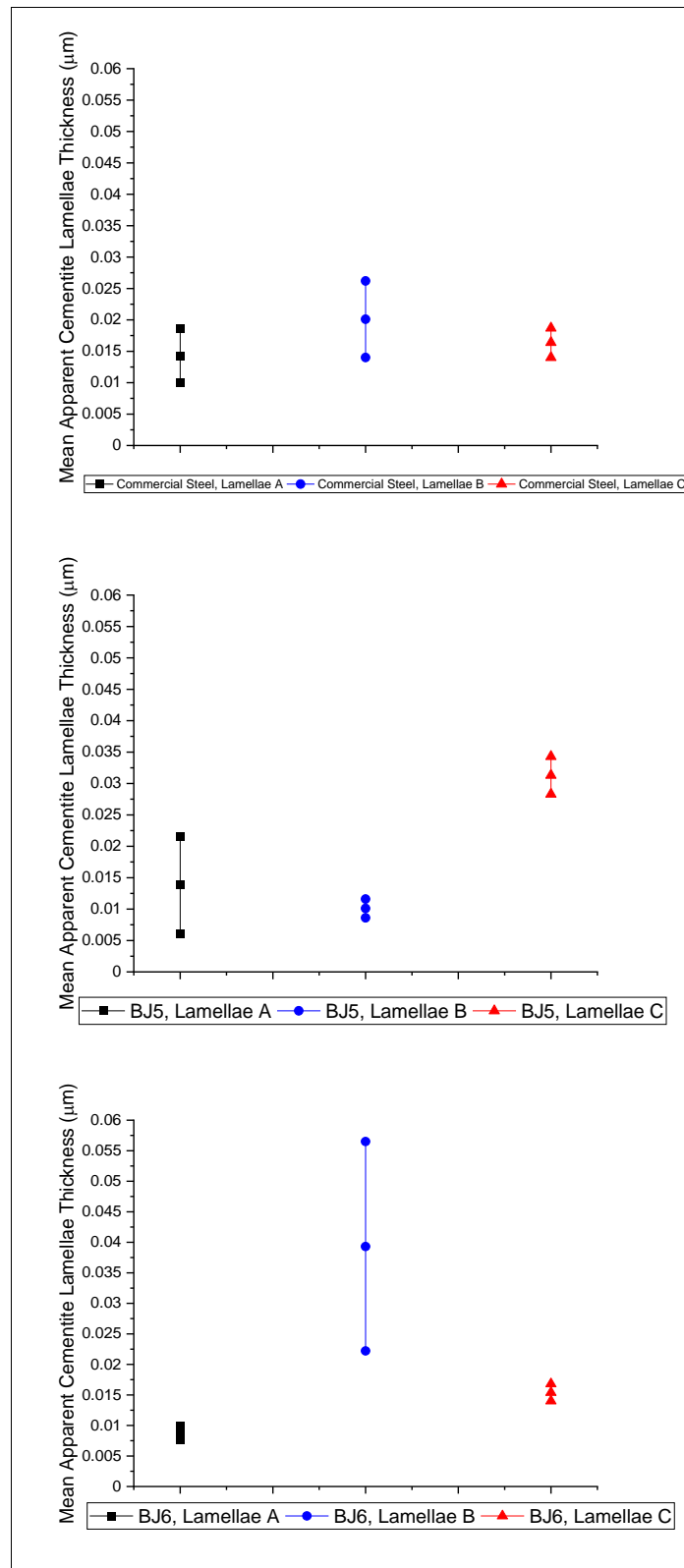


Figure 5:28 - Mean apparent cementite lamellae thickness with 95% confidence limits.

5.6 Chemical Analysis

5.6.1 STEM Energy Dispersive X-ray Spectroscopy

5.6.1.1 Commercial Steel

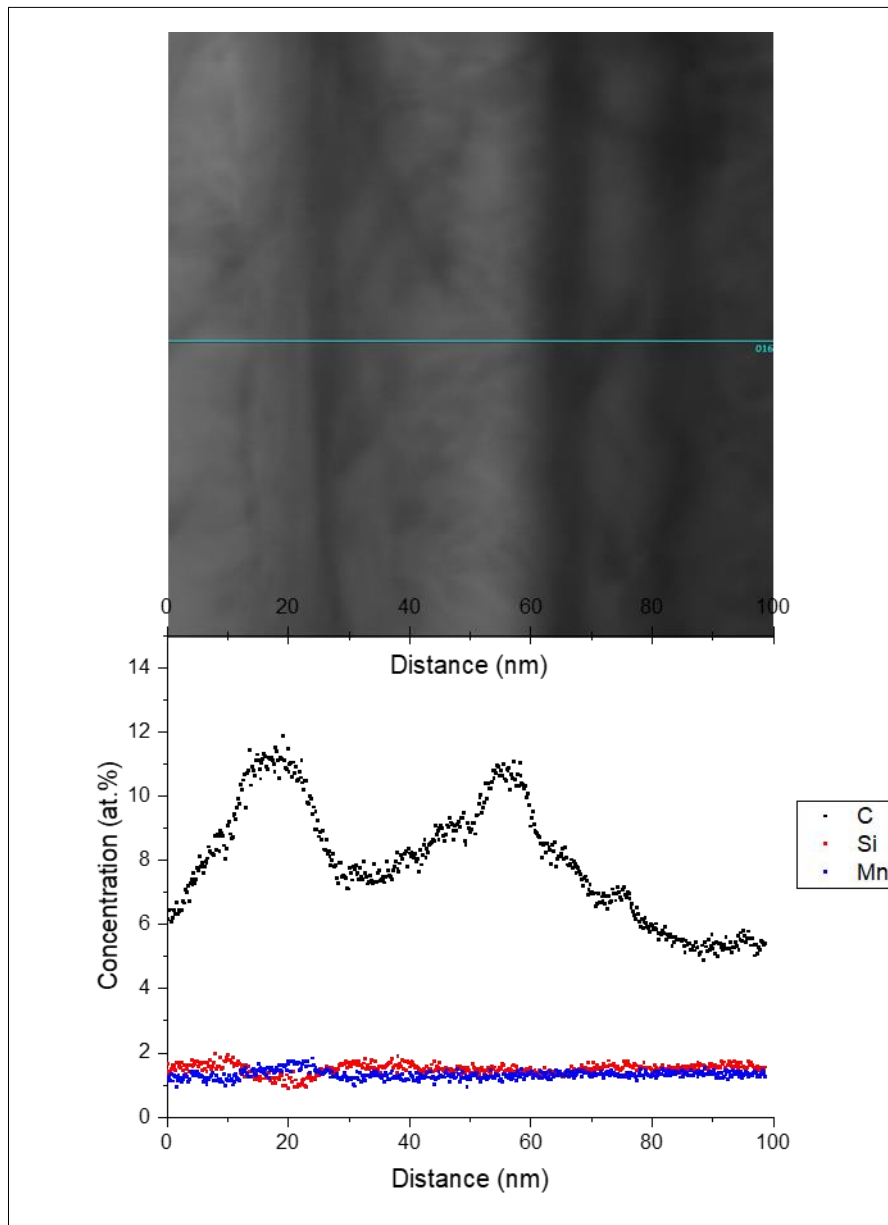


Figure 5:29 - Commercial Steel 4 month artificial ageing condition STEM HAADF - EDS Line Scan.

Figure 5:29 is an EDS Line scan showing two carbon peaks. Increased carbon concentrations peaking at around 11at. % carbon are observed at 20 and 60nm. The reduced silicon concentration and increased manganese concentration which occur in line with the first peak at 20nm suggest this is a cementite lamellar. Manganese and silicon levels for the initial cementite lamella are in agreement with atom probe data in section: 3.1 - British Steel R&D Study - Influence of Nickel on Pearlite Stability and 5.6.2.1 - Commercial Steel. However, for the second carbon peak at 60nm, there does not appear to be a distinct increase in manganese and reduction in silicon concentration, suggesting this may not be a cementite lamella. Another minor peak is observed at around 80nm, over what appears to be a dislocation in the corresponding micrograph of Figure 5:29. Therefore, carbon peaks at 60 and 80nm may be due to the segregation of carbon to dislocations. Although, the carbon content in the ferrite matrix is significantly higher than the solubility of carbon in iron, which is ~0.09 at. %, therefore, the observed peaks may be due to carbon contamination on the sample surface. The differences in composition between the lamellae may also be a sectioning effect. Note, the measured carbon concentration is significantly lower than stoichiometric cementite which has a carbon concentration of 25 at.%, but this is likely a result of X-ray absorption, which is a well known problem for light elements.

5.6.1.2 0.8Si + 0.5Ni + 0.1Co Steel BJ5

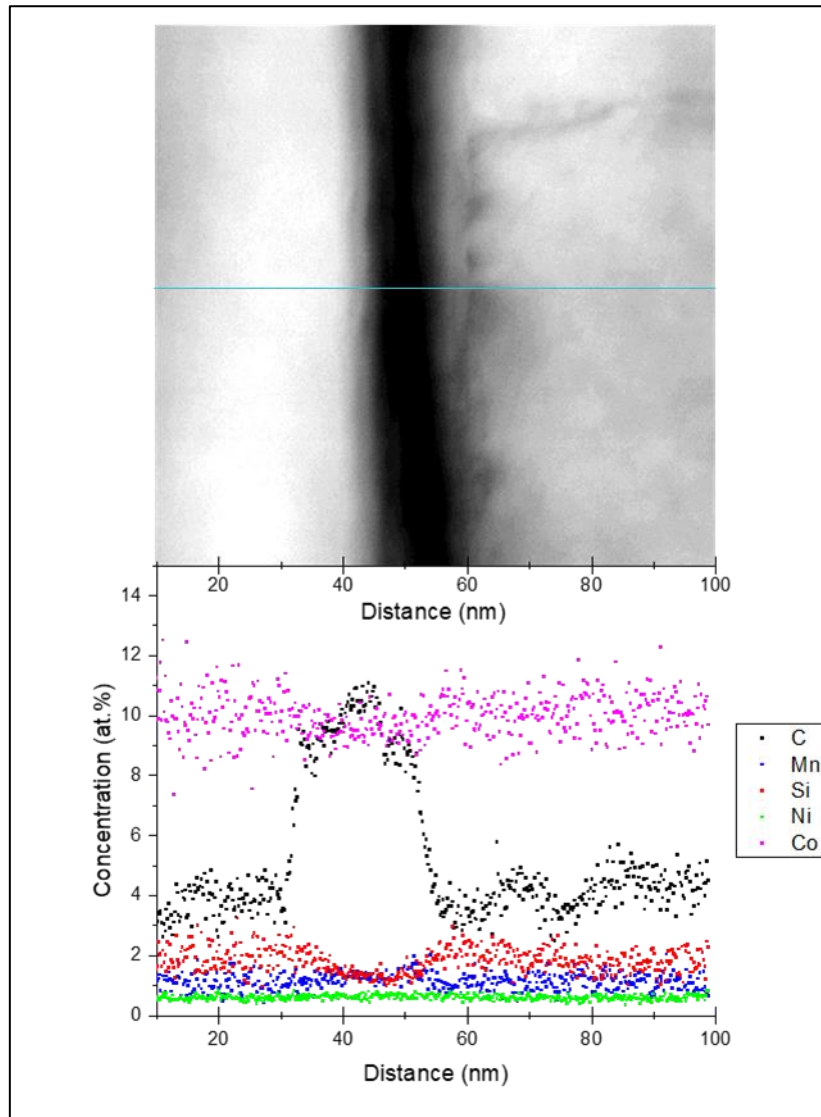


Figure 5:30 - Steel BJ5 4 month artificial ageing condition STEM HAADF EDS line scan.

Figure 5:30 shows an EDS line scan across a single cementite lamella, identified by a carbon peak of 11 at. % at approximately 40 nm. Figure 5:30, in line with atom probe data presented in section 3.1 - British Steel R&D Study - Influence of Nickel on Pearlite Stability, also shows a reduced concentration of silicon within the cementite compared to the ferrite matrix. A minor increase in the concentration of silicon at the ferrite cementite interface is also present. Figure 5:30 also shows a higher concentration of manganese in the cementite lamella than in

the ferrite matrix, which is in agreement with section: 3.1 - British Steel R&D Study - Influence of Nickel on Pearlite Stability. Figure 5:30 shows nickel is homogeneously distributed between the ferrite matrix and cementite lamella. Figure 5:30 shows a much greater concentration of cobalt than the bulk composition. This could be due to an agglomeration of cobalt in this region of the microstructure but is likely an EDS measurement error. However, cobalt appears to be distributed homogeneously throughout the microstructure.

A small carbon peak is observed at 70nm, where there does not appear to be a reduced concentration of silicon and an increased manganese concentration. The corresponding micrograph in Figure 5:30 shows the line scan passes through a dislocation. As carbon has been observed segregating to dislocations [45], it is possible this is a real increase in carbon concentration at the dislocation. Although, carbon concentrations in the ferrite matrix are significantly higher than the carbon solubility in ferrite, so it is also possible this is due to carbon contamination on the sample. Given the apparent cementite thickness of around 20nm, the peak of 11 at.% carbon is significantly lower than expected. This is also likely due to X-ray absorption.

5.6.1.3 0.8Si + 0.5Ni + 0.1Co + 0.1V Steel BJ6

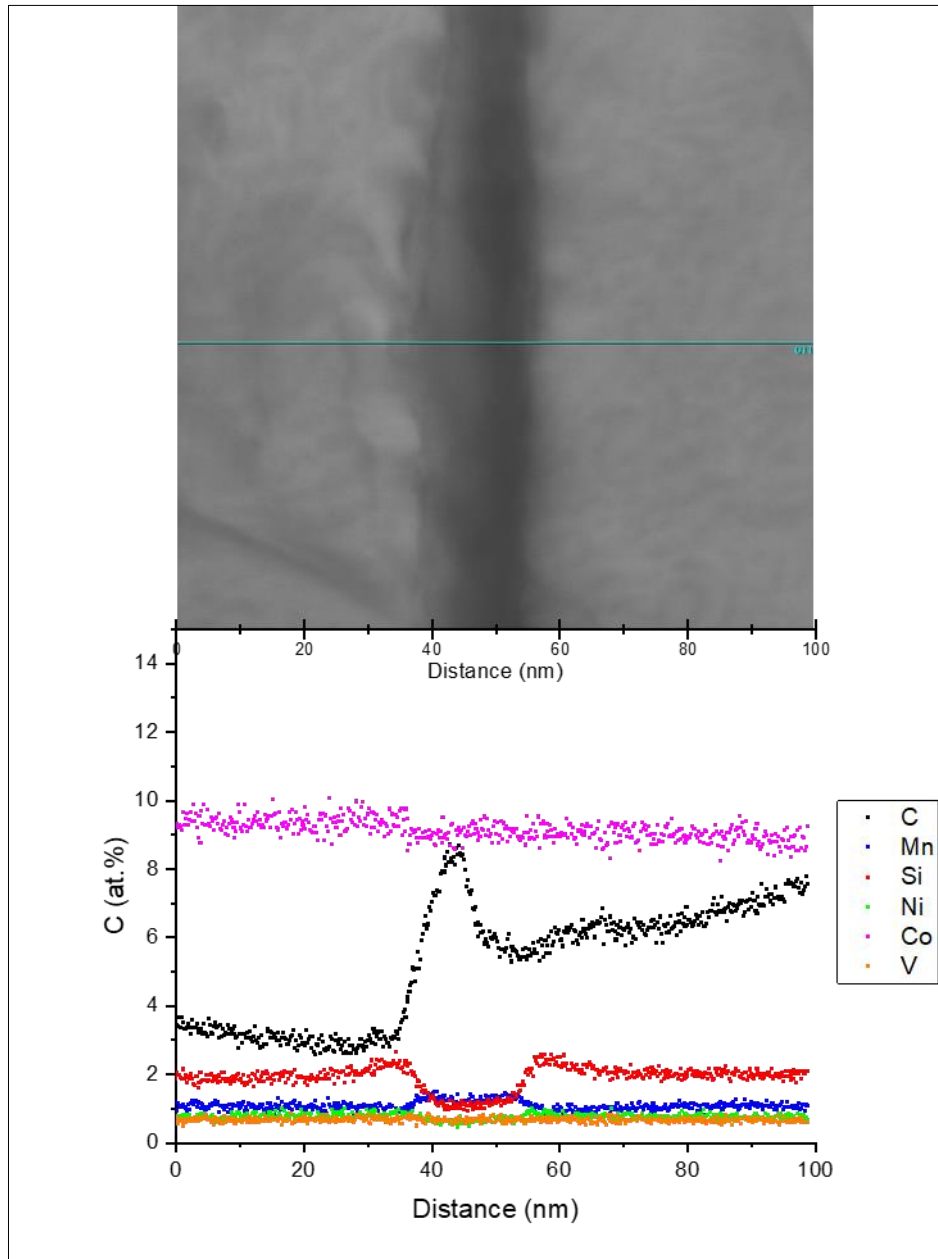


Figure 5:31 - BJ6 4 month artificial ageing condition STEM HAADF - EDS Line Scan.

Figure 5:31 shows an EDS line scan across a cementite lamella, which is identifiable by the peak carbon concentration of 9 at.% at 40nm. The ferrite matrix carbon concentration is varied and significantly higher than the carbon solubility in ferrite, suggesting carbon

contamination. Figure 5:31 shows a reduced concentration of silicon in the cementite lamella compared to the ferrite matrix. There is a minor increase in concentration of silicon at the ferrite cementite interface. Figure 5:31 shows an increased concentration of manganese in the cementite compared to the ferrite matrix. Figure 5:31 shows a slightly reduced concentration of nickel in the cementite lamella, whereas vanadium appears to be distributed homogeneously. Vanadium is expected to dissolve within the cementite whereas nickel is not.

5.6.2 Atom Probe Tomography

Atom probe tomography was completed by Dr. Paul Baggot at Oxford University. Samples were frozen for 18 months prior to testing. A large number of samples were prepared, but due to Covid-19 restrictions the majority of these could not be examined in the atom probe and were lost. Only two samples from the commercial steel in the 2 month ageing condition and a single sample from Steel BJ5 in the 4 months artificially aged condition were completed.

5.6.2.1 Commercial Steel

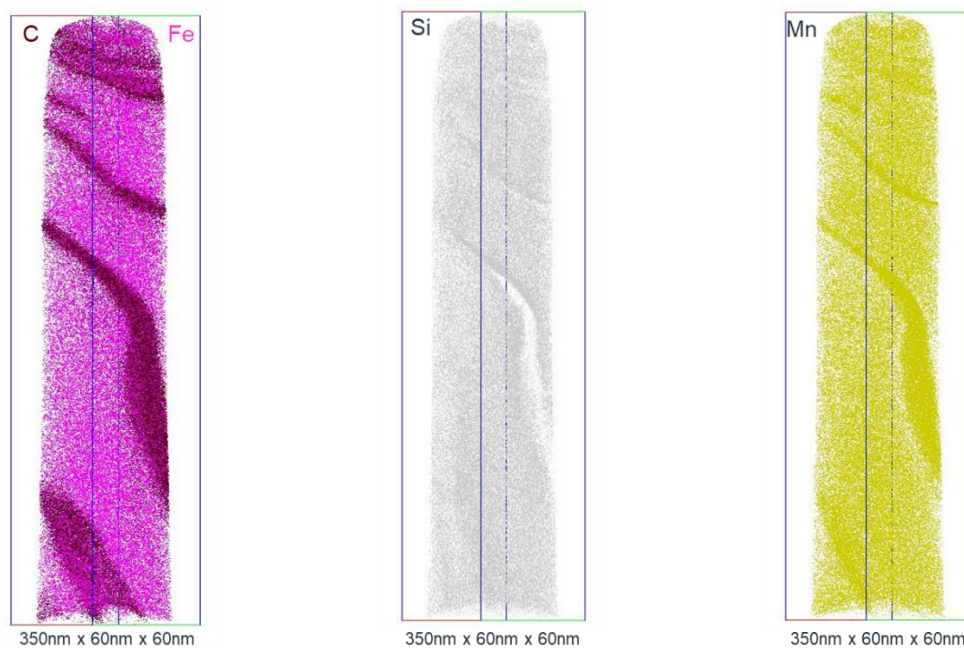


Figure 5:32 - 2 month artificial ageing condition: Commercial steel sample 1, atom probe reconstruction.

Figure 5:31 shows the distribution of iron, carbon, silicon and manganese from a sample of the commercial steel in the two months ageing condition. Several cementite lamellae can be identified from the carbon distribution. Silicon is rejected from the cementite lamellae, manganese is distributed throughout the ferrite matrix and cementite lamellae, with an increased concentration within the cementite lamellae. This is in agreement with section 3.1 - British Steel R&D Study - Influence of Nickel on Pearlite Stability and [24].

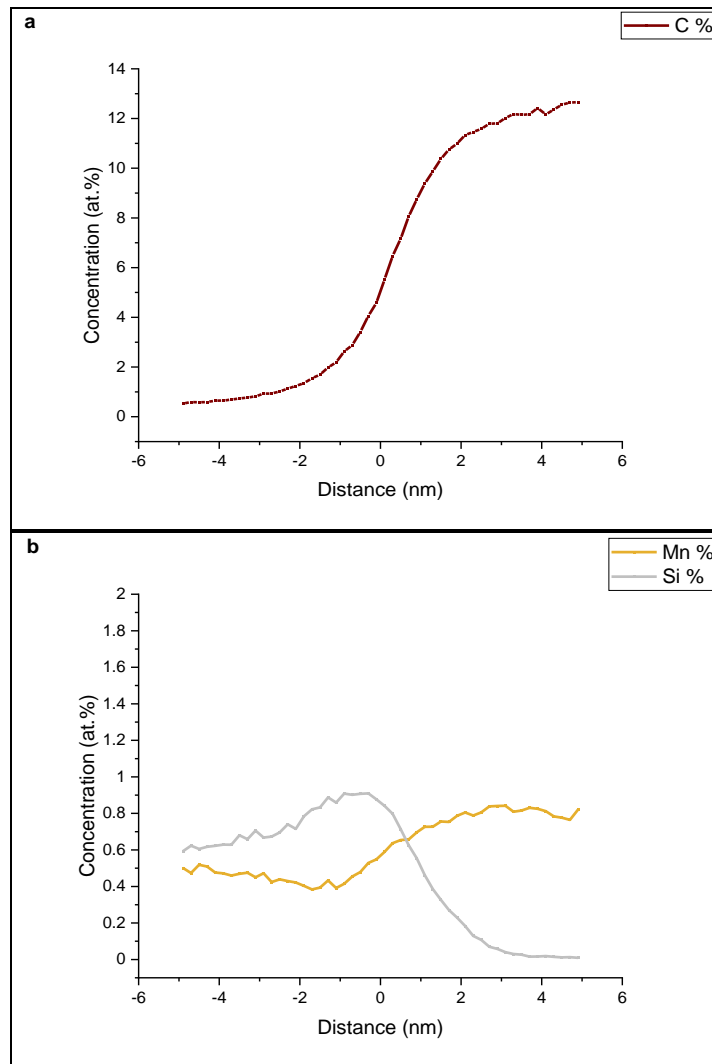


Figure 5:33 - Commercial Steel Sample 1: 7 at.% C Iso concentration surface Proxigram: a. carbon concentration, b. manganese and silicon concentration.

Figure 5:33 confirms the increased concentration of manganese within cementite lamellae and the rejection of silicon from cementite lamellae observed in Figure 5:32.

Table 5:16 - Commercial Steel Sample 1: 7 at% C iso-concentration average composition of cementite and ferrite matrix.

Avg Concentration (at.%)	Fe	Si	Ni	Mn	Co	C	Cr	P
Matrix	97.1	0.7	-	0.46	-	1.5	0.02	0.02
Cementite	87.6	0.2	-	0.77	-	10.7	0.02	0.02

Table 5:16 shows the average carbon concentration throughout the cementite lamellae is 10.7 at.%, which is significantly less than the stoichiometric carbon concentration of cementite (25.at%). This is unexpected as the relatively mild drawing strain of 2.03 and artificial ageing

treatments used in this study, appear to have retained a distinct lamellae microstructure in this region.

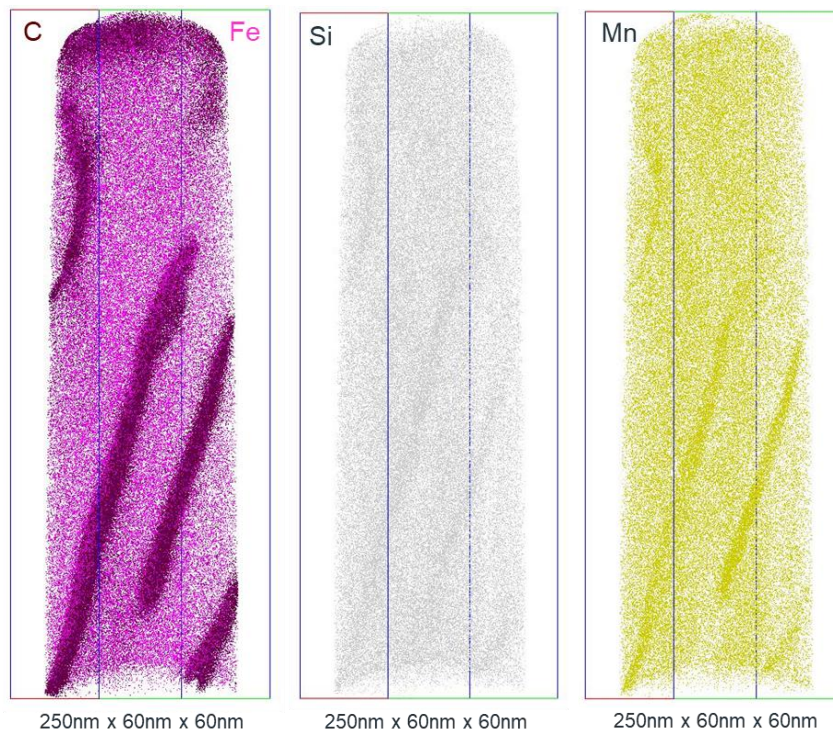


Figure 5:34 - 2 month artificial ageing condition: Commercial steel sample 2, atom probe reconstruction.

Figure 5:34 shows the second atom probe data set of the commercial steel grade in the 2 month artificially aged condition. The carbon distribution shows several cementite lamellae. As with the initial sample, a higher concentration of manganese is present within the observed cementite lamellae. Silicon is also partially observed within the cementite lamellae, contrary to the previous sample.

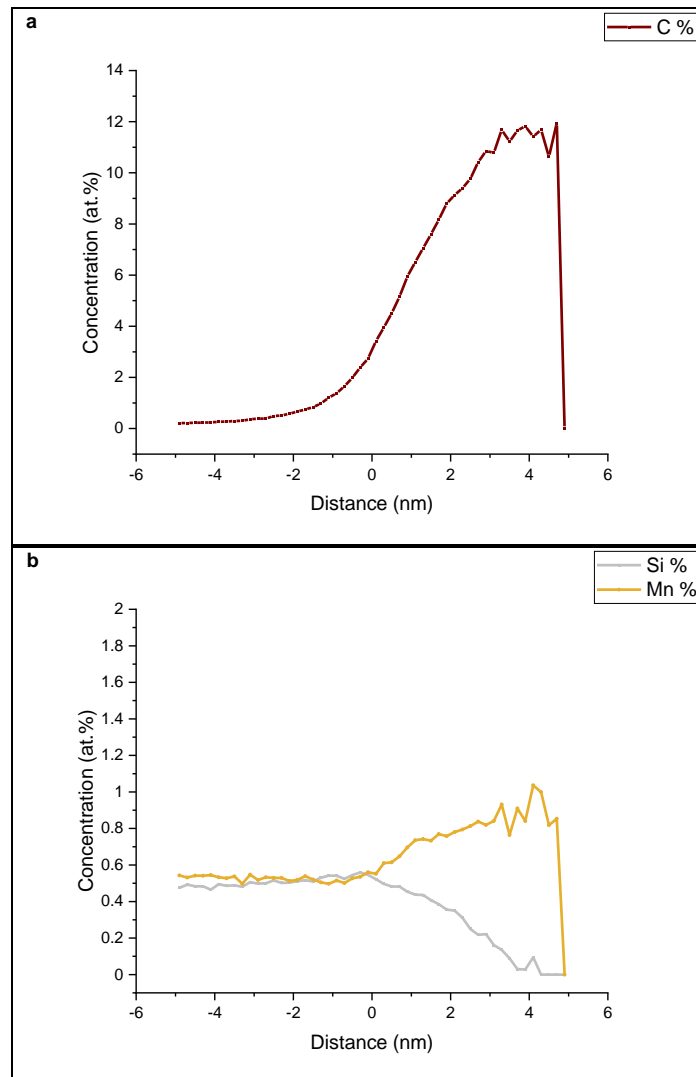


Figure 5:35 - Commercial Steel Sample 2: 7 at.% carbon Iso-surface Proxigram: a. carbon concentration, b. manganese and silicon concentration.

Figure 5:35b shows a higher concentration of manganese in cementite lamellae than in the ferrite matrix. Figure 5:35b shows the average concentration of silicon is higher in the ferrite matrix than in the cementite lamellae. Figure 5:35 and Table 5:17 show the average carbon concentration of the cementite is 8.5 at. %, which is also significantly lower than the stoichiometric carbon concentration of cementite (25.at%).

Table 5:17 - Commercial Steel Sample 2: 7 at% C iso-concentration average composition of cementite and ferrite matrix.

Avg Concentration (at.%)	Fe	Si	Ni	Mn	Co	C	Cr	P
Matrix	98.2	0.51	-	0.53	-	0.78	-	0.03
Cementite	90.4	0.25	-	0.76	-	8.54	-	0.02

The distinct cementite lamellae structure of samples 1 and 2 of the commercial steel, shown in Figure 5:32 and Figure 5:34, display a similar structure to the wire with a similar drawing strain of 2 in Figure 2:21. Therefore, the discrepancy between the measured carbon concentration within the cementite and that of Li et al. (20-25 at.% in Figure 2:21) and the 8-10 at.% measured in this study are likely due to differences in data analysis method. As the lamellae structure of the cementite lamellae is preserved, lower carbon concentrations observed in this study are likely an underestimate of the true cementite carbon concentration.

5.6.2.2 0.8Si + 0.5Ni + 0.1Co Steel BJ5

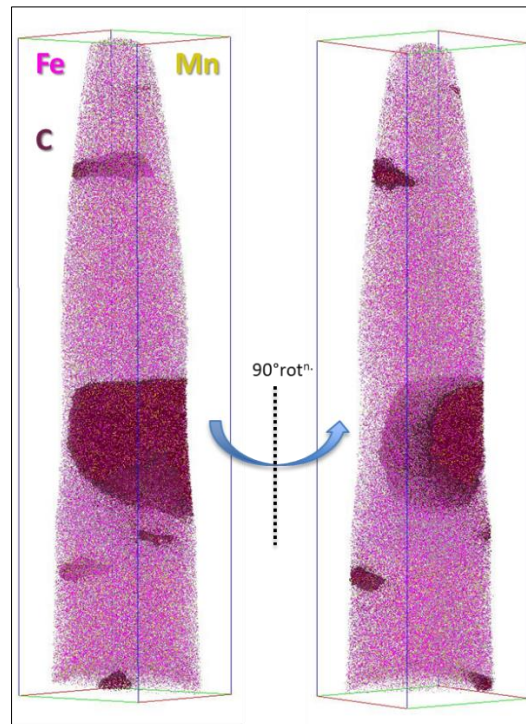


Figure 5:36 - Steel BJ5 4 month artificial ageing condition, atom probe reconstruction.

Figure 5:36 shows the atom probe data set of steel BJ5 in the 4 month artificial ageing condition. The morphology of the cementite does not appear to be lamellar in this region. This is likely due to the heterogeneity of the microstructure. The atom probe reconstruction shows the carbon distribution is more in line with the initial sample in Figure 2:21, suggesting cementite carbon concentration should be closer to stoichiometry than the measured 14.2 at.%.

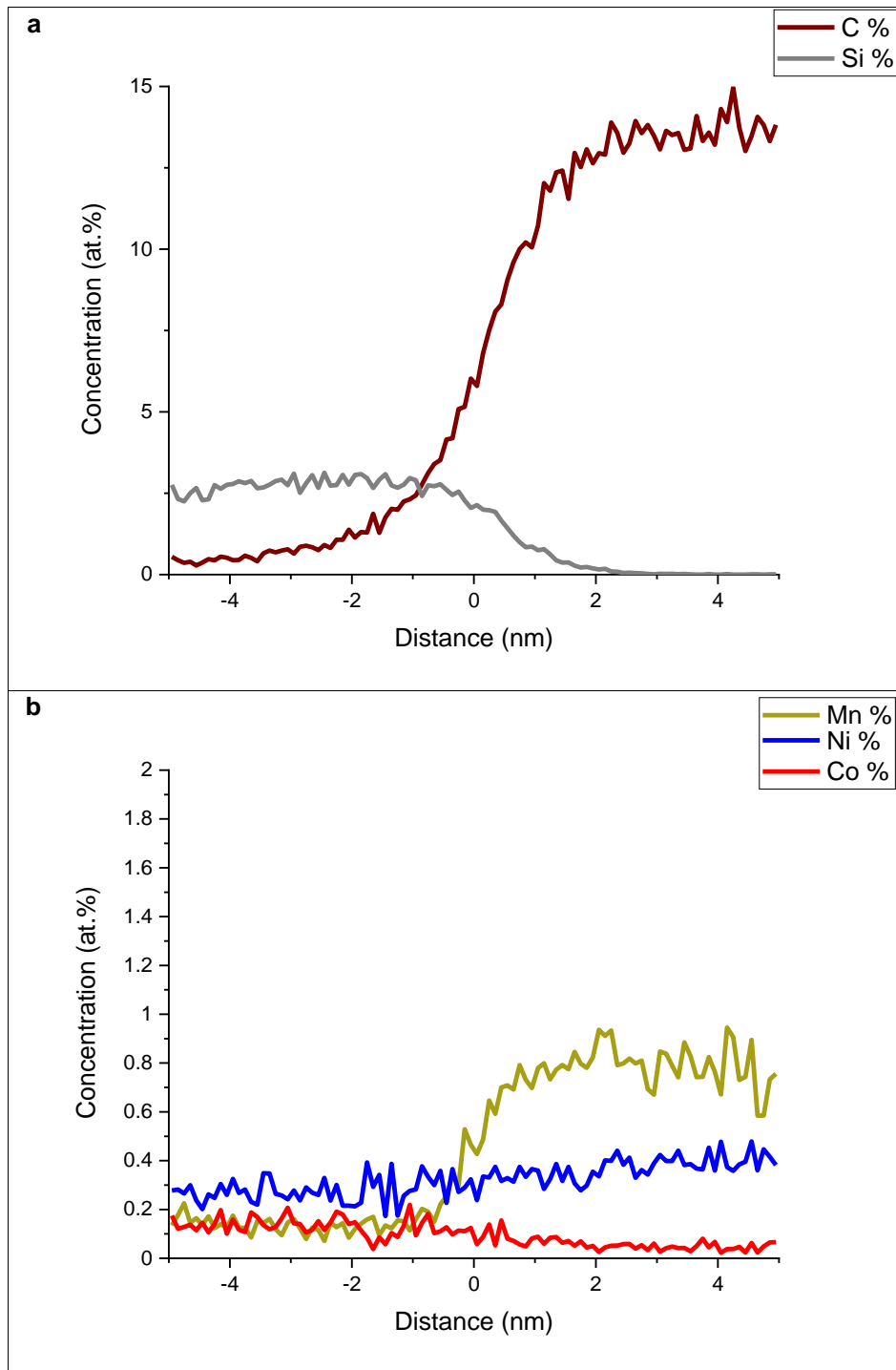


Figure 5:37 - 7 at.% carbon iso-surface average concentration: a. carbon and silicon concentration, b. manganese, nickel and cobalt concentrations.

Figure 5:37a shows a higher concentration of silicon in the ferrite matrix than in the cementite lamellae. Figure 5:37a shows the concentration of carbon in cementite is 14 at.%, which is also significantly lower than the stoichiometric carbon concentration of cementite (25.at%).

Figure 5:37b shows a higher concentration of manganese in the cementite than in the ferrite matrix. This is in agreement with section 3.1 - British Steel R&D Study - Influence of Nickel on Pearlite Stability and ref. [24]. Table 5:18 shows cobalt is predominantly located in the ferrite matrix and a higher concentration of nickel is located in the cementite than in the ferrite matrix.

Table 5:18 - Steel BJ5: 7 at% C iso-concentration average composition of cementite and ferrite matrix.

Average Concentration (at.%)	Fe	Si	Ni	Mn	Co	C	Cr	P
Ferrite Matrix	97.1	1.98	0.48	0.26	0.1	0.08	0.03	-
Cementite/Carbide	84.2	0.03	0.66	0.64	0.06	14.2	0.17	-

5.6.3 Chemical Analysis Summary

TEM sample thickness was matched as closely as possible to allow for comparison between steel compositions. Although, EDS chemical analysis measured significantly larger carbon concentrations in ferrite than the equilibrium carbon solubility of ferrite, there was also high variation measured in the carbon concentrations throughout ferrite. Thus, suggesting carbon contamination was present. Cementite lamellae with a drawing strain of 2, with apparent cementite thickness values greater than ~8nm, are expected to retain close to stoichiometric cementite concentrations [51]. Therefore, the reduced cementite carbon concentrations of 9-11 at.% is likely a result of X-ray absorption.

Figure 5:30 and Figure 5:31 show cobalt and vanadium homogeneously distributed between the ferrite matrix and cementite lamella. The homogeneous distribution of vanadium is unexpected given it is a potent carbide former, it would be expected to be predominantly located in the cementite lamella. Vanadium has been reported in both ferrite and cementite,

and the presence and morphology of vanadium carbides and nitrides in the ferrite matrix is dependent on processing conditions such as cooling rate and ageing treatment [63], [69]. As the nitrogen levels in VIM produced steels are negligible, the presence of vanadium nitrides is unlikely.

Higher drawing strains have been shown to increase the carbon solubility of ferrite, overestimation of cementite dissolution has been widely reported when using atom probe tomography, as summarised in ref. [45]. Figure 2:21 shows at higher drawing strains or in more severe strain ageing conditions which results in a reduction of the carbon concentration of cementite to around 10-15 at.%, significantly more carbon is located throughout the ferrite matrix and the lamella structure is notably less distinct as the gradual change towards amorphous cementite occurs.

As the lamellae structure was still clear across atom probe and EDS samples, it is likely stoichiometric cementite is predominantly remaining and the measured carbon concentrations in cementite are an underestimate, overestimating the amount of cementite dissolution which is occurring. Nevertheless, the consistencies in sample preparation and data analysis ensure the data is suitable for comparison of alloying element distribution between steel compositions. Although, significantly more data would be required to ensure results are not due to experimental variation and are representative of the microstructure.

The atom probe tomography of steel BJ5 (Table 5:18) showed only 0.06 at.% cobalt in the cementite, and 0.1 at.% cobalt in the ferrite matrix. This is almost double the concentration

in the ferrite matrix than in the cementite lamellae. Table 5:18 also showed a higher concentration of nickel in cementite (0.66 at.%) than in the ferrite matrix (0.48 at.%).

6 Discussion

The interlamellar spacing measurements from the pearlite in the BJ4 steel rod showed an increase in interlamellar spacing in the starting condition compared to the other steels, Figure 4:6. The differences were assessed via 95% confidence limits, which did not overlap, suggesting the differences were likely real. This was also the method used to assess the change in mechanical properties with ageing time during mechanical testing. This is expected to reduce the kinetics of the strain ageing compared to smaller lamellar spacings, which must be taken into account when comparing compositions. To ensure consistency of initial rod microstructure between steel compositions, the measurement of prior austenite grain size is also recommended. Also, the VIM furnace produced experimental steels will have less impurities/residuals such as nitrogen and sulphur, which will probably result in reduced strain ageing kinetics (lower N) and increased ductility (lower residuals).

Table 6:1 - Commercial and Experimental Steel Compositions (wt.%).

Steel Grade	C	Mn	Si	Ni	Co	V	P	S
Commercial Grade X85LM (BJ7)	0.84	0.52	0.23	0.02	-	0.001	0.013	0.016
BQ3/BJ3	0.82	0.3	0.8	-	-	-	0.01	0.007
BQ4/BJ4	0.82	0.3	0.8	0.5	-	-	0.01	0.007
BQ5/BJ5	0.82	0.3	0.8	0.5	0.1	-	0.01	0.007
BQ6/BJ6	0.82	0.3	0.8	0.5	0.1	0.1	0.01	0.007

6.1 Mechanical Testing

Following the mechanical testing, steels BJ5 and BJ6 were selected for further analysis alongside the commercial steel for comparison. Steels BJ5 and BJ6 were selected in part for the differences in ageing response observed throughout the mechanical testing. The high variation observed during the tensile testing can be seen in Figure 5:1. In Figure 5:1e, steel BJ6 undergoes a reduction in UTS between the one and two month artificial ageing condition,

suggesting the softening of the microstructure has begun prior to the two month artificial ageing condition. In contrast for steel BJ4, shown in Figure 5:1c, a increase in UTS between the one and two months artificial ageing condition is observed. This suggests that the strength of BJ4 microstructure is still increasing at the 2 months artificial ageing condition.

Whilst the inconsistent variation observed in the tensile testing cannot be exclusively attributed to strain ageing, a more consistent amount of variation may indicate a different ageing response. When comparing tensile elongation to failure in Figure 5:3d and Figure 5:3e, steels BJ5 and BJ6 show more consistent levels of variation in properties, which may be indicative of a lesser or different strain ageing response. Proof to UTS ratio, shown in Figure 5:5, also displays high variation. In Figure 5:6a, the commercial steel shows a peak in proof to UTS ratio in the 2 month artificial ageing condition, suggesting a reduction of ductility in the commercial steel. This observation is confirmed by the brittle torsion testing fractures of the commercial steel in the 2 month artificial ageing condition, shown in Figure 9:52.

Torsion testing produced a higher variation than the tensile tests (Figure 5:7) as expected, thus making trends difficult to determine. However, the fracture type of the torsion tests showed a clear difference between the commercial steel and experimental steels. Brittle fractures of the commercial steel are highlighted in red boxes in Figure 5:8a. For samples tested in the 2 month artificial ageing condition, three out of four tests of the commercial steel failed by brittle fracture (Figure 9:52). This suggests the ductility of the commercial steel is reduced in this ageing condition, however there was no observed reduction in revolutions to failure. For samples tested in the 4 month artificial ageing condition, one out of four tests

of the commercial steel failed in a brittle fracture type (Figure 9:53). The reduction in the number of brittle fractures indicates the commercial steel has partially recovered ductility due to strain ageing. It is probable the point at which the softening of the microstructure begins is not consistent throughout the steel compositions and is between the measured artificial ageing conditions. Therefore, mechanical testing suggests that the softening of the microstructure for the commercial steel occurs in the region of two months artificial ageing condition, whereas steel BJ6 appears to begin softening prior to this, between the one and two month artificial ageing condition. This difference in UTS may also be influenced by the formation of vanadium precipitates. The changes in strength are not necessarily indicative of an accelerated strain ageing response, as there is no measurable change in the 0.2 % proof to UTS for steel BJ6.

6.2 Magnetic Sensors

The non-destructive nature of magnetic measurements allows accurate monitoring of the strain ageing response of a drawn wire in a level of detail which has not been reasonably achievable with current testing methods. Material restrictions allowed for only three artificial ageing conditions to be tested with the magnetic sensors. Therefore, the observed inflection points may shift for each steel composition, if more artificial ageing conditions were measured. As the primary benefit of this technique is the ability to measure the same sample frequently over a period of time, a weekly or even daily testing schedule is possible and recommended for future studies.

The change in real inductance with artificial ageing time (Figure 5:10) shows a difference between steel compositions. Grain size, inclusions or precipitates, dislocation densities, phase

balance and grain orientation have all been shown to influence magnetic properties of a microstructure [30]. Given the small variation of inductance between samples of the same composition, and the consistency in the wire drawing production method, and the initial microstructures (with the exception of the larger interlamellar spacing measured in steel BJ4, and the commercial steels alternative production route), it can be concluded the differences observed between the different steels are real. These differences are likely due to composition, dislocation densities and potentially the presence of precipitates or redistribution of alloying elements. As dislocations are known to be strong pinning sites for domain walls [31], differences in dislocation densities, carbon redistribution and the pinning of dislocations by carbon atoms are likely contributing to the measured differences in inductance.

The presence or precipitation of vanadium carbides may be responsible for the magnitude and differences observed in the real inductance of steel BJ6. No vanadium carbides were definitively observed in this study, although further imaging and chemical analysis of steel BJ6 is required to confirm the presence of vanadium precipitates, or lack thereof. As Maejima demonstrated, vanadium carbides can form via ageing precipitation [63], which suggests an increased temperature would promote the precipitation of vanadium carbides. Therefore, it is possible that static strain ageing may precipitate vanadium carbides, which may have been accelerated by the artificial ageing heat treatments given to simulate extended time at room temperature. An experiment which measured vanadium distribution with varying ageing temperatures and times, with a comparison to a naturally aged sample would reveal if this is the case. If this is the case, artificial ageing may not be suitable to simulate time at extended

temperatures in vanadium containing steels. It is possible the diffusion of alloying elements are contributing to the differences in inductance between steels, although nickel and silicon have been shown to diffuse slowly within ferrite [20][54].

Therefore, the larger reduction of inductance measured in steel BJ6 is not necessarily indicative of increased cementite dissolution. It is likely that the ferrite was super-saturated with vanadium following wire drawing, which led to vanadium carbide formation. An alternative possibility is the dissolution of cementite containing vanadium results in vanadium being located in the ferrite matrix, which results in the formation of vanadium carbides. STEM EDS chemical analysis found vanadium distributed homogeneously throughout the microstructure, which is not expected thermodynamically and is therefore unexpected. It may also be the case that carbon redistribution and dislocation pinning due to strain ageing are predominantly responsible for the changes in real inductance measured.

6.3 DSC

Differential scanning calorimetry measurements, particularly the enthalpy of change, showed high levels of variation. No distinct differences were measured between steel compositions. This may be due to the experimental method, which used an empty reference pan as comparison. Several authors have performed DSC analysis with differing heating profiles or the use of a reference sample, which was prohibited with the experimental setup used. An alternative method would be to measure the analysis as per the method used in this study but continue to record the sample during cooling to provide the base line. This would allow the comparison between the as drawn microstructure and the partially reset microstructure. Not every DSC has the capacity to use liquid nitrogen to control the cooling rate, therefore

analysis of a previously ran sample in the reference pan or running the same sample twice is recommended instead.

Figure 6:1 shows two DSC scans from the commercial steel and two from steel BJ4. Only two out of five DSC scans per steel composition are displayed to improve clarity. Sample 4 and 5 from the commercial steel and sample 2 and 4 from steel BJ4. The complete DSC data are presented in section: 9.4 - Differential Scanning Calorimetry Data. Exothermic peaks in Figure 6:1 (troughs) occur at around 130 °C, 330 °C, 490 °C and 560 °C. These are taken as the stages of strain ageing.

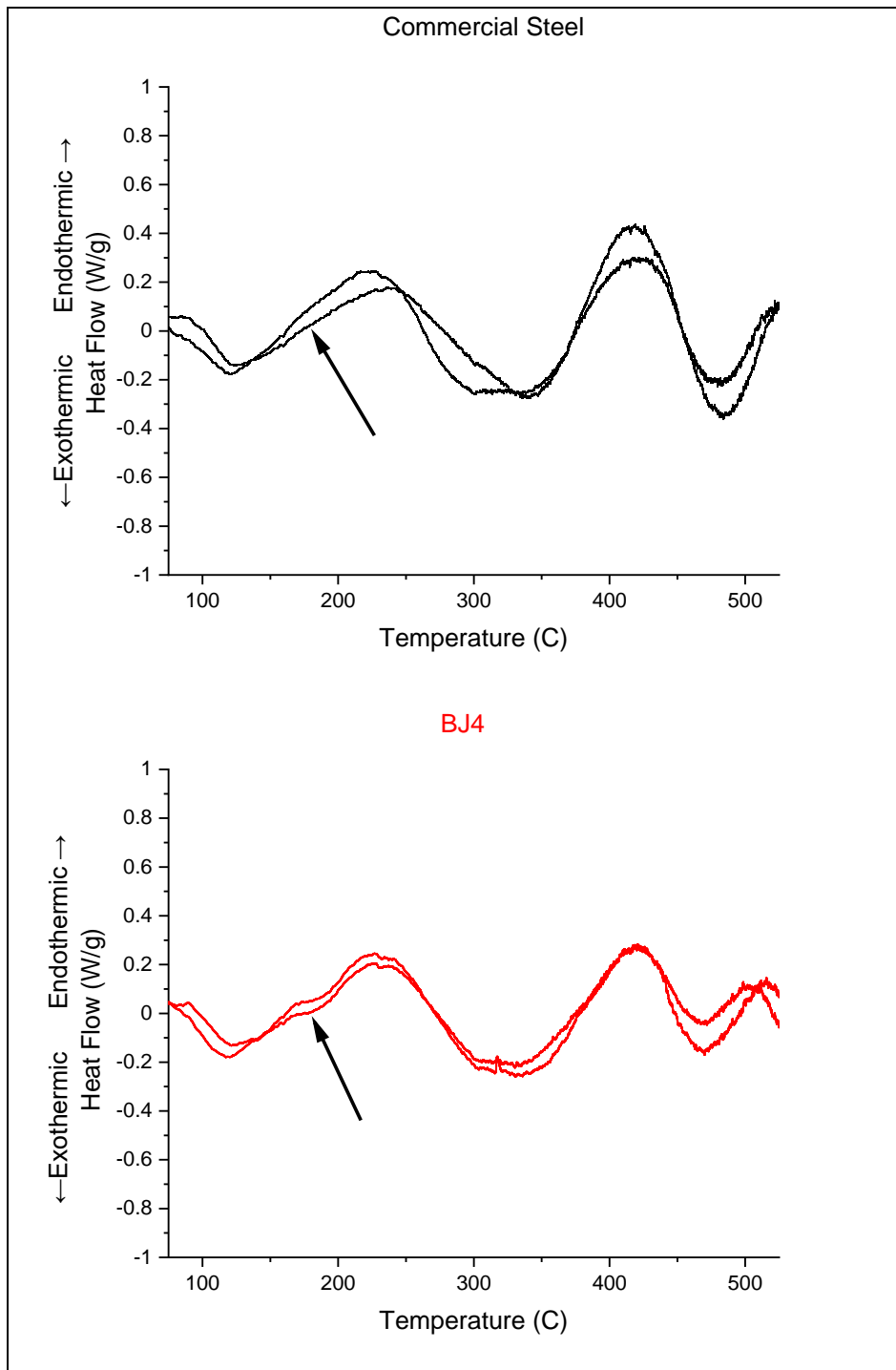


Figure 6:1 - DSC Scans of the commercial steel and steel BJ4. Observed delay in first stage of ageing with nickel and silicon addition.

Interestingly, for steels BJ4, BJ5 and BJ6, two parts of the initial exothermic peak were consistently identified, suggesting two processes are occurring in these compositions during the first stage of ageing. This observation is highlighted with an arrow in Figure 6:1, see

section: 9.4 -Differential Scanning Calorimetry Data for all DSC data plots. Given cementite dissolution has been demonstrated to begin immediately upon wire drawing [9], the initial exothermic event which occurs consistently throughout all compositions is most likely due to partial cementite dissolution.

The splitting of the initial stage initially occurs in steel BJ4 and is not significantly more pronounced with additional alloying elements in steels BJ5 and BJ6, therefore it is likely nickel is responsible. As steel BJ4 also contains 0.8 wt.% silicon, it may be the case that nickel, and silicon are exhibiting a synergistic effect which delays the initial cementite dissolution process somewhat. This is likely a kinetic effect as thermodynamic modelling showed nickel reduced thermal stability of cementite (Figure 3:22). The presence of nickel in ferrite may be inhibiting dislocation motion or the diffusion of carbon through the ferrite. This may be aided by silicon which accumulates at the ferrite cementite interface. A DSC scan on a study on a steel containing nickel with no silicon addition could confirm whether silicon is contributing to this observation.

6.4 Transmission Electron Microscopy

Bright field TEM micrographs of the commercial steel, BJ5 and BJ6 (Figure 5:13, Figure 5:17 and Figure 5:23 respectively) highlight the inherent variation in the microstructure of drawn pearlite. STEM imaging of the commercial steel, BJ5 and BJ6 (Figure 5:14, Figure 5:18 and Figure 5:24 respectively) reveals regions of high dislocation densities which are not clearly visible in equivalent TEM micrographs. Higher magnification STEM micrographs of the commercial steel, BJ5 and BJ6 (Figure 5:15, Figure 5:21 and Figure 5:27 respectively) show dislocation structures visible within the ferrite phase. STEM imaging was crucial in obtaining micrographs capable of measuring cementite lamellae thickness. Cementite lamellae thickness measurements were completed in an attempt to quantify the morphology and dissolution of cementite lamellae, allowing for comparison between the steel compositions. However, as time constraints prevented the measurements being completed on as-drawn samples, the change in the variation of lamellae thickness with artificial ageing time could not be obtained. Therefore, the coefficient of variance of a single ageing condition is a measure of lath morphology. The coefficient of variance was calculated from the cementite lamellae thickness measurements, as a non-dimensional parameter to allow for comparison between compositions.

Table 6:2 - Mean coefficient of variance of 3 measured cementite lamellae.

Steel Grade	Coefficient of Variance of Cementite Lamellae Thickness
Commercial Steel	0.90
BJ5	0.96
BJ6	0.79

The differences in the coefficient of variance in this case are within the error of measurement due to the limited data. The variation in cementite lath morphology is also influenced by the

heterogeneities within the microstructure. The variation in cementite lamellae thickness may be influenced by the plasticity of cementite during wire drawing, the findings of Gavriljuk suggest that alloying additions which influence cementite plasticity and mechanical properties may also influence cementite dissolution. Although significantly more data would be required to establish if a correlation between the plasticity or morphology of cementite and cementite dissolution exists.

6.5 Chemical Analysis

Chemical analysis was completed on the commercial steel, BJ5 and BJ6 to measure carbon distribution and to establish where each alloying element was located within the microstructure. Time constraints prevented the full range of analysis of as drawn and artificially aged samples for comparison. A summary of measured carbon concentration within cementite lamellae is shown in Table 6:3:

Table 6:3 - Chemical Analysis Summary.

Steel Grade	Ageing Condition	Experimental Technique	Mean Cementite Carbon Concentration (at.%)	
Commercial Steel	2 months	APT	10.75 & 8.54	Figure 1:39 - Figure 1:42, Table 1:9 & Table 1:10
Commercial Steel	4 months	STEM-EDS	8.94	Figure 1:35
Steel BJ5	4 months	APT & STEM-EDS	APT: 14.20 & EDS :9.38	Figure 1:43, Figure 1:44, Table 1:11 & Figure 1:36
Steel BJ6	4 months	STEM-EDS	7.92	Figure 1:37

As discussed, the measured carbon concentrations in the cementite and ferrite are likely overestimating the amount of cementite dissolution which is occurring. The carbon concentration of cementite under these drawing strains and ageing conditions is expected to be close to the stoichiometric concentration of cementite (~25 at.%).

The differences in the measured carbon concentrations are most likely due to experimental variation and the inherent heterogeneous microstructure of drawn pearlite. Significantly more EDS and atom probe data are required to establish and compare any differences in the remaining carbon concentrations of cementite between steel compositions.

6.6 Commercial Steel

See Table 6:1 on page 225 for a summary of the commercial steel composition. 0.2% Proof stress to UTS ratio (Figure 5:5a) and the brittle torsion fractures of the commercial steel (Figure 9:52 and Figure 9:54) demonstrated the increase in strength up to the two month artificial ageing condition, and partial recovery by the 4 month artificial ageing condition. The commercial steel was the only steel composition in this study which failed with brittle torsion fractures. Although it is worth noting, no significant reduction in revolutions to failure were measured. This is likely due to a combination of the alternative production route and differences in composition. The commercially produced steel has around double the sulphur content of the experimental steels which contributes to reducing ductility, whilst increased nitrogen levels contribute to strain ageing kinetics. The commercial steel also contained a higher manganese content than the experimental steels. Manganese has also been shown to enhance strain ageing kinetics (Table 2:2 and ref. [19]). Manganese is located in both the ferrite matrix and cementite lamellae. Although a higher concentration of manganese is present in cementite, suggesting any effects of manganese on cementite may be contributing to the observed brittle fractures. In conclusion, the alternative steel production method is likely contributing to the brittle torsion fractures observed with strain ageing, the larger manganese addition may also be contributing to the strain ageing response of the material.

6.7 Steel BJ3

See Table 6:1 on page 225 for the composition of steel BJ3. The main alloying addition of steel BJ3 is a 0.8 wt.% addition of silicon. No experimental steels showed brittle fractures. The VIM produced experimental steels had a reduced nitrogen content and residual levels compared to the commercial steel. The similar UTS and 0.2% proof stress between the commercial steel and steel BJ3 shows a 0.8 wt.% silicon addition and 0.3 wt.% manganese addition provides an approximately equal amount of strengthening as a 0.5 wt.% manganese addition and a 0.2 wt.% silicon addition. Silicon is located in the ferrite matrix [17] [24], has been observed accumulating at the ferrite cementite interface [43] and is a solid solution strengthener in ferrite [66]. The location of silicon reported in the literature is in line with atom probe tomography data in sections: 3.1 - British Steel R&D Study - Influence of Nickel on Pearlite Stability and 5.6.2 - Atom Probe Tomography. Gavriljuk reported (summarised in Table 2:2) a silicon addition had little effect on amount of cementite dissolution [35]. The data from this study also suggests silicon does not have a significant effect on the initial stages of strain ageing. However, the relatively low cost of silicon and its effectiveness in delaying spheroidisation, combined with the solid solution strengthening effect within ferrite (which allows for reduced levels of manganese), ensures a silicon addition can be recommended.

6.8 Steel BJ4

See Table 6:1 on page 225 for the composition of steel BJ4. In addition to the 0.8 wt.% silicon addition of steel BJ3, steel BJ4 contains a 0.5 wt.% nickel addition. A larger interlamellar spacing was measured in rods for this composition, which reduces strain ageing kinetics. DSC showed the temperature and enthalpy of change of the first stage of ageing remained

indistinguishable from the previous compositions. However, the nickel addition appeared to delay a part of the initial stage of strain ageing to a higher temperature, suggesting an additional process is occurring for this composition. This is highlighted in Figure 6:1. As this is not observed in the commercial steel and steel BJ3 and does not appear more pronounced in steels BJ5 and BJ6, it is probable nickel, or the combined effects of nickel and silicon are responsible. As silicon is reported to help delay the latter stages of strain ageing by slowing diffusion and accumulating at the ferrite cementite interface [20], it is surprising that a silicon addition does not produce this effect without the presence of nickel. Nickel is reported to reduce cementite bond energy and cementite containing nickel is also reported to activate additional slip planes during deformation [55]. This results in cementite with increased plasticity. This is in line with results from section: 3.1 - British Steel R&D Study - Influence of Nickel on Pearlite Stability, where a nickel addition resulted in more ductile torsion fractures. Thermodynamic modelling revealed a nickel addition reduced the transformation temperature of cementite (Figure 3:22), which confirms nickel reduces the thermal stability of cementite. Therefore, cementite with increased ductility may increase the capacity of a microstructure to tolerate strain ageing before a brittle fracture occurs. However, the combined addition of nickel and silicon proved challenging to draw on the multi pass machine, shown in Table 9:7. This is likely due to the solid solution strengthening effects of nickel and silicon in the ferrite matrix. Therefore, a nickel addition is recommended, although further testing of nickel containing steel compositions is required to ascertain how much nickel can be added without impairing drawability.

6.9 Steel BJ5

See Table 6:1 on page 225 for the composition of steel BJ5. In addition to the 0.8 wt.% silicon and 0.5 wt.% nickel addition, steel BJ5 also contained a 0.1 wt.% cobalt addition. Cobalt has been reported to increase cementite plasticity and reduce cementite bond strength [56][57]. Cobalt has also been reported to improve drawability, to be a pearlite refiner and not produce a solid solution strengthening effect in ferrite [58]. The findings of this study agree with these observations. No notable increase in tensile properties were observed with a cobalt addition. A cobalt addition improved drawability, fewer breakages occurred during wire drawing of steel BJ5 compared to steel BJ4 on the multipass wire drawing machine at Bekaert technology centre, see Table 9:7 and Table 9:8. This may be due to the increased plasticity of cementite containing cobalt. Nickel and cobalt have both been reported to reduce cementite bond energy, yet cobalt improved drawability and a nickel addition appears to be detrimental. Although the nickel addition was significantly larger in this study, these findings suggest nickel has a solid solution strengthening effect in ferrite and cobalt does not.

EDS (Figure 5:30) showed cobalt was distributed homogeneously throughout the microstructure in the 4 month artificial ageing condition. Atom probe tomography (Figure 5:37) suggested that cobalt was predominantly located in the ferrite matrix. These discrepancies may be due error or, or due to heterogeneities within the wire microstructure. Thermodynamic modelling (Figure 3:23) shows immediately after the austenite to pearlite transformation, cobalt is predominantly located within the ferrite yet 3% of the cobalt was present in the cementite. Upon cooling cobalt relocated entirely to ferrite, suggesting a small amount of diffusion between the phases may be possible. This may have been accelerated

during the artificial ageing of wires. In summary, cobalt improves drawability, which is likely due to the increased plasticity of cementite containing cobalt. Further chemical analysis is required to ascertain if this results in a reduced amount of cementite dissolution.

6.10 Steel BJ6

See Table 6:1 on page 225 for the composition of steel BJ6. In addition to the 0.8 wt.% silicon, 0.5 wt.% nickel and 0.1 wt.% cobalt, steel BJ6 also contains a 0.1 wt.% vanadium addition. The effects of vanadium on the mechanical properties of the microstructure vary depending on steel composition and processing conditions: Vanadium is reported to increase cementite bond strength significantly [55]; to improve strength and fracture toughness of cementite [59]; to improve cementite stability and toughness [60]; increase elongation to failure but reduce UTS and yield [61]; and increase strength and cementite fragmentation [27]. The presence, distribution and morphology of vanadium and vanadium precipitates are determined by steel composition and processing conditions such as casting parameters, rolling conditions strain rates or heat treatments/cooling rates. Therefore, the variety of steel compositions and processing conditions are likely to be responsible for the differing effects of vanadium reported in the literature.

Tensile testing demonstrated a vanadium addition results in an increase in UTS from the as drawn condition to the one month artificial ageing condition followed by a decrease in UTS from the one to two month artificial ageing condition (Figure 5:1e). The increase in strength is unlikely to be exclusively due to strain ageing, as the 0.2% proof to UTS ratio remained consistent in these ageing conditions. As steel BJ6 did not display a corresponding reduction in ductility, expected with a strain ageing response (Figure 5:5e), it is likely the precipitation

of vanadium carbides is responsible for the change in mechanical properties. Thermodynamic modelling (Figure 3:30), in line with [60], showed immediately following the austenite to pearlite transformation, vanadium is located predominantly within the cementite. EDS line scans of steel BJ6 in the 4 month artificial ageing condition show a marginally reduced amount of nickel is present within the cementite lamellae (Figure 5:31), compared to steel BJ5 (Figure 5:30). Figure 5:31 shows vanadium is located homogeneously throughout ferrite and cementite, given the potent carbide forming potential of vanadium, this is unexpected. One would expect vanadium to be predominantly located within the cementite lamellae.

Magnetic sensor measurements of steel BJ6 also suggests a significant change in the microstructure of BJ6 is occurring between as drawn and the two month artificial ageing condition. As vanadium has been shown to form precipitates by ageing precipitation at high temperatures [63], static strain ageing may result in the precipitation of vanadium carbides. Which may have been accelerated during the artificial ageing heat treatments. No clear vanadium carbides were observed in this study, although the high dislocation density made the observation of fine carbides difficult. Atom probe of analysis of steel BJ6 is required to confirm the presence of vanadium precipitates, or lack thereof. Therefore, characterisation of the as-drawn microstructure is required to establish whether the formation of vanadium precipitates is responsible for the change in mechanical properties, which is crucial in furthering the understanding of the magnetic sensor measurements.

6.11 Cementite Dissolution

EDS and atom probe tomography analysis of the cementite lamellae suggested a significant amount of cementite dissolution had occurred across the steel compositions analysed. However, this was likely an overestimate of the amount of cementite dissolution which had occurred. Li et al. reported two microstructures of drawn wires (Figure 2:21 from ref. [45]): the first with lamellae cementite predominantly thicker than 8nm and intact ($\epsilon = 2$), where the structure and carbon concentration of cementite lamellae remained close to stoichiometric cementite of 20-25 at.% carbon; and the second, where cementite lamellae thickness was less than 8nm as cementite had begun a gradual change towards an amorphous structure with a significant amount of cementite dissolution occurring ($\epsilon = 5$), 10-15 at.% carbon was measured remaining within the cementite. As the wire drawing strain in this study was also 2 and a distinct lamellae cementite was frequently observed thicker than 8nm, the cementite carbon concentration is expected to be around stoichiometric carbon concentration of 20-25 at.%.

EDS analysis suggested an increased carbon concentration was located at a dislocation, suggesting carbon may segregate to a dislocation adjacent to cementite lamellae. The increased carbon solubility of ferrite with increased dislocation density has been observed by Li et al. [45], therefore these observations may be real. Although, significantly more data of carbon concentration at dislocations would be required to confirm this observation.

6.12 Discussions Summary

A correlation exists in the literature suggesting alloying elements which increase the plasticity in cementite result in a reduced amount of cementite dissolution. It was not possible to establish if this was the case during this study, due to time constraints, which prevented the full range samples being analysed. The investigation of how, or if cementite lamellae morphology (in the form of comprehensive cementite lamellae thickness measurement) changes during strain ageing and how it affects the remaining carbon concentration within cementite lamellae may provide further evidence for a physical, dislocation based mechanism of cementite dissolution.

Differences between observed in APT, STEM EDS analysis and the literature of cementite carbon concentrations were likely due to differences in analyses technique and experimental error. Proxigram analysis of APT data appears to be less accurate at determining true carbon concentrations, although is a good indication of alloying element distribution. The purpose of this study was also to determine the location and influence of alloying additions, therefore a proxigram is suitable for precisely mapping alloying element distribution.

Whilst determining true carbon concentration was challenging APT and EDS analysis was effective in mapping alloying element distribution, summarised below in Table 6:4.

Table 6:4 - Alloying element location summary.

Element	Reported Element Location in Drawn Pearlite:	Experimentally observed element distribution:	
Si	Predominantly located in ferrite, slight accumulation at α/Fe_3C interface [24], Silicon is rejected from cementite [19]	In line with literature, silicon was observed predominantly within the ferrite matrix.	Table 5:16, Table 5:17, Table 5:18, Figure 5:29, Figure 5:30, Figure 5:31.
V	Higher concentration within cementite [24] [27], also present in ferrite [19].	Distributed homogeneously in the 4 month artificial ageing condition (EDS).	Figure 5:31.
Mn	Located in ferrite and cementite, higher concentration in cementite [19] [24] [27].	In line with literature, manganese was located in a higher concentration in the cementite than ferrite.	Table 5:16, Table 5:17, Table 5:18, Figure 5:29, Figure 5:30, Figure 5:31.
Co	-	STEM EDS line scan in the 4 month artificial ageing condition showed cobalt located homogeneously. APT in the 4 month artificial ageing condition showed approximately double the concentration in ferrite matrix compared to cementite.	Figure 5:30 and Figure 5:31, Table 5:18.
Ni	Higher concentration present in cementite than ferrite (See Section: 3.1 - British Steel R&D Study - Influence of Nickel on Pearlite Stability).	STEM EDS show Ni in BJ5 located homogeneously. STEM EDS suggested a reduced concentration of nickel in cementite when vanadium present. APT showed a higher concentration of nickel in cementite than ferrite matrix.	Figure 5:30 and Figure 5:31. Figure 3:3 and Table 5:18

7 Conclusions

The aim of the EngD programme of work was to identify if cost effective compositional adjustments can be made to a commercial high carbon steel to retard or even eliminate the strain ageing reaction observed in cold drawn high strength wire. This was tested via the production of a set of experimental steels, with systematically varied compositions, identified after a literature review, discussions with British Steel on previous work/experience and thermodynamic modelling of the cementite stability. The experimental steels were produced in a vacuum induction melt furnace to ensure precise control over composition, forged and hot rolled to rod. The rod samples were then heat treated to the appropriate starting microstructure (fully pearlitic) and drawn to wire. The set of experimental steels were artificially aged and tested alongside a commercially produced steel wire for comparison. A selection of available global and localised experimental techniques was used to characterise the strain ageing response: DSC, Torsion and Tensile Testing, Magnetic Sensors, (S)TEM and APT.

Global experimental techniques generally did not result in clear differences between steel compositions, with the exception of magnetic sensor measurements. Mechanical tests which measured a wires ability to deform, which is influenced by dislocation motion and interaction, resulted in the greatest variation. This is unlikely to simply be experimental variation as properties such as UTS showed comparatively little variation. The heterogeneous pearlitic microstructure following severe plastic deformation and the subsequent strain ageing

response leads to localised regions of enhanced cementite dissolution, which leads to variation of mechanical properties during testing.

The most notable difference observed during the mechanical testing was the brittle torsion fractures of the commercial steel in the 2 month artificial ageing condition, and recovery of the microstructure in the 4 month artificial ageing condition. 0.2% proof to UTS ratio also suggested ductility was reduced in the commercial steel in the two month artificial ageing condition. All tensile and torsion testing for the experimental steels failed in ductile cup cone or type 1 A fractures, respectively.

Magnetic sensors measured differences between steel compositions in the magnitude and the change in inductance with artificial ageing time. The large differences measured in steel BJ6 is likely due to the formation of vanadium precipitates or potentially the diffusion of alloying elements during static strain ageing. As discussed, this is not necessary indicative of increased cementite dissolution, as element distribution and precipitation may be responsible for measured differences.

DSC was not able to determine any distinct differences in temperatures or the enthalpy of change of each stage of ageing between steel compositions. However, differences in the first stage of ageing were observed in all steel compositions containing nickel. An alternative experimental method for DSC analysis has been suggested and is recommended for future use.

STEM imaging provided enough imaging contrast to clearly observe dislocation structures and complete measurements of cementite lamellae thickness. Due to time constraints, significantly more measurements would be required to confirm any differences in cementite lamellae thickness. Without measurements of lamellae in the as drawn condition, the coefficient of variance is a measure of cementite lamellae morphology, rather than a measure of cementite dissolution.

Chemical analysis consistently found the cementite carbon concentration of all measured lamellae to be less than the stoichiometric concentration of 25 at.% carbon, although this was likely due to experimental error. Despite the error, the carbon supersaturation of ferrite observed is likely real. EDS analysis suggested an increased carbon concentration was present across a dislocation, which has also been observed with atom probe tomography [45]. Thus, suggesting a dislocation based mechanism of cementite dissolution is occurring. Therefore, alloying additions which affect dislocation motion and the mechanical properties of cementite, may be able to influence cementite dissolution.

The effects of silicon, nickel, cobalt and vanadium on the strain ageing kinetics require further characterisation over a wider range of drawing and ageing conditions to determine their suitability for commercial use. However, when considering the improved ductility of a nickel containing steel shown in section 3.1 - British Steel R&D Study - Influence of Nickel on Pearlite Stability and the potentially delayed initial stage of strain ageing, as observed by DSC observations (Figure 6:1), a nickel addition may in fact have a minor beneficial effect. Further study is required to confirm if a nickel addition results in improved torsional ductility with

artificial ageing which was observed in section 3.1 - British Steel R&D Study - Influence of Nickel on Pearlite Stability. Characterisation of the change in cementite lamellae hardness for example, may reveal if any correlation exists between the mechanical properties of alloyed ferrite or cementite correlates with cementite dissolution. Reducing manganese content as much as reasonably achievable is also recommended.

7.1 Recommendations and Future work

As suggested by Gavriljuk [35], steel composition may indeed be capable of influencing strain ageing kinetics. Further work in the following areas would therefore be recommended:

- Given the high variation observed in this study, the completion of more chemical analyses to confirm any differences in cementite dissolution between steel compositions is recommended. The application of electrolytic phase extraction to strain ageing, as detailed in ref. [9], to confirm if alloying elements can influence the amount of cementite dissolution is recommended.
- The characterisation of the as drawn microstructure is key in identifying how strain ageing affects both element (re)distribution, precipitation and cementite lamellae morphology. A significant number of measurements would be needed to obtain a representative measure of cementite lamellae morphology and chemical composition.
- The effect of artificial ageing on the precipitation of vanadium carbide and nitrides may provide alternative strengthening means following the dissolution of cementite, or where amorphous cementite is present following severe wire drawing [77] [39].

- Development of magnetic sensors with the aim of monitoring the strain ageing response in a level of detail which has not been completed with currently available methods is recommended. It is hoped this will lead to in-line sensors for use during production or in service.

8 References

- [1] Christine Borchers and Reiner Kirchheim, "Cold-drawn pearlitic steel wires," *Prog. Mater. Sci.*, vol. 82, pp. 405–444, 2016, doi: 10.1016/j.pmatsci.2016.06.001.
- [2] H. K. D. H. Bhadeshia, "Cementite," *Int. Mater. Rev.*, vol. 65, no. 1, pp. 1–27, 2020, doi: 10.1080/09506608.2018.1560984.
- [3] Feng Fang, Yufei Zhao, Lichu Zhou, Xianjun Hu, Zonghan Xie, and Jianqing Jiang, "Texture inheritance of cold drawn pearlite steel wires after austenitization," *Mater. Sci. Eng. A*, vol. 618, pp. 505–510, 2014, doi: 10.1016/j.msea.2014.09.061.
- [4] Xiaodan Zhang, Niels Hansen, Andrew Godfrey, and Xiaoxu Huang, "Structure and strength of sub-100 nm lamellar structures in cold-drawn pearlitic steel wire," *Mater. Sci. Technol. (United Kingdom)*, vol. 34, no. 7, pp. 794–808, 2018, doi: 10.1080/02670836.2018.1440155.
- [5] K. Maurer and D. H. Warrington, "Deformation of cementation," *Philos. Mag.*, vol. 15, no. 134, pp. 321–327, 1967, doi: 10.1080/14786436708227704.
- [6] A. S. Keh, "Imperfections and plastic deformation of cementite in steel," *Acta Metall.*, vol. 11, no. 9, pp. 1101–1103, 1963, doi: 10.1016/0001-6160(63)90201-3.
- [7] Feng Fang, Yufei Zhao, Peipei Liu, Lichu Zhou, Xian jun Hu, Xuefeng Zhou, and Zong han Xie, "Deformation of cementite in cold drawn pearlitic steel wire," *Mater. Sci. Eng. A*, vol. 608, pp. 11–15, 2014, doi: 10.1016/j.msea.2014.04.050.
- [8] Michael Zelin, "Microstructure evolution in pearlitic steels during wire drawing," *Acta Mater.*, vol. 50, no. 17, pp. 4431–4447, 2002, doi: 10.1016/S1359-6454(02)00281-1.
- [9] Nicolas Guelton and Marc François, "Strain-Induced Dissolution of Cementite in Cold-

- Drawn Pearlitic Steel Wires," *Metall. Mater. Trans. A Phys. Metall. Mater. Sci.*, vol. 51, no. 4, pp. 1602–1613, 2020, doi: 10.1007/s11661-020-05640-4.
- [10] M. X. Zhang and P. M. Kelly, "Accurate orientation relationships between ferrite and cementite in pearlite," *Scr. Mater.*, vol. 37, no. 12, pp. 2009–2015, 1997, doi: 10.1016/S1359-6462(97)00396-5.
- [11] Jaemin Kim, Keonwook Kang, and Seunghwa Ryu, "Characterization of the misfit dislocations at the ferrite/cementite interface in pearlitic steel: An atomistic simulation study," *Int. J. Plast.*, vol. 83, pp. 302–312, 2016, doi: 10.1016/j.ijplas.2016.04.016.
- [12] M. Kriška, J. Tacq, K. V. Van Acker, M. Seefeldt, and S. V. Van Petegem, "Neutron and X-ray diffraction study of residual and internal stress evolution in pearlitic steel during cold drawing," *J. Phys. Conf. Ser.*, vol. 340, 2012, doi: 10.1088/1742-6596/340/1/012101.
- [13] P. Watté, J. Van Humbeeck, E. Aernoudt, and I. Lefever, "Strain ageing in heavily drawn eutectoid steel wires," *Scr. Mater.*, vol. 34, no. 1, pp. 89–95, 1996, doi: 10.1016/1359-6462(95)00479-3.
- [14] A. Lamontagne, V. Massardier, X. Sauvage, X. Kléber, and D. Mari, "Evolution of carbon distribution and mechanical properties during the static strain ageing of heavily drawn pearlitic steel wires," *Mater. Sci. Eng. A*, vol. 667, pp. 115–124, 2016, doi: 10.1016/j.msea.2016.04.091.
- [15] Lichu Zhou, Feng Fang, Xuefeng Zhou, Yiyu Tu, Zonghan Xie, and Jianqing Jiang, "Cementite nano-crystallization in cold drawn pearlitic wires instigated by low temperature annealing," *Scr. Mater.*, vol. 120, pp. 5–8, 2016, doi: 10.1016/j.scriptamat.2016.04.002.

- [16] Jun Takahashi, Makoto Kosaka, Kazuto Kawakami, and Toshimi Tarui, "Change in carbon state by low-temperature aging in heavily drawn pearlitic steel wires," *Acta Mater.*, vol. 60, no. 1, pp. 387–395, 2012, doi: 10.1016/j.actamat.2011.09.014.
- [17] Y. J. Li, P. Choi, S. Goto, C. Borchers, D. Raabe, and R. Kirchheim, "Evolution of strength and microstructure during annealing of heavily cold-drawn 6.3 GPa hypereutectoid pearlitic steel wire," *Acta Mater.*, vol. 60, no. 9, pp. 4005–4016, 2012, doi: 10.1016/j.actamat.2012.03.006.
- [18] N. Maruyama, T. Tarui, and H. Tashiro, "Atom probe study on the ductility of drawn pearlitic steels," *Scr. Mater.*, vol. 46, no. 8, pp. 599–603, 2002, doi: 10.1016/S1359-6462(02)00037-4.
- [19] Walther Van Raemdonck, "Mordica Lecture: Trends and Challenges in Steel Wire Technologies." *Wire Journal International*, April 2010, pp. 68–80.
- [20] Toshimi Tarui, Naoki Maruyama, Jun Takahashi, Seiki Nishida, and Hitoshi Tashiro, "Microstructure control and strengthening of high-carbon steel wires," *Nippon Steel Tech. Rep.*, no. 91, pp. 56–61, 2005.
- [21] K. Hono, M. Ohnuma, M. Murayama, S. Nishida, A. Yoshie, and T. Takahashi, "Cementite-decomposition-in-heavily-drawn-pearlite-steel-wire_2001_Scripta-Materialia.pdf," vol. 44, pp. 977–983, 2001.
- [22] V. T. L. Bueno, M. S. Andrade, and B. M. Gonzalez, "Kinetics of strain aging in drawn pearlitic steels," *Metall. Mater. Trans. A Phys. Metall. Mater. Sci.*, vol. 29, no. 5, pp. 1415–1423, 1998, doi: 10.1007/s11661-998-0356-y.
- [23] S. W. Joung, U. G. Kang, S. P. Hong, Y. W. Kim, and W. J. Nam, "Aging behavior and delamination in cold drawn and post-deformation annealed hyper-eutectoid steel

- wires,” *Mater. Sci. Eng. A*, vol. 586, pp. 171–177, 2013, doi: 10.1016/j.msea.2013.07.095.
- [24] C. E. Hinchliffe and G. D. W. Smith, “Strain aging of pearlitic steel wire during post-drawing heat treatments,” *Mater. Sci. Technol.*, vol. 17, no. 2, pp. 148–154, 2001, doi: 10.1179/026708301101509935.
- [25] A. Lamontagne, X. Kleber, V. Massardier-Jourdan, and D. Mari, “Identification of the mechanisms responsible for static strain ageing in heavily drawn pearlitic steel wires,” *Philos. Mag. Lett.*, vol. 94, no. 8, pp. 495–502, 2014, doi: 10.1080/09500839.2014.938137.
- [26] Dasheng Wei, Long Li, Xuegang Min, Feng Fang, Zonghan Xie, and Jianqing Jiang, “Microstructure and mechanical properties of heavily cold drawn pearlitic steel wires: Effects of low temperature annealing,” *Mater. Charact.*, vol. 153, no. February, pp. 108–114, 2019, doi: 10.1016/j.matchar.2019.05.003.
- [27] F. Fang, X. Hu, L. Zhou, Z. Xie, and J. Jiang, “Effect of vanadium on microstructure and property of pearlitic steel wire,” *Mater. Res. Innov.*, vol. 19, pp. 394–396, 2015, doi: 10.1179/1432891715Z.0000000001705.
- [28] Feng Fang, Lichu Zhou, Xianjun Hu, Xuefeng Zhou, Yiyou Tu, Zonghan Xie, and Jianqing Jiang, “Microstructure and mechanical properties of cold-drawn pearlitic wires affect by inherited texture,” *Mater. Des.*, vol. 79, pp. 60–67, 2015, doi: 10.1016/j.matdes.2015.04.036.
- [29] A. Lamontagne, V. Massardier, X. Kléber, X. Sauvage, and D. Mari, “Comparative study and quantification of cementite decomposition in heavily drawn pearlitic steel wires,” *Mater. Sci. Eng. A*, vol. 644, pp. 105–113, 2015, doi: 10.1016/j.msea.2015.07.048.

- [30] C. L. Davis, M. Strangwood, and A. J. Peyton, "Overview of non-destructive evaluation of steel microstructures using multifrequency electromagnetic sensors," *Ironmak. Steelmak.*, vol. 38, no. 7, pp. 510–517, 2011, doi: 10.1179/030192311X13135947813816.
- [31] Haibing Yang, F. D. Van den Berg, A. Luinenburg, Cornelis Bos, Gedo Kuiper, Jos Mosk, Peter Hunt, Mark Dolby, Michael Flicos, Anthony Peyton, and Claire Davis, "In-Line Quantitative Measurement of Transformed Phase Fraction by EM Sensors during Controlled Cooling on the Run-Out Table of a Hot Strip Mill," *19th World Conf. Non-Destructive Test.*, pp. 1–8, 2016.
- [32] X. J. Hao, W. Yin, M. Strangwood, A. J. Peyton, P. F. Morris, and C. L. Davis, "Characterization of decarburization of steels using a multifrequency electromagnetic sensor: Experiment and modeling," *Metall. Mater. Trans. A Phys. Metall. Mater. Sci.*, vol. 40, no. 4, pp. 745–756, 2009, doi: 10.1007/s11661-008-9776-y.
- [33] A. Refaat Ali, Z. Farid, M. A. Fahim, and F. Z. Ghobrial, "Study on the effect of decoration of carbon–vacancy pairs by carbon atoms in quenched α -Fe and Cr 25%-type steel alloy by magnetic measurements," *Phys. Status Solidi*, vol. 143, no. 1, pp. 35–49, 1994, doi: 10.1002/pssa.2211430105.
- [34] Wong Jong Nam, Chul Min Bae, Sei J. Oh, and Soon Ju Kwon, "Effect of interlamellar spacing on cementite dissolution during wire drawing of pearlitic steel wires," *Scr. Mater.*, vol. 42, no. 5, pp. 457–463, 2000, doi: 10.1016/S1359-6462(99)00372-3.
- [35] V. G. Gavriljuk, "Decomposition of cementite in pearlitic steel due to plastic deformation," *Mater. Sci. Eng. A*, vol. 345, no. 1–2, pp. 81–89, 2003, doi: 10.1016/S0921-5093(02)00358-1.

- [36] F. Danoix, D. Julien, X. Sauvage, and J. Copreaux, "Direct evidence of cementite dissolution in drawn pearlitic steels observed by tomographic atom probe," *Mater. Sci. Eng. A*, vol. 250, no. 1, pp. 8–13, 1998, doi: 10.1016/S0921-5093(98)00529-2.
- [37] J. Languillaume, G. Kapelski, and B. Baudalet, "Cementite dissolution in heavily cold drawn pearlitic steel wires," *Acta Mater.*, vol. 45, no. 3, pp. 1201–1212, 1997, doi: 10.1016/S1359-6454(96)00216-9.
- [38] David B. Williams and C. Barry Carter, *Transmission electron microscopy: A textbook for materials science*, no. September. 2009.
- [39] Christine Borchers, Talaat Al-Kassab, Shoji Goto, and Reiner Kirchheim, "Partially amorphous nanocomposite obtained from heavily deformed pearlitic steel," *Mater. Sci. Eng. A*, vol. 502, no. 1–2, pp. 131–138, 2009, doi: 10.1016/j.msea.2008.10.018.
- [40] A. Durgaprasad, S. Giri, S. Lenka, Sudip Kumar Sarkar, Aniruddha Biswas, S. Kundu, S. Mishra, S. Chandra, R. D. Doherty, and I. Samajdar, "Delamination of Pearlitic Steel Wires: The Defining Role of Prior-Drawing Microstructure," *Metall. Mater. Trans. A Phys. Metall. Mater. Sci.*, vol. 49, no. 6, pp. 2037–2047, 2018, doi: 10.1007/s11661-018-4564-9.
- [41] Na Min, Wei Li, Hongyan Li, and Xuejun Jin, "Atom probe and mössbauer spectroscopy investigations of cementite dissolution in a cold drawn eutectoid steel," *J. Mater. Sci. Technol.*, vol. 26, no. 9, pp. 776–782, 2010, doi: 10.1016/S1005-0302(10)60123-5.
- [42] Chan Woo Bang, Jae Bok Seol, Yo Sep Yang, and Chan Gyung Park, "Atomically resolved cementite dissolution governed by the strain state in pearlite steel wires," *Scr. Mater.*, vol. 108, pp. 151–155, 2015, doi: 10.1016/j.scriptamat.2015.07.004.
- [43] M. H. Hong, W. T. Reynolds, T. Tarui, and K. Hono, "Atom probe and transmission

- electron microscopy investigations of heavily drawn pearlitic steel wire,” *Metall. Mater. Trans. A Phys. Metall. Mater. Sci.*, vol. 30, no. 3, pp. 717–727, 1999, doi: 10.1007/s11661-999-0063-3.
- [44] Jun Takahashi, Toshimi Tarui, and Kazuto Kawakami, “Three-dimensional atom probe analysis of heavily drawn steel wires by probing perpendicular to the pearlitic lamellae,” *Ultramicroscopy*, vol. 109, no. 2, pp. 193–199, 2009, doi: 10.1016/j.ultramic.2008.10.013.
- [45] Y. J. Li, P. Choi, C. Borchers, S. Westerkamp, S. Goto, D. Raabe, and R. Kirchheim, “Atomic-scale mechanisms of deformation-induced cementite decomposition in pearlite,” *Acta Mater.*, vol. 59, no. 10, pp. 3965–3977, Mar. 2011, doi: 10.1016/j.actamat.2011.03.022.
- [46] N. Gridnev, “Mossbauer Effect in Deformed Fe-C Alloys,” vol. 201, pp. 201–210, 1975.
- [47] Xiaodan Zhang, Andy Godfrey, Xiaoxu Huang, Niels Hansen, and Qing Liu, “Microstructure and strengthening mechanisms in cold-drawn pearlitic steel wire,” *Acta Mater.*, vol. 59, no. 9, pp. 3422–3430, 2011, doi: 10.1016/j.actamat.2011.02.017.
- [48] J. Gil Sevillano, “Room temperature plastic deformation of pearlitic cementite,” *Mater. Sci. Eng.*, vol. 21, no. C, pp. 221–225, 1975, doi: 10.1016/0025-5416(75)90218-9.
- [49] Y. J. Lia, P. Choi, C. Borchers, Y. Z. Chen, S. Goto, D. Raabe, and R. Kirchheim, “Atom probe tomography characterization of heavily cold drawn pearlitic steel wire,” *Ultramicroscopy*, vol. 111, no. 6, pp. 628–632, 2011, doi: 10.1016/j.ultramic.2010.11.010.
- [50] Matthew Guziewski, Shawn P. Coleman, and Christopher R. Weinberger, “Atomistic investigation into the mechanical properties of the ferrite-cementite interface: The

- Bagaryatskii orientation,” *Acta Mater.*, vol. 144, pp. 656–665, 2018, doi: 10.1016/j.actamat.2017.10.070.
- [51] Y. J. Li, P. Choi, C. Borchers, S. Westerkamp, S. Goto, D. Raabe, and R. Kirchheim, “Atomic-scale mechanisms of deformation-induced cementite decomposition in pearlite,” *Acta Mater.*, vol. 59, no. 10, pp. 3965–3977, 2011, doi: 10.1016/j.actamat.2011.03.022.
- [52] L. S. Vasil’ev, I. L. Lomaev, and E. P. Elsukov, “On the analysis of the mechanisms of the strain-induced dissolution of phases in metals,” *Phys. Met. Metallogr.*, vol. 102, no. 2, pp. 186–197, 2006, doi: 10.1134/S0031918X06080102.
- [53] Gh Ali Nematollahi, Blazej Grabowski, Dierk Raabe, and Jörg Neugebauer, “Multiscale description of carbon-supersaturated ferrite in severely drawn pearlitic wires,” *Acta Mater.*, vol. 111, pp. 321–334, 2016, doi: 10.1016/j.actamat.2016.03.052.
- [54] T. Kresse, Y. .. Li, T. Boll, Christine Borchers, P. Choi, T. Al-Kassab, Raabe D, and Kirchheim R, “Influence of supersaturated carbon on the diffusion of Ni in ferrite determined by atom probe tomography,” *Scr. Mater.*, vol. 69, no. 5, pp. 424–427, 2013, doi: 10.1016/j.scriptamat.2013.05.039.
- [55] Masataka Mizuno, Isao Tanaka, and Hirohiko Adachi, “Effect of solute atoms on the chemical bonding of Fe₃C (cementite),” *Philos. Mag. B Phys. Condens. Matter; Stat. Mech. Electron. Opt. Magn. Prop.*, vol. 75, no. 2, pp. 237–248, 1997, doi: 10.1080/13642819708202312.
- [56] Akihisa Inoue and Tsuyoshi Masumoto, “EFFECTS OF ALLOYING ELEMENTS (Cr, Mn, Ni, AND Co) ON THE DEFORMATION BEHAVIOUR OF CEMENTITE IN STEEL,” *Trans Iron Steel Inst Jpn*, vol. 17, no. 3, pp. 143–149, 1977.

- [57] Xiangrong Wang and Mufa Yan, "Effect of cobalt and nickel on the structural stability for FE 3C: first-principles calculations," *Int. J. Mod. Phys. B*, vol. 23, no. 6–7, pp. 1135–1140, 2009, doi: 10.1142/s0217979209060580.
- [58] Yutaka Kanetsuki, Nobuhiko Ibaraki, and Shinzo Ashida, "Effect of Cobalt Addition on Transformation Behavior and Drawability of Hypereutectoid Steel Wire," *ISIJ Int.*, vol. 31, no. 3, pp. 304–311, 1991, doi: 10.2355/isijinternational.31.304.
- [59] John Jairo Coronado and Sara Aida Rodríguez, "Cementite Characterization with Chromium and Vanadium Contents Using Indentation Technique," *J. Iron Steel Res. Int.*, vol. 22, no. 4, pp. 366–370, 2015, doi: 10.1016/S1006-706X(15)30013-3.
- [60] W. Solano-Alvarez, L. Fernandez Gonzalez, and H. K. D. H. Bhadeshia, "The effect of vanadium alloying on the wear resistance of pearlitic rails," *Wear*, vol. 436–437, no. July, p. 203004, 2019, doi: 10.1016/j.wear.2019.203004.
- [61] Hasan Karabulut and Süleyman Gündüz, "Effect of vanadium content on dynamic strain ageing in microalloyed medium carbon steel," *Mater. Des.*, vol. 25, no. 6, pp. 521–527, 2004, doi: 10.1016/j.matdes.2004.01.005.
- [62] Stephanie L. Miller and Walther Van Raemdonck Emmanuel De Moor, *MICROALLOYED HIGH CARBON WIRE STEELS Emmanuel*. 2014.
- [63] Taketo Maejima, Mitsuharu Yonemura, Kaori Kawano, and Goro Miyamoto, "Lattice strain and strength evaluation on V microalloyed pearlite steel," *ISIJ Int.*, vol. 60, no. 8, pp. 1810–1818, 2020, doi: 10.2355/isijinternational.ISIJINT-2019-708.
- [64] E. V. Pereloma, V. Bata, R. I. Scott, and R. M. Smith, "Effect of Cr and Mo on strain ageing behaviour of low carbon steel," *Mater. Sci. Eng. A*, vol. 527, no. 10–11, pp. 2538–2546, 2010, doi: 10.1016/j.msea.2009.12.040.

- [65] Lichu Zhou, Linfeng Wang, Huaqing Chen, Zonghan Xie, and Feng Fang, "Effects of Chromium Additions upon Microstructure and Mechanical Properties of Cold Drawn Pearlitic Steel Wires," *J. Mater. Eng. Perform.*, vol. 27, no. 7, pp. 3619–3628, 2018, doi: 10.1007/s11665-018-3464-x.
- [66] Ryan E. Pennington, Walther Van Raemdonck, David K. Matlock, and George Krauss, "The effect of silicon and aging on mechanical properties and fracture response of drawn high-strength pearlitic steel wire," *2010 Conference Proceedings of the Wire Association International, Inc. - Wire and Cable Technical Symposium, 80th Annual Convention*. Wire Journal International, pp. 1–17, 2010, doi: ISSN-0277-4275.
- [67] E. Kozeschnik and H. K. D. H. Bhadeshia, "Influence of silicon on cementite precipitation in steels," *Mater. Sci. Technol.*, vol. 24, no. 3, pp. 343–347, 2008, doi: 10.1179/174328408X275973.
- [68] S Hobson, "Private communication," 2015.
- [69] W. Solano-Alvarez and H. K. D. H. Bhadeshia, L. Fernandez Gonzalez, "The effect of vanadium alloying on the wear resistance of pearlitic rails," *Wear* 436-437. 2019, doi: <https://doi.org/10.1016/j.wear.2019.203004>.
- [70] Pussegoda Lakshman Nissanka, "STRAIN AGE EMBRITTLEMENT IN REINFORCING STEELS," *PhD Thesis, Universtiy Canteury*, 1978.
- [71] "BS ISO 7800 : 2012 BSI Standards Publication Metallic materials — Wire — Simple torsion test," 2012.
- [72] Dr Frank Zhou, "Private Communication." 2017.
- [73] Dr Mohsen Aghadavoudi Jolfaei, "Private communication." 2018.
- [74] Dr Paul Baggot, "Private communication." 2019.

- [75] M. K. Miller and K. F. Russell, "Atom probe specimen preparation with a dual beam SEM/FIB miller," *Ultramicroscopy*, vol. 107, no. 9, pp. 761–766, 2007, doi: 10.1016/j.ultramic.2007.02.023.
- [76] Stuart Robertson, "Private Communication." 2019.
- [77] M. Nago, H. Yaguchi, and K. Ochiai, "High-strength steel wire excelling in resistance to strain aging embrittlement and longitudinal cracking, and method for production thereof," EP 1293582 B1.

9 Appendix

9.1 Multi-Pass Wire Drawing Machine - Bekaert Technology

Centre

6 x 300mm lengths of rod from each experimental steel were welded 3 metres apart into a commercial carrier coil in preparation for drawing. The carrier coil containing the experimental steel rods was then pickled, coated and dry drawn on the pilot scale 9-pass drawing machine at Bekaert Technology Centre.

9.1.1 Rod Preparation and Characterisation

10 rods per steel composition were cut into 300mm lengths and heat treated for drawing on the multi pass drawing machine at BTC. The cooling rates are presented in Table 9:1, Table 9:2,

Table 9:3 and Table 9:4. Note, the forced air-cooling rig produced a variation of $\pm 3 \frac{^{\circ}\text{C}}{\text{s}}$.

Table 9:1 - 17BQ3 F1 - F10 Rod Characterisation.

Steel Composition (Wt. %)	Rod ID	Measured Cooling Rate $\left(\frac{^{\circ}\text{C}}{\text{s}}\right)$	Unresolvable Pearlite (%)	Degenerate Pearlite (%)	Resolvable Pearlite (%)	Ferrite (%)	Martensite (%)
0.8Si	BQ3 F1	20	84.3	-	14.0	1.7	-
0.8Si	BQ3 F2	21	85.7	-	13.0	1.3	-
0.8Si	BQ3 F3	21	86.7	-	11.4	1.9	-
0.8Si	BQ3 F4	19	86.7	-	11.4	1.9	-
0.8Si	BQ3 F5	19	86.2	-	12.0	1.8	-
0.8Si	BQ3 F6	20	87.2	-	11.0	1.8	-
0.8Si	BQ3 F7	20	86.1	-	12.0	1.9	-
0.8Si	BQ3 F8	21	87.6	4.5	5.5	2.4	-
0.8Si	BQ3 F9	19	88.5	-	9.7	1.8	-
0.8Si	BQ3 F10	21	89.4	-	8.0	2.6	-

Table 9:2 - 17BQ4 F1 - F10 Rod Characterisation.

Steel Composition	Rod ID	Measured Cooling Rate	Unresolvable Pearlite	Degenerate Pearlite	Resolvable Pearlite	Ferrite	Martensite
(wt.%)	-	$\left(\frac{^{\circ}\text{C}}{\text{s}}\right)$	(%)	(%)	(%)	(%)	(%)
0.8Si + 0.5Ni	BQ4 F1	18	86.6	4.4	7.2	1.8	-
0.8Si + 0.5Ni	BQ4 F2	20	91.4	1.8	4.9	1.9	-
0.8Si + 0.5Ni	BQ4 F3	19	95.0	2.0	2.4	0.6	-
0.8Si + 0.5Ni	BQ4 F4	17	91.7	3.0	4.1	1.2	-
0.8Si + 0.5Ni	BQ4 F5	14	87.2	5.6	5.4	1.8	-
0.8Si + 0.5Ni	BQ4 F6	18	89.4	3.0	6.0	1.6	-
0.8Si + 0.5Ni	BQ4 F7	18	92.7	1.8	3.7	1.8	-
0.8Si + 0.5Ni	BQ4 F8	16	89.1	1.2	8.9	0.8	-
0.8Si + 0.5Ni	BQ4 F9	18	88.7	3.0	7.5	0.8	-
0.8Si + 0.5Ni	BQ4 F10	17	92.7	2.0	4.7	0.6	-

Table 9:3 - 17BQ5 F1 - F10 Rod Characterisation.

Steel Composition	Rod ID	Measured Cooling Rate	Unresolvable Pearlite	Degenerate Pearlite	Resolvable Pearlite	Ferrite	Martensite
(wt.%)	-	$\left(\frac{^{\circ}\text{C}}{\text{s}}\right)$	(%)	(%)	(%)	(%)	(%)
0.8Si + 0.5Ni + 0.1 Co	BQ5 F1	16	85.0	-	12.2	2.8	-
0.8Si + 0.5Ni + 0.1 Co	BQ5 F2	17	88.0	-	9.6	2.4	-
0.8Si + 0.5Ni + 0.1 Co	BQ5 F3	18	86.5	-	10.3	3.2	-
0.8Si + 0.5Ni + 0.1 Co	BQ5 F4	18	88.0	-	9.1	2.9	-
0.8Si + 0.5Ni + 0.1 Co	BQ5 F5	18	88.4	3.0	6.3	2.3	-
0.8Si + 0.5Ni + 0.1 Co	BQ5 F6	18	89.0	-	7.8	3.2	-
0.8Si + 0.5Ni + 0.1 Co	BQ5 F7	18	87.8	-	9.4	2.8	-
0.8Si + 0.5Ni + 0.1 Co	BQ5 F8	17	84.0	-	12.8	3.2	-
0.8Si + 0.5Ni + 0.1 Co	BQ5 F9	18	88.1	-	9.6	2.3	-
0.8Si + 0.5Ni + 0.1 Co	BQ5 F10	18	86.2	-	11.0	2.8	-

Table 9:4 - 17BQ6 F1 - F10 Rod Characterisation.

Steel Composition (wt.%)	Rod ID	Measured Cooling Rate $\left(\frac{^{\circ}\text{C}}{\text{s}}\right)$	Unresolvable Pearlite (%)	Degenerate Pearlite (%)	Resolvable Pearlite (%)	Ferrite (%)	Martensite (%)
0.8Si + 0.5Ni + 0.1 Co + 0.1V	BQ6 F1	15	90.5	-	6.1	3.4	-
0.8Si + 0.5Ni + 0.1 Co + 0.1V	BQ6 F2	16	92.1	1.2	5.5	1.2	-
0.8Si + 0.5Ni + 0.1 Co + 0.1V	BQ6 F3	15	88.6	5.6	5.0	0.8	-
0.8Si + 0.5Ni + 0.1 Co + 0.1V	BQ6 F4	16	83.6	10.2	5.6	0.6	-
0.8Si + 0.5Ni + 0.1 Co + 0.1V	BQ6 F5	15	90.0	-	7.2	2.8	-
0.8Si + 0.5Ni + 0.1 Co + 0.1V	BQ6 F6	14	91.0	1.2	6.6	1.2	-
0.8Si + 0.5Ni + 0.1 Co + 0.1V	BQ6 F7	14	89.0	1.8	6.4	2.8	-
0.8Si + 0.5Ni + 0.1 Co + 0.1V	BQ6 F8	15	85.2	7.0	7.0	0.8	-
0.8Si + 0.5Ni + 0.1 Co + 0.1V	BQ6 F9	15	90.5	-	8.3	1.2	-
0.8Si + 0.5Ni + 0.1 Co + 0.1V	BQ6 F10	15	90.3	1.9	5.8	2.0	-

9.1.2 Wire Drawing

6 rods from each experimental steel were selected and welded into the carrier coil. All rods were drawn to 2.5mm ($\epsilon = 1.6$), 2 rods were drawn further to 1.6mm ($\epsilon = 2.4$). Drawing from 5.5mm to 2.5mm diameter ($\epsilon=1.6$) was completed over 7 drawing passes. Drawing from 2.5mm to 1.65mm diameter wire ($\epsilon = 2.4$) was completed with a further 5 passes. Prior to drawing, the rods were painted and coated in borax. The paint was for identification through the wire drawing process.

9.1.2.1 2.5mm wire

Wire drawing parameters are summarised in Figure 9:2 and Table 9:5.

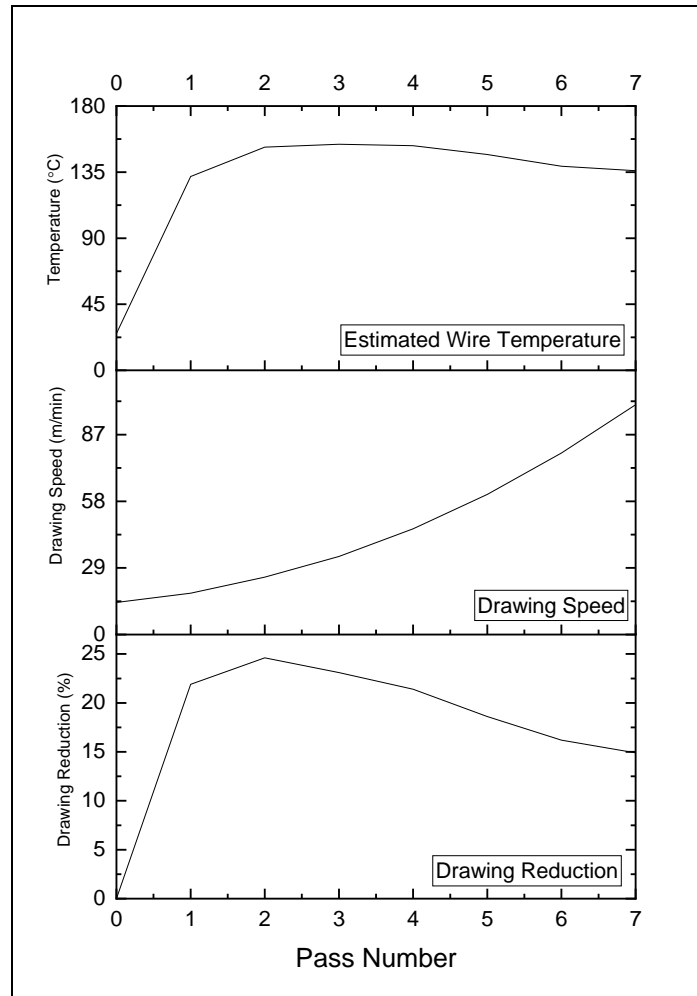


Figure 9:1 - 5.5mm to 2.5mm wire drawing parameters.

Table 9:5 - BTC Drawing Schedule 5.5mm rod to 2.5mm diameter wire.

Pass Number	Die Diameter (mm)	Wire Reduction (%)	Wire Speed (m/min)	Estimated Wire Temperature (°C)
0	5.5	0.0	14.0	25.0
1	4.86	21.9	18.0	132.0
2	4.22	24.6	25.0	152.0
3	3.7	23.1	34.0	154.0
4	3.28	21.4	46.0	153.0
5	2.96	18.6	61.0	147.0
6	2.71	16.2	79.0	139.0
7	2.5	14.9	100.0	136.0

Wire breakages frequently occurred in the welded region between the carrier coil and the experimental rods. The coating of paint used to mark and follow the experimental rods through the drawing machine rapidly spread and faded during drawing, making the identification of rod difficult. Steel BQ4, the 0.8 Si + 0.5 Ni steel, repeatedly failed in the welded region and within the experimental rod. The difficulty in drawing, as noted in Table 9:7, may be due to the presence of degenerate pearlite in the majority of the rods, shown in Table 9:2, which was therefore unavoidable.

Table 9:6 - 0.8 Si Steel 2.5mm Drawing Summary.

Rod ID	Comment
BQ3 F2	Successfully Drawn
BQ3 F3	Successfully Drawn
BQ3 F4	Failed at Weld
BQ3 F5	Successfully Drawn

Table 9:7 - 0.8 Si + 0.5 Ni Steel 2.5mm Drawing Summary.

Rod ID	Comment
BQ4 F2	Successfully Drawn
BQ4 F3	Failed in Rod
BQ4 F4	Failed in Rod
BQ4 F5	Failed at Weld

Table 9:8 - 0.8 Si + 0.5 Ni + 0.1 Co Steel 2.5mm Drawing Summary.

Rod ID	Comment
BQ5 F1	Successfully Drawn
BQ5 F2	Failed at Weld
BQ5 F3	Successfully Drawn
BQ5 F5	Successfully Drawn

Table 9:9 - 0.8 Si + 0.5 Ni + 0.1 Co + 0.1 V Steel 2.5mm Drawing Summary.

Rod ID	Comment
BQ6 F5	Successfully Drawn
BQ6 F6	Successfully Drawn
BQ6 F9	Failed at weld twice
BQ6 F10	Successfully Drawn

9.1.2.2 1.65mm Wire

5 additional passes were required to produce 1.65mm diameter wire. Wire drawn to 1.65mm was left overnight after being drawn to 2.5mm. Wire drawing parameters are summarised in Figure 9:2 and Table 9:10.

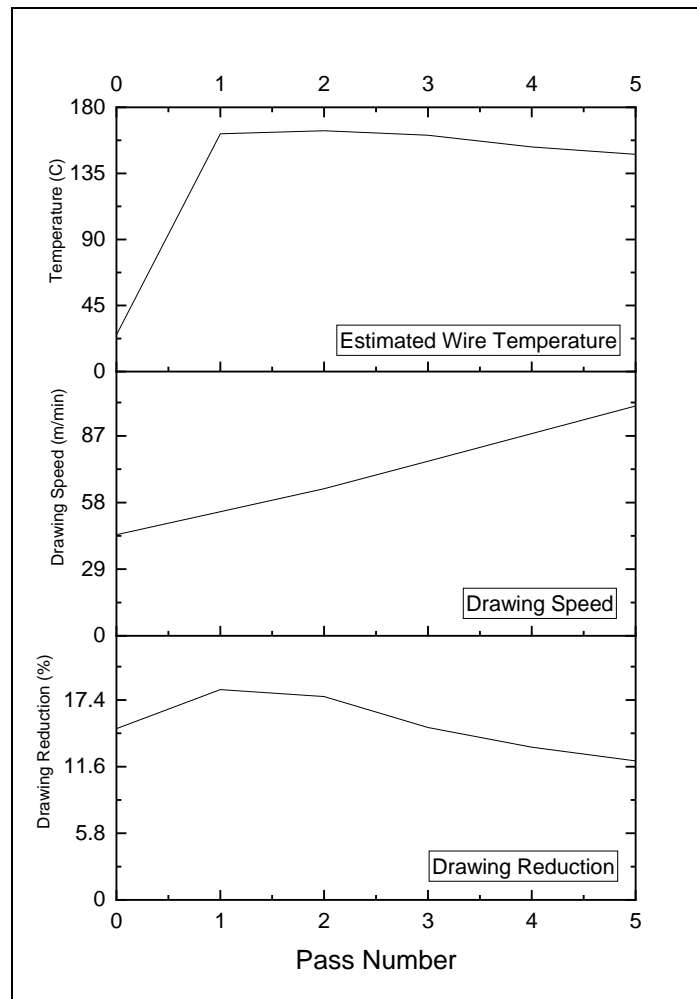


Figure 9:2 - 2.5mm - 1.65mm Wire Drawing Parameters.

Table 9:10 - BTC Schedule 2.5mm to 1.65mm.

Pass Number	Die Diameter (mm)	Wire Reduction (%)	Wire Speed (m/min)	Estimated Wire Temperature (°C)
0	2.5	-	44.0	25.0
1	2.26	18.3	54.0	162.0
2	2.05	17.7	64.0	164.0
3	1.89	15.0	76.0	161.0
4	1.76	13.3	88.0	153.0
5	1.65	12.1	100.0	148.0

Further wire breakages occurred when drawing to 1.65mm wire. The coating of paint used to mark and follow the experimental rods was reapplied prior to further drawing. As before, paint rapidly spread and faded during drawing, and rod identification was challenging.

Table 9:11 - 0.8 Si 1.65mm Drawing Summary.

Rod ID	Comment
BQ3 F3	Initially failed at weld, successfully drawn after rewelding
BQ3 F8	Initially failed at weld, successfully drawn after rewelding

Table 9:12 - 0.8 Si + 0.5 Ni 1.65mm Drawing Summary.

Rod ID	Comment
BQ4 F6	Successfully drawn
BQ4 F7	Successfully drawn

Table 9:13 - 0.8 Si + 0.5 Ni + 0.1 Co 1.65mm Drawing Summary.

Rod ID	Comment
BQ5 F7	Successfully drawn
BQ5 F8	Failed at Weld

Table 9:14 - 0.8 Si + 0.5 Ni + 0.1 Co + 0.1 V 1.65mm Drawing Summary.

Rod ID	Comment
BQ6 F6	Successfully drawn
BQ6 F7	Successfully drawn

9.1.3 Spark Analysis

The rapid fading and spreading of paint used to mark the experimental steel rods created the possibility of sample misidentification. After wire drawing, spark analysis was completed to ensure the correct composition was present. The analysis was completed at Scunthorpe central labs. Spark analysis was performed on each end of a coil; if the expected composition was not identified, 10cm of wire was removed and the spark analyses was repeated until the correct composition was measured. Spark analysis was completed on all 2.5mm wire to ensure the correct material had been identified. The 1.65mm diameter wire was too narrow to be analysed with the spark analyser, so this material was not assessed any further. The results from this analysis are shown in Figure 9:3 Figure 9:4, Figure 9:5 and Figure 9:6.

One coil from each composition was correctly identified as experimental steels, with the remaining material all identified as the carrier coil composition. Thus, approximately 2 metres of wire was available per composition. With the exception of BQ4 (0.8 Si + 0.5 Ni), due to failures during drawing, only one coil was successfully drawn, of which, 0.5m was identified as the correct composition.

Friday, June 8, 2018 11:43:41 AM

Sample Result Name	Type	Method Name	Operator Name
.I.I.	Unknown	Fe-10-MO	

Measure Date Time	Instrument	Recalculation Date Time
6/8/2018 11:28 AM	PXC01	6/8/2018 11:29 AM

Coil 1	SHIFT	Lot Number	Coil 2	Coil 3	Coil 4
.	DAYS	17BQ3F10	.	.	.

			1	2	<X>
C	%	Conc	0.86	0.78	0.82
Si	%	Conc	0.71	0.73	0.72
Mn	%	Conc	0.34	0.34	0.34
P	%	Conc	0.0094	0.0077	0.0086
S	%	Conc	[C<]0.0020	[C<]0.0020	[C<]0.0020
Cr	%	Conc	[C<]0.0110	[C<]0.0110	[C<]0.0110
Mo	%	Conc	[C<]0.0070	[C<]0.0070	[C<]0.0070
Ni	%	Conc	[C<]0.0110	[C<]0.0110	[C<]0.0110
Al	%	Conc	[C<]0.0040	[C<]0.0040	[C<]0.0040
Co	%	Conc	[C<]0.0040	[C<]0.0040	[C<]0.0040
Cu	%	Conc	[C<]0.0040	[C<]0.0040	[C<]0.0040
Nb	%	Conc	[C<]0.0070	[C<]0.0070	[C<]0.0070
Ti	%	Conc	[C<]0.0020	[C<]0.0020	[C<]0.0020
V	%	Conc	0.0041	[C<]0.0040	0.0040
W	%	Conc	[C<]0.040	[C<]0.040	[C<]0.040
Pb	%	Conc	[C<]0.0110	[C<]0.0110	[C<]0.0110
Sn	%	Conc	0.0031	[C<]0.0020	0.0025
As	%	Conc	[C<]0.0050	[C<]0.0050	[C<]0.0050
Zr	%	Conc	[C<]0.0070	[C<]0.0070	[C<]0.0070
B	%	Conc	0.0006	0.0008	0.0007
Fe	%	Conc	98.0	98.0	98.0

Figure 9:3 - Spark Analysis Report - 17BQ3F10 2.5mm Wire.

Friday, June 8, 2018 11:44:52 AM

Sample Result Name	Type	Method Name	Operator Name
1/2/3	Unknown	Fe-10-MO	

Measure Date Time	Instrument	Recalculation Date Time
6/8/2018 11:38 AM	PXC01	6/8/2018 11:39 AM

Coil 1	SHIFT	Lot Number	Coil 2	Coil 3	Coil 4
1	DAYS	17BQ4F4	2	3	

		1	2	3	<X>
C	% Conc	1.49	1.23	1.42	1.38
Si	% Conc	0.76	0.70	0.72	0.73
Mn	% Conc	0.32	0.33	0.33	0.33
P	% Conc	0.0162	0.0217	0.0250	0.0210
S	% Conc	0.0073	0.0174	0.0206	0.0151
Cr	% Conc	[C<]0.0110	[C<]0.0110	[C<]0.0110	[C<]0.0110
Mo	% Conc	0.0088	0.0078	0.0091	0.0086
Ni	% Conc	0.47	0.49	0.49	0.48
Al	% Conc	0.0068	[C<]0.0040	[C<]0.0040	0.0049
Co	% Conc	0.099	0.057	0.062	0.072
Cu	% Conc	[C<]0.0040	[C<]0.0040	[C<]0.0040	[C<]0.0040
Nb	% Conc	[C<]0.0070	[C<]0.0070	[C<]0.0070	[C<]0.0070
Ti	% Conc	[C<]0.0020	[C<]0.0020	[C<]0.0020	[C<]0.0020
V	% Conc	0.0074	0.0091	0.0107	0.0091
W	% Conc	[C<]0.040	[C<]0.040	[C<]0.040	[C<]0.040
Pb	% Conc	[C<]0.0110	[C<]0.0110	[C<]0.0110	[C<]0.0110
Sn	% Conc	0.0030	0.0053	0.0054	0.0046
As	% Conc	[C<]0.0050	[C<]0.0050	[C<]0.0050	[C<]0.0050
Zr	% Conc	[C<]0.0070	[C<]0.0070	[C<]0.0070	[C<]0.0070
B	% Conc	0.0138	[C>]0.0180	[C>]0.0180	0.0166
Fe	% Conc	96.7	97.0	96.8	96.8

Figure 9:4 - Spark Analysis Report- 17BQ4 2.5mm wire.

Friday, June 8, 2018 11:44:13 AM

Sample Result Name	Type	Method Name	Operator Name
J.J.J.	Unknown	Fe-10-MO	

Measure Date Time	Instrument	Recalculation Date Time
6/8/2018 11:32 AM	PXC01	6/8/2018 11:32 AM

Coil 1	SHIFT	Lot Number	Coil 2	Coil 3	Coil 4
.	DAYS	17BQ5F8	.	.	.

			1	2	<X>
C	%	Conc	0.72	0.67	0.69
Si	%	Conc	0.74	0.74	0.74
Mn	%	Conc	0.33	0.32	0.33
P	%	Conc	0.0077	0.0070	0.0074
S	%	Conc	[C<]0.0020	[C<]0.0020	[C<]0.0020
Cr	%	Conc	[C<]0.0110	[C<]0.0110	[C<]0.0110
Mo	%	Conc	[C<]0.0070	[C<]0.0070	[C<]0.0070
Ni	%	Conc	0.52	0.52	0.52
Al	%	Conc	0.0058	0.0066	0.0062
Co	%	Conc	[C<]0.0040	[C<]0.0040	[C<]0.0040
Cu	%	Conc	[C<]0.0040	[C<]0.0040	[C<]0.0040
Nb	%	Conc	[C<]0.0070	[C<]0.0070	[C<]0.0070
Ti	%	Conc	[C<]0.0020	[C<]0.0020	[C<]0.0020
V	%	Conc	[C<]0.0040	[C<]0.0040	[C<]0.0040
W	%	Conc	[C<]0.040	[C<]0.040	[C<]0.040
Pb	%	Conc	[C<]0.0110	[C<]0.0110	[C<]0.0110
Sn	%	Conc	[C<]0.0020	[C<]0.0020	[C<]0.0020
As	%	Conc	[C<]0.0050	[C<]0.0050	[C<]0.0050
Zr	%	Conc	[C<]0.0070	[C<]0.0070	[C<]0.0070
B	%	Conc	0.0009	0.0006	0.0008
Fe	%	Conc	97.6	97.6	97.6

Figure 9:5 - Spark Analysis Report - 17BQ5F5 2.5mm wire.

Friday, June 8, 2018 11:44:30 AM

Sample Result Name	Type	Method Name	Operator Name
J.J.J.	Unknown	Fe-10-MO	

Measure Date Time	Instrument	Recalculation Date Time
6/8/2018 11:33 AM	PXC01	6/8/2018 11:34 AM

Coil 1	SHIFT	Lot Number	Coil 2	Coil 3	Coil 4
.	DAYS	17BQ6F7	.	.	.

			1	2	<X>
C	%	Conc	0.74	0.70	0.72
Si	%	Conc	0.75	0.76	0.75
Mn	%	Conc	0.31	0.31	0.31
P	%	Conc	0.0098	0.0103	0.0100
S	%	Conc	[C<]0.0020	[C<]0.0020	[C<]0.0020
Cr	%	Conc	[C<]0.0110	[C<]0.0110	[C<]0.0110
Mo	%	Conc	[C<]0.0070	[C<]0.0070	[C<]0.0070
Ni	%	Conc	0.48	0.47	0.47
Al	%	Conc	[C<]0.0040	[C<]0.0040	[C<]0.0040
Co	%	Conc	0.091	0.104	0.097
Cu	%	Conc	[C<]0.0040	[C<]0.0040	[C<]0.0040
Nb	%	Conc	[C<]0.0070	[C<]0.0070	[C<]0.0070
Ti	%	Conc	[C<]0.0020	[C<]0.0020	[C<]0.0020
V	%	Conc	0.103	0.102	0.102
W	%	Conc	[C<]0.040	[C<]0.040	[C<]0.040
Pb	%	Conc	[C<]0.0110	[C<]0.0110	[C<]0.0110
Sn	%	Conc	0.0022	[C<]0.0020	0.0021
As	%	Conc	[C<]0.0050	[C<]0.0050	[C<]0.0050
Zr	%	Conc	[C<]0.0070	[C<]0.0070	[C<]0.0070
B	%	Conc	0.0008	0.0008	0.0008
Fe	%	Conc	97.4	97.4	97.4

Figure 9:6 - Spark Analysis Report - 17BQ6F7 2.5mm wire.

9.1.4 Multi-pass Wire Drawing Machine Summary

Welding rods into a carrier coil resulted in the majority of drawn wire being misidentified, owing to a loss of the paint in the finished wire. Previous work has utilised a copper coating, which performed much better and should be considered essential for any further trials of a similar nature. The wire also frequently failed at the welds during drawing and so it is recommended to heat treat much longer lengths of rods in any future work, which may be possible via longer tube furnace or in-line patenting, if available.

9.2 Tensile Testing Data

9.2.1 Commercial Steel

9.2.1.1.1 As-drawn

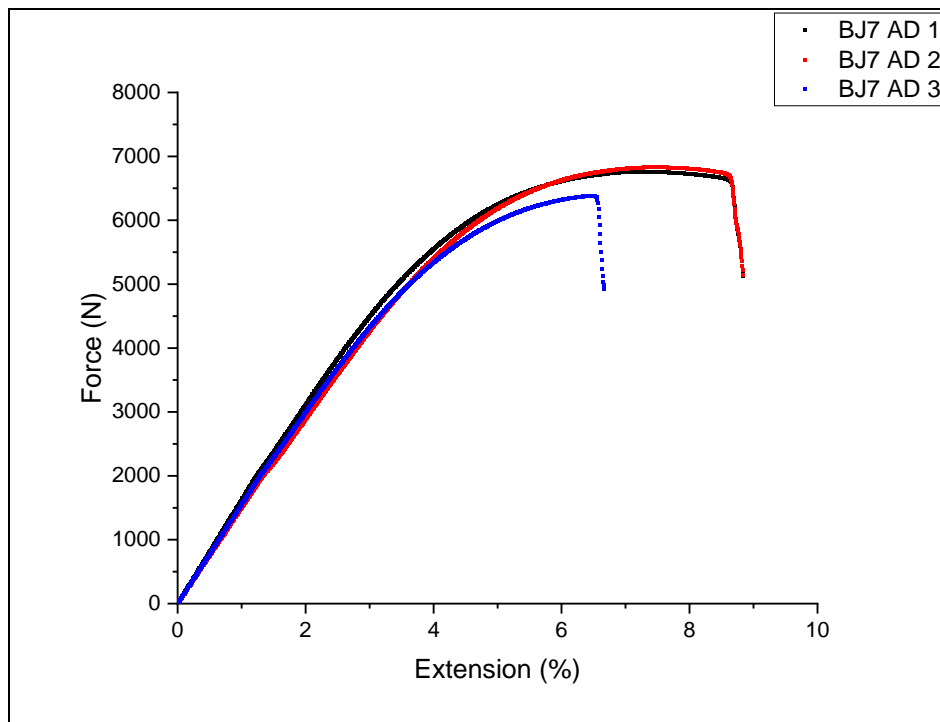


Figure 9:7 - Tensile testing data of the commercial steel in the as-drawn condition.

Table 9:15 - Tensile testing results of the commercial steel in the as-drawn condition.

Sample ID	0.2% Proof (MPa)	UTS (MPa)	0.2%Proof / UTS	Elongation to Failure (%)	Fracture Type
-	(MPa)	(MPa)	-	(%)	-
BJ7 AD T1	1509.85	1828.01	0.83	8.84	Cup & Cone
BJ7 AD T2	1578.79	1846.55	0.86	8.84	Cup & Cone
BJ7 AD T3	1476.13	1725.53	0.86	6.67	Cup & Cone
Mean	1521.59	1800.03	0.85	8.12	-
Lower 95% CL	1391.60	1638.11	0.80	5.00	-
Upper 95% CL	1651.58	1961.95	0.89	11.23	-

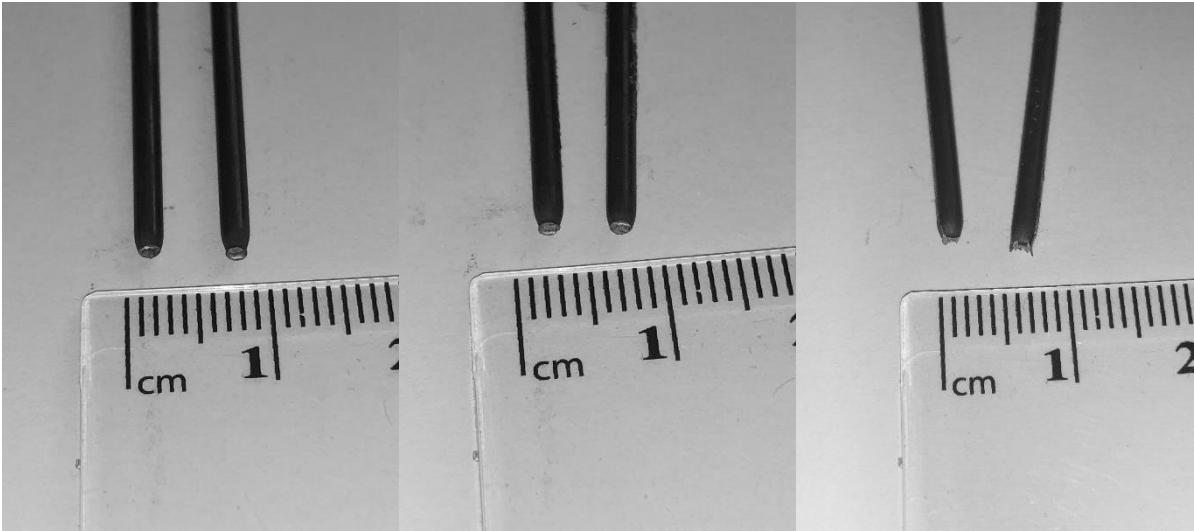


Figure 9:8 - Commercial steel as drawn tensile fractures.

9.2.1.1.2 1 Month Artificial Ageing Condition

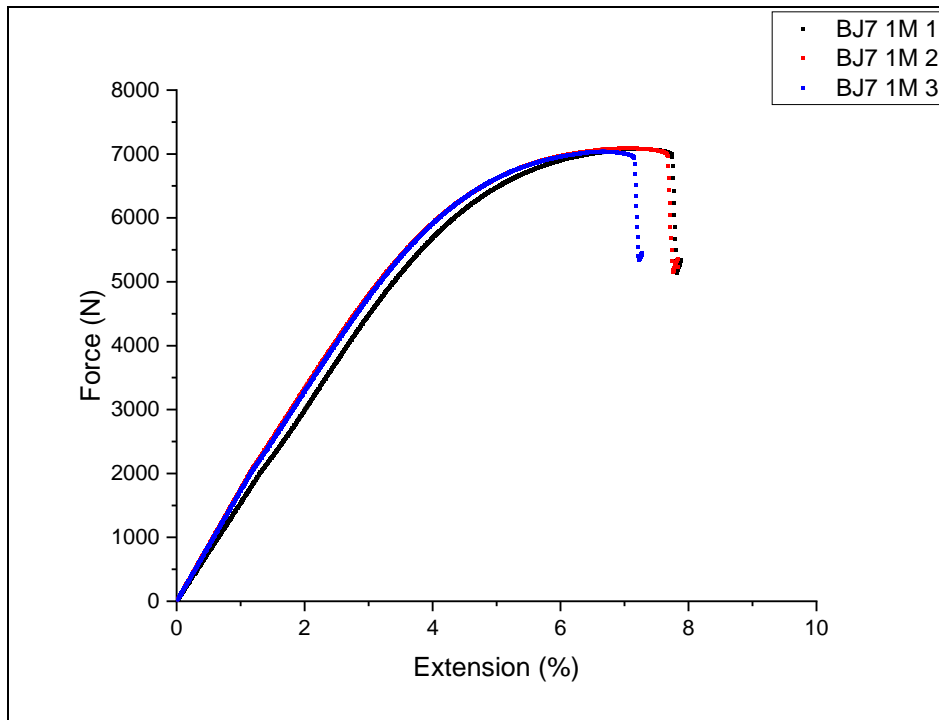


Figure 9:9 - Tensile testing data of the commercial steel in the 1 month artificial ageing condition.

Table 9:16 - Tensile testing results of the commercial steel in the 1 month artificial ageing condition.

Sample ID	0.2% Proof (MPa)	UTS (MPa)	0.2%Proof / UTS	Elongation to Failure (%)	Fracture Type
-			-		-
BJ7 1M 1	1705.46	1913.58	0.89	7.89	Cup & Cone
BJ7 1M 2	1628.82	1916.69	0.85	7.84	Cup & Cone
BJ7 1M 3	1643.28	1902.84	0.86	7.28	Cup & Cone
Mean	1659.19	1911.04	0.87	7.67	-
Lower 95% CL	1558.04	1892.99	0.82	6.82	-
Upper 95% CL	1760.34	1929.09	0.92	8.51	-

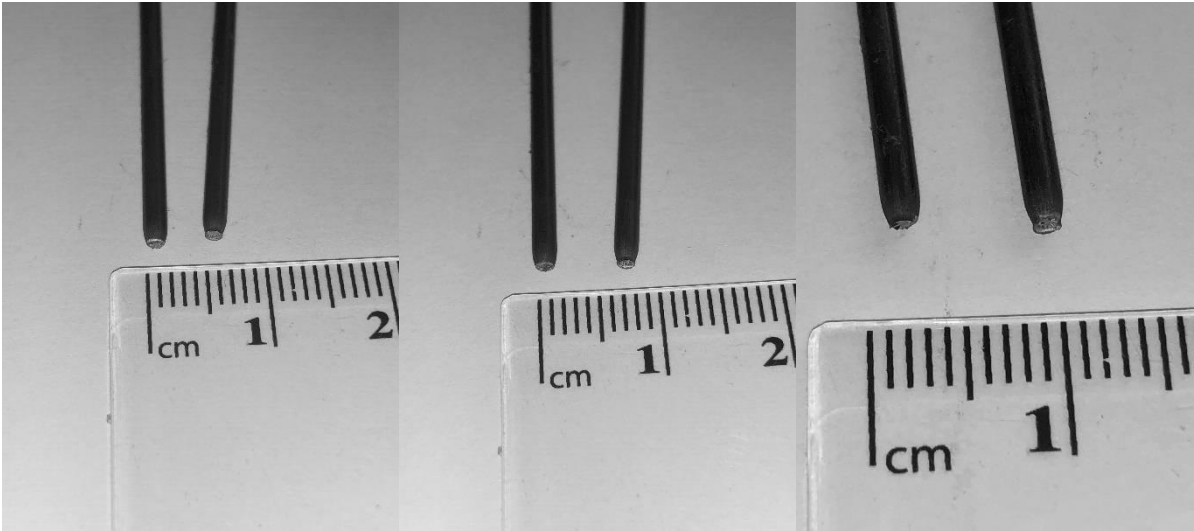


Figure 9:10 - Commercial Steel 1 month artificial ageing condition tensile fractures.

9.2.1.1.3 2 Month Artificial Ageing Condition

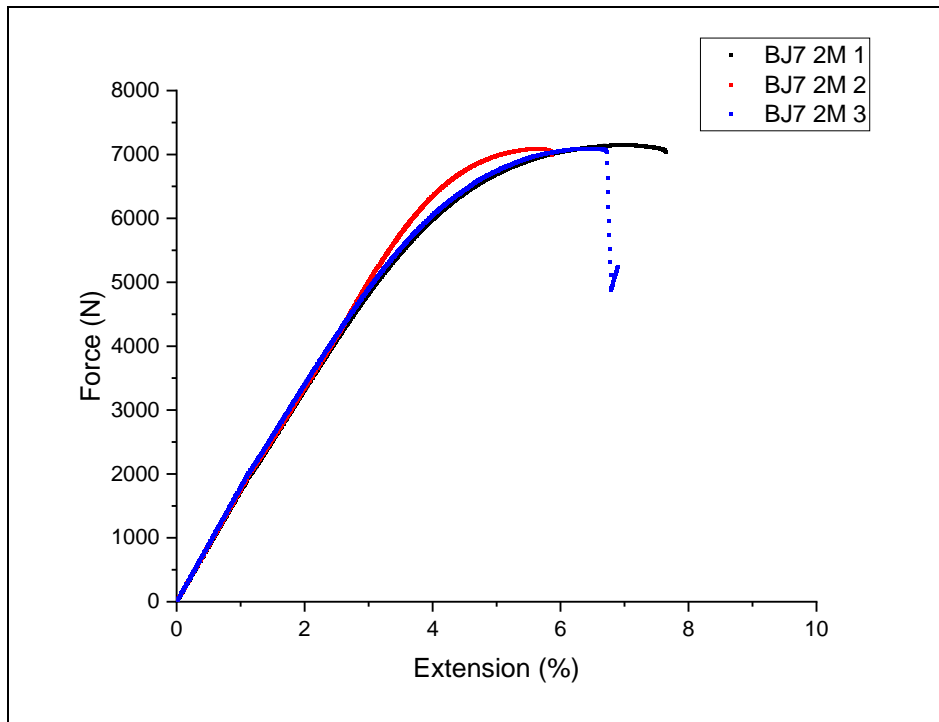


Figure 9:11 - Tensile testing data of the commercial steel in the 2 month artificial ageing condition.

Table 9:17 - Tensile testing results of the commercial steel in the 2 month artificial ageing condition.

Sample ID	0.2% Proof (MPa)	UTS (MPa)	0.2%Proof / UTS	Elongation to Failure (%)	Fracture Type
-	(MPa)	(MPa)	-	(%)	-
BJ7 2M 1	1693.45	1932.19	0.88	7.64	Cup & Cone
BJ7 2M 2	1680.51	1917.11	0.88	5.87	Cup & Cone
BJ7 2M 3	1785.56	1918.17	0.93	6.89	Cup & Cone
Mean	1719.84	1922.49	0.89	6.80	-
Lower 95% CL	1577.54	1901.57	0.82	4.59	-
Upper 95% CL	1862.14	1943.40	0.97	9.01	-

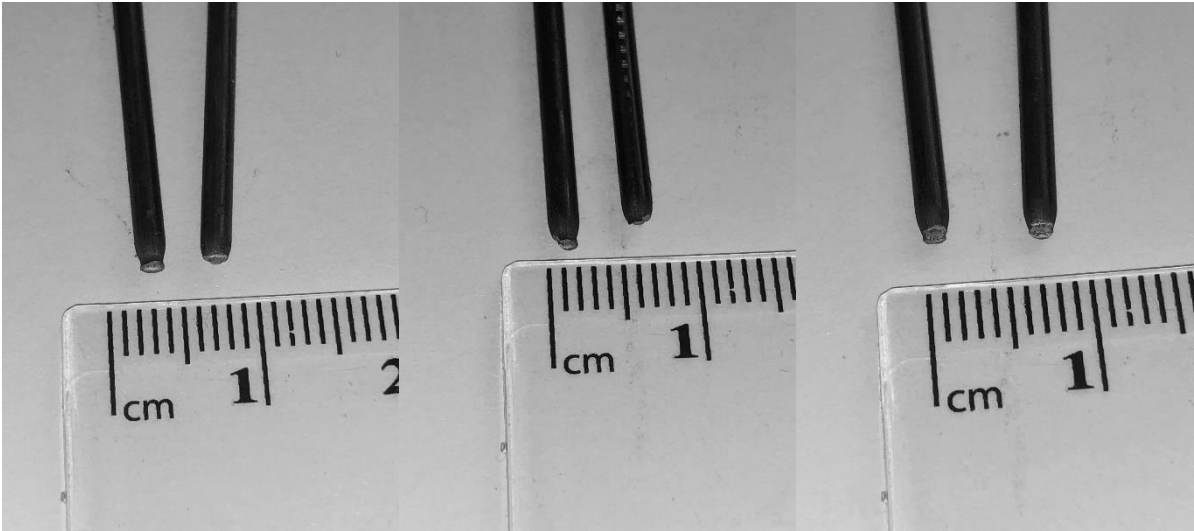


Figure 9:12 - Commercial Steel 2 month artificial ageing condition tensile fractures.

9.2.1.1.4 4 Month Artificial Ageing Condition

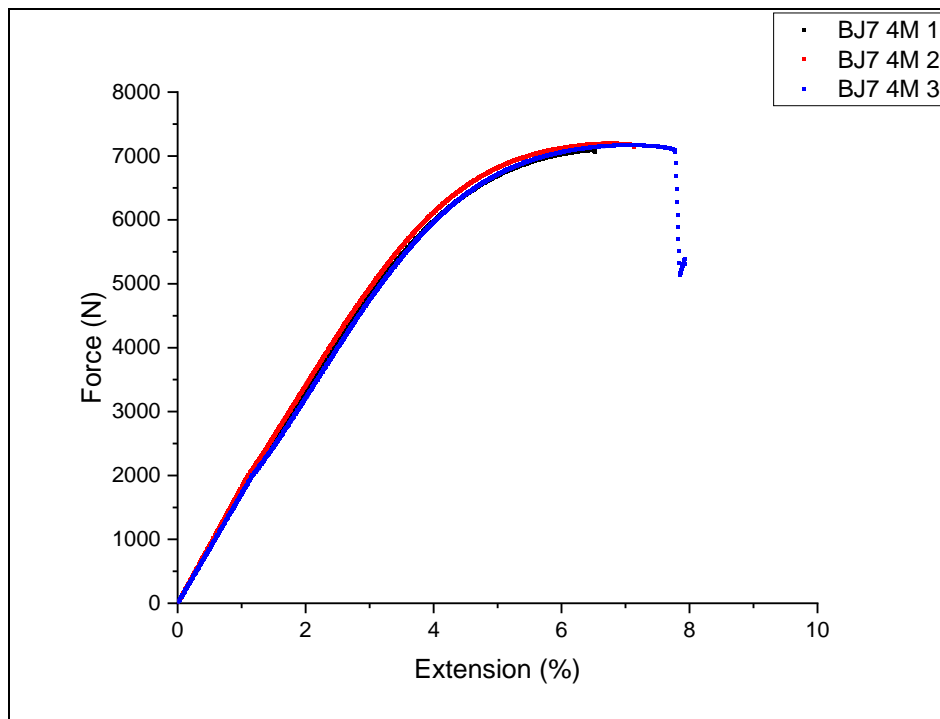


Figure 9:13 - Tensile testing data of the commercial steel in the 2 month artificial ageing condition.

Table 9:18 - Tensile testing results of the commercial steel in the 2 month artificial ageing condition.

Sample ID	0.2% Proof (MPa)	UTS (MPa)	0.2%Proof / UTS	Elongation to Failure (%)	Fracture Type
-			-		-
BJ7 4M 1	1630.84	1916.65	0.85	6.53	Cup & Cone
BJ7 4M 2	1663.61	1946.39	0.85	7.14	Cup & Cone
BJ7 4M 3	1696.19	1939.08	0.87	7.93	Cup & Cone
Mean	1663.55	1934.04	0.86	7.20	-
Lower 95% CL	1582.38	1895.55	0.83	5.45	-
Upper 95% CL	1744.72	1972.53	0.89	8.95	-

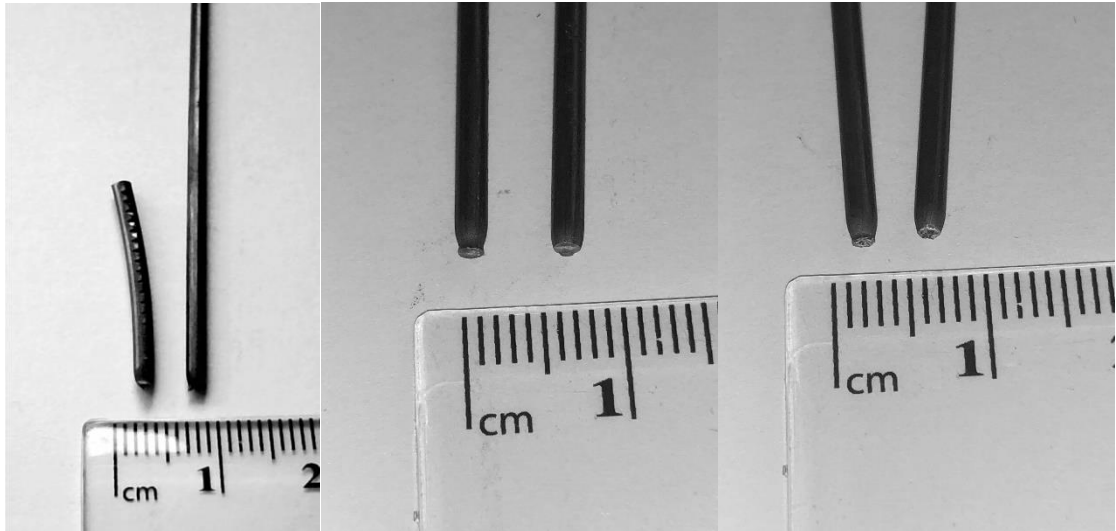


Figure 9:14 - Commercial Steel 4 month artificial ageing condition tensile fractures.

9.2.2 0.8Si Steel (BJ3)

9.2.2.1.1 As-drawn

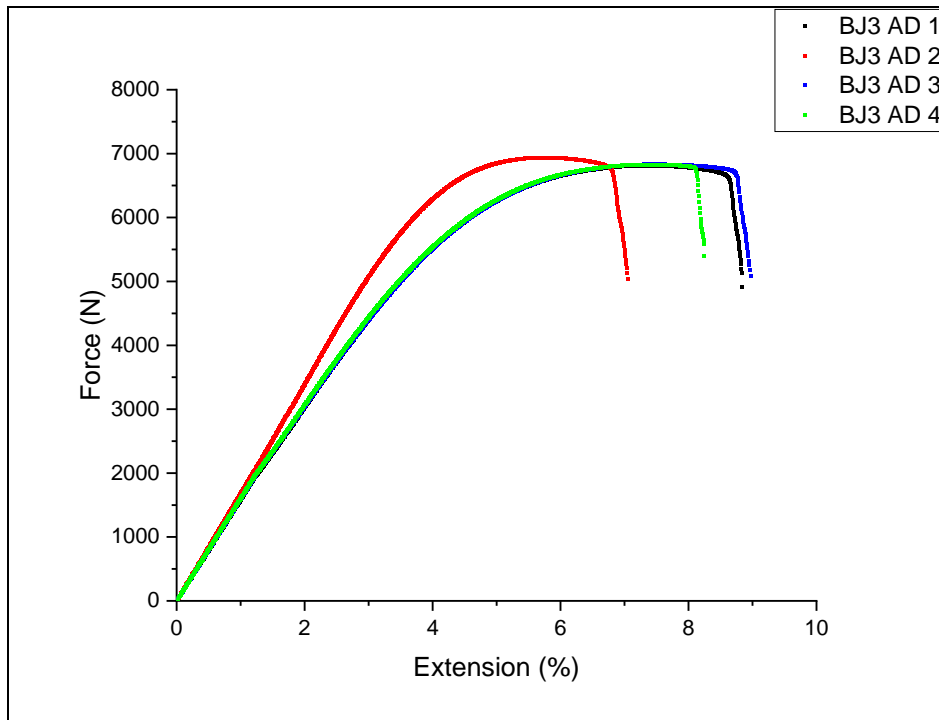


Figure 9:15 - Tensile testing data of steel BJ3 in the as-drawn condition.

Table 9:19 - Tensile testing results of steel BJ3 in the as-drawn condition.

Sample ID	0.2% Proof (MPa)	UTS (MPa)	0.2%Proof / UTS	Elongation to Failure (%)	Fracture Type
-	-	-	-	-	-
BJ3 AD 1	1535.59	1841.67	0.83	8.84	Cup & Cone
BJ3 AD 2	1665.62	1876.26	0.89	7.05	Cup & Cone
BJ3 AD 3	1528.10	1847.33	0.83	8.97	Cup & Cone
BJ3 AD 4	1518.39	1845.98	0.82	8.25	Cup & Cone
Mean	1561.93	1852.81	0.84	8.28	-
Lower 95% CL	1451.35	1827.64	0.79	6.88	-
Upper 95% CL	1672.50	1877.98	0.89	9.67	-

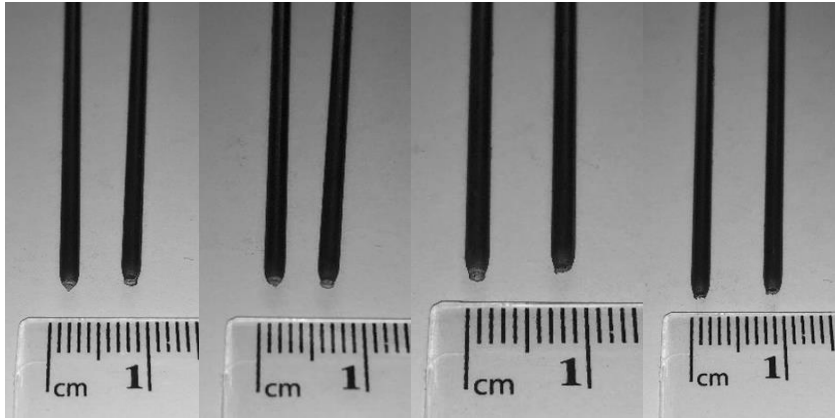


Figure 9:16 - Steel BJ3 as drawn tensile fractures.

9.2.2.1.2 1 Month Artificial Ageing Condition

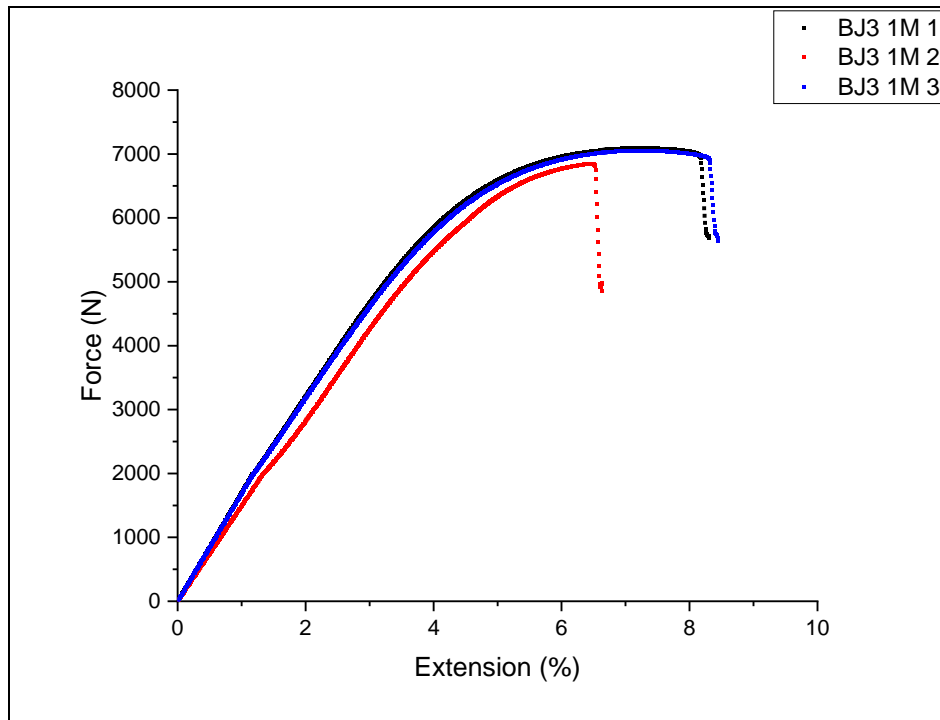


Figure 9:17 - Tensile testing data of steel BJ3 in the 1 month artificial ageing condition.

Table 9:20 - Tensile testing results of steel BJ3 in the 1 month artificial ageing condition.

Sample ID	0.2% Proof (MPa)	UTS (MPa)	0.2%Proof / UTS	Elongation to Failure (%)	Fracture Type
-			-		-
BJ3 1M 1	1606.69	1917.72	0.84	8.30	Cup & Cone
BJ3 1M 2	1658.95	1851.60	0.90	6.64	Cup & Cone
BJ3 1M 3	1635.98	1907.66	0.86	8.44	Cup & Cone
Mean	1633.87	1892.32	0.86	7.79	-
Lower 95% CL	1568.81	1803.82	0.79	5.30	-
Upper 95% CL	1698.94	1980.83	0.94	10.29	-

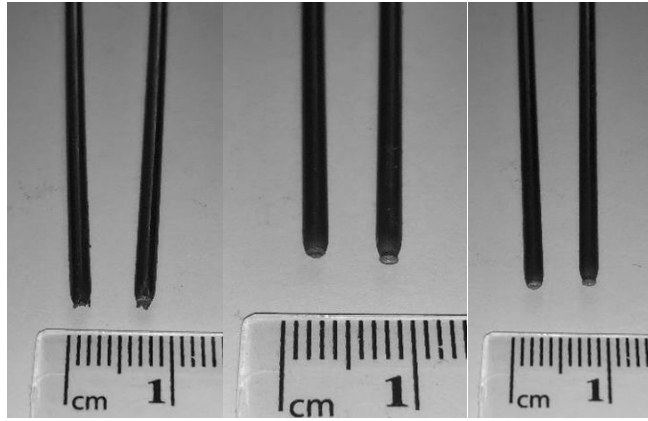


Figure 9:18 - Steel BJ3 1 month artificial ageing condition tensile fractures.

9.2.2.1.3 2 Month Artificial Ageing Condition

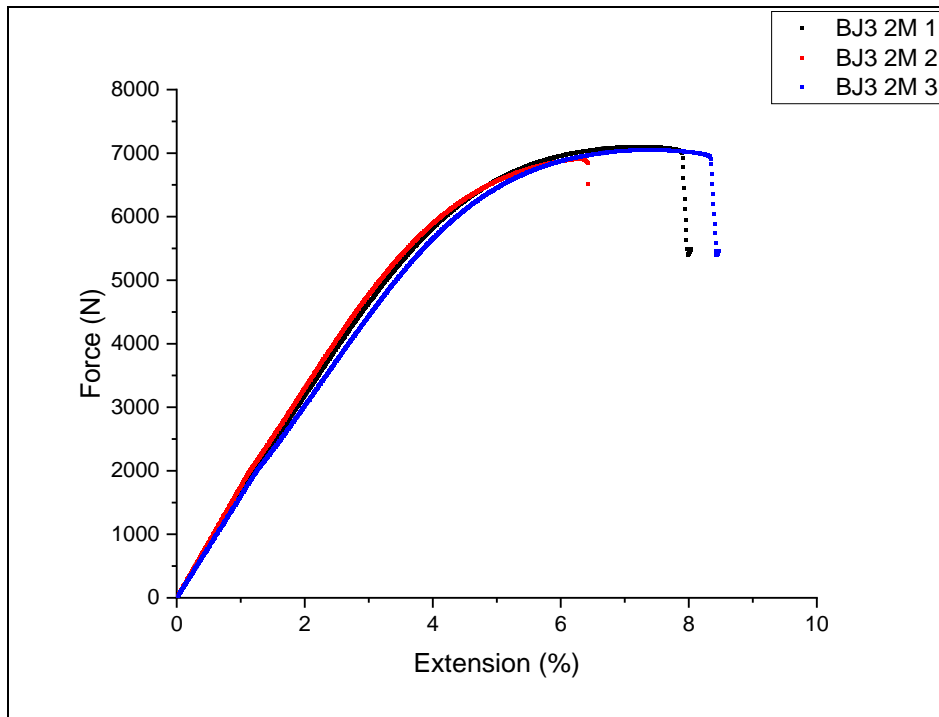


Figure 9:19 - Tensile testing data of steel BJ3 in the 2 month artificial ageing condition.

Table 9:21 - Tensile testing results of steel BJ3 in the 2 month artificial ageing condition.

Sample ID	0.2% Proof (MPa)	UTS (MPa)	0.2%Proof / UTS	Elongation to Failure (%)	Fracture Type
-	-	-	-	-	-
BJ3 2M 1	1657.31	1920.61	0.86	8.04	Cup & Cone
BJ3 2M 2	1564.04	1867.99	0.84	6.42	Cup & Cone
BJ3 2M 3	1631.57	1906.56	0.86	8.48	Cup & Cone
Mean	1617.64	1898.38	0.85	7.64	-
Lower 95% CL	1497.97	1830.71	0.82	4.96	-
Upper 95% CL	1737.30	1966.06	0.88	10.33	-

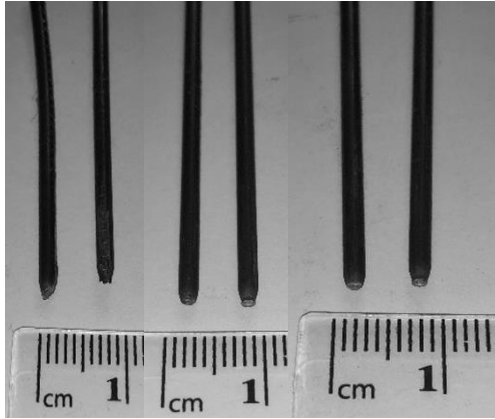


Figure 9:20 - Steel BJ3 1 month artificial ageing condition tensile fractures.

9.2.2.1.4 4 Month Artificial Ageing Condition

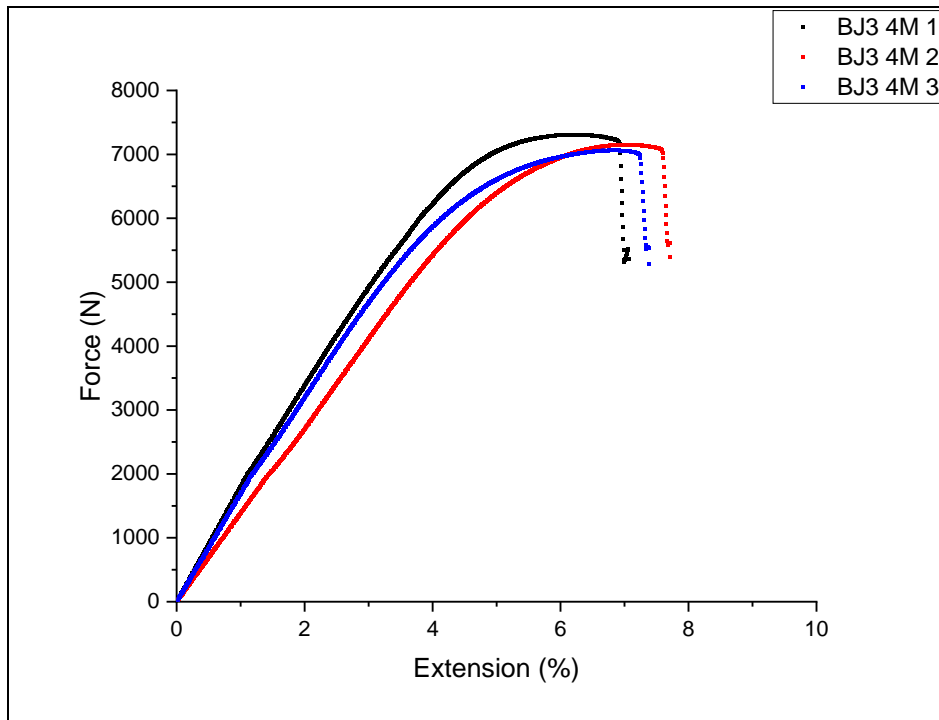


Figure 9:21 - Tensile testing data of steel BJ3 in the 4 month artificial ageing condition.

Table 9:22 - Tensile testing results of steel BJ3 in the 4 month artificial ageing condition.

Sample ID	0.2% Proof (MPa)	UTS (MPa)	0.2%Proof / UTS	Elongation to Failure (%)	Fracture Type
-			-		-
BJ3 4M 1	1706.95	1976.51	0.86	7.06	Cup & Cone
BJ3 4M 2	1805.43	1934.12	0.93	7.71	Cup & Cone
BJ3 4M 3	1625.61	1909.77	0.85	7.38	Cup & Cone
Mean	1712.67	1940.13	0.88	7.39	-
Lower 95% CL	1488.98	1856.24	0.77	6.58	-
Upper 95% CL	1936.35	2024.03	0.99	8.19	-

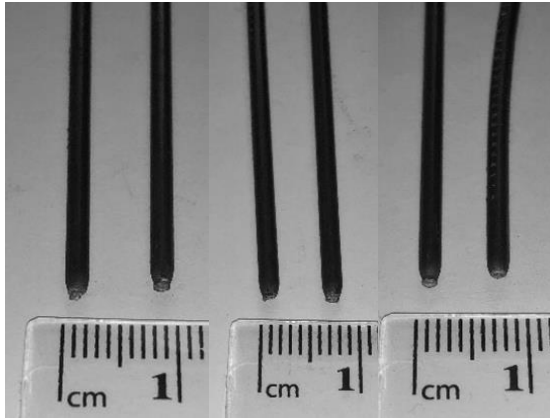


Figure 9:22 - Steel BJ3 1 month artificial ageing condition tensile fractures.

9.2.3 0.8Si + 0.5Ni Steel (BJ4)

9.2.3.1.1 As-drawn

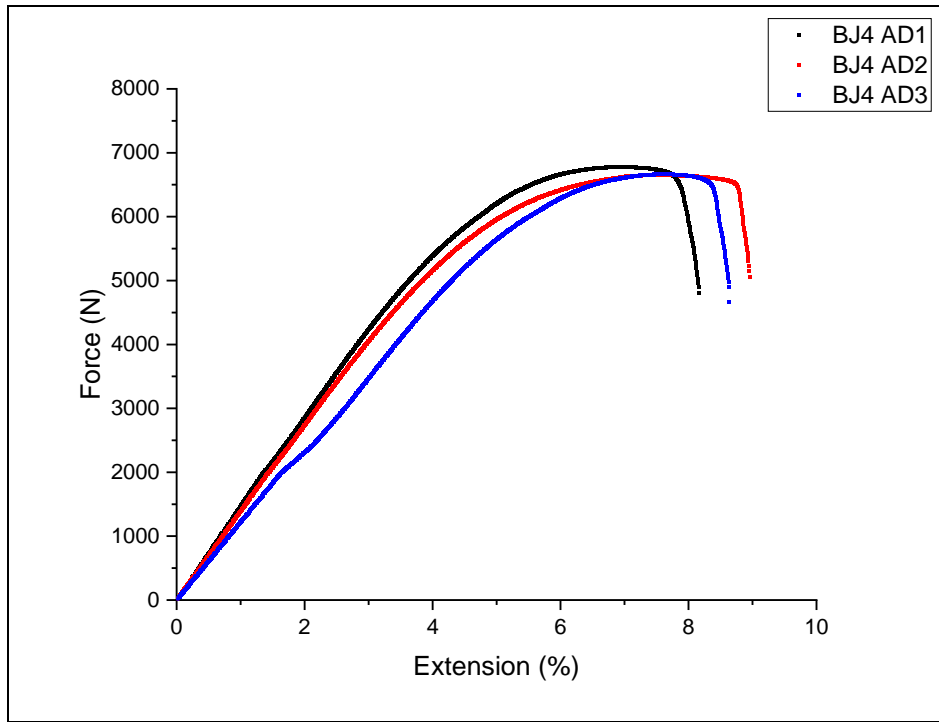


Figure 9:23 - Tensile testing data of steel BJ4 in the as-drawn condition.

Table 9:23 - Tensile testing results of steel BJ4 in the as drawn condition.

	0.2% Proof (MPa)	UTS (MPa)	0.2%Proof / UTS -	Elongation to Failure (%)	Fracture Type -
BJ4 AD1 1	1648.20	1832.71	0.90	8.16	Cup & Cone
BJ4 AD1 2	1598.19	1798.61	0.89	8.96	Cup & Cone
BJ4 AD1 3	1681.74	1801.83	0.93	8.64	Cup & Cone
Mean	1642.71	1811.05	0.91	8.59	-
Lower 95% CL	1538.26	1764.28	0.85	7.59	-
Upper 95% CL	1747.16	1857.81	0.97	9.58	-

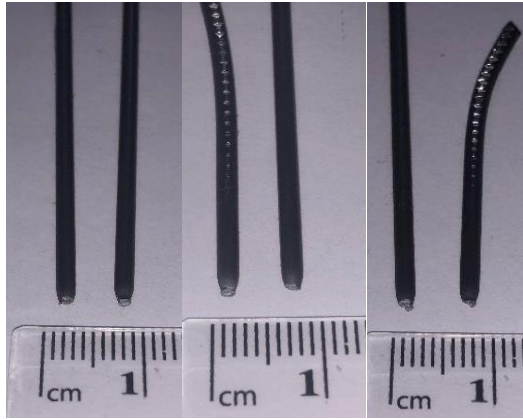


Figure 9:24 - Steel BJ4 1 as-drawn tensile fractures.

9.2.3.1.2 1 Month Artificial Ageing Condition

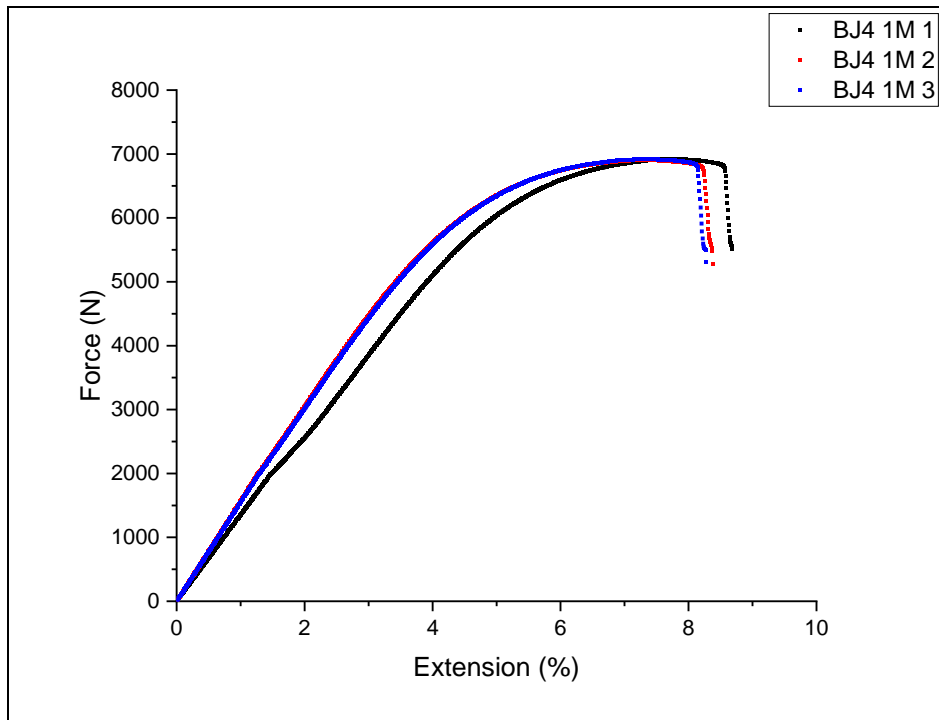


Figure 9:25 - Tensile testing data of steel BJ4 in the 1 month artificial ageing condition.

Table 9:24 - Tensile testing results of steel BJ4 in the 1 month artificial ageing condition.

Sample ID	0.2% Proof (MPa)	UTS (MPa)	0.2%Proof / UTS	Elongation to Failure (%)	Fracture Type
-			-		-
BJ4 1M 1	1685.31	1870.89	0.90	8.68	Cup & Cone
BJ4 1M 2	1621.56	1866.47	0.87	8.37	Cup & Cone
BJ4 1M 3	1622.16	1870.44	0.87	8.27	Cup & Cone
Mean	1643.01	1869.27	0.88	8.44	-
Lower 95% CL	1552.00	1863.23	0.83	7.92	-
Upper 95% CL	1734.02	1875.30	0.93	8.97	-

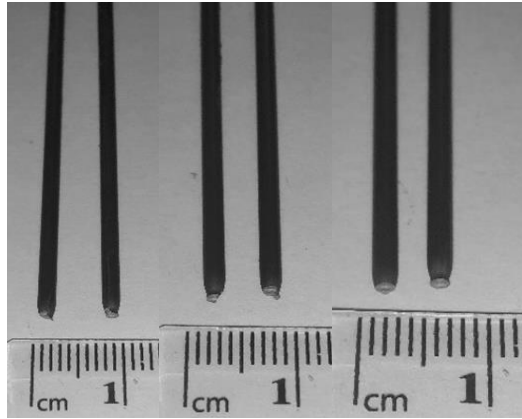


Figure 9:26 - Steel BJ4 1 month artificial ageing condition tensile fractures.

9.2.3.1.3 2 Month Artificial Ageing Condition

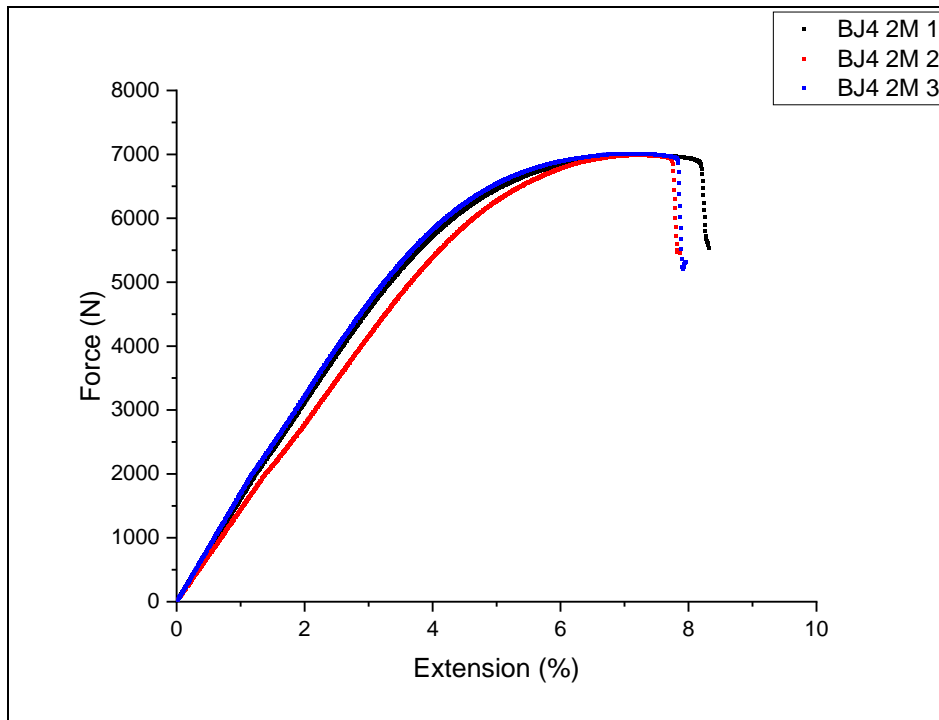


Figure 9:27 - Tensile testing data of steel BJ4 in the 2 month artificial ageing condition.

Table 9:25 - Tensile testing results of steel BJ4 in the 2 month artificial ageing condition.

Sample ID	0.2% Proof (MPa)	UTS (MPa)	0.2%Proof / UTS	Elongation to Failure (%)	Fracture Type
-			-		-
BJ4 2M 1	1679.89	1889.89	0.89	8.31	Cup & Cone
BJ4 2M 2	1722.63	1889.50	0.91	7.86	Cup & Cone
BJ4 2M 3	1604.88	1895.48	0.85	7.95	Cup & Cone
Mean	1669.13	1891.62	0.88	8.04	-
Lower 95% CL	1521.06	1883.31	0.80	7.45	-
Upper 95% CL	1817.21	1899.94	0.96	8.63	-

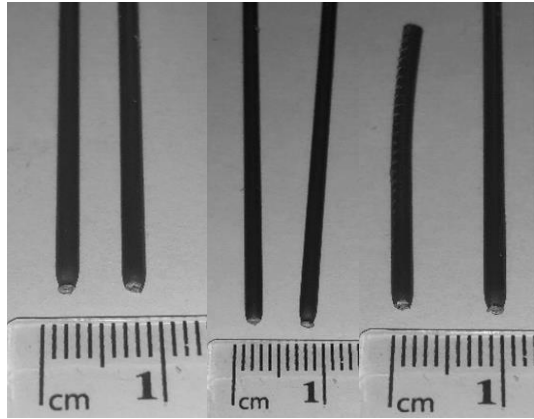


Figure 9:28 - Steel BJ4 2 month artificial ageing condition tensile fractures.

9.2.3.1.4 4 Month Artificial Ageing Condition

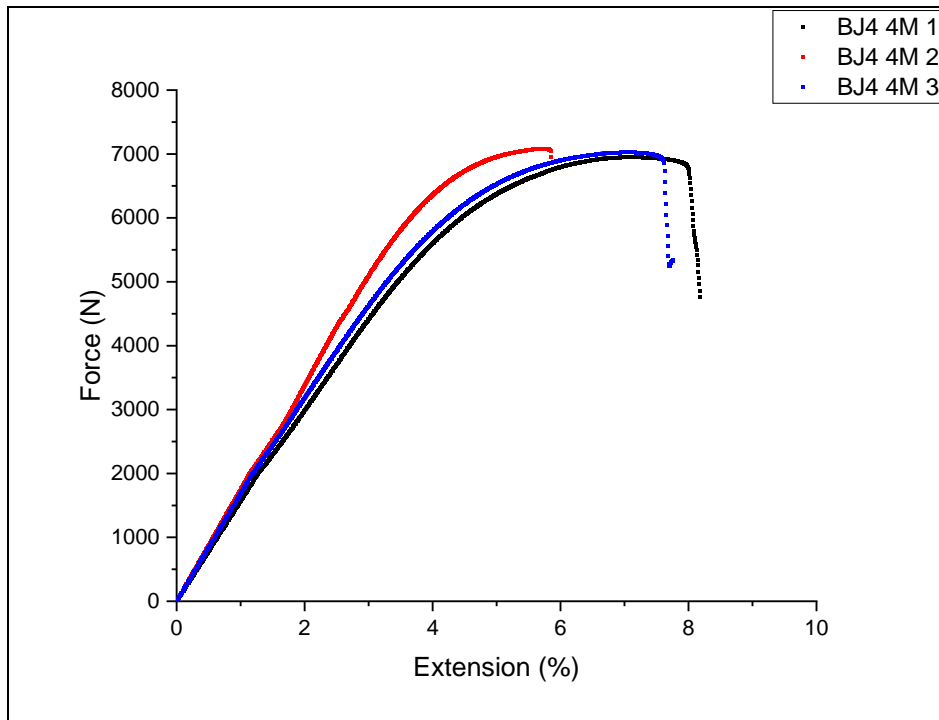


Figure 9:29 - Tensile testing data of steel BJ4 in the 4 month artificial ageing condition.

Table 9:26 - Tensile testing results of steel BJ4 in the 4 month artificial ageing condition.

Sample ID	0.2% Proof (MPa)	UTS (MPa)	0.2%Proof / UTS	Elongation to Failure (%)	Fracture Type
-			-		-
BJ4 4M 1	1664.18	1878.95	0.89	8.18	Cup & Cone
BJ4 4M 2	1697.13	1914.68	0.89	5.85	Cup & Cone
BJ4 4M 3	1620.55	1900.11	0.85	7.76	Cup & Cone
Mean	1660.62	1897.91	0.87	7.26	-
Lower 95% CL	1565.19	1853.29	0.83	4.18	-
Upper 95% CL	1756.05	1942.54	0.92	10.35	-

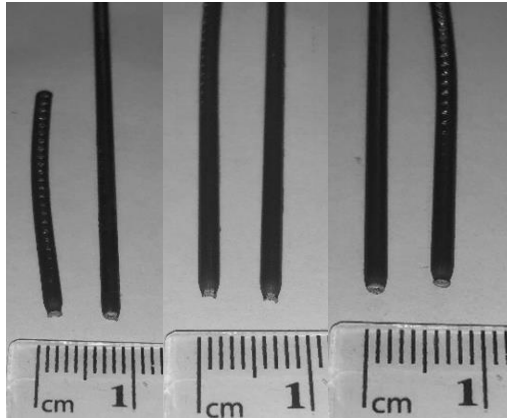


Figure 9:30 - Steel BJ4 4 month artificial ageing condition tensile fractures.

9.2.4 0.8Si + 0.5Ni + 0.1Co Steel (BJ5)

9.2.4.1.1 As-drawn

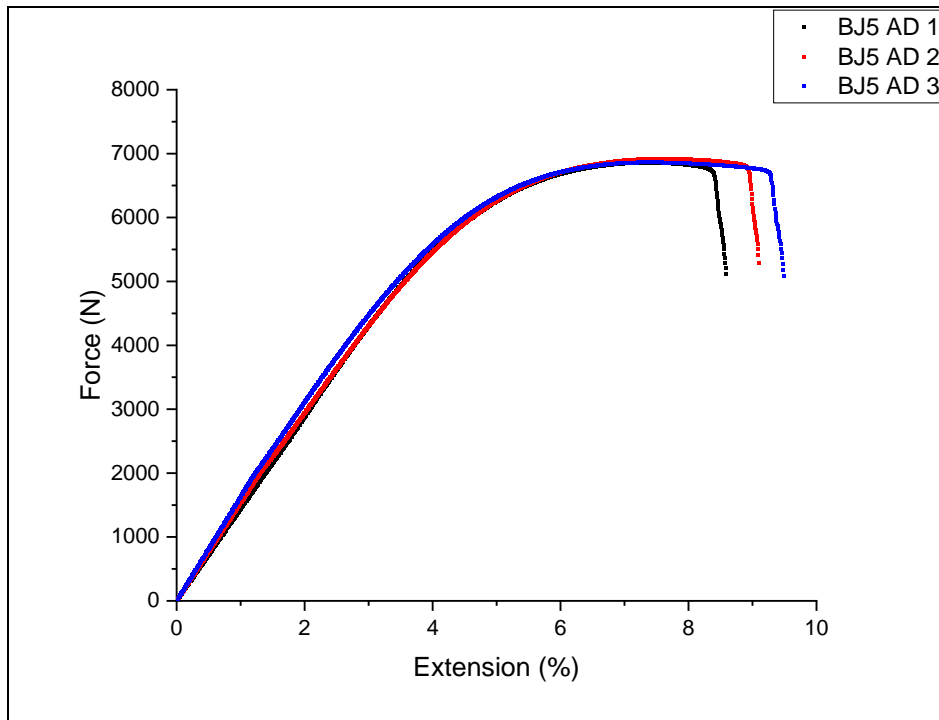


Figure 9:31 - Tensile testing data of steel BJ5 in the as-drawn condition.

Table 9:27 - Tensile testing results of steel BJ5 in the as-drawn condition.

Sample ID	0.2% Proof (MPa)	UTS (MPa)	0.2%Proof / UTS	Elongation to Failure (%)	Fracture Type
-	-	-	-	-	-
BJ5 AD 1	1669.70	1854.75	0.90	8.59	Cup & Cone
BJ5 AD 2	1596.72	1870.99	0.85	9.10	Cup & Cone
BJ5 AD 3	1527.40	1855.99	0.82	9.49	Cup & Cone
Mean	1597.94	1860.58	0.86	9.06	-
Lower 95% CL	1421.17	1838.12	0.76	7.94	-
Upper 95% CL	1774.71	1883.03	0.96	10.18	-

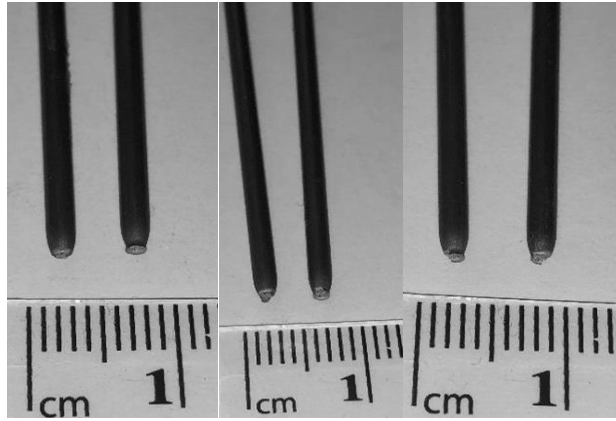


Figure 9:32 - Steel BJ5 as-drawn condition tensile fractures.

9.2.4.1.2 1 Month Artificial Ageing Condition

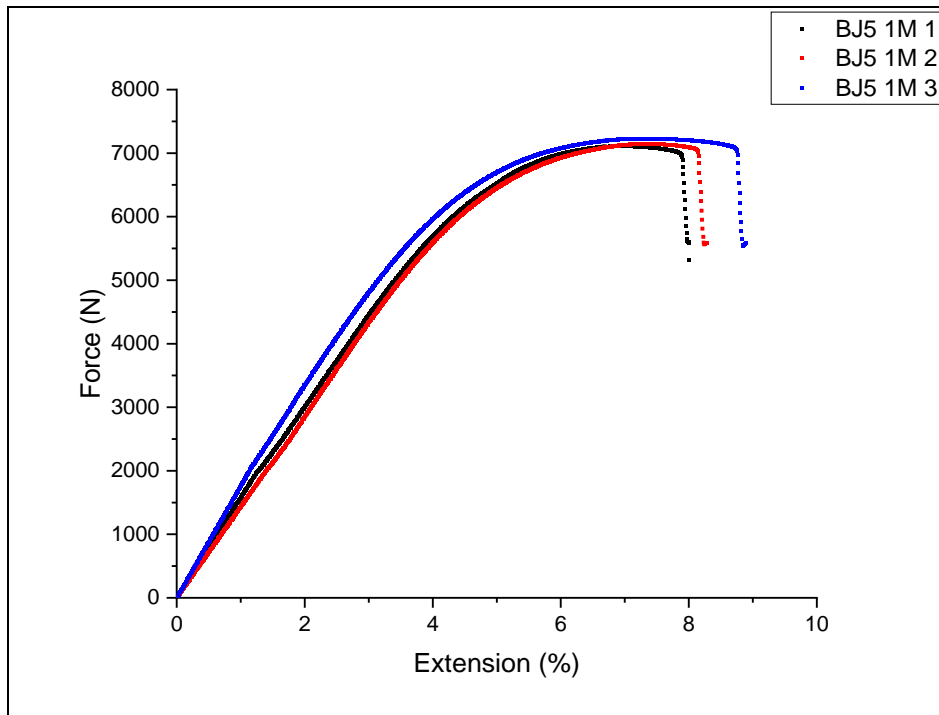


Figure 9:33 - Tensile testing data of steel BJ5 in the 1 month artificial ageing condition.

Table 9:28 - Tensile testing results of steel BJ5 in the 1 month artificial ageing condition.

Sample ID	0.2% Proof (MPa)	UTS (MPa)	0.2%Proof / UTS	Elongation to Failure (%)	Fracture Type
-	(MPa)	(MPa)	-	(%)	-
BJ5 1M 1	1711.37	1922.81	0.89	8.01	Cup & Cone
BJ5 1M 2	1781.02	1932.46	0.92	8.28	Cup & Cone
BJ5 1M 3	1604.97	1954.68	0.82	8.89	Cup & Cone
Mean	1699.12	1936.65	0.88	8.39	-
Lower 95% CL	1478.87	1896.06	0.75	7.27	-
Upper 95% CL	1919.38	1977.24	1.00	9.52	-

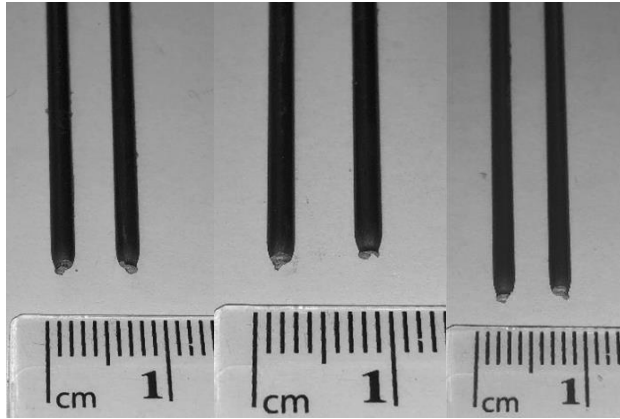


Figure 9:34 - Steel BJ5 1 month artificial ageing condition tensile fractures.

9.2.4.1.3 2 Month Artificial Ageing Condition

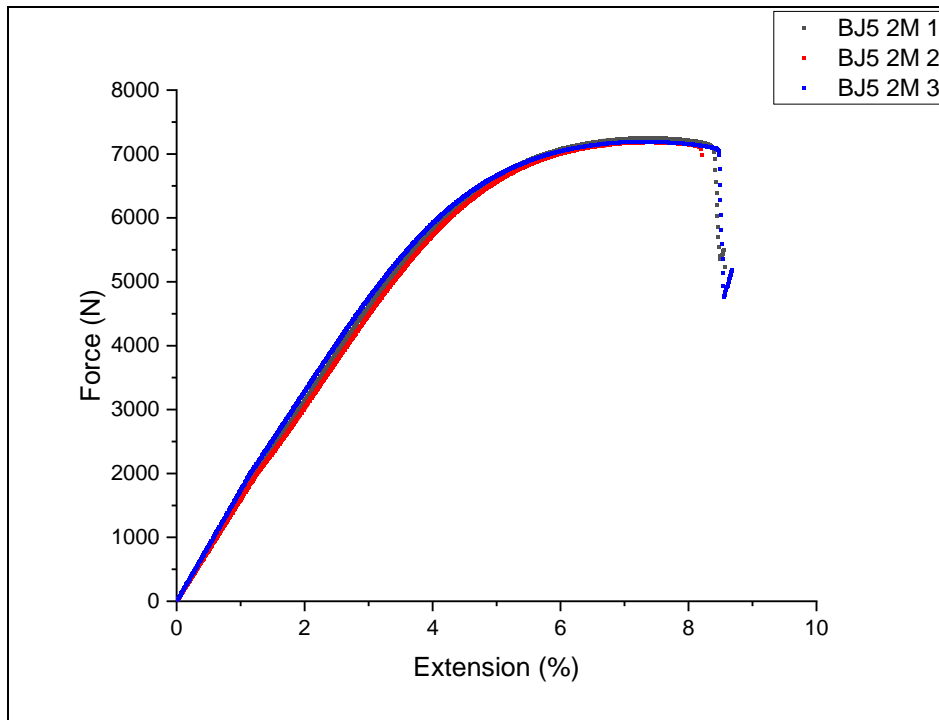


Figure 9:35 - Tensile testing data of steel BJ5 in the 2 month artificial ageing condition.

Table 9:29 - Tensile testing results of steel BJ5 in the 2 month artificial ageing condition.

Sample ID	0.2% Proof (MPa)	UTS (MPa)	0.2%Proof / UTS	Elongation to Failure (%)	Fracture Type
-			-		-
BJ5 2M 1	1674.11	1960.77	0.85	8.56	Cup & Cone
BJ5 2M 2	1705.80	1942.00	0.88	8.21	Cup & Cone
BJ5 2M 3	1635.30	1944.75	0.84	8.68	Cup & Cone
Mean	1671.73	1949.17	0.86	8.48	-
Lower 95% CL	1584.02	1923.99	0.81	7.87	-
Upper 95% CL	1759.45	1974.36	0.91	9.10	-

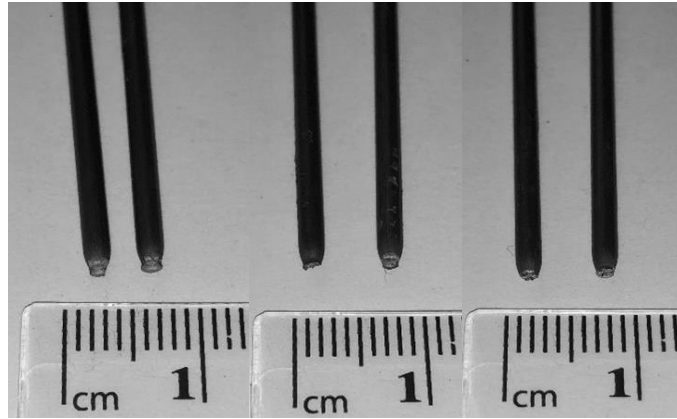


Figure 9:36 - Steel BJ5 2 month artificial ageing condition tensile fractures.

9.2.4.1.4 4 Month Artificial Ageing Condition

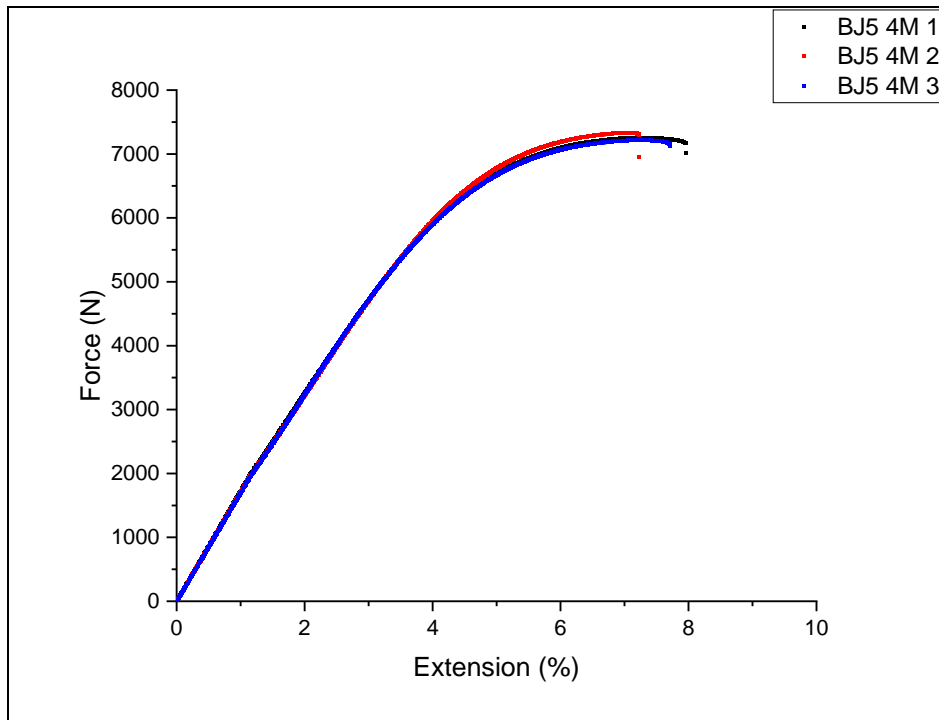


Figure 9:37 - Tensile testing data of steel BJ5 in the 4 month artificial ageing condition.

Table 9:30 - Tensile testing results of steel BJ5 in the 4 month artificial ageing condition.

Sample ID	0.2% Proof (MPa)	UTS (MPa)	0.2%Proof / UTS	Elongation to Failure (%)	Fracture Type
-			-		-
BJ5 4M 1	1635.24	1962.13	0.83	7.96	Cup & Cone
BJ5 4M 2	1684.88	1982.23	0.85	7.23	Cup & Cone
BJ5 4M 3	1643.04	1951.41	0.84	7.72	Cup & Cone
Mean	1654.39	1965.25	0.84	7.64	-
Lower 95% CL	1588.07	1926.39	0.82	6.72	-
Upper 95% CL	1720.71	2004.12	0.86	8.55	-

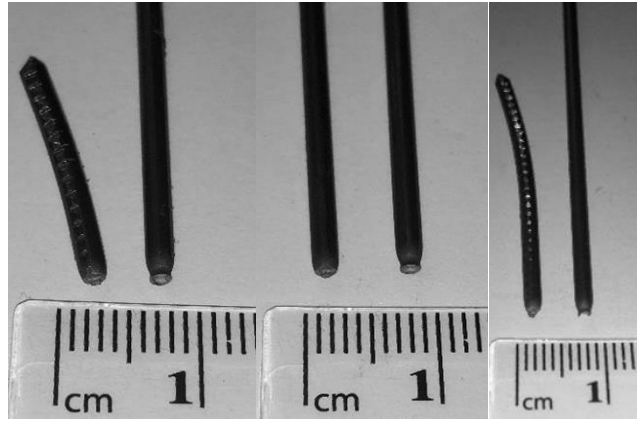


Figure 9:38 - Steel BJ5 4 month artificial ageing condition tensile fractures.

9.2.5 0.8Si + 0.5Ni + 0.1Co + 0.1V Steel BJ6

9.2.5.1.1 As-drawn

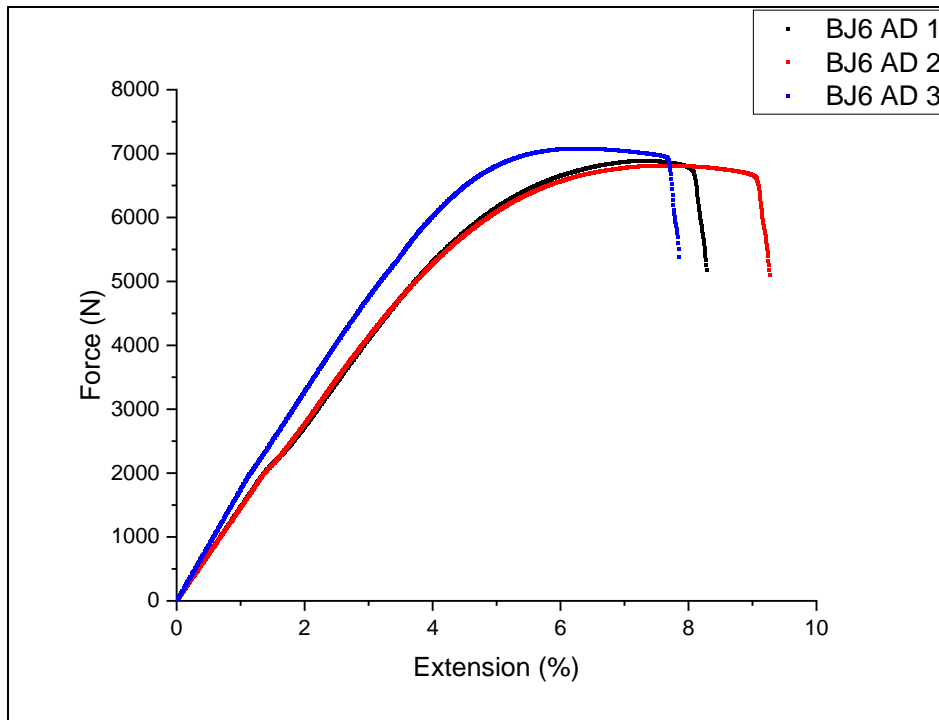


Figure 9:39 - Tensile testing data of steel BJ6 in the as-drawn condition.

Table 9:31 - Tensile testing results of steel BJ6 in the as-drawn condition.

Sample ID	0.2% Proof (MPa)	UTS (MPa)	0.2%Proof / UTS	Elongation to Failure (%)	Fracture Type
-	(MPa)	(MPa)	-	(%)	-
BJ6 AD T1	1628.76	1862.33	0.87	8.28	Cup & Cone
BJ6 AD T2	1606.75	1842.43	0.87	9.27	Cup & Cone
BJ6 AD T3	1626.54	1914.72	0.85	7.85	Cup & Cone
Mean	1620.68	1873.16	0.87	8.47	-
Lower 95% CL	1590.58	1780.40	0.83	6.66	-
Upper 95% CL	1650.79	1965.92	0.90	10.27	-

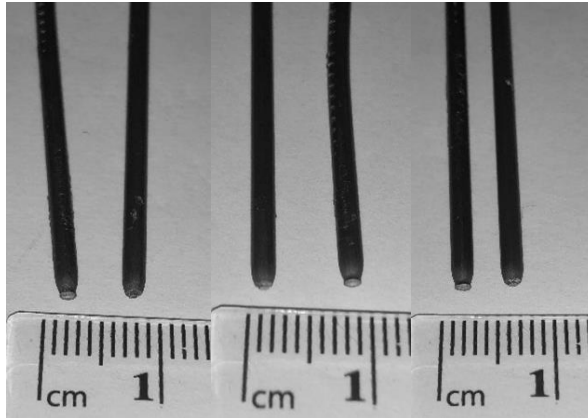


Figure 9:40 - Steel BJ6 as-drawn tensile fractures.

9.2.5.1.2 1 Month Artificial Ageing Condition

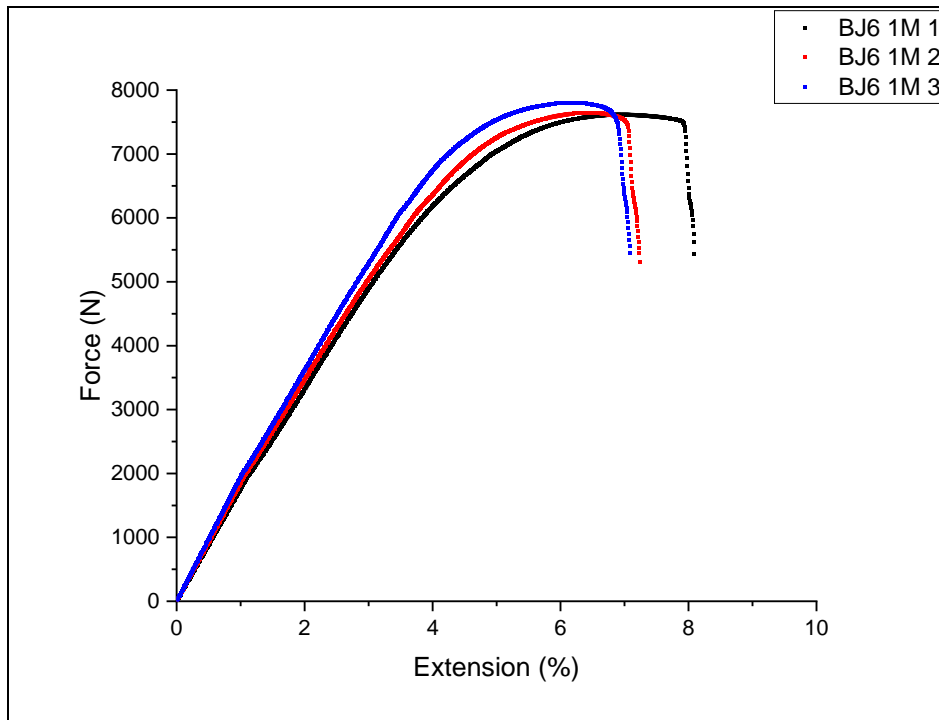


Figure 9:41 - Tensile testing data of steel BJ6 in the 1 month artificial ageing condition.

Table 9:32 - Tensile testing results of steel BJ6 in the 1 month artificial ageing condition.

Sample ID	0.2% Proof (MPa)	UTS (MPa)	0.2%Proof / UTS	Elongation to Failure (%)	Fracture Type
-	(MPa)	(MPa)	-	(%)	-
BJ6 1M T1	1751.35	2059.37	0.85	8.09	Cup & Cone
BJ6 1M T2	1737.08	2067.94	0.84	7.24	Cup & Cone
BJ6 1M T3	1812.30	2109.94	0.86	7.08	Cup & Cone
Mean	1766.91	2079.08	0.85	7.47	-
Lower 95% CL	1667.67	2011.85	0.83	6.12	-
Upper 95% CL	1866.15	2146.31	0.87	8.82	-

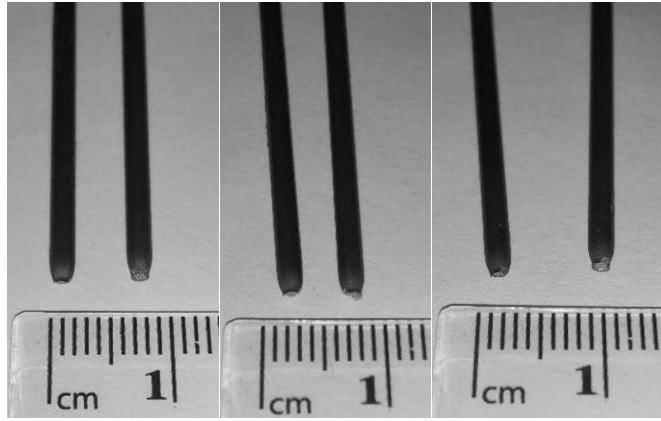


Figure 9:42 - Steel BJ6 1 month artificial ageing condition tensile fractures.

9.2.5.1.3 2 Month Artificial Ageing Condition

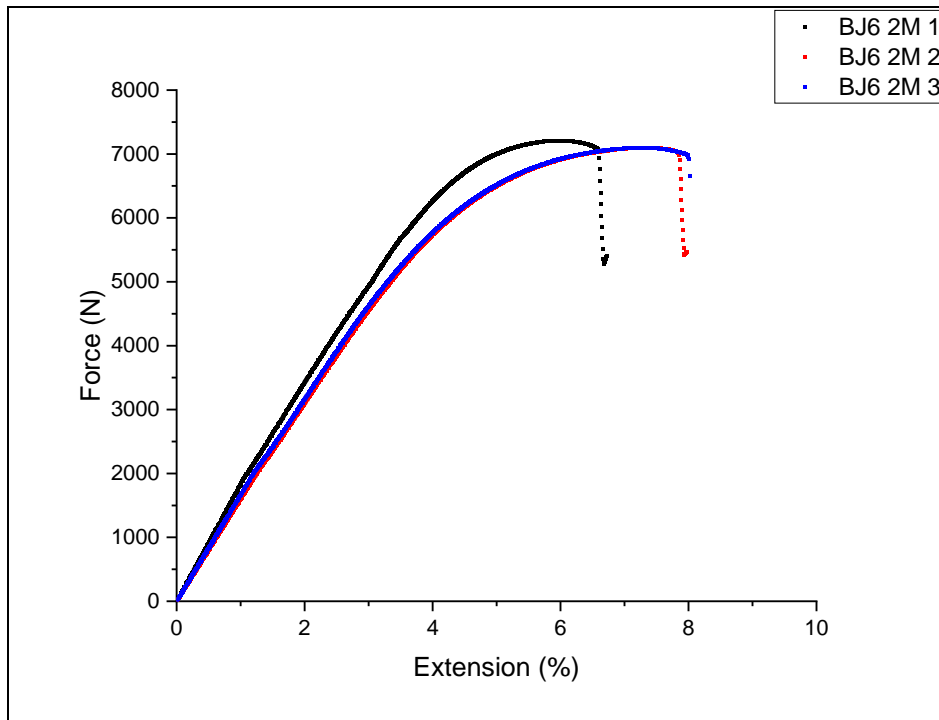


Figure 9:43 - Tensile testing data of steel BJ6 in the 2 month artificial ageing condition.

Table 9:33 - Tensile testing results of steel BJ6 in the 2 month artificial ageing condition.

Sample ID	0.2% Proof (MPa)	UTS (MPa)	0.2%Proof / UTS	Elongation to Failure (%)	Fracture Type
-			-		-
BJ6 2M T1	1655.84	1950.28	0.85	6.72	Cup & Cone
BJ6 2M T2	1679.92	1918.93	0.88	7.97	Cup & Cone
BJ6 2M T3	1599.59	1918.86	0.83	8.02	Cup & Cone
Mean	1645.12	1929.36	0.85	7.57	-
Lower 95% CL	1542.71	1884.34	0.80	5.75	-
Upper 95% CL	1747.53	1974.37	0.91	9.39	-

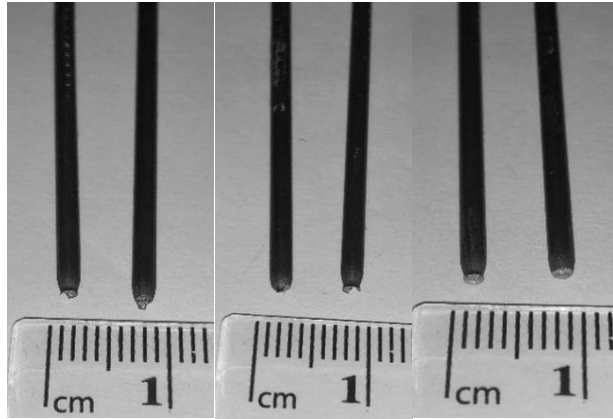


Figure 9:44 - Steel BJ6 2 month artificial ageing condition tensile fractures.

9.2.5.1.4 4 Month Artificial Ageing Condition

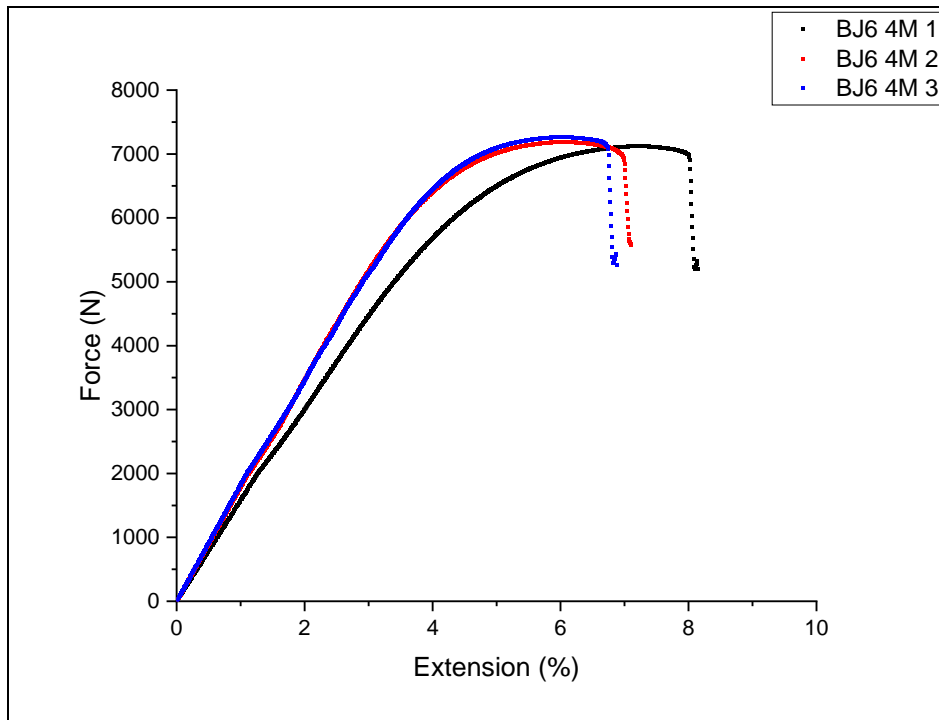


Figure 9:45 - Tensile testing data of steel BJ6 in the 4 month artificial ageing condition.

Table 9:34 - Tensile testing results of steel BJ6 in the 4 month artificial ageing condition.

Sample ID	0.2% Proof (MPa)	UTS (MPa)	0.2%Proof / UTS	Elongation to Failure (%)	Fracture Type
-	(MPa)	(MPa)	-	(%)	-
BJ6 4M T1	1682.96	1925.58	0.87	8.15	Cup & Cone
BJ6 4M T2	1632.67	1943.29	0.84	7.10	Cup & Cone
BJ6 4M T3	1669.69	1963.84	0.85	6.88	Cup & Cone
Mean	1661.77	1944.24	0.85	7.37	-
Lower 95% CL	1597.04	1896.66	0.81	5.69	-
Upper 95% CL	1726.51	1991.81	0.90	9.06	-

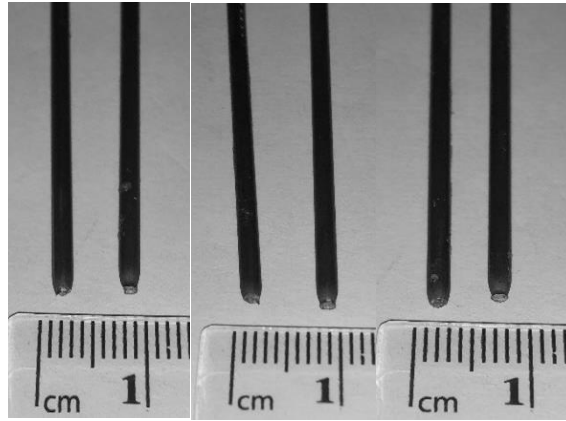


Figure 9:46 - Steel BJ6 4 month artificial ageing condition tensile fractures.

9.3 Torsion Testing Data

9.3.1 Commercial Steel

9.3.1.1.1 As-drawn

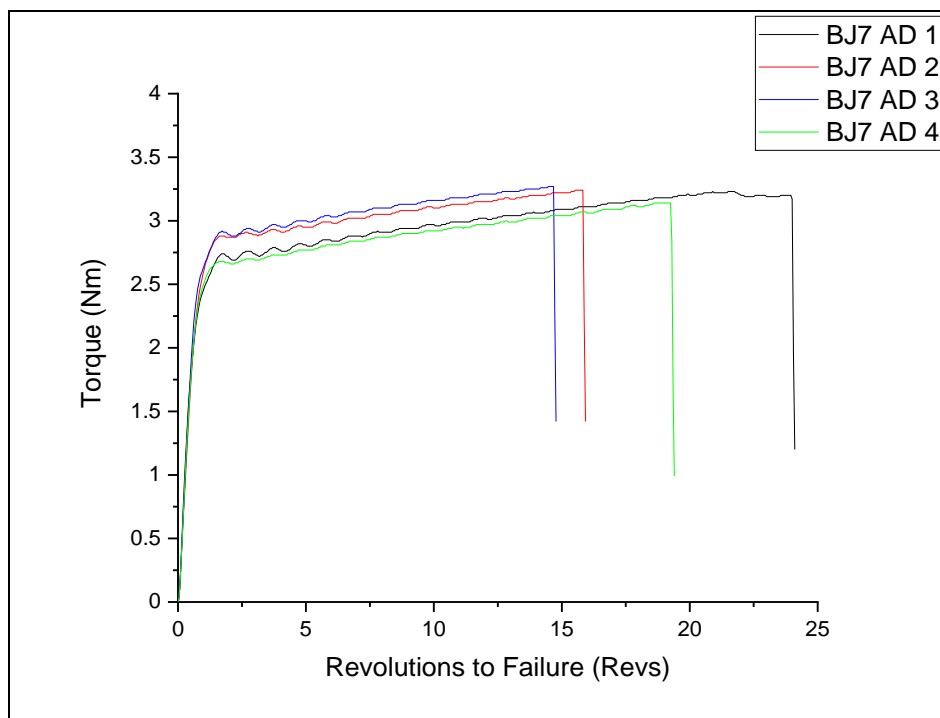


Figure 9:47 - Torsion testing plot of the commercial steel in the as-drawn condition.

Table 9:35 - Torsion testing results of the commercial steel in the as-drawn condition.

Sample ID	Revolutions to Failure (Revs)	Peak Torque (Nm)	Fracture Type
-	(Revs)	(Nm)	-
BJ7 AD 1	24.05	3.23	1A
BJ7 AD 2	15.88	3.24	1A
BJ7 AD 3	14.73	3.27	1A
BJ7 AD 4	19.35	3.14	1A
Mean	18.50	3.22	-
Lower 95% CL	11.83	3.13	-
Upper 95% CL	25.17	3.31	-

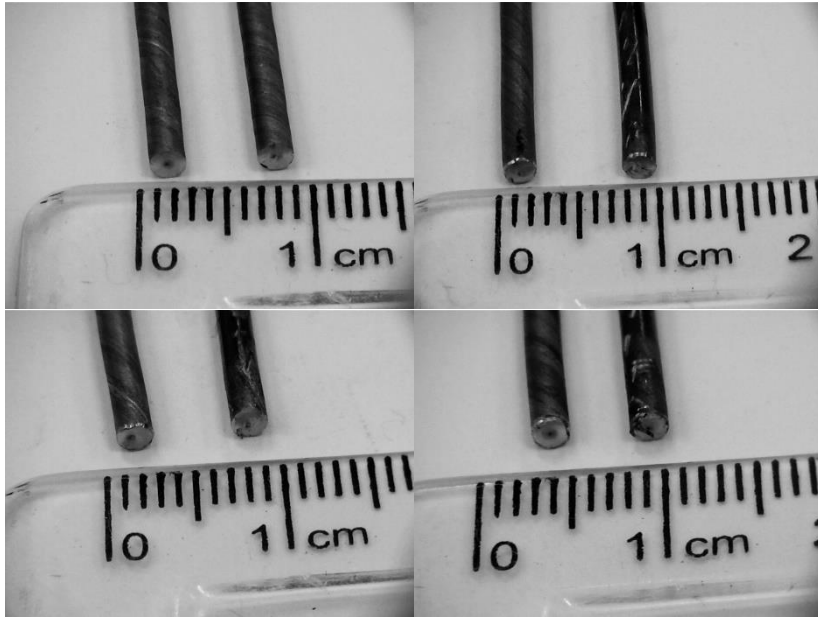


Figure 9:48 - Commercial steel as-drawn, type A fractures.

9.3.1.1.2 1 Month Artificial Ageing Condition

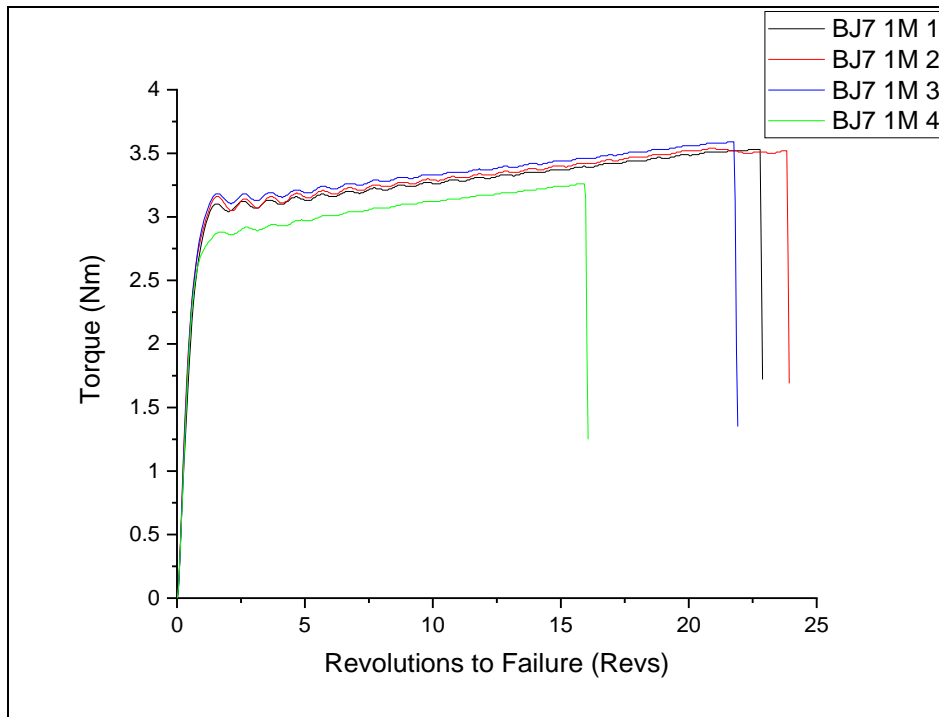


Figure 9:49 - Torsion testing plot of the commercial steel in the 1 month artificial ageing condition.

Table 9:36 - Torsion testing results of the commercial steel in the 1 month artificial ageing condition.

Sample ID	Revolutions to Failure (Revs)	Peak Torque (Nm)	Fracture Type
-	(Revs)	(Nm)	-
BJ7 1M 1	22.84	3.53	A
BJ7 1M 2	23.88	3.54	A
BJ7 1M 3	21.86	3.59	A
BJ7 1M 4	16.02	3.26	A
Mean	21.15	3.48	-
Lower 95% CL	15.55	3.24	-
Upper 95% CL	26.75	3.72	-

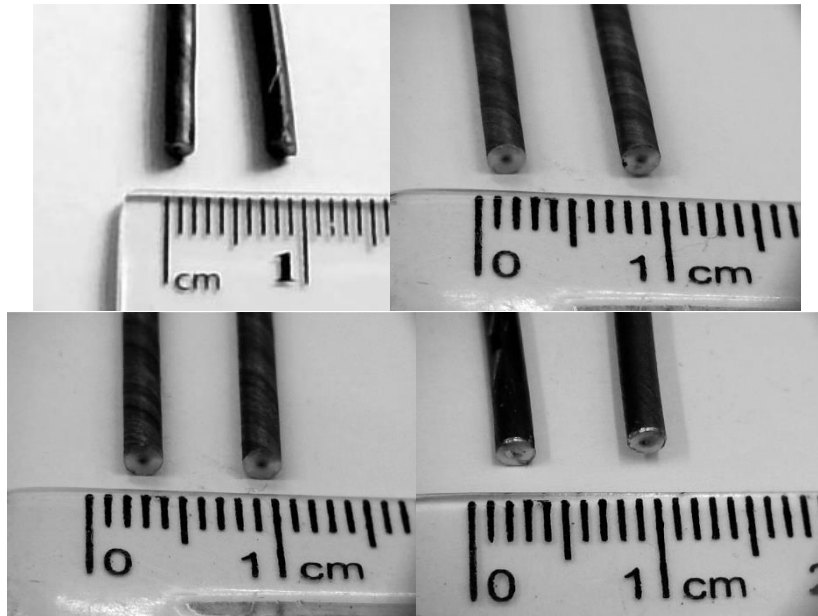


Figure 9:50 - Commercial steel 1 month artificial ageing condition, type A fracture.

9.3.1.1.3 2 Month Artificial Ageing Condition

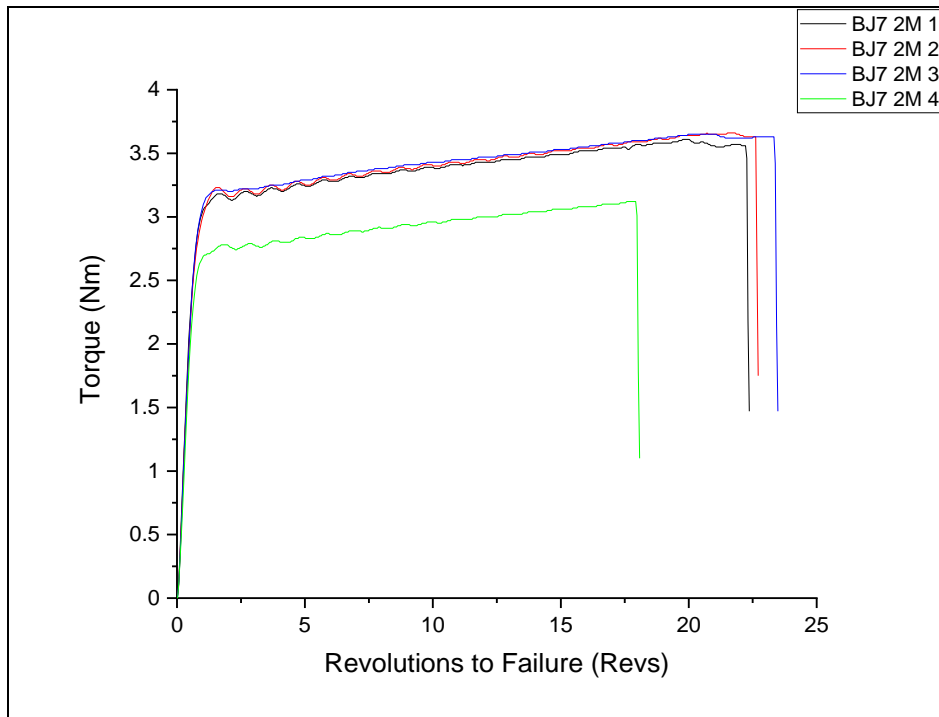


Figure 9:51 - Torsion testing plot of the commercial steel in the 2 month artificial ageing condition.

Table 9:37 - Torsion testing results of the commercial steel in the 2 month artificial ageing condition.

Sample ID	Revolutions to Failure (Revs)	Peak Torque (Nm)	Fracture Type
-	(Revs)	(Nm)	-
BJ7 2M 1	22.32	3.61	C
BJ7 2M 2	22.67	3.66	C
BJ7 2M 3	23.43	3.65	C
BJ7 2M 4	18.03	3.12	A
Mean	21.61	3.51	-
Lower 95% CL	17.74	3.09	-
Upper 95% CL	25.48	3.93	-

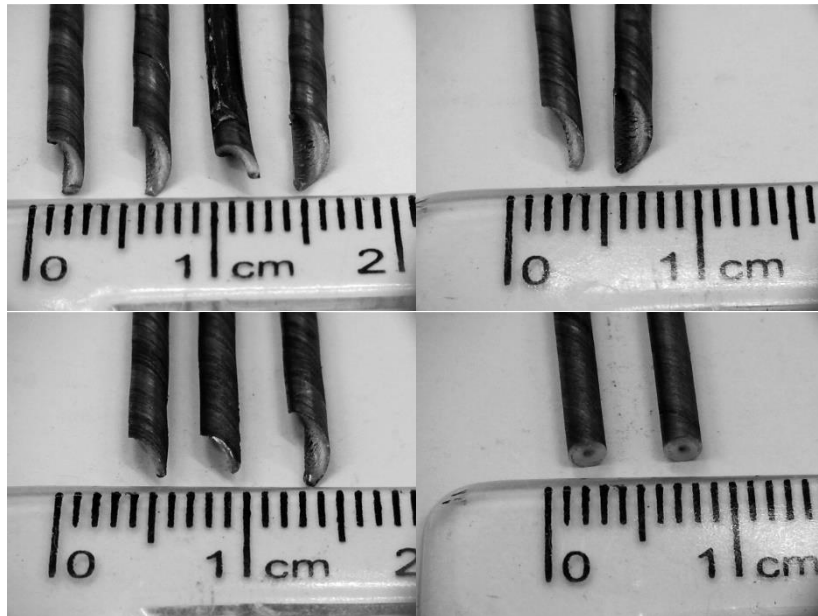


Figure 9:52 - Commercial steel 2 month artificial ageing condition, 3 type C and 1 type A fracture.

9.3.1.1.4 4 Month Artificial Ageing Condition

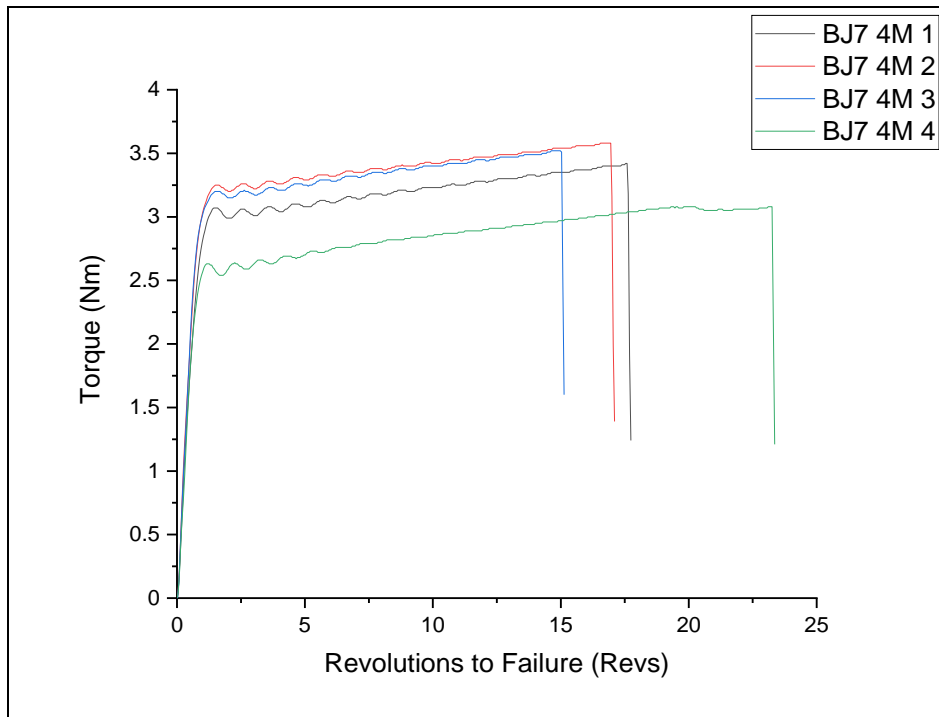


Figure 9:53 - Torsion testing plot of the commercial steel in the 4 month artificial ageing condition.

Table 9:38 - Torsion testing results of the commercial steel in the 4 month artificial ageing condition.

Sample ID	Revolutions to Failure (Revs)	Peak Torque (Nm)	Fracture Type
-	(Revs)	(Nm)	-
BJ7 4M 1	17.69	3.42	C
BJ7 4M 2	17.05	3.58	A
BJ7 4M 3	15.08	3.52	A
BJ7 4M 4	23.31	3.08	A
Mean	18.28	3.40	-
Lower 95% CL	12.66	3.04	-
Upper 95% CL	23.90	3.76	-

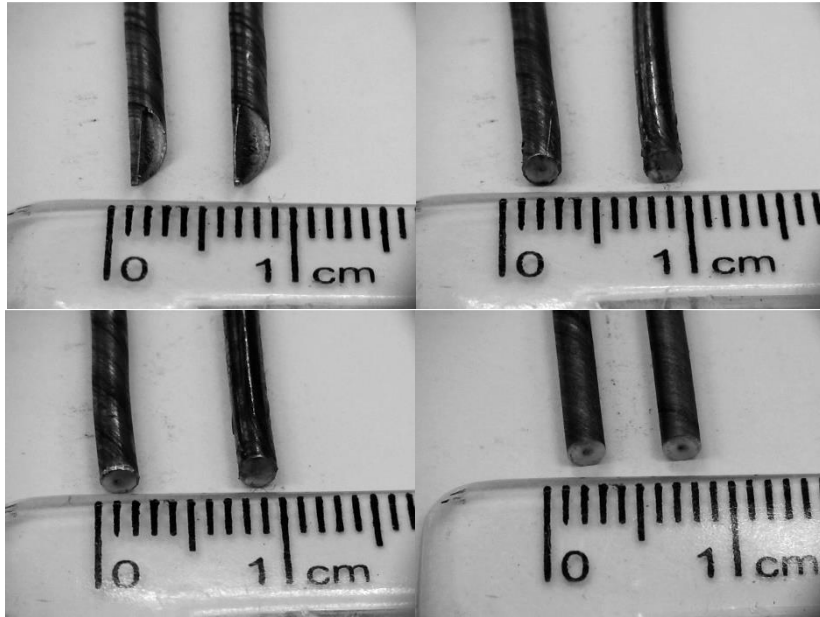


Figure 9:54 - Commercial steel 4 month artificial ageing condition, type A fracture.

9.3.2 0.8Si Steel (BJ3)

9.3.2.1.1 As-drawn

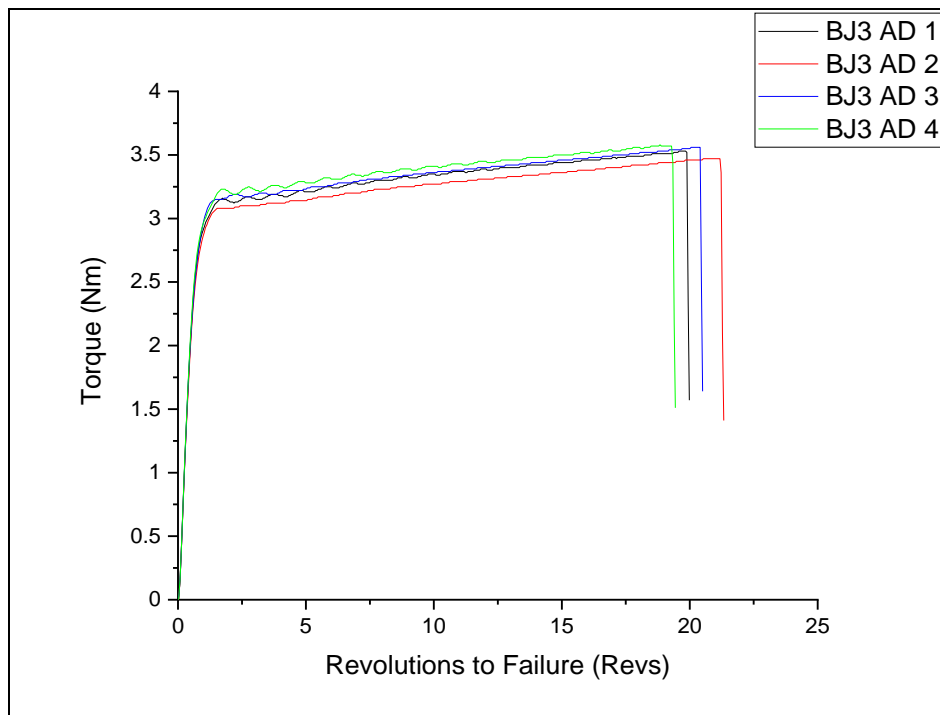


Figure 9:55 - Torsion testing plot of steel BJ3 in the as-drawn condition.

Table 9:39 - Torsion testing results of steel BJ3 in the as-drawn condition.

Sample ID	Revolutions to Failure (Revs)	Peak Torque (Nm)	Fracture Type
-	(Revs)	(Nm)	-
BJ3 AD 1	19.94	3.53	A
BJ3 AD 2	21.28	3.47	A
BJ3 AD 3	20.46	3.56	A
BJ3 AD 4	19.39	3.58	A
Mean	20.26	3.54	-
Lower 95% CL	18.99	3.46	-
Upper 95% CL	21.54	3.61	-

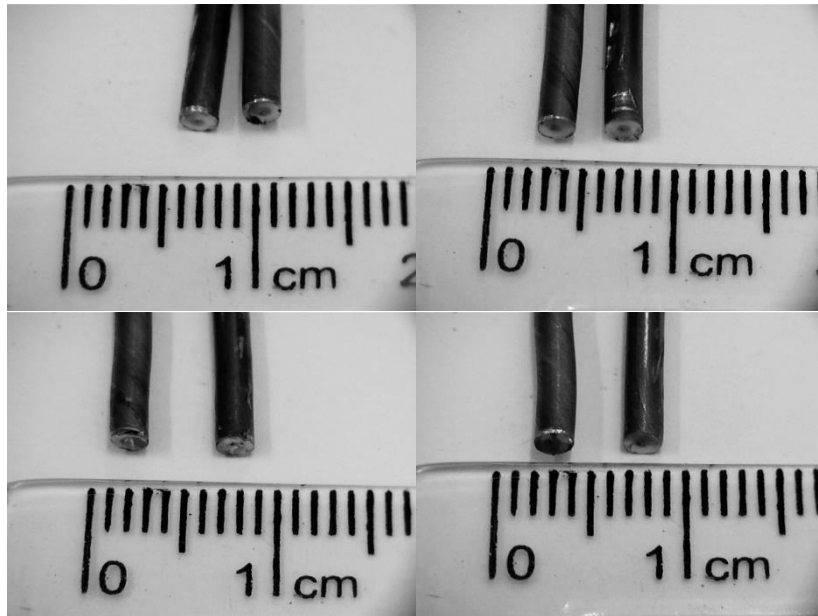


Figure 9:56 - Steel BJ3 Torsion test fractures.

9.3.2.1.2 1 Month Artificial Ageing Condition

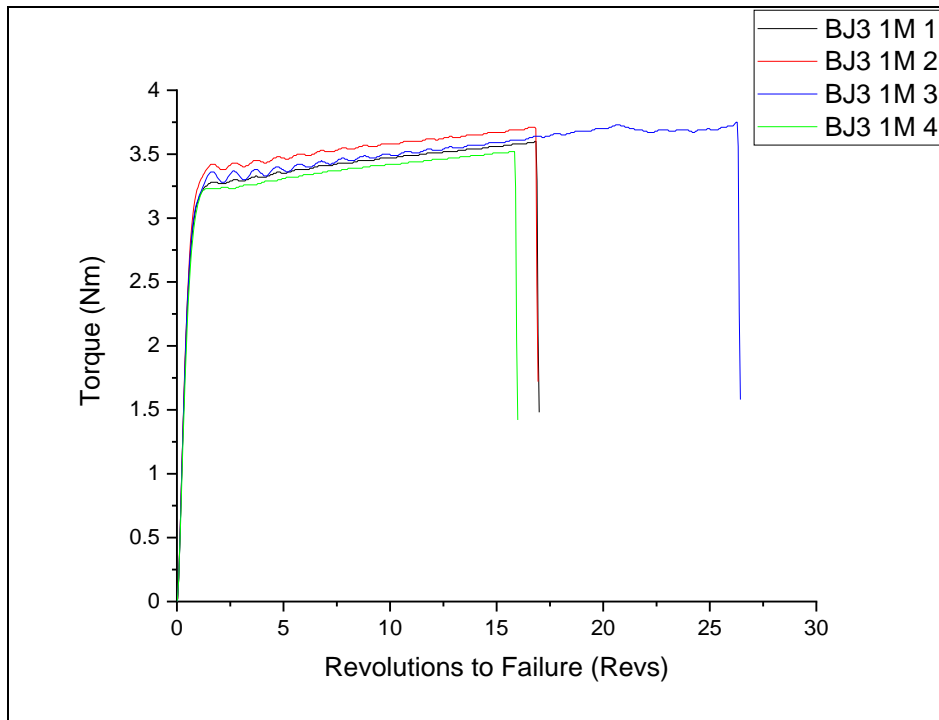


Figure 9:57 - Torsion testing plot of steel BJ3 in the 1 month artificial ageing condition.

Table 9:40 - Torsion testing results of BJ3 in the 1 month artificial ageing condition.

Sample ID	Revolutions to Failure	Peak Torque	Fracture Type
-	(Revs)	(Nm)	-
BJ3 1M 1	16.94	3.60	A
BJ3 1M 2	16.89	3.71	A
BJ3 1M 3	26.39	3.75	A
BJ3 1M 4	15.94	3.52	A
Mean	19.04	3.65	-
Lower 95% CL	11.21	3.48	-
Upper 95% CL	26.87	3.81	-

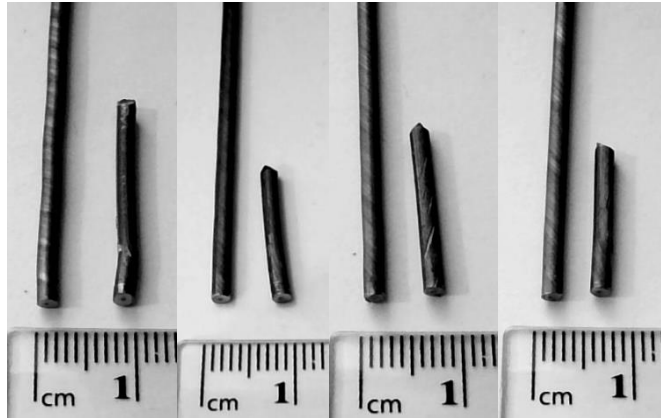


Figure 9:58 - Steel BJ3 1 month artificial ageing torsion test fractures.

9.3.2.1.3 2 Month Artificial Ageing Condition

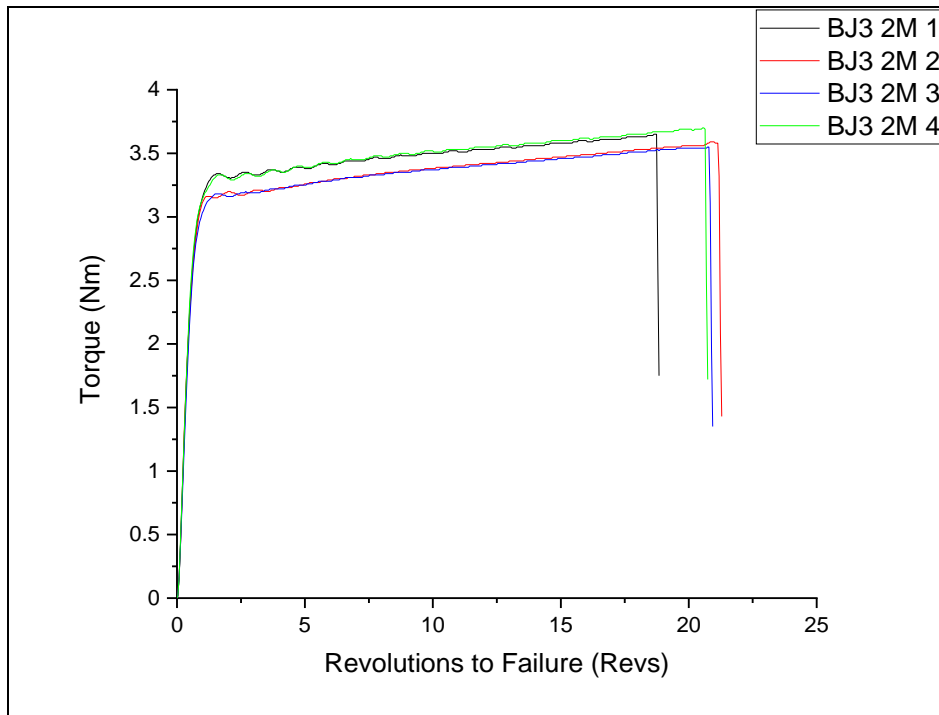


Figure 9:59 - Torsion testing plot of steel BJ3 in the 2 month artificial ageing condition.

Table 9:41 - Torsion testing results of BJ3 in the 2 month artificial ageing condition.

Sample ID	Revolutions to Failure (Revs)	Peak Torque (Nm)	Fracture Type
-	(Revs)	(Nm)	-
BJ3 2M 1	18.79	3.65	A
BJ3 2M 2	21.24	3.59	A
BJ3 2M 3	20.89	3.55	A
BJ3 2M 4	20.69	3.70	A
Mean	20.40	3.62	-
Lower 95% CL	18.66	3.52	-
Upper 95% CL	22.15	3.73	-

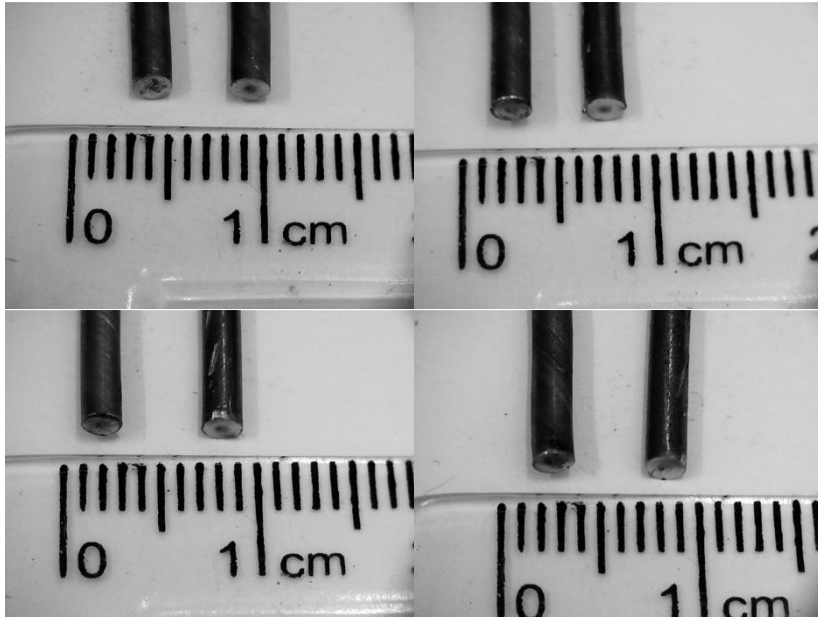


Figure 9:60 - Steel BJ3 2 month artificial ageing condition, type A fractures.

9.3.2.1.4 4 Month Artificial Ageing Condition

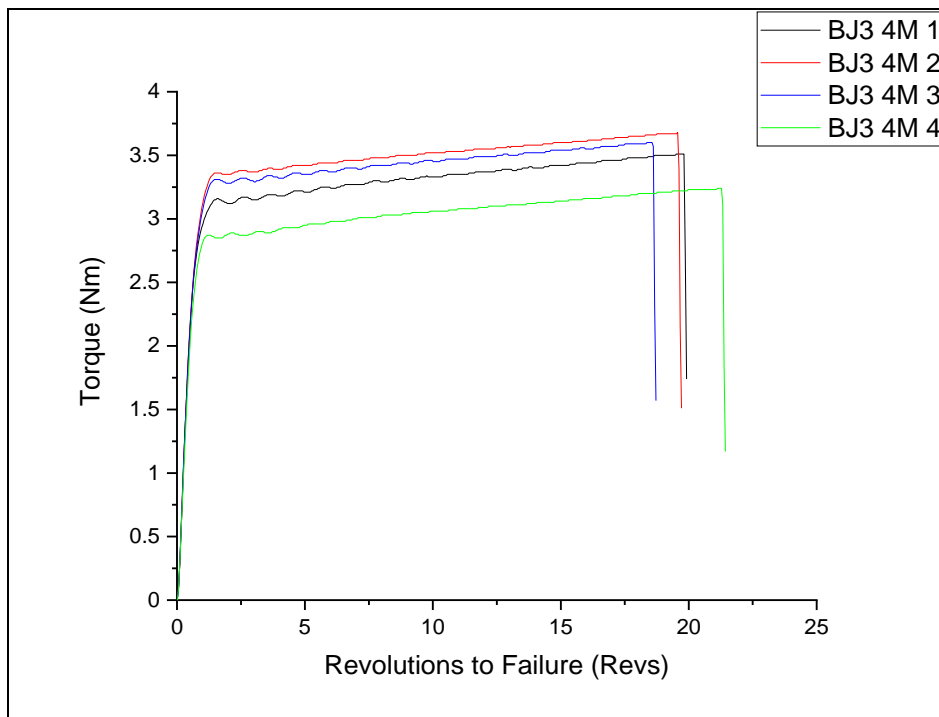


Figure 9:61 - Torsion testing plot of steel BJ3 in the 4 month artificial ageing condition.

Table 9:42 - Torsion testing results of BJ3 in the 4 month artificial ageing condition.

Sample ID	Revolutions to Failure (Revs)	Peak Torque (Nm)	Fracture Type
-	(Revs)	(Nm)	-
BJ3 4M 1	19.87	3.51	A
BJ3 4M 2	19.67	3.68	A
BJ3 4M 3	18.67	3.60	A
BJ3 4M 4	15.43	3.43	A
Mean	18.41	3.56	-
Lower 95% CL	15.14	3.38	-
Upper 95% CL	21.68	3.73	-

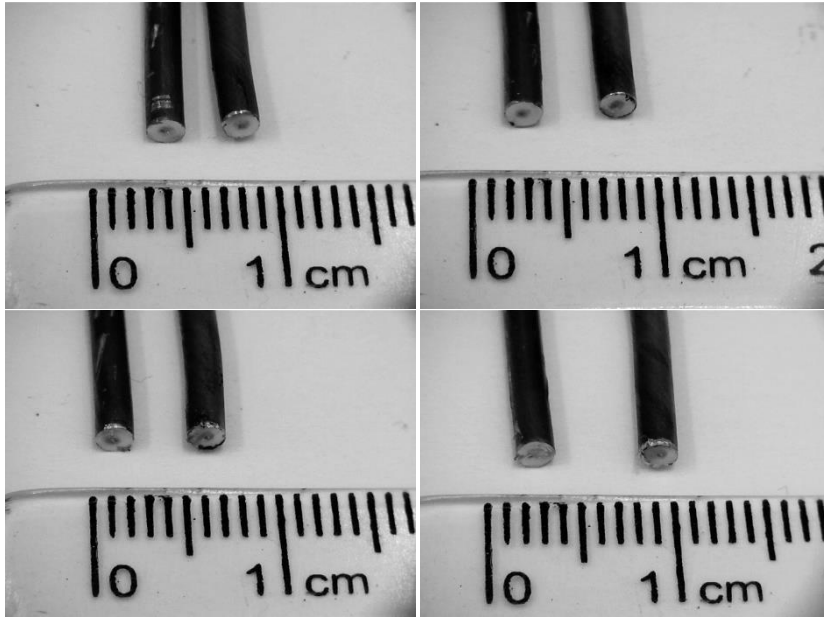


Figure 9:62 - Steel BJ3 4 month artificial ageing condition, type A fracture.

9.3.3 0.8Si + 0.5 Ni Steel (BJ4)

9.3.3.1.1 As-drawn

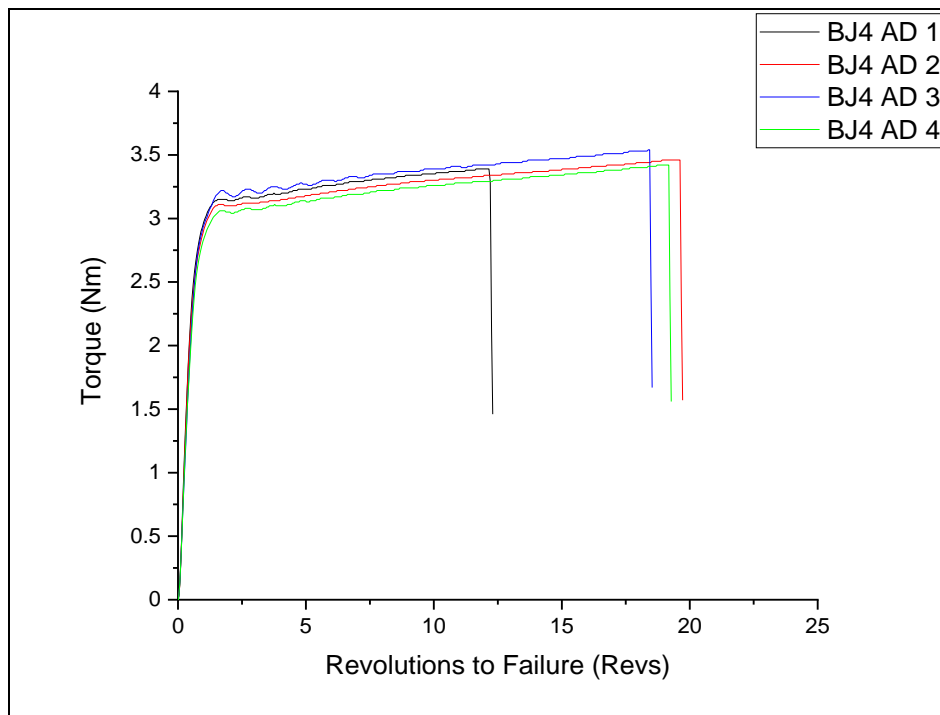


Figure 9:63 - Torsion testing plot of steel BJ4 in the as-drawn condition.

Table 9:43 - Torsion testing results of steel BJ4 in the as-drawn condition.

Sample ID	Revolutions to Failure (Revs)	Peak Torque (Nm)	Fracture Type
-	(Revs)	(Nm)	-
BJ4 AD 1	12.25	3.39	A
BJ4 AD 2	19.67	3.46	A
BJ4 AD 3	18.48	3.54	A
BJ4 AD 4	19.23	3.42	A
Mean	17.41	3.45	-
Lower 95% CL	11.88	3.35	-
Upper 95% CL	22.93	3.56	-

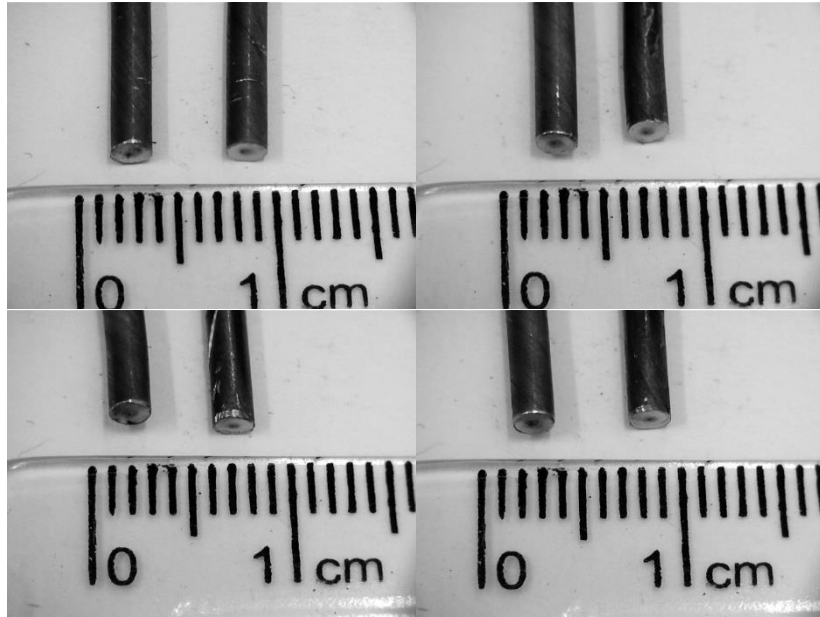


Figure 9:64 - Steel BJ4 as-drawn, type A fracture.

9.3.3.1.2 1 Month Artificial Ageing Condition

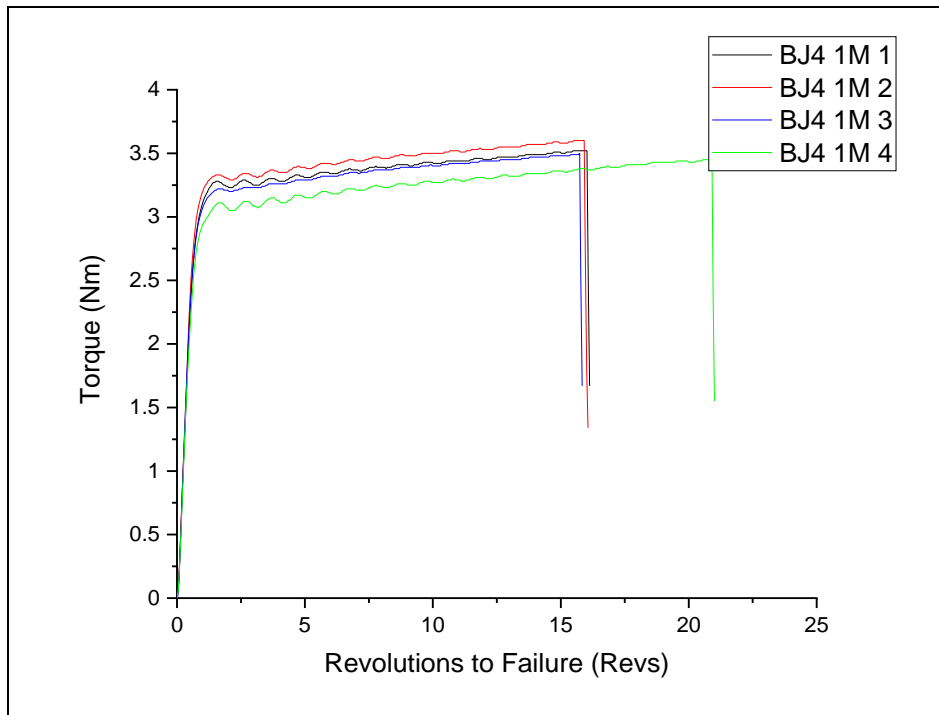


Figure 9:65 - Torsion testing plot of steel BJ4 in the 1 month artificial ageing condition.

Table 9:44 - Torsion testing results of BJ4 in the 1 month artificial ageing condition.

Sample ID	Revolutions to Failure (Revs)	Peak Torque (Nm)	Fracture Type
-	(Revs)	(Nm)	-
BJ4 1M 1	16.07	3.52	A
BJ4 1M 2	16.01	3.60	A
BJ4 1M 3	15.79	3.50	A
BJ4 1M 4	20.96	3.47	A
Mean	17.21	3.52	-
Lower 95% CL	13.23	3.43	-
Upper 95% CL	21.19	3.61	-

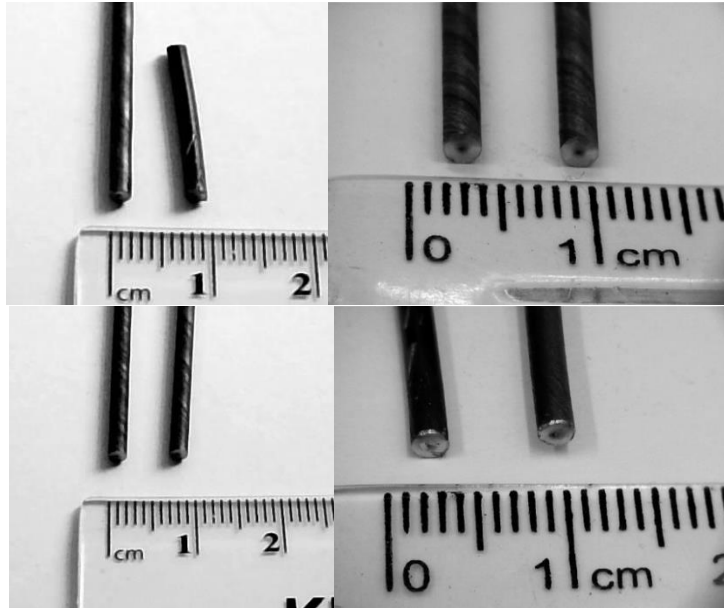


Figure 9:66 - Steel BJ4 1 month artificial ageing condition, type A fracture.

9.3.3.1.3 2 Month Artificial Ageing Condition

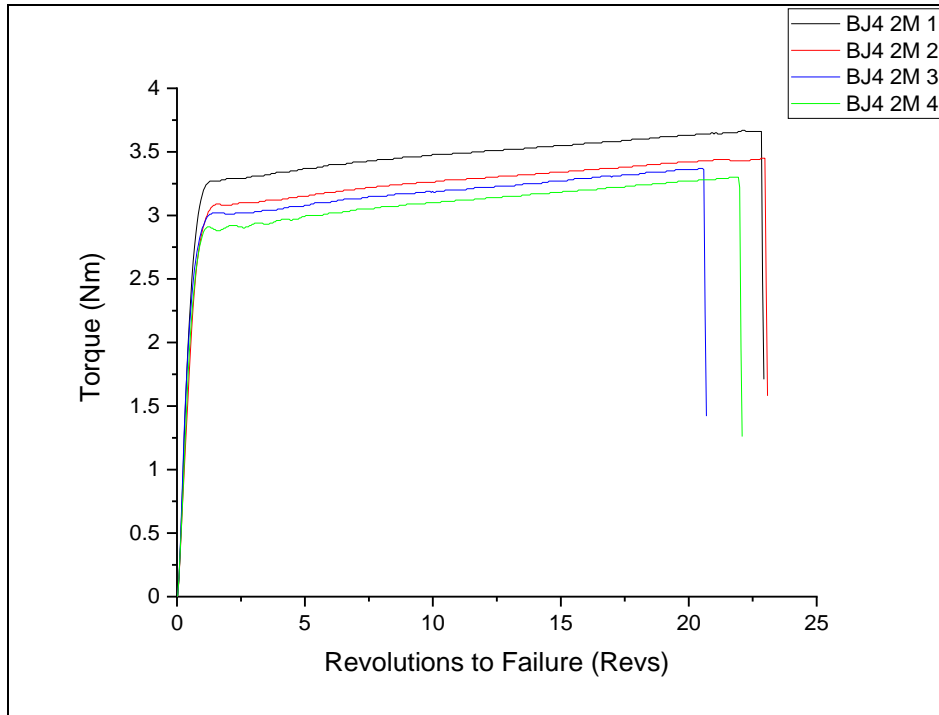


Figure 9:67 - Torsion testing plot of steel BJ4 in the 2 month artificial ageing condition.

Table 9:45 - Torsion testing results of BJ4 in the 2 month artificial ageing condition.

Sample ID	Revolutions to Failure (Revs)	Peak Torque (Nm)	Fracture Type
-	(Revs)	(Nm)	-
BJ4 2M 1	22.89	3.67	A
BJ4 2M 2	23.03	3.45	A
BJ4 2M 3	20.64	3.37	A
BJ4 2M 4	22.04	3.30	A
Mean	22.15	3.45	-
Lower 95% CL	20.40	3.19	-
Upper 95% CL	23.90	3.70	-

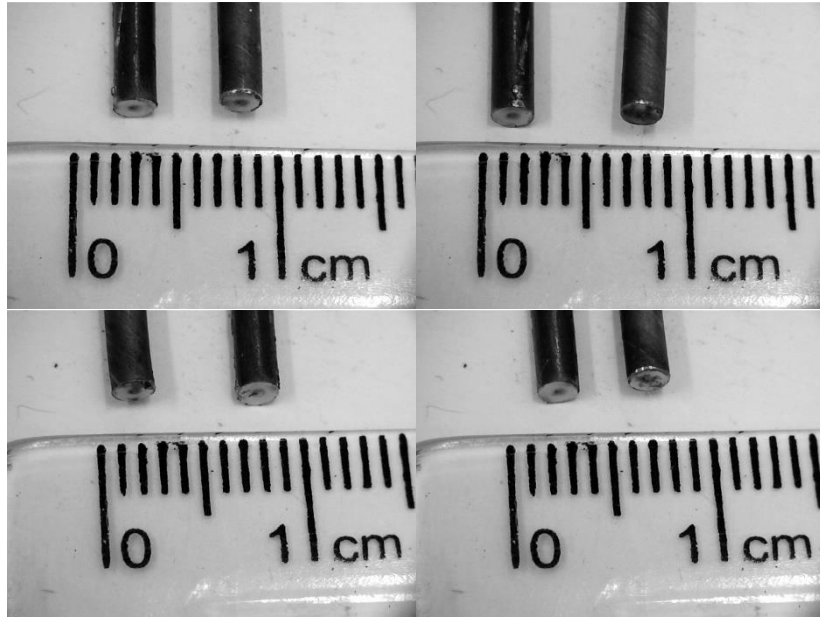


Figure 9:68 - Steel BJ4 2 month artificial ageing condition, type A fracture.

9.3.3.1.4 4 Month Ageing Condition

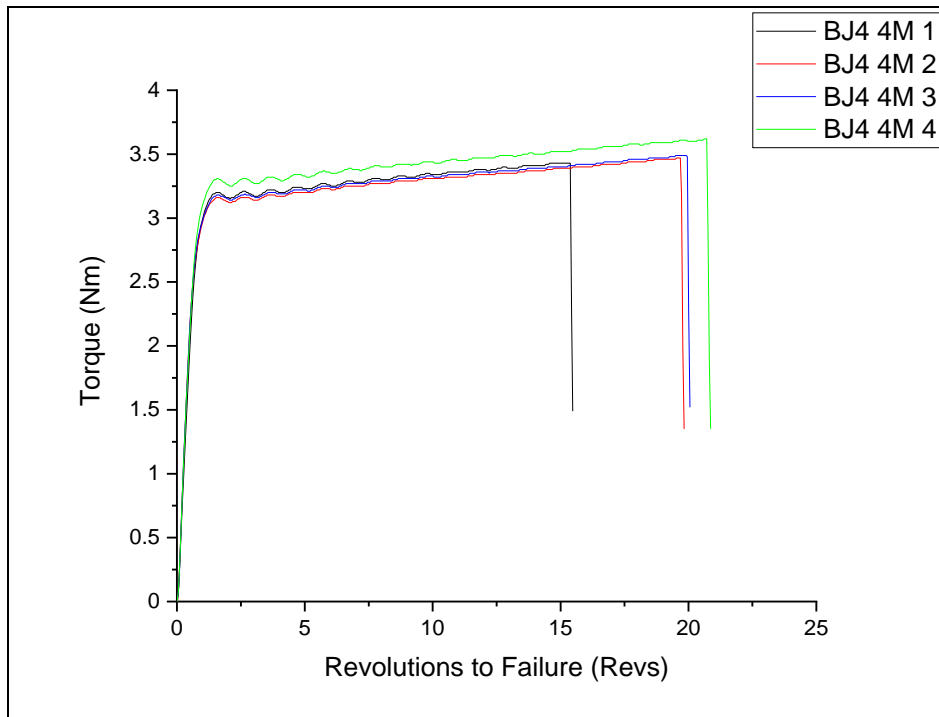


Figure 9:69 - Torsion testing plot of steel BJ4 in the 4 month artificial ageing condition.

Table 9:46 - Torsion testing results of BJ4 in the 4 month artificial ageing condition.

Sample ID	Revolutions to Failure (Revs)	Peak Torque (Nm)	Fracture Type
-	(Revs)	(Nm)	-
BJ4 4M 1	21.38	3.24	A
BJ4 4M 2	19.78	3.47	A
BJ4 4M 3	20.01	3.49	A
BJ4 4M 4	20.82	3.62	A
Mean	20.50	3.46	-
Lower 95% CL	19.32	3.20	-
Upper 95% CL	21.67	3.71	-

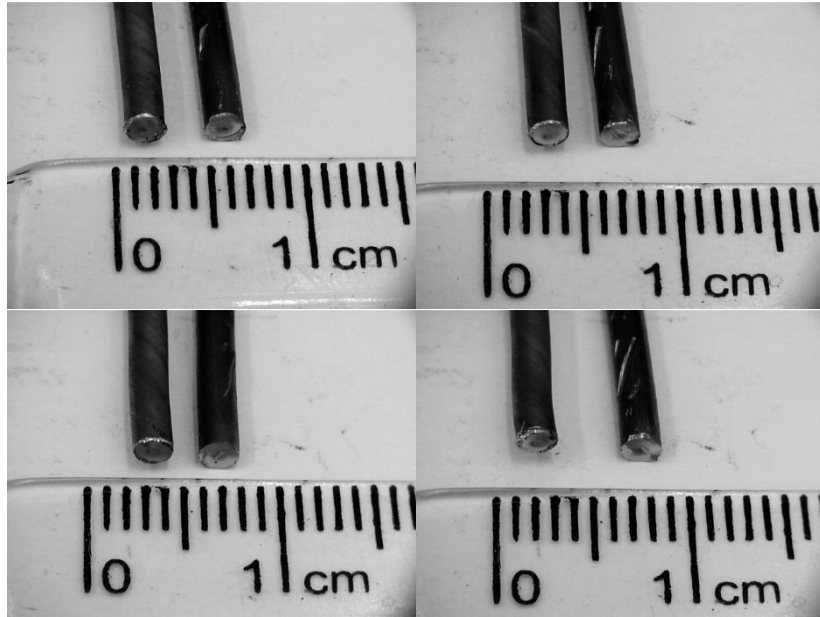


Figure 9:70 - Steel BJ4 4 month artificial ageing condition, type A fracture.

9.3.4 0.8Si + 0.5Ni + 0.1Co Steel (BJ5)

9.3.4.1.1 As-drawn

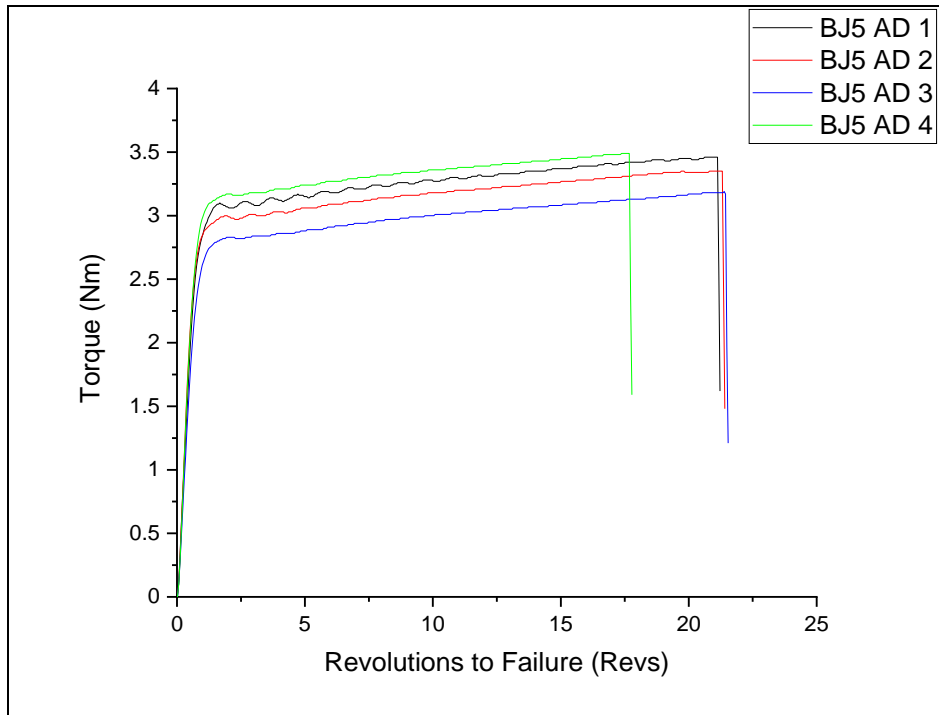


Figure 9:71 - Torsion testing plot of steel BJ5 in the as-drawn condition

Table 9:47 - Torsion testing results of steel BJ5 in the as-drawn condition.

Sample ID	Revolutions to Failure (Revs)	Peak Torque (Nm)	Fracture Type
-	(Revs)	(Nm)	-
BJ5 AD 1	21.17	3.46	A
BJ5 AD 2	21.36	3.35	A
BJ5 AD 3	21.49	3.19	A
BJ5 AD 4	17.73	3.49	A
Mean	20.44	3.37	-
Lower 95% CL	17.55	3.16	-
Upper 95% CL	23.32	3.59	-

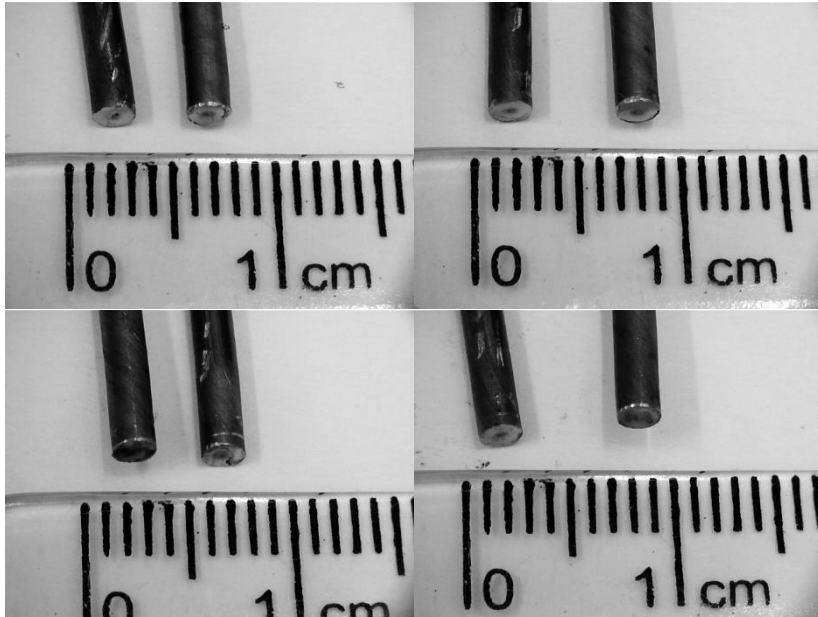


Figure 9:72 Steel BJ5 as-drawn, type A fractures.

9.3.4.1.2 1 Month Artificial Ageing Condition

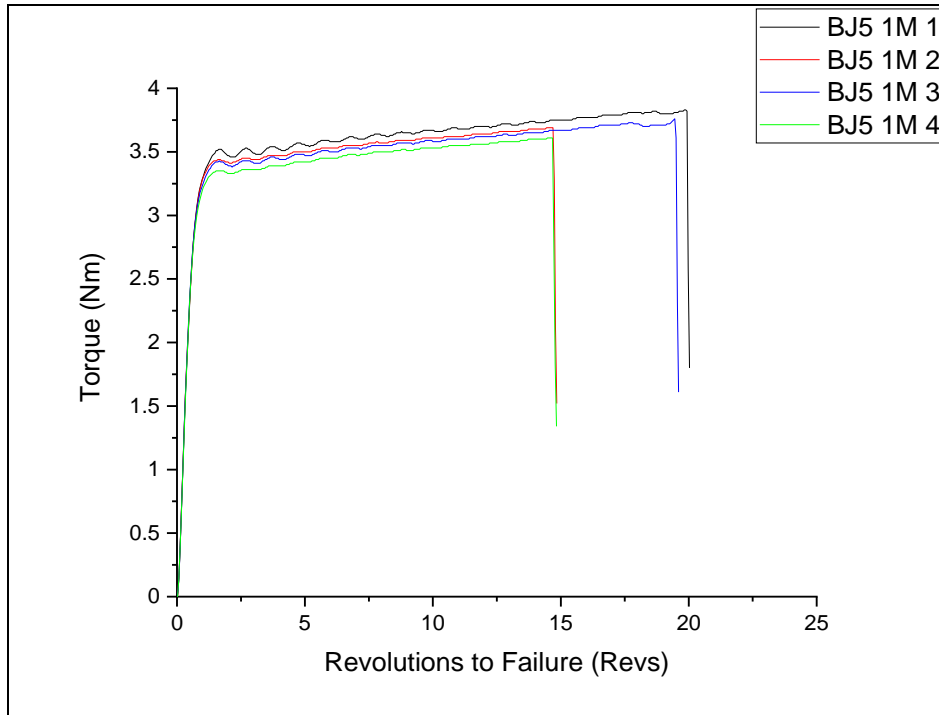


Figure 9:73 - Torsion testing plot of steel BJ5 in the 1 month artificial ageing condition.

Table 9:48 - Torsion testing results of BJ5 in the 1 month artificial ageing condition.

Sample ID	Revolutions to Failure (Revs)	Peak Torque (Nm)	Fracture Type
-	(Revs)	(Nm)	-
BJ5 1M 1	19.98	3.83	A
BJ5 1M 2	14.79	3.69	A
BJ5 1M 3	19.55	3.76	A
BJ5 1M 4	14.78	3.61	A
Mean	17.28	3.72	-
Lower 95% CL	12.69	3.57	-
Upper 95% CL	21.86	3.87	-

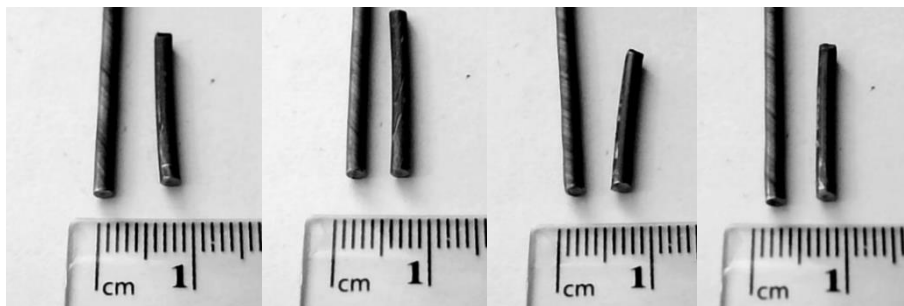


Figure 9:74 - Steel BJ5 1 month artificial ageing condition, type A fractures.

9.3.4.1.3 2 Month Artificial Ageing Condition

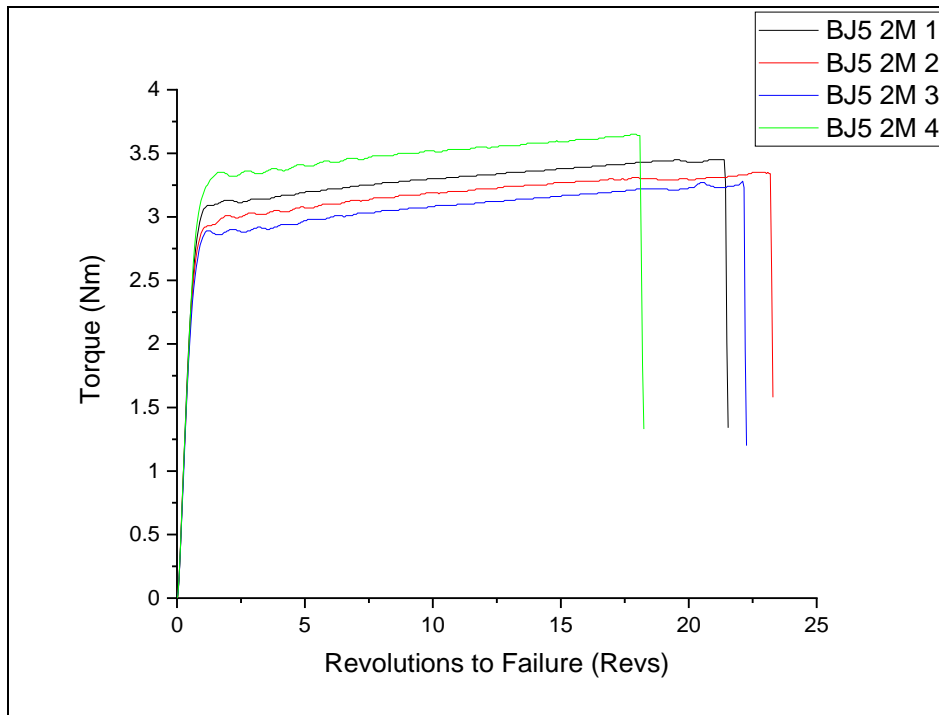


Figure 9:75 - Torsion testing plot of steel BJ5 in the 2 month artificial ageing condition.

Table 9:49 - Torsion testing results of BJ5 in the 2 month artificial ageing condition.

Sample ID	Revolutions to Failure (Revs)	Peak Torque (Nm)	Fracture Type
-	(Revs)	(Nm)	-
BJ5 2M 1	21.49	3.45	A
BJ5 2M 2	23.24	3.35	A
BJ5 2M 3	22.21	3.28	A
BJ5 2M 4	18.19	3.65	A
Mean	21.28	3.43	-
Lower 95% CL	17.81	3.18	-
Upper 95% CL	24.75	3.69	-

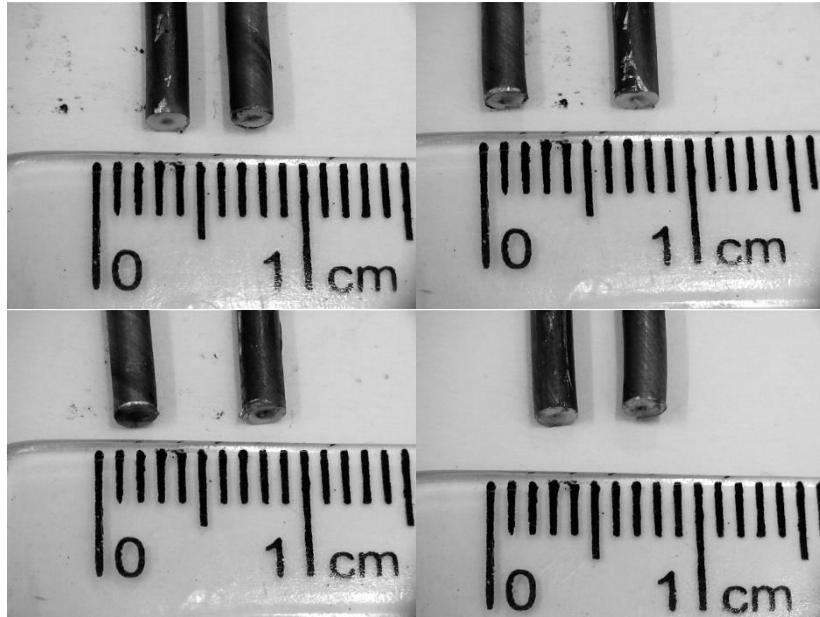


Figure 9:76 Steel BJ5 2 month artificial ageing condition, type A fractures.

9.3.4.1.4 4 Month Artificial Ageing Condition

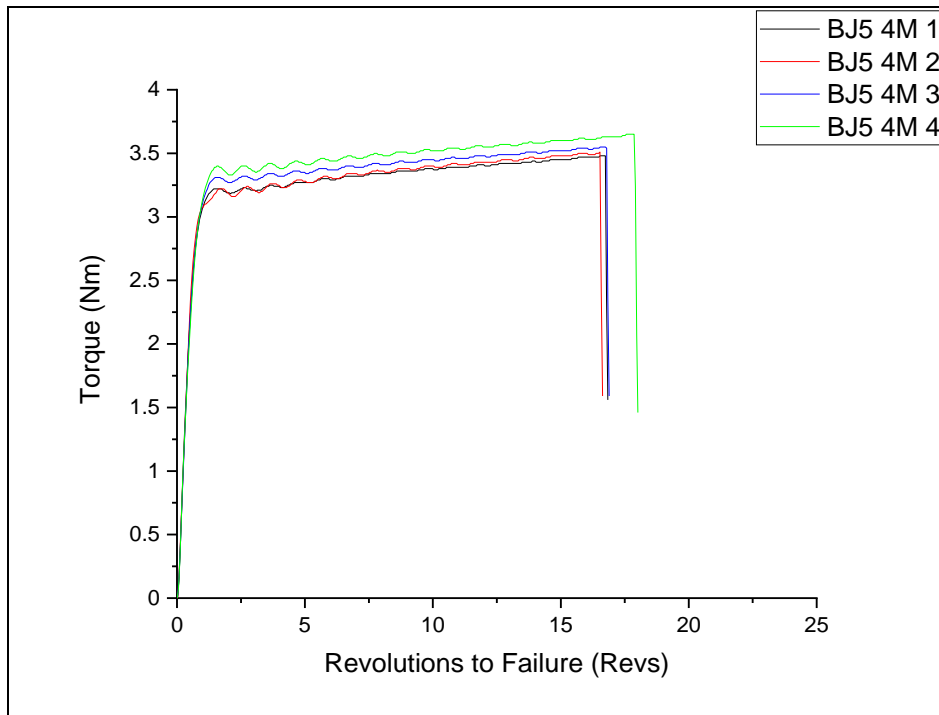


Figure 9:77 - Torsion testing plot of steel BJ5 in the 4 month artificial ageing condition.

Table 9:50 - Torsion testing results of BJ5 in the 4 month artificial ageing condition.

Sample ID	Revolutions to Failure (Revs)	Peak Torque (Nm)	Fracture Type
-	(Revs)	(Nm)	-
BJ5 4M 1	16.79	3.48	A
BJ5 4M 2	16.58	3.51	A
BJ5 4M 3	16.84	3.55	A
BJ5 4M 4	17.96	3.65	A
Mean	17.04	3.55	-
Lower 95% CL	16.05	3.43	-
Upper 95% CL	18.04	3.67	-

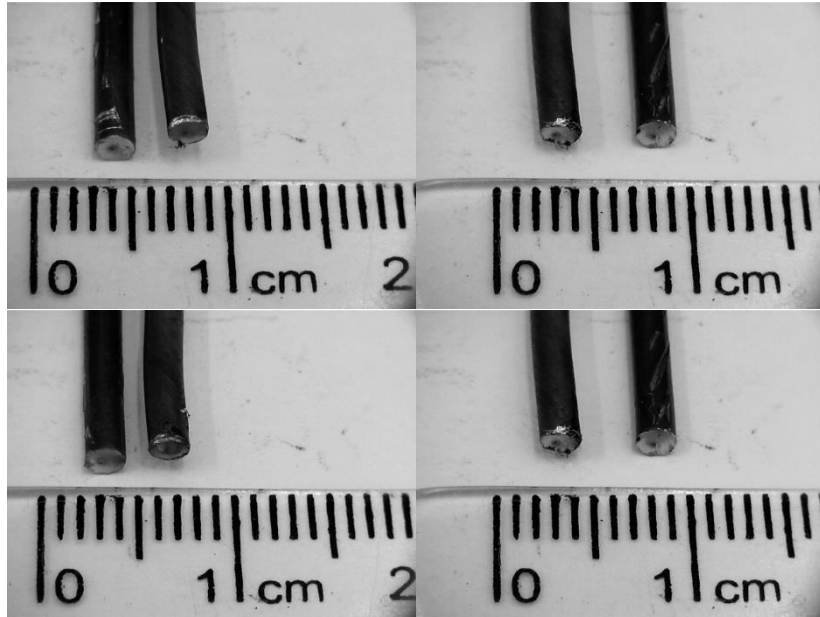


Figure 9:78 - Steel BJ5 4 month artificial ageing condition, type A fractures.

9.3.5 0.8Si + 0.5Ni + 0.1Co + 0.1V Steel (BJ6)

9.3.5.1.1 As-drawn

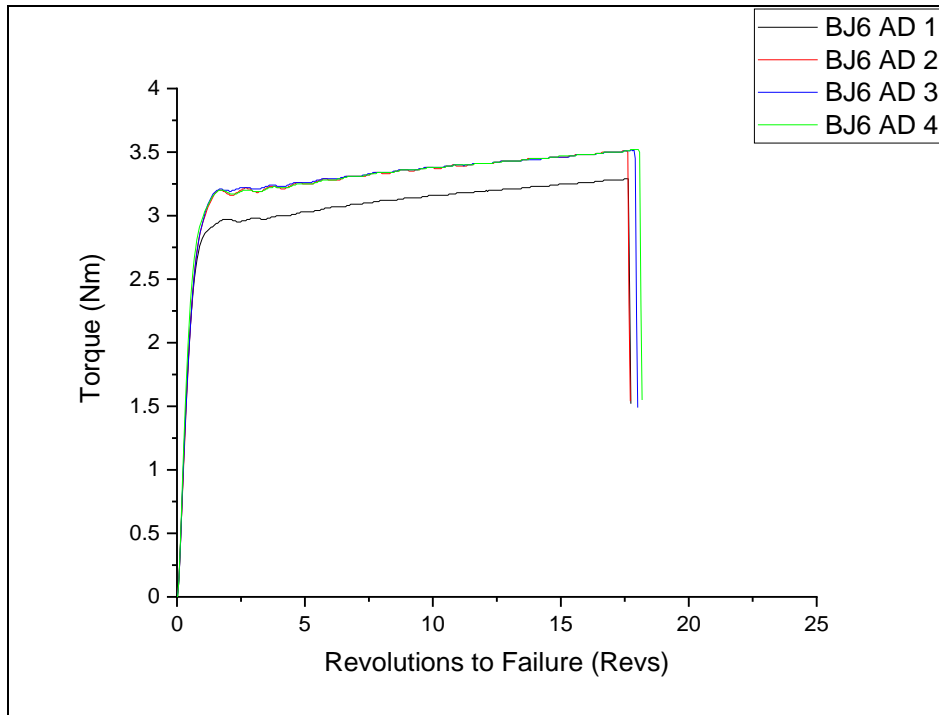


Figure 9:79 - Torsion testing plot of steel BJ6 in the as-drawn condition.

Table 9:51 - Torsion testing results of BJ6 in the as-drawn condition.

Sample ID	Revolutions to Failure (Revs)	Peak Torque (Nm)	Fracture Type
-	(Revs)	(Nm)	-
BJ6 AD 1	17.69	3.29	A
BJ6 AD 2	17.67	3.51	A
BJ6 AD 3	17.96	3.52	A
BJ6 AD 4	18.13	3.52	A
Mean	17.86	3.46	-
Lower 95% CL	17.51	3.28	-
Upper 95% CL	18.22	3.64	-

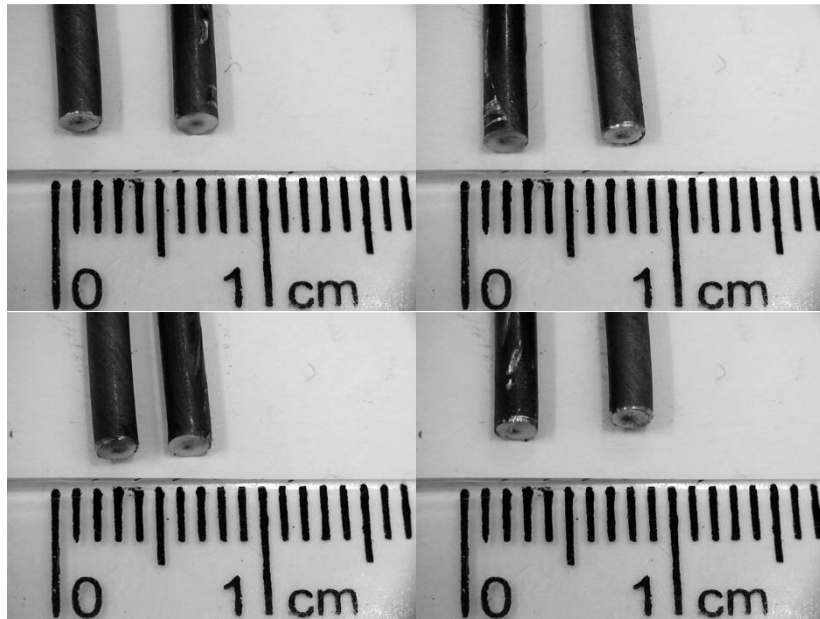


Figure 9:80 Steel BJ6 as-drawn, type A fractures.

9.3.5.1.2 1 Month Artificial Ageing Condition

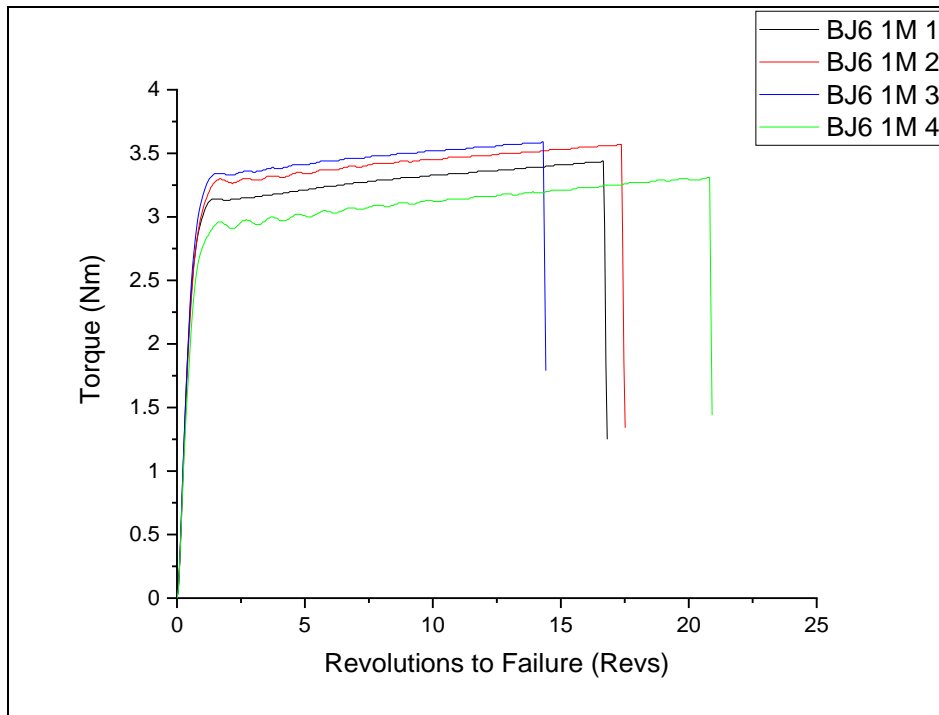


Figure 9:81 - Torsion testing plot of steel BJ6 in the 1 month artificial ageing condition.

Table 9:52 - Torsion testing results of BJ6 in the 1 month artificial ageing condition.

Sample ID	Revolutions to Failure (Revs)	Peak Torque (Nm)	Fracture Type
-	(Revs)	(Nm)	-
BJ6 1M 1	16.76	3.44	A
BJ6 1M 2	17.47	3.57	A
BJ6 1M 3	14.36	3.59	A
BJ6 1M 4	20.86	3.31	A
Mean	17.36	3.48	-
Lower 95% CL	13.09	3.27	-
Upper 95% CL	21.64	3.68	-

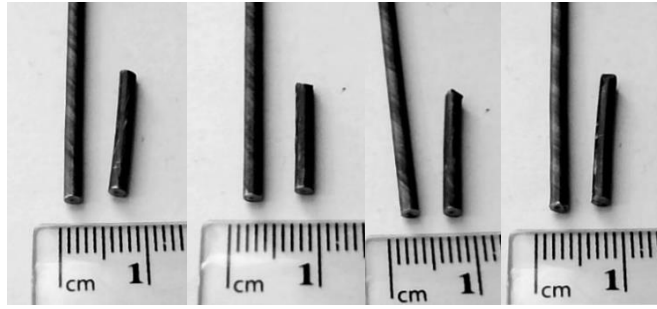


Figure 9:82 Steel BJ6 1 month artificial ageing condition, type A fractures.

9.3.5.1.3 2 Months Artificial Ageing Condition

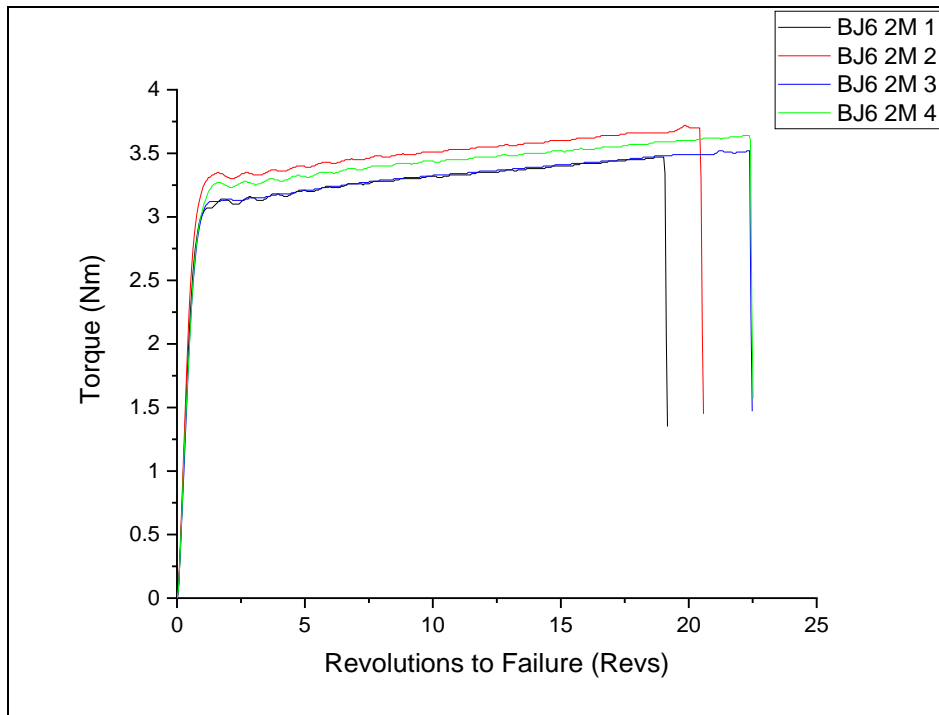


Figure 9:83 - Torsion testing plot of steel BJ6 in the 2 month artificial ageing condition.

Table 9:53 - Torsion testing results of BJ6 in the 2 month artificial ageing condition.

Sample ID	Revolutions to Failure (Revs)	Peak Torque (Nm)	Fracture Type
-	(Revs)	(Nm)	-
BJ6 2M 1	19.12	3.47	A
BJ6 2M 2	20.53	3.72	A
BJ6 2M 3	22.43	3.52	A
BJ6 2M 4	22.47	3.64	A
Mean	21.14	3.59	-
Lower 95% CL	18.56	3.41	-
Upper 95% CL	23.71	3.77	-

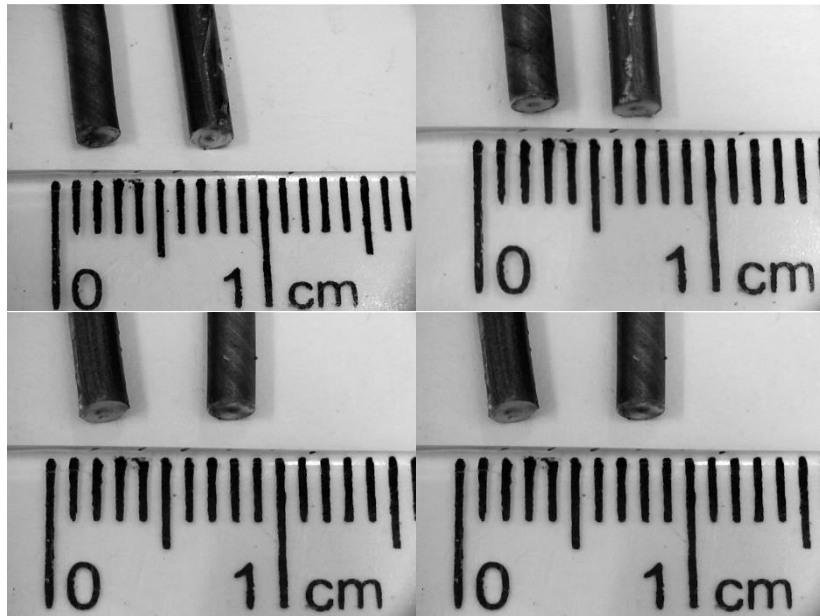


Figure 9:84 - Steel BJ6 3 month artificial ageing condition, type A fractures.

9.3.5.1.4 4 Month Artificial Ageing Condition

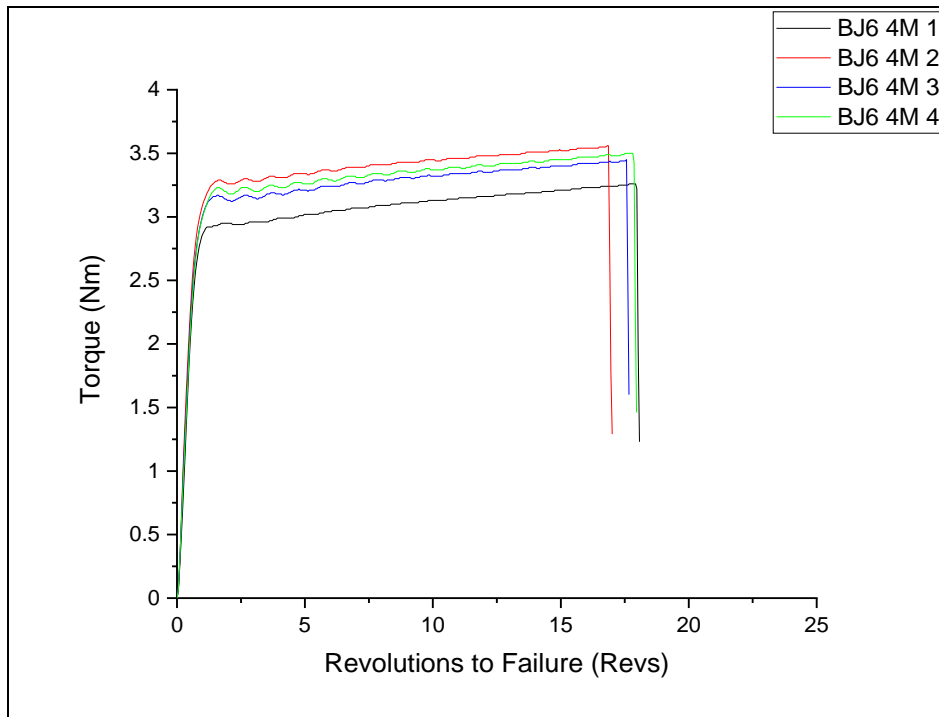


Figure 9:85 - Torsion testing plot of steel BJ6 in the 4 month artificial ageing condition.

Table 9:54 - Torsion testing results of BJ6 in the 4 month artificial ageing condition.

Sample ID	Revolutions to Failure (Revs)	Peak Torque (Nm)	Fracture Type
-	(Revs)	(Nm)	-
BJ6 4M 1	18.02	3.26	A
BJ6 4M 2	16.96	3.56	A
BJ6 4M 3	17.62	3.45	A
BJ6 4M 4	17.91	3.50	A
Mean	17.63	3.44	-
Lower 95% CL	16.87	3.24	-
Upper 95% CL	18.39	3.65	-

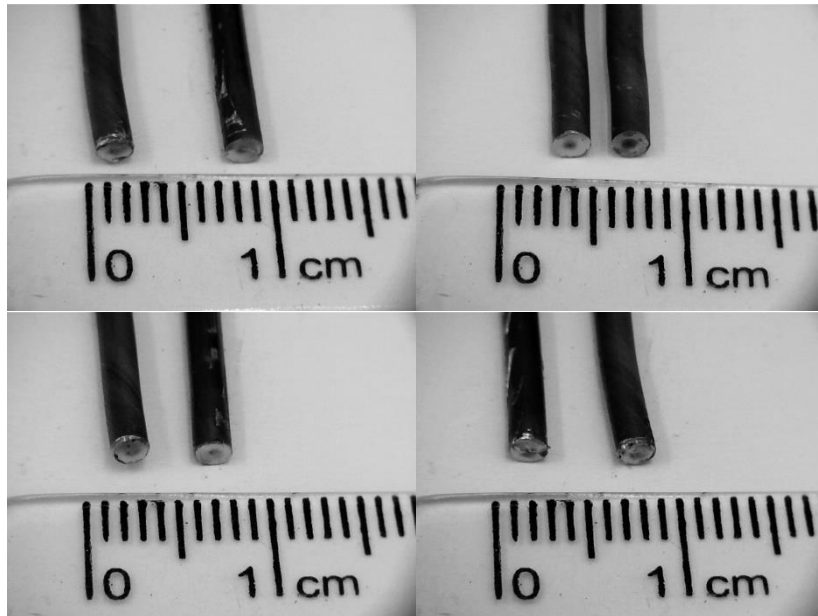


Figure 9:86 - Steel BJ6 4 month artificial ageing condition, type A fractures.

9.4 Differential Scanning Calorimetry Data

9.4.1 Commercial Steel

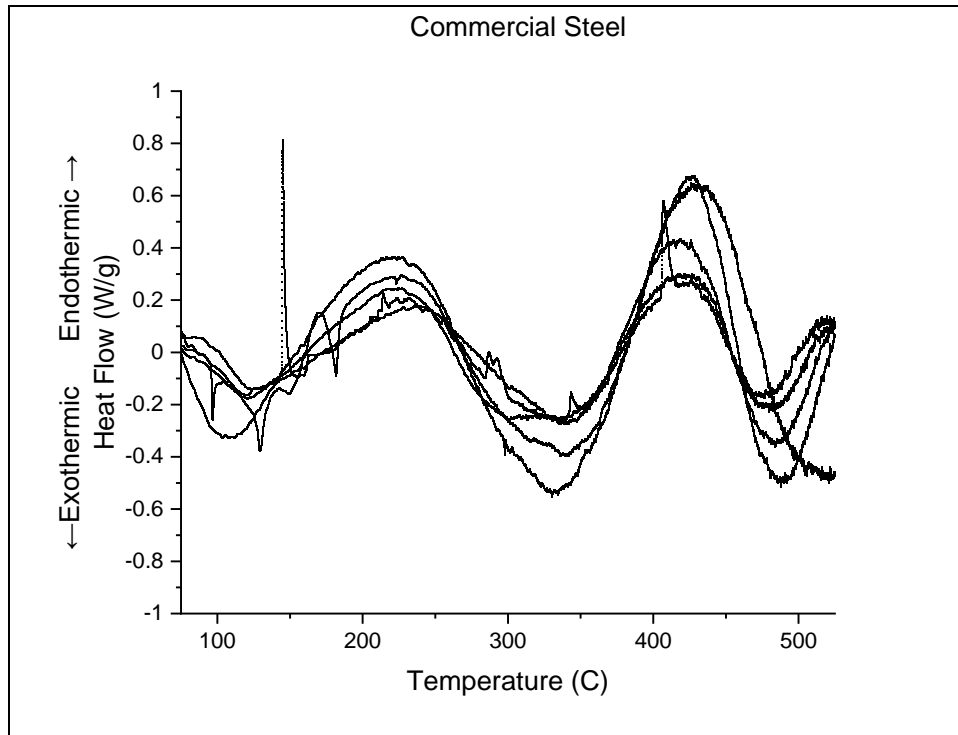


Figure 9:87 - Commercial Steel DSC heat flow plots.

Table 9:55 - Commercial Steel DSC data points.

Sample ID	Peak 1 Temperature (°C)	Peak 1 Enthalpy of Change (J/g) (exothermic)	Peak 2 Temperature (°C)	Peak 2 Enthalpy of Change (J/g) (exothermic)	Peak 3 Temperature (°C)	Peak 3 Enthalpy of Change (J/g) (exothermic)	Peak 4 Temperature (°C)	Peak 4 Enthalpy of Change (J/g) (exothermic)
BJ7 1	107.8	65.9	330.4	111.1	541.1	184.8	-	-
BJ7 2	129.3	33.9	341.7	98.3	488.0	52.7	572.0	8.6
BJ7 3	129.4	22.3	339.5	46.2	476.2	17.3	561.4	28.5
BJ7 4	120.9	30.5	335.0	68.4	483.9	33.3	568.0	13.9
BJ7 5	128.5	17.6	340.5	46.8	479.9	20.9	569.9	24.8
Mean	123.2	34.0	337.4	74.1	493.8	61.7	567.8	19.0
Lower 95% CL	111.6	57.6	331.6	110.9	460.5	-25.2	560.6	4.2
Upper 95% CL	134.8	10.5	343.2	37.4	527.1	148.6	575.1	33.7

9.4.2 0.8 Si Steel (BJ3)

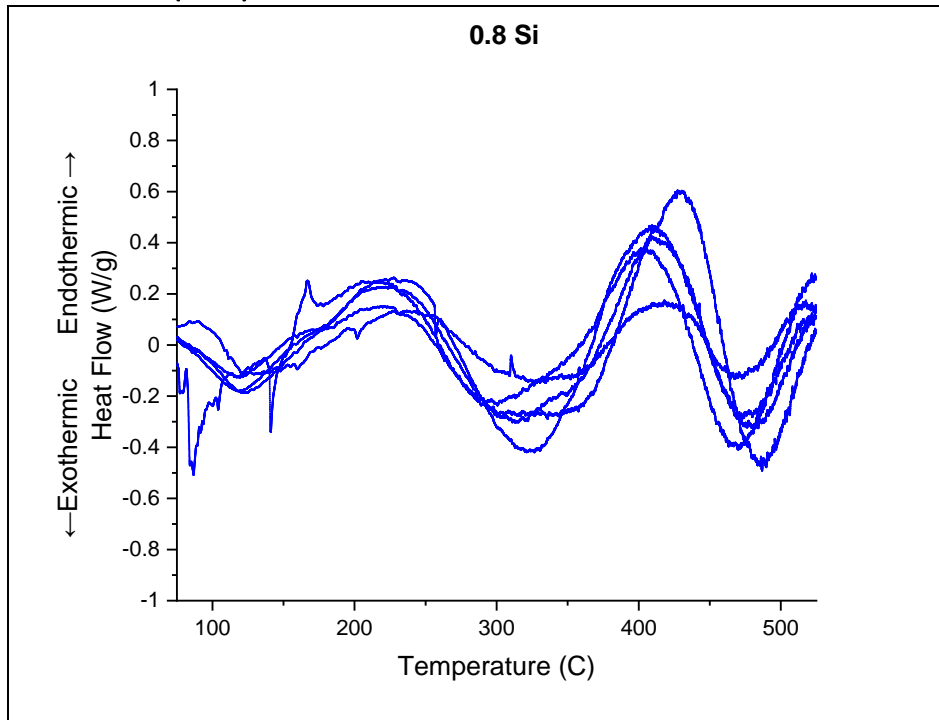


Figure 9:88 - Steel BJ3 DSC heat flow plots.

Table 9:56 - Steel BJ3 DSC data points.

Sample ID	Peak 1 Temperature (°C)	Peak 1 Enthalpy of Change (J/g) (exothermic)	Peak 2 Temperature (°C)	Peak 2 Enthalpy of Change (J/g) (exothermic)	Peak 3 Temperature (°C)	Peak 3 Enthalpy of Change (J/g) (exothermic)	Peak 4 Temperature (°C)	Peak 4 Enthalpy of Change (J/g) (exothermic)
BJ3 1	113.1	43.1	357.6	92.3	486.9	41.4	570.5	11.8
BJ3 2	121.1	15.0	300.7	49.8	470.1	41.6	568.6	17.8
BJ3 3	118.7	29.8	322.2	66.1	470.1	26.6	569.8	23.0
BJ3 4	129.6	15.7	326.5	28.2	467.6	13.4	562.4	35.4
BJ3 5	125.0	29.6	326.6	70.3	473.7	37.3	569.8	17.6
Mean	121.5	26.6	326.7	61.3	473.6	32.0	568.2	21.1
Lower 95% CL	113.8	41.1	301.5	91.1	464.1	17.0	564.1	10.0
Upper 95% CL	129.3	12.2	352.0	31.6	483.2	47.1	572.4	32.2

9.4.3 0.8 Si + 0.5 Ni Steel (BJ4)

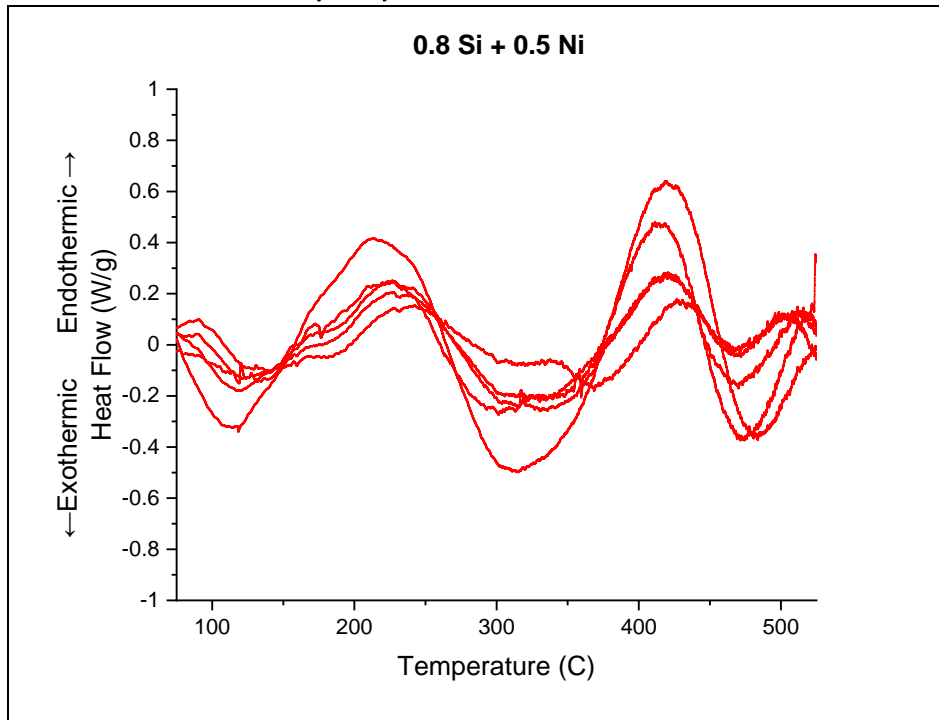


Figure 9:89 - Steel BJ4 DSC heat flow plots.

Table 9:57 - Steel BJ4 DSC data points.

Sample ID	Peak 1 Temperature (°C)	Peak 1 Enthalpy of Change (J/g) (exothermic)	Peak 2 Temperature (°C)	Peak 2 Enthalpy of Change (J/g) (exothermic)	Peak 3 Temperature (°C)	Peak 3 Enthalpy of Change (J/g) (exothermic)	Peak 4 Temperature (°C)	Peak 4 Enthalpy of Change (J/g) (exothermic)
BJ4 1	118.6	57.4	315.3	112.0	480.8	31.8	569.9	29.2
BJ4 2	120.7	27.7	330.6	54.8	464.9	9.5	562.5	54.0
BJ4 3	134.7	33.6	313.3	71.0	469.2	36.0	567.3	19.2
BJ4 4	125.5	19.4	330.4	45.9	470.2	16.1	562.5	28.6
BJ4 5	140.7	19.0	368.6	32.9	464.9	6.4	560.6	27.7
Mean	128.0	31.4	331.7	63.3	470.0	20.0	564.6	31.7
Lower 95% CL	116.3	51.0	304.1	101.3	461.9	3.5	559.8	15.5
Upper 95% CL	139.7	11.9	359.2	25.4	478.1	36.5	569.3	48.0

9.4.4 0.8 Si + 0.5 Ni + 0.1 Co Steel (BJ5)

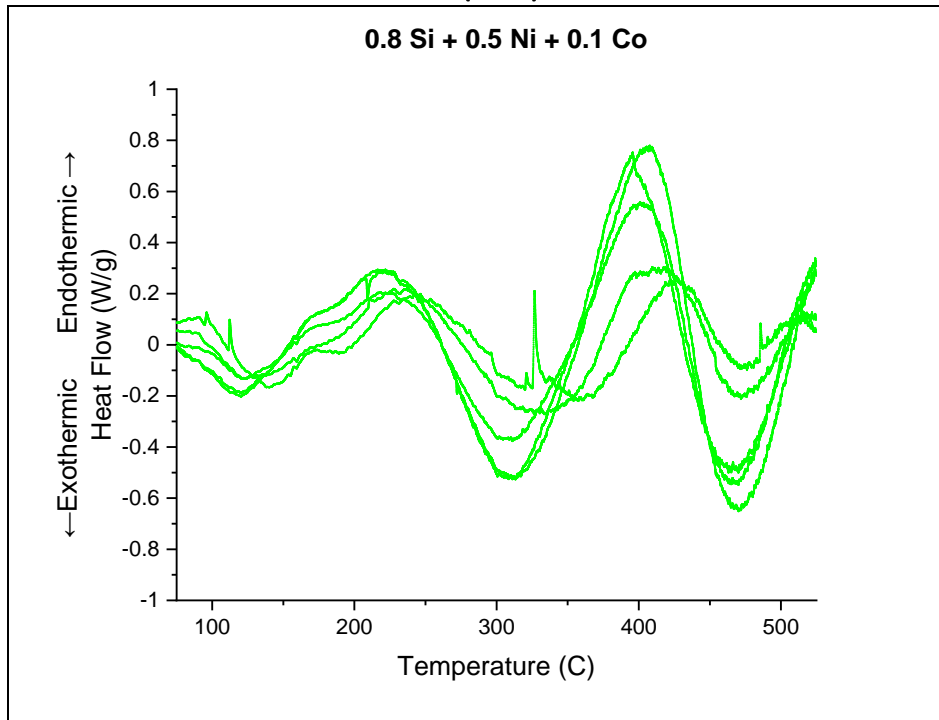


Figure 9:90 - Steel BJ5 DSC heat flow plots.

Table 9:58 - Steel BJ5 DSC data points.

Sample ID	Peak 1 Temperature (°C)	Peak 1 Enthalpy of Change (J/g) (exothermic)	Peak 2 Temperature (°C)	Peak 2 Enthalpy of Change (J/g) (exothermic)	Peak 3 Temperature (°C)	Peak 3 Enthalpy of Change (J/g) (exothermic)	Peak 4 Temperature (°C)	Peak 4 Enthalpy of Change (J/g) (exothermic)
BJ5 1	129.2	21.6	335.1	49.6	471.9	19.6	562.5	31.3
BJ5 2	140.1	23.1	357.7	44.0	471.9	10.5	561.5	33.3
BJ5 3	120.5	39.2	313.4	100.0	464.9	83.3	-	-
BJ5 4	121.2	20.7	311.3	68.3	465.1	61.7	-	-
BJ5 5	120.4	37.1	313.3	94.2	463.2	71.8	585.0	51.0
Mean	126.3	28.3	326.2	71.2	467.4	49.4	569.6	38.5
Lower 95% CL	115.6	39.6	301.2	102.8	462.2	9.1	536.7	11.6
Upper 95% CL	136.9	17.1	351.1	39.7	472.6	89.6	602.6	65.5

9.4.5 0.8 Si + 0.5 Ni + 0.1 Co + 0.1 V Steel (BJ6)

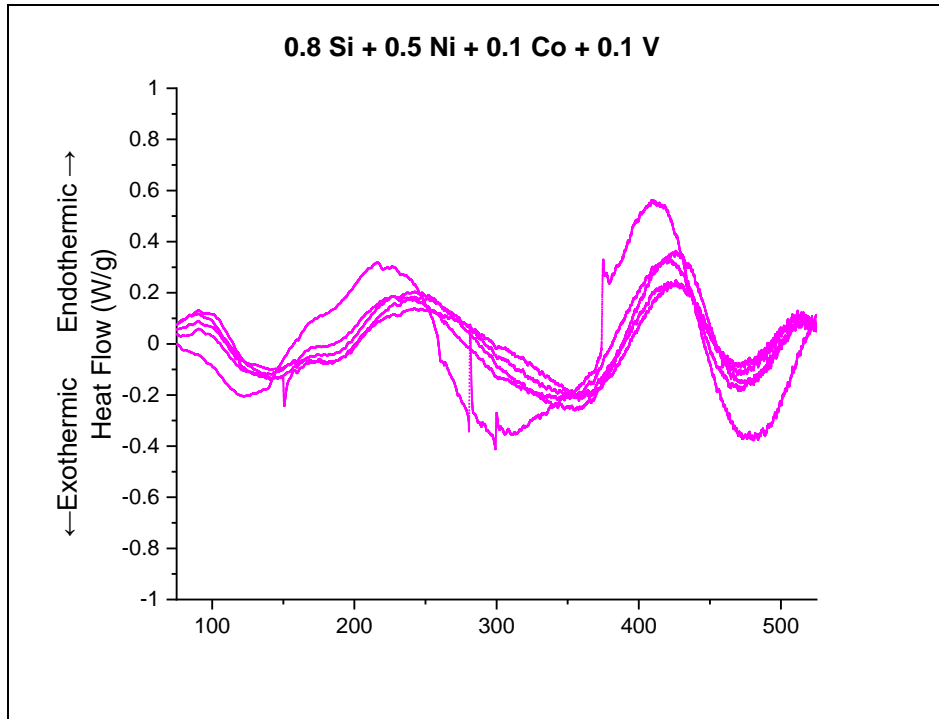


Figure 9:91 - BJ6 DSC heat flow plots.

Table 9:59 - Steel BJ6 DSC data points.

Sample ID	Peak 1 Temperature (°C)	Peak 1 Enthalpy of Change (J/g) (exothermic)	Peak 2 Temperature (°C)	Peak 2 Enthalpy of Change (J/g) (exothermic)	Peak 3 Temperature (°C)	Peak 3 Enthalpy of Change (J/g) (exothermic)	Peak 4 Temperature (°C)	Peak 4 Enthalpy of Change (J/g) (exothermic)
BJ6 1	122.9	40.7	299.3	84.3	472.9	47.8	-	-
BJ6 2	142.3	18.0	347.8	50.4	464.9	18.9	567.3	28.1
BJ6 3	141.4	20.5	355.1	53.7	465.0	17.2	562.5	28.8
BJ6 4	141.4	23.3	358.0	34.9	469.8	12.2	562.5	32.6
BJ6 5	150.8	23.4	360.4	38.1	469.3	13.2	561.8	28.8
Mean	139.8	25.2	344.1	52.3	468.4	21.9	563.5	29.6
Lower 95% CL	152.5	36.3	312.4	76.6	464.1	3.5	559.5	26.3
Upper 95% CL	127.1	14.1	375.8	28.0	472.6	40.2	567.5	32.9